The Dissertation Committee for Sunil George Thomas
certifies that this is the approved version of the following dissertation:

On Some Problems in the Simulation of Flow and Transport through Porous Media

Committee:

Mary F. Wheeler, Supervisor

Todd J. Arbogast

Clinton N. Dawson

Ivan P. Yotov

Steven L. Bryant

On Some Problems in the Simulation of Flow and Transport through Porous Media

by

Sunil George Thomas, B.Tech.; M.S.

DISSERTATION
Presented to the Faculty of the Graduate School of
The University of Texas at Austin
in Partial Fulfillment
of the Requirements
for the Degree of

DOCTOR OF PHILOSOPHY

THE UNIVERSITY OF TEXAS AT AUSTIN
August 2009

To my father, Thomas Koshy.
(03/03/1940 – 01/24/2007)

Acknowledgments

I wish to extend my sincere gratitude to Professor Mary F. Wheeler for advising me through the years on various research topics as well as for introducing to me the subject of sub-surface flow modeling. I would also like to thank my committee members, Professors Todd J. Arbogast, Steven L. Bryant, Clinton N. Dawson, and Ivan P. Yotov for kindly agreeing to serve on my committee as well as for their constructive comments on my research work. It helped streamline the dissertation to a much better shape than it was before. Special thanks go to all the faculty of the Institute for Computational Engineering Sciences (ICES) who have always inspired me to pursue research with great interest. A really special thanks goes to Dr. John Wheeler, who, though I have not had the pleasure of meeting, taught me a whole lot more about reservoir simulation by the sheer volume of work he left behind in the simulator IPARS, than anybody else I can imagine. A note of gratitude is also due to the CSM Industrial affiliates and the various Departments that funded this research.

I would also like to make special mention of research associates Dr. H. Klie, Dr. A. Rodriguez (both currently at Conoco Phillips), Dr. X. Gai (currently at Exxon Mobil Research), and Dr. S. Sun (presently a faculty member at Clemson University) who have advised me at various times during my research. Another special mention goes to post-doctoral researchers, Dr. M. Balhoff (currently a faculty member at the Petroleum Engineering Department at UT Austin), Dr. G. Pencheva, Dr. E. Gildin, Dr. T. Wildey, and Dr. G. Xue, for their collaboration and advise on technical issues and mathematical aspects of this research. I would also like to extend special thanks to Professor M. Delshad for advising me on my research work in compositional flow and applications to the field of petroleum engineering in general. I have benefited a lot from her vast knowledge of the subject. A similar thanks is due to Dr. R. Dean (now at Chevron) for prior work in IPARS and helpful documentation.

I also extend my gratitude to the technical staff of the Texas Advanced Computing Center (Dr. K. Schulz and others) and the IBM technical team (Dr. K. Jordan, Dr. A. Zekulin and others) where I performed many of the parallel computations in this work.

Another special thanks is due to Connie Baxter, Luci Garci, Cynthia Steiner and Stephanie Rodriguez for their administrative help during my studies. A warm thanks also goes to all my friends (Dr. O. Eslinger, Dr. D. Fuentes, Dr. J. Baird, Dr. R. Heath, Dr. J. Rath, Dr. M. Santillana, Dr. J. DeBasabe, Dr. B. Lu, the Florez brothers Horacio and Jorge, and Dr. V. Calo to mention a few) and colleagues in the CAM/CES and many of the other engineering departments. I learnt a lot from their diverse academic and cultural backgrounds and greatly enjoyed their friendship over the years. To anyone whose name I may have forgotten to mention, I sincerely apologise. Finally, I would like to thank my wife, Smitha, for her unconditional love and many sacrifices, my parents for their constant support, and my siblings for their understanding. Thanks to you all for putting up with me during the unusually hard times and long hours that are frequently encountered in graduate studies.

On Some Problems in the Simulation of Flow and Transport through Porous Media

Publication No. ____________________

Sunil George Thomas, Ph.D.
The University of Texas at Austin, 2009

Supervisor: Mary F. Wheeler

The dynamic solution of multiphase flow through porous media is of special interest to several fields of science and engineering, such as petroleum, geology and geophysics, bio-medical, civil and environmental, chemical engineering and many other disciplines. A natural application is the modeling of the flow of two immiscible fluids (phases) in a reservoir. Others, that are broadly based and considered in this work include the hydrodynamic dispersion (as in reactive transport) of a solute or tracer chemical through a fluid phase. Reservoir properties like permeability and porosity greatly influence the flow of these phases. Often, these vary across several orders of magnitude and can be discontinuous functions. Furthermore, they are generally not known to a desired level of accuracy or detail and special inverse problems need to be solved in order to obtain their estimates. Based on the physics dominating a given sub-region of the porous medium, numerical solutions to such flow problems may require different discretization schemes or different governing equations in adjacent regions. The need to couple solutions to such schemes gives rise to challenging domain decomposition problems. Finally, on an application level, present day environment concerns have resulted in a widespread increase in CO_2 capture and storage experiments across the globe. This presents a huge modeling challenge for the future.

This research work is divided into sections that aim to study various inter-connected problems that are of significance in sub-surface porous media applications. The first section studies an application of mortar (as well as non-mortar, i.e., enhanced velocity) mixed finite element methods (MMFEM and EV-MFEM) to problems in porous media flow. The mortar spaces are first used to develop a multiscale approach for parabolic problems in porous media applications. The implementation of the mortar mixed method is presented for two-phase immiscible flow and some *a priori* error estimates are then derived for the case of slightly compressible single-phase Darcy flow. Following this, the problem of modeling flow coupled to reactive transport is studied. Applications of such problems include modeling bio-remediation of oil spills and other subsurface hazardous wastes, angiogenesis in the transition of tumors from a dormant to a malignant state, contaminant transport in groundwater flow and acid injection around well bores to increase the permeability of the surrounding rock. Several numerical results are presented that demonstrate the efficiency of the method when compared to traditional approaches. The section following this examines (non-mortar) enhanced velocity finite element methods for solving multiphase flow coupled to species transport on non-matching multiblock grids. The results from this section indicate that this is the recommended method of choice for such problems.

Next, a mortar finite element method is formulated and implemented that extends the scope of the classical mortar mixed finite element method developed by Arbogast *et al* [12] for elliptic problems and Girault *et al* [62] for coupling different numerical discretization schemes. Some significant areas of application include the coupling of pore-scale network models with the classical continuum models for steady single-phase Darcy flow as well as the coupling of different numerical methods such as discontinuous Galerkin and mixed finite element methods in different sub-domains for the case of single phase flow [21, 109]. These hold promise for applications where a high level of detail and accuracy is desired in one part of the domain (often associated with very small length scales as in pore-scale network models) and a much lower level of detail

at other parts of the domain (at much larger length scales). Examples include modeling of the flow around well bores or through faulted reservoirs.

The next section presents a parallel stochastic approximation method [68, 76] applied to inverse modeling and gives several promising results that address the problem of uncertainty associated with the parameters governing multiphase flow partial differential equations. For example, medium properties such as absolute permeability and porosity greatly influence the flow behavior, but are rarely known to even a reasonable level of accuracy and are very often upscaled to large areas or volumes based on seismic measurements at discrete points. The results in this section show that by using a few measurements of the primary unknowns in multiphase flow such as fluid pressures and concentrations as well as well-log data, one can define an objective function of the medium properties to be determined, which is then minimized to determine the properties using (as in this case) a stochastic analog of Newton's method. The last section is devoted to a significant and current application area. It presents a parallel and efficient iteratively coupled implicit pressure, explicit concentration formulation (IMPEC) [52–54] for non-isothermal compositional flow problems. The goal is to perform predictive modeling simulations for CO_2 sequestration experiments.

While the sections presented in this work cover a broad range of topics they are actually tied to each other and serve to achieve the unifying, ultimate goal of developing a complete and robust reservoir simulator. The major results of this work, particularly in the application of MMFEM and EV-MFEM to multiphysics couplings of multiphase flow and transport as well as in the modeling of EOS non-isothermal compositional flow applied to CO_2 sequestration, suggest that multiblock/multimodel methods applied in a robust parallel computational framework is invaluable when attempting to solve problems as described in Chapter 7. As an example, one may consider a closed loop control system for managing oil production or CO_2 sequestration experiments in huge formations (the "instrumented oil field"). Most of the computationally costly activity occurs around a few wells. Thus one has to be able to seamlessly connect the above components while running many forward simulations on parallel clusters in a multiblock and multimodel setting where most domains employ an isothermal single-phase flow model except a few around well bores that employ, say, a non-isothermal compositional model. Simultaneously, cheap and efficient stochastic methods as in Chapter 8, may be used to generate history matches of well and/or sensor-measured solution data, to arrive at better estimates of the medium properties on the fly. This is obviously beyond the scope of the current work but represents the over-arching goal of this research.

Table of Contents

List of Tables

List of Figures

Chapter 1

Introduction

1.1 Motivation

Finite element methods (FEM) have been successfully applied to several areas of science and engineering over the last 60 years - in particular to modeling fluid flows through porous media, which is the subject of this work. Mixed FEM [142] (MFEM) and variants thereof, emerged among these methods as the more common methods of choice because of their local mass conservation property and better approximation of the flux variable. In most real-world problems, however, the properties of the medium vary on two distinct scales: a fine or microscopic scale and a coarse or macroscopic scale. In addition, these properties can be discontinuous; for e.g., the permeability across stratified subsurface layers. The mortar MFEM (MMFEM) [12, 15] is proving to be an efficient numerical scheme in the areas of multiscale flow modeling, since it offers all the features that the mixed method enjoys such as local mass conservation and accurate approximation of fluxes that are continuous across inter-element faces and sub-domain interfaces while lending itself easy to implement in parallel. Similarly methods such as enhanced velocity MFEM (EVMFEM) [136], that enjoy the useful features of MMFEM, offer very attractive alternatives in multiblock modeling of couple flow and transport through porous media, as presented in this work.

The MMFEM theory is now well established for the case of single phase incompressible flow [15]. More recently, the extension to slightly compressible single phase flow has been developed in [91] and is presented here for completeness. This research also extends the analysis and implementation of the theory of MMFEM to transient flow problems, with the focus being on miscible displacement applications such as the solute transport problem. Moreover, in many applications it is desirable to allow for different numerical approximation schemes and/or different physical models via different governing partial differential equations (PDEs) based on the physics prevailing in adjacent sub-domains. Examples of such problems include the coupling of porescale and continuum-scale discretizations of single phase flow or the coupling of mixed FEM and discontinuous Galerkin (DG) FEM in adjacent sub-domains. Consequently, this research examines the theory and implementation of coupling such physics/numerics using mortar finite element spaces. Results to potential future applications in the oil/gas industry are also demonstrated.

The first problem is the application of mortar and non-mortar methods (EV-MFEM) for solving coupled multiphase flow and transport problems. A related problem is the study of MFEM for spatial discretization and an iteratively coupled implicit pressure, explicit concentration formulation (IMPEC) for time discretization to model [52–54] highly complex compositional flow. A natural application of this problem is in the modeling of CO_2 sequestration experiments [18], many of which are either planned or underway at various sites across the globe. The last few decades have witnessed a widespread increase in emissions of "greenhouse" gases by most of the major developing nations of the world. The greenhouse gases comprise CO_2, CH_4, water vapor, N_2O, O_3 and chlorofluorocarbons (CFCs) of which CO_2 is the main human influenced contributor [72] by effect (26%). The other major contributors are water vapor (65%) and ozone (8%) and the rest from trace gases. The increase in emissions of greenhouse gases has therefore put the Earth's atmosphere at peril and has contributed to global warming as well as several other environmental concerns.

The sequestration of CO_2 in the subsurface is widely recognized today as the most feasible and economical method to counter the threat of global warming caused by the widespread consumption of fossil fuels by the major developing nations of the world. But the impact and consequences of injecting massive volumes of CO_2 into the subsurface is poorly understood. For instance, injected CO_2 can leak out of poorly sealed (leaky) abandoned wells in the proximity of the injection well. This could render the whole experiment futile and waste a lot of time and money. CO_2 injection is usually carried out in the supercritical state several thousand feet below the surface, typically beneath impearmeable shale barriers. After the CO_2 is injected it can flow horizontally until it reaches faults in the subsurface from where it can rise to surface. As it rises, the CO_2 can undergo dramatic change in properties as it changes in state due to pressure and temperature changes. Hence, an efficient equation of state (EOS) non-isothermal compositional model is imperative in order to accurately predict the flow of CO_2 in the subsurface, whether it is for capture and storage or for enhanced oil/gas recovery (EOR/EGR) operations. Examples of such problems with computations performed on different parallel clusters are presented in Chapter 7.

The second problem presented is one commonly encountered in porous media flow modeling, i.e., the uncertainty associated with medium properties such as permeability and porosity. While some crude understanding of the rock properties can be obtained from lab studies on core samples or seismic imaging experiments, these are often inadequate for the purpose of modeling multiphase flow. To that end, this research also studies the problem of parameter estimation and presents attractive results using a parallel algorithm implementing a simultaneous perturbation, stochastic approximation (SPSA) method. The main idea behind the method is to find a reduced system that characterizes a number of prior realizations of the rock properties using methods such as principle component analysis (sometimes also called the "Karhunen-Loève" transform or "proper orthogonal decomposition (POD)" depending on the applications). Some details can be found in [71, 108]. Then any given realization can be expressed as a linear combination of the eigen basis resulting from the reduced system. The coefficients are then determined by seeking a vector of unknowns that minimizes an objective function that measures a weighted time and space integrated error between observed measurements (such as pressures, concentrations, well log data, etc.) and calculated solutions [68, 76]. This is achieved by using the parallel SPSA method in this work. Results from several challenging problems with computations performed on parallel clusters are presented in Chapter 8.

The major results of this work, particularly in the areas of multiphysics coupling of flow and reactive transport using MMFEM and EV-MFEM as well as in the EOS compositional flow modeling applied to CO_2 sequestration, together serve to justify the importance of studing multiblock methods such as mortar FEM and non-mortar FEM such as EV-MFEM for physical domain decomposition. These methods when applied in a multimodel setting within a robust parallel computational framework, may prove to be invaluable for solving such real-world problems. In such problems fine grids are typically required in several small parts of the domain (around wells, etc.) and coarser grids can be used elsewhere, thus making these methods ideal candidates for the job. The nature of the problem (size and data) allows a multiblock/multimodel approach to be employed with non-matching grids across blocks and complex models (such as EOS compositional flow) restricted to regions (blocks) where a majority of the physical dynamics occurs while simpler (and cheaper) models (such as single phase flow) are employed in a majority of the domain.

1.2 Literature review

Flows through porous media have been studied extensively during the last century. Among the classical works in this area are those of Muskat [94, 95], Bear [23] and DeWiest [55]. Numerical methods to solve equations governing porous media flow fall broadly under the finite difference and finite element categories. One of the earliest works in finite differences is that of Peaceman and Rachford [107], which has significantly impacted the work of petroleum engineers and has since spawned several books and papers. Variational methods were studied extensively during the end of the 19th and early 20th centuries for deformation problems on plates and shells by Rayleigh, Galerkin and others like [42, 117]. After the formal introduction of the theory of finite elements

[150], most research work in hydrology and civil engineering has shifted in that direction because of its greater flexibility and ability to solve a much broader class of problems. However, only in the last couple of decades has finite elements become a major research topic in reservoir engineering, where the traditional approach has been cell-centered finite differences.

Mixed finite element methods were introduced as a numerical method to solve systems of elliptic partial differential equations in the late 70s. The mixed method leads to the formulation of a saddle-point problem in the unknowns, velocity and pressure. Their advantage over Galerkin methods lie in the better approximation of the flux variable and the satisfaction of local mass conservation, both of which are of utmost importance in reservoir simulation. For the analysis and implementation of the classical mixed finite element method applied to the class of linear elliptic problems such as in the case of incompressible single phase flow, the reader is referred to [96, 116]. Non-linear elliptic problems using mixed methods have been successfully treated in [103, 105]. In [122], Russell and Wheeler established that special quadrature rules reduce the lowest order mixed methods on rectangles to cell-centered finite differences. The convergence as well as super-convergence properties of mixed methods are now well-understood for most problems [15, 142].

Expanded mixed finite element methods were introduced in [16] to handle full-tensor coefficients on rectangles after generalizing the result of Russel and Wheeler [122]. Mixed finite elements have also been applied to quadrilateral grids using a generalization of the multi-point flux approximation [147]. Therein, all computations are performed on a regular grid after mapping the problem to a reference domain. Under assumptions of smoothness of the map, optimal convergence results can be obtained for pressure and flux [142]. But in most applications, the medium is highly heterogeneous and the permeability field is very discontinuous. Thus, a natural choice in describing such problems is to use a multiblock structure. In such a formulation, extra unknowns called “Lagrange multipliers” are introduced along sub-domain interfaces as boundary conditions for the sub-domain problems. Often, non-matching grids are needed in adjacent sub-domains. This allows for greater flexibility in describing irregular geometries. This is closely related to the domain decomposition method for mixed finite element methods introduced in [63]. One of the early "mortar finite element methods" is analysed in [25], using the Galerkin finite element method.

The mortar method in a mixed finite element setting was first introduced by Kuznetsov and Wheeler [79] for the incompressible single phase problem. Further analysis was carried out in [12, 142]. Existence of a weak solution to an incompressible model for multiphase flow was investigated in [10, 11]. A common approach taken to modeling multiphase flow is to re-write the system as a pressure and saturation equation in primary unknowns. The latter is a degenerate advection-diffusion equation since the diffusion term vanishes when $S = 0, 1$. The mixed method was extended to the case of a non-linear degenerate parabolic equation arising in two phase flow in a single block domain by Arbogast *et al* [17] and to the case of non-matching multiblock grids by Yotov [143]. In both these works, the degeneracy in the diffusion term is handled using a Kirchoff transform. Recently, the nonlinear compressible single phase problem is studied in [91] and some error estimates are derived as well as presented in this work.

Owing to the complexity of multiphase compositional flow equations coupled to an equation of state and phase equilibrium thermodynamics, very little theory of convergence of finite difference or finite element methods exist. Some classical references in this area include those by Coats [40], Watts [135] and Acs [5] and their collaborators. An analysis of some numerical methods for the compositional model due to Chen, Ewing and collaborators can be found in [34, 35, 37]. A defining reference in the field of equation of state compositional modeling and its applications is the work of Yih-Bor Chang [33]. An extension of this work to the case of non-isothermal compostional flow including treatment of steamflooding can be found in [26, 27]. The latter two deal with fully-implicit methods and can be quite expensive for the large problems that are commonly encountered in CO_2 sequestration experiments or multiphase flow problems.

This work presents an efficient iteratively coupled pressure-concetration formulation for flow that is sequentially coupled to thermal energy balance and chemistry.

There are a variety of methods available for parameter estimation and inverse modeling in reservoir simulation. A classical reference is due to Ewing and George [58]. A review of the progress made and some "current" work undertaken is given in [101]. The Ensemble Kalman Filter method has been proposed in [100]. Adjoint or gradient based methods are applied in [123]. Representer methods have been extensively researched by Dawson and Baird for single- and two phase Darcy flow [19, 45, 46]. Multiscale methods for uncertainty quantification have been explored using gradient based methods in [2] as well as stochastic optimization based methods in [77]. In general, the computation of adjoint or gradients for multiphase Darcy flow is a challenging task. Stochastic methods [126] that take advantage of prior ensemble of realizations (or measurements) appear to be more effective in this regard. In such methods an eigen basis is constructed from the ensemble of realizations using the principle component analysis [71, 108] or wavelet analysis [88]. The current research extends the results presented in previous publications by the author [68, 76, 77] as well as others [118] to the case of more challenging problems while introducing and applying a parallel algorithm to increase the computational efficiency.

1.3 Thesis layout

The remainder of the thesis is organized in chapters as follows. Chapter 2 formulates transient multiphase flow problems in porous media. The equations governing immiscible and miscible fluid flow are presented. Some basic definitions and constitutive laws are stated. Chapter 3 describes a domain decomposition method using mortar spaces and presents a brief analysis on immiscible two phase flow using an expanded mixed finite element weak formulation. Error estimates are derived for the case of slightly compressible single phase flow. An analysis is presented for the miscible displacement problem (the solute transport problem) using mortar mixed methods for flow and a projection based method for transport. Some numerical examples are presented for the case of coupled flow and transport on non-matching multiblock grids showing the advantage of using such an approach. Chapter 4 presentes an alternative to MMFEM - the enhanced velocity mixed finite element method (EVMFEM) for solving coupled multiphase flow-transport problem on non-matching multiblock grids. Convergence analysis including error estimates for the unsteady flow as well as the coupled flow and transport problem is presented. Several numerical examples are presented for validation and to demonstrate its advantages over the MMFEM.

Chapter 5 presents a formal analysis of the coupling of discontinuous Galerkin FEM (DGFEM) and MFEM using mortars for the case of slightly compressible single phase flow. Implementation methods and several numerical examples simulating real world problems are presented. Chapter 6 presents a formal analysis of the coupling of porescale network models and continuum scale models for steady single phase flow. Implementation details, error computation experiments and some numerical examples modeling practical problems are also presented to justify the study. Chapter 7 presents an iterative coupled IMPEC method discussed in Section 1.1 above. Many validation examples as well as results from many challenging benchmark and field tests are also presented therein. Chapter 8 concludes by presenting analysis, implementation and numerical results in reservoir parameter estimation from some challenging examples using the SPSA method discussed in Section 1.1. Finally Chapter 9 presents some concluding remarks and future works.

Chapter 2

Dynamics of multiphase flow through porous media

This chapter presents the basic transient multiphase flow equations for porous media applications. For simplicity, the focus is on the two-phase flow problem. Some of the commonly used terms arising in the development of the governing equations are defined in [57]. In essence, the equations form a system of degenerate parabolic partial differential equations, comprising of a mass conservation statement and a constitutive law; in this case, Darcy's law relating the phase flux to phase pressure gradients. For a classical treatise, the reader is referred to the works of Bear and Muskat [23, 94, 95]. There are two basic kinds of multiphase flow:

Immiscible displacement. In this type, there is a simultaneous flow of two or more immiscible fluids (e.g., oil and water) in the porous medium. The surface tension between the two fluids is non-zero and a distinct interface separates the two phases within every pore. There is a capillary pressure difference across the interface.

Miscible displacement. Here, the two fluids (phases) are completely soluble in one another. The surface tension between the two fluids is zero. A distinct interface does not exist between the two phases within any pore. It is sometimes referred to as "hydrodynamic dispersion".

2.1 Immiscible displacement

When two immiscible fluids are in contact in the interstices of a porous medium, a discontinuity in pressure exists across the interface separating them.

This difference is called “capillary pressure”, given by,

$$p_c \equiv p_c(S_w) = p_{nw} - p_w, \tag{2.1}$$

where p_{nw} is the pressure of the non-wetting phase and p_w is the pressure of the wetting phase. It is safely assumed to be a function of phase saturation, although it actually depends on the direction of saturation change (drainage or imbibition) as well. There are several empirical formulas that specify the relationship between p_c and S_w [23]. A typical curve is shown in Figure 2.1.

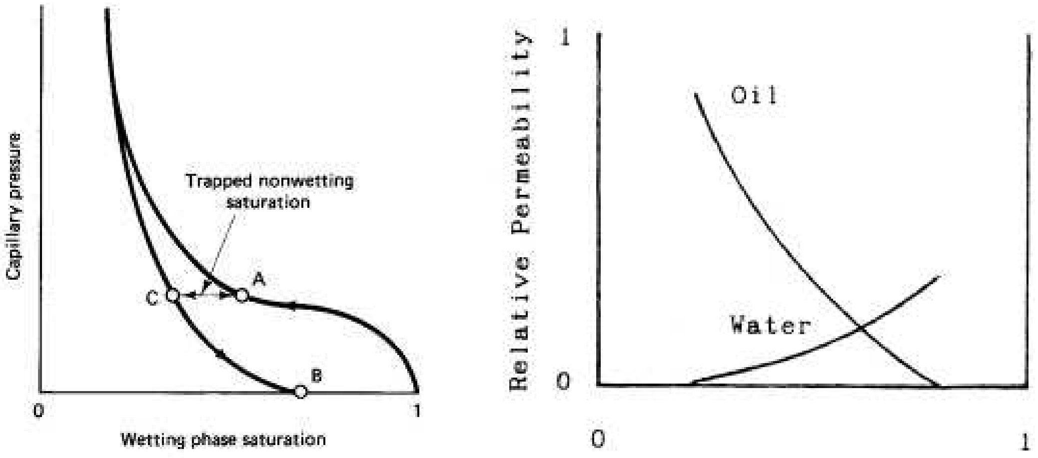

Figure 2.1: Example of typical capillary pressure (left) and relative permeability curves (right)

From experiments, it is now understood that when two immiscible fluids flow simulateneously through a porous medium, each follows its own “preferred” channel. These channels vary at different levels of saturation of the individual phases. Hence it makes sense to apply the concept of permeability established for single phase flow [142], adjusting its value to accomodate the presence of the second phase. After a steady flow is reached for both phases, it is assumed that Darcy’s law holds for each phase. Thus for each phase α, the Darcy velocity, $\mathbf{u}_\alpha$ and its mass flux form (extensive), $\hat{\mathbf{u}}_\alpha$ are given by

$$\mathbf{u}_\alpha = -\frac{\mathbf{K}_\alpha}{\mu_\alpha}[\nabla p_\alpha - \rho_\alpha \mathbf{g}]; \quad \hat{\mathbf{u}}_\alpha = \rho_\alpha \mathbf{u}_\alpha. \tag{2.2}$$

In (2.2), ρ_α, μ_α denote the density and viscosity, respectively, of phase α; $\mathbf{g}$ is the acceleration due to gravity vector. Further, $\mathbf{K}_\alpha$ is the "effective" permeability of phase α. This clearly depends on the porous medium, i.e., the permeability of the porous medium to a single-phase fluid that saturates it completely. This is described by introducing the concept of relative permeability given for phase α by

$$\mathbf{K}_\alpha = \kappa_{r\alpha}\mathbf{K}. \tag{2.3}$$

The function $\kappa_{r\alpha}$ indicates the tendency of phase α to wet the porous medium. Typically $\kappa_{r\alpha}$ is measured through idealized capillary tube models by conducting experiments in which two fluids are pumped at a constant rate through a horizontal porous medium column of given cross-section and finite length. For more details on such experiments, the reader is referred to [23]. For most practical purposes, the relative permeability is assumed to be a function of phase saturation alone. However, it also depends on the direction of saturation change, i.e., there is a hysteresis effect. An example of a typical relative permeability curve is shown in Figure 2.1.

2.1.1 Continuity equations

The mass conservation equation for phase α, with density ρ_α, saturation S_α, flowing through a porous medium with a porosity of ϕ, can be derived from first principles and is given by

$$\frac{\partial(\phi S_\alpha \rho_\alpha)}{\partial t} + \nabla \cdot \hat{\mathbf{u}}_\alpha = \hat{q}_\alpha, \tag{2.4}$$

where $\hat{q}_\alpha$ is the source term. The porous medium is assumed non-deformable in (2.4). In general, however, this may not be true, in which case, ϕ is a function of pressure. The density ρ_α is in general a function of phase pressure and temperature, and is given by the equation of state

$$\rho_\alpha \equiv \rho_\alpha(p_\alpha, T_\alpha). \tag{2.5}$$

For most fluids, the equation of state takes the simple form

$$\rho_\alpha = \frac{p_\alpha}{RT_\alpha}; \quad \frac{\partial \rho_\alpha}{\partial p_\alpha} = \frac{\rho_\alpha}{p_\alpha}; \quad \beta_\alpha = (\frac{1}{\rho_\alpha})\frac{\partial \rho_\alpha}{\partial p_\alpha} = \frac{1}{p_\alpha}, \tag{2.6}$$

where β_α is the phase compressibility. For liquids, this is small and assumed approximately independent of pressure. Then from (2.6) one arrives at

$$\rho_\alpha = \rho_{\alpha 0} \exp[\beta_\alpha (p_\alpha - p_{\alpha 0})]. \tag{2.7}$$

In a similar manner the viscosity, μ_α in (2.2) of the phase α measures the resistance to shear in flow. It is, in general, a function of phase pressure and temperature and for isothermal flow it is given by the equation of state (for specific constitutive laws, the reader is referred to [23])

$$\mu_\alpha \equiv \mu_\alpha(p_\alpha, T_\alpha) = \mu_\alpha(p_\alpha). \tag{2.8}$$

2.1.2 Problem statement

Following the discussion above and writing the phase velocity $\hat{\mathbf{u}}_\alpha$ in terms of phase pressure p_α using Darcy's Law, the saturation constraint, the equations of state for density and viscosity, the equations of continuity (or mass balance) and the capillary pressure relation, the problem of the flow of two compressible immiscible phases or fluids in an anisotropic porous medium reduces to the solution of

$$\begin{aligned}
\frac{\partial(\phi S_\alpha \rho_\alpha)}{\partial t} + \nabla \cdot \hat{\mathbf{u}}_\alpha &= \hat{q}_\alpha, \ \alpha = \ w, nw && \text{in} \quad \Omega \times J, \\
\hat{\mathbf{u}}_\alpha &= -\frac{\rho_\alpha \mathbf{K} \kappa_{r\alpha}}{\mu_\alpha} \left[\nabla p_\alpha - \rho_\alpha \mathbf{g} \right], \ \alpha = \ w, nw && \text{in} \quad \Omega \times J, \\
\sum_\alpha S_\alpha &= 1, \\
p_{nw} - p_w &= p_c(S_w),
\end{aligned} \tag{2.9}$$

for the unknowns p_α, S_α. Here $\Omega \subset \mathbb{R}^d$, $d = 2, 3$ is the computational domain and $J = [0, T]$ denotes the time interval over which the solution is sought. In its mixed form, solution is sought for p_α, $\mathbf{u}_\alpha$ and S_α. A solution can be obtained to the initial value problem (2.9) only if appropriate initial and boundary conditions are provided. The phases are typically assumed to be in hydrostatic equilibrium at initial time. Hence the initial conditions take the form

$$\begin{aligned}
p_\alpha &= p_{\alpha,0} \quad \text{in } \Omega \times \{0\}, \quad \alpha = w \text{ or } nw, \\
S_\alpha &= S_{\alpha,0} \quad \text{in } \Omega \times \{0\}, \quad \alpha = w \text{ or } nw.
\end{aligned} \tag{2.10}$$

Dirichlet boundary conditions take the form

$$\begin{aligned} p_\alpha &= p_\alpha^D \quad \text{on} \quad \partial\Omega^D \times J, \quad \alpha = w \text{ or } nw, \\ S_\alpha &= S_\alpha^D \quad \text{on} \quad \partial\Omega^D \times J, \quad \alpha = w \text{ or } nw, \end{aligned} \tag{2.11}$$

and Neumann boundary conditions take the form

$$\mathbf{u}_\alpha \cdot \mathbf{n} = u^N \quad \text{on} \quad \partial\Omega^N \times J, \quad \alpha = w, nw, \tag{2.12}$$

where $\partial\Omega^D, \partial\Omega^N$ represent the Dirichlet and Neumann portions, respectively, of the boundary of the computational domain, $\partial\Omega$. Different assumptions for different flow scenarios lead to some well known continuity equations; for e.g., the Buckley-Leverett assumptions, the unsaturated flow assumption and many others. For more details and solution methods, the reader is referred to the classical treatises of Bear and Muskat [23, 94, 95].

2.2 Miscible displacement

In a saturated flow, where only one phase is flowing through a porous medium, consider a certain mass of solute (tracer chemical, etc.) released from a specified location in the flow domain. It is known from experiments that the tracer gradually spreads (it is typically identified by its color, density or some other distinctive property) over an increasing portion of the flow domain. This phenomenon is called "hydrodynamic dispersion" and is an unsteady, irreversible process. The sharp interface that separates the tracer from the rest of the fluid at initial time gets smeared out gradually into a transition zone. The tracer concentrations within the zone varies from that of the tracer at the source to the unmarked liquid at the other end.

The location of the interface can be calculated using a mean velocity derived from Darcy's law. In what follows, the equations describing hydrodynamic dispersion are presented. From experiments it is now understood that there are two driving factors behind hydrodynamic dispersion: *convection* and *molecular diffusion*. While the former enables the actual movement of the solute from one location to another, the latter enables the “spreading” of the solute into the fluid.

2.2.1 Continuity equations

Ignoring the effect of radioactive decay, adsorption and other factors that may contribute to the change in the concentration of the solute, the conservation of mass of the solute in the fluid phase is given by [36]

$$\begin{aligned}\frac{\partial(\phi c)}{\partial t} &+ \nabla\cdot(c\mathbf{u}-\mathbf{D}\nabla c) = -\sum_i q_1^{(i)}(t)\delta(\mathbf{x}-\mathbf{x}^{(i)})c(\mathbf{x},t)\\ &+ \sum_j q_2^{(j)}(t)\delta(\mathbf{x}-\mathbf{x}^{(j)})c^{(j)}(\mathbf{x},t), \quad \text{in } \Omega\times J \qquad (2.13)\end{aligned}$$

where c is the concentration (mass fraction) of the solute, $\mathbf{D}$ is the diffusion-dispersion tensor, $q_1^{(i)}$ and $q_2^{(j)}$ are the phase production and injection (mass) rates at locations $\mathbf{x}^{(i)}$ and $\mathbf{x}^{(j)}$, respectively, and $c^{(j)}$ is the given concentration at the source j. If the effect of radioactive decay, adsorption and other factors are not negligible, there is an extra term $r(c)$ that appears on the right hand side. For instance, in the case of radioactive decay, $r(c) = -\lambda c$, where λ is the coefficient of radioactive decay. Thus, this term may be absorbed into the right hand side of (2.13) to give the general form

$$\frac{\partial(\phi c)}{\partial t} + \nabla\cdot(c\mathbf{u}-\mathbf{D}\nabla c) = r(c) \quad \text{in } \Omega\times J. \qquad (2.14)$$

The mass balance of the fluid phase is described by

$$\frac{\partial(\phi\rho)}{\partial t} + \nabla\cdot(\rho\mathbf{u}) = \hat{q} \quad \text{in } \Omega\times J, \qquad (2.15)$$

with $\hat{q}(\mathbf{x},t) = \sum_j q_2^j(t)\delta(\mathbf{x}-\mathbf{x}^{(j)}) - \sum_i q_1^i(t)\delta(\mathbf{x}-\mathbf{x}^{(i)})$.

2.2.2 Constitutive equations and problem statement

The phase velocity, $\mathbf{u}$, is given again by Darcy’s law

$$\mathbf{u} = -\frac{\mathbf{K}}{\mu}[\nabla p - \rho\mathbf{g}]. \qquad (2.16)$$

The diffusion-dispersion tensor **D** in (2.14) is a function of phase velocity **u**, and takes the form

$$\mathbf{D}(\mathbf{u}) = \phi \left\{ d_m \mathbf{I} + \mid \mathbf{u} \mid \left(d_l \mathbf{E}(\mathbf{u}) + d_t \mathbf{E}^{\perp}(\mathbf{u}) \right) \right\}, \tag{2.17}$$

where d_m is the *molecular diffusion coefficient*; d_l and d_t are the *longitudinal* and *transverse dispersion coefficients.* $\mid \mathbf{u} \mid$ is the Euclidean norm of **u**, $\mathbf{E}(\mathbf{u})$ is the orthogonal projection along the flux

$$\mathbf{E}(\mathbf{u}) = \frac{1}{\mid \mathbf{u} \mid^2} \begin{pmatrix} u_1^2 & u_1 u_2 & u_1 u_3 \\ u_2 u_1 & u_2^2 & u_2 u_3 \\ u_3 u_1 & u_3 u_2 & u_3^2 \end{pmatrix}, \tag{2.18}$$

and $\mathbf{E}^{\perp}(\mathbf{u}) = \mathbf{I} - \mathbf{E}(\mathbf{u})$. The density ρ and viscosity μ are assumed to be known functions of p and c from equations of state of the form

$$\rho \equiv \rho(p, c), \quad \mu \equiv \mu(p, c). \tag{2.19}$$

Substituting (2.16) into (2.14) and (2.15), leads to a coupled system of partial differential equations in p and c, which can be solved given suitable initial conditions of the form

$$c = c_0, \quad p = p_0 \quad \text{in } \Omega \times \{0\}. \tag{2.20}$$

Boundary conditions can occur in several types. Solving the coupled system for flow and transport can be computationally challenging. Thus, it is common to time-split the system (2.14)-(2.15) to one of solving the flow and transport separately. The Dirchlet boundary condition for flow is similar to that discussed in Section 2.1.2. Boundary conditions for transport are specified along $\Gamma_0 = \{\mathbf{x} : \mathbf{u} \cdot \mathbf{n} = 0\}$, $\Gamma_{\text{in}} = \{\mathbf{x} \in \partial\Omega : \mathbf{u} \cdot \mathbf{n} < 0\}$ and $\Gamma_{\text{out}} = \{\mathbf{x} \in \partial\Omega : \mathbf{u} \cdot \mathbf{n} > 0\}$, i.e., the no-flow, in-flow and out-flow regions respectively, of $\partial\Omega$. This is because, while traditionally in elliptic or parabolic theory, one distinguishes between Dirichlet, Neumann or Robin boundary conditions, these names can be confusing and have little meaning because the advection-diffusion problem (2.14) can be elliptic-parabolic-hyperbolic in different parts of the domain, Ω or at different times

t. For example, one can specify a boundary of the form (in general, when the external medium is a liquid continuum with a specified solute concentration)

$$(c\mathbf{u} - \mathbf{D}\nabla c) \cdot \mathbf{n} = c_B \mathbf{u} \cdot \mathbf{n}, \quad \text{on } \Gamma_{\text{in}} \times J. \tag{2.21}$$

For this condition to hold, it is necessary to satisfy $c = c_B$ on the exterior of Γ_{in}. These values typically propogate along "characteristic curves" determined by the advection component of (2.14). Thus, if there is no diffusive component, i.e., if $\mathbf{D} \equiv 0$, then one cannot arbitrarily set c on Γ_{out}, since it has to be consistent with the value propagating from Γ_{in} and requires knowing the solution in advance. But if $\mathbf{D} \not\equiv 0$, then this is accomodated by a boundary layer that shows up in the solution depending on $\mathbf{D}$. No-flow boundary conditions take the form

$$(c\mathbf{u} - \mathbf{D}\nabla c) \cdot \mathbf{n} = 0, \quad \text{on } \Gamma_0 \times J, \tag{2.22}$$

which together with the fact that $\mathbf{u} \cdot \mathbf{n} = 0$ means the diffusive flux is zero, i.e., $\mathbf{D}\nabla c \cdot \mathbf{n} = 0$.

If the external domain is also a porous medium, a common requirement is that the mass flux of the solute, normal to a segment of the boundary, say $\partial\Omega^N$, must be equal on either side. Suppose the external domain has a porosity ϕ^e and the interior has a porosity ϕ^i; then, such a boundary condition may take the form

$$\phi^i \left(c\mathbf{u} - \mathbf{D}\nabla c\right)^i \cdot \mathbf{n} = \phi^e \left(c\mathbf{u} - \mathbf{D}\nabla c\right)^e \cdot \mathbf{n} \quad \text{on } \partial\Omega^N \times J. \tag{2.23}$$

Further details and analytic solutions to some special problems can be found in [23, 94, 95].

Chapter 3

Mortar finite elements for coupled flow and transport on non-matching multiblock grids

This chapter presents the mortar finite element method for approximate (numerical) solutions to the equations presented in Chapter 2. For details on the formulation for single phase flow, the reader is referred to [91, 142]. First, a partitioning of the domain into a multiblock structure is described. A backward Euler expanded mixed formulation [136] is then introduced to solve the immiscible displacement two phase flow problem (2.9). The function spaces in which the solutions (true and approximate) lie are presented and a weak formulation is developed. Quadrature rules that reduce the problem to a cell-centered finite difference approximation are also discussed. Some *a priori* error estimates are then derived for the problem for the special case of slightly compressible single phase Darcy flow. Next, a mixed formulation for the miscible displacement problem for reactive transport processes is presented. An upwinding scheme is adopted to handle the convection term in the formulation. Methods of solution are presented by exploring different discrete-time approximations to solve the transient problem.

3.1 Domain decomposition and some preliminaries

Consider (2.9), on a computational reference domain, Ω, of a regular shape (assumed rectangular for simplicity) with Dirichlet boundary conditions (2.11). The analysis presented can be extended to other types of boundary conditions. For general geometry, an analysis using (piecewise) smooth maps can be applied to the original irregular shaped physical domain, similar to that in [142, 147]. Assume that Ω can be decomposed into a set of

n non-overlapping sub-domains, such that the permeability restricted to each sub-domain is smooth. This is achieved by aligning sub-domain interfaces along the discontinuities in $\mathbf{K}$. For small-scale variations in $\mathbf{K}$, homegenization techniques such as in [14] need to be applied within each sub-domain. $\mathbf{K}$ is assumed to be a symmetric and uniformly positive definite tensor in this work.

Let

$$\Omega = \bigcup_{i=1}^{n_b} \Omega_i, \quad \Gamma_{ij} = \partial\Omega_i \bigcap \partial\Omega_j, \quad \Gamma_i = \partial\Omega_i \backslash \Gamma^D, \text{ and } \quad \Gamma = \bigcup_{i=1}^{n_b} \Gamma_i$$

describe the decomposition of the computational domain into n_b blocks or sub-domains, the interfaces between any two sub-domains, the interior block interface for a given block and the union of all such interfaces, respectively. A schematic of such a decomposition is shown in Figure 3.1 with mappings shown that map the irregular domain to a standard rectangular shape.

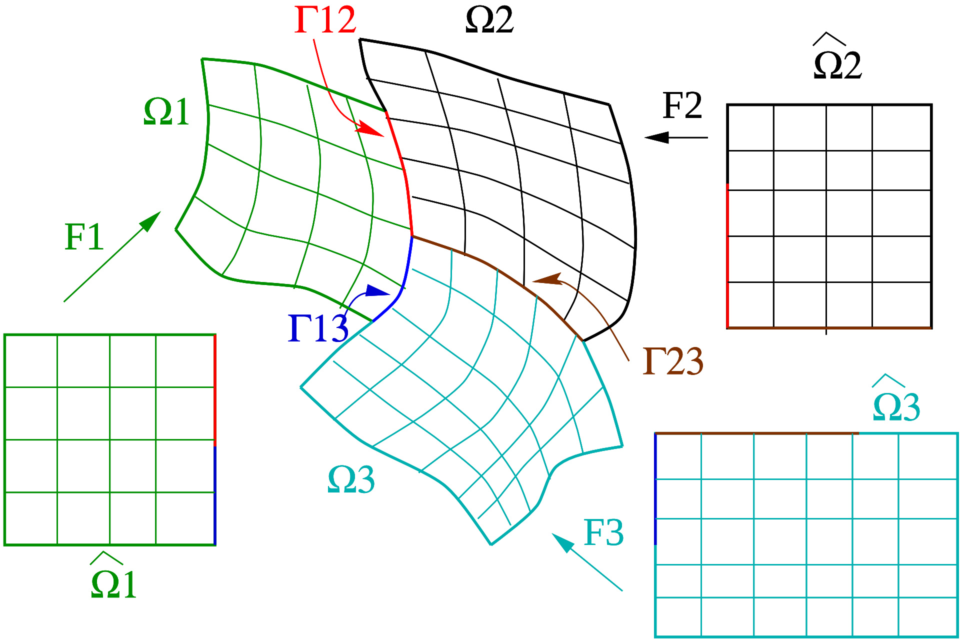

Figure 3.1: Example of a domain decomposition

Let $W^{k,p}(S)$ be the standard Sobolev space of k–differentiable functions in $L^p(S)$. Let $\|\cdot\|_{k,S}$ be the norm of $H^k(S) = W^{k,2}(S)$ or $H^k(S)^d$, where S and k are omitted if $S = \Omega$ and $k = 0$ respectively, unless otherwise specified. Let

$W^{k,p}(J; W^{j,q}(\Omega))$ be the usual set of functions with the norm,

$$\|\psi\|_{W^{k,p}(J;W^{j,q}(\Omega))} = \left\{ \sum_{i=0}^{k} \int_J \left\| \frac{\partial^i}{\partial t^i} \psi(\cdot, t) \right\|_{W^{j,q}(\Omega)}^p dt \right\}^{\frac{1}{p}}$$

where if $p = \infty$, the integral is replaced by the essential supremum.

The following assumptions are made on the data that will be used in the analysis later. There is a positive constant γ, such that,

(A1) $\phi \in L^\infty(\Omega)$ and $\frac{1}{\gamma} \leq \phi(\mathbf{x}) \leq \gamma$,

(A2) $\rho_\alpha \in W^{2,\infty}(\mathbb{R})$ and $\frac{1}{\gamma} \leq \rho_\alpha, \rho'_\alpha,\ \rho''_\alpha \leq \gamma$,

(A3) $\mathbf{K} \in L^\infty(\Omega)^{d\times d}$ and $\frac{1}{\gamma} \leq \xi^T \mathbf{K}(\mathbf{x}) \xi \leq \gamma$ for any $\xi \in \mathbb{R}^d$.

3.2 The immiscible displacement problem

In order to handle the degenerate nature of the parabolic system (2.9) (recall that the relative permeability, $k_{r\alpha} = 0$, when $S_\alpha = 0$), it becomes necessary to introduce an intermediate flux variable into the formulation as will be discussed in this section. First, some definitions are in order. A pressure gradient term is introduced as an intermediate velocity term $\tilde{\mathbf{u}}_\alpha$, for $\alpha = w, nw$, given by

$$\tilde{\mathbf{u}}_\alpha = -\mathbf{K}(\nabla p_\alpha - \rho_\alpha \mathbf{g}). \tag{3.1}$$

Then the extensive form of the Darcy velocity, (2.2) is given by,

$$\hat{\mathbf{u}}_\alpha = \frac{\rho_\alpha \kappa_{r\alpha}}{\mu_\alpha} \tilde{\mathbf{u}}_\alpha. \tag{3.2}$$

For simplicity we consider no-flow boundary conditions of the form

$$\mathbf{u}_w \cdot \mathbf{n} = 0\ , \mathbf{u}_{nw} \cdot \mathbf{n} = 0 \quad \text{on} \quad \partial\Omega^N \times J, \tag{3.3}$$

where $\partial\Omega^N = \partial\Omega$. Dirichlet and mixed boundary conditions can also be implemented. For a transient problem, initial conditions are provided such that they satisfy the no-flow boundary condition. These take the form,

$$p_w = p_w^0\ , \quad S_w = S_w^0 \quad \text{in} \quad \Omega \times \{0\}. \tag{3.4}$$

Then the two phase problem (2.9) reduces to finding a solution for p_α, S_α, $\tilde{\mathbf{u}}_\alpha, \hat{\mathbf{u}}_\alpha$ that satisfies, for $\alpha = w, nw$,

$$\frac{\partial(\phi S_\alpha \rho_\alpha)}{\partial t} + \nabla \cdot \hat{\mathbf{u}}_\alpha = \hat{q}_\alpha \quad \text{in} \quad \Omega \times J, \tag{3.5a}$$

$$\tilde{\mathbf{u}}_\alpha = -\mathbf{K}(\nabla p_\alpha - \rho_\alpha \mathbf{g}) \quad \text{in} \quad \Omega \times J, \tag{3.5b}$$

$$\hat{\mathbf{u}}_\alpha = \frac{\rho_\alpha \kappa_{r\alpha}}{\mu_\alpha} \tilde{\mathbf{u}}_\alpha \quad \text{in} \quad \Omega \times J, \tag{3.5c}$$

$$\hat{\mathbf{u}}_\alpha \cdot \mathbf{n} = 0\ , \quad \text{on} \quad \partial\Omega^N \times J, \tag{3.5d}$$

$$p_\alpha = p_\alpha^0 \quad \text{and} \quad S_\alpha = S_\alpha^0 \quad \text{in} \quad \Omega \times \{0\}. \tag{3.5e}$$

It is noted again that the system (3.5) reduces to a system of four equations in four unknowns, say, $p_w, S_w, \hat{\mathbf{u}}_w, \tilde{\mathbf{u}}_w$, after p_{nw}, S_{nw} are eliminated using the capillary pressure relation (2.1) and the saturation constraint $\sum_\alpha S_\alpha = 1$. Hence even though the boundary and initial conditions are given only in terms of p_w, S_w in (3.3) and (3.4), one can readily infer the corresponding values of p_{nw}, S_{nw}.

3.3 A mortar mixed weak formulation

The following function spaces are required in the analysis:

$$\mathbf{V}_i = \left\{\mathbf{v} \in H(\text{div}; \Omega_i) : \mathbf{v} \cdot \mathbf{n} \in L^2(\Gamma_i), \mathbf{v} \cdot \mathbf{n} = 0 \text{ on } \Gamma^N \cap \partial\Omega_i\right\}, \quad \mathbf{V} = \bigoplus_{i=1}^{n_b} \mathbf{V}_i,$$

$$\bar{\mathbf{V}}_i = (L^2(\Omega_i))^d, \quad \bar{\mathbf{V}} = \bigoplus_{i=1}^{n_b} \bar{\mathbf{V}}_i = (L^2(\Omega))^d,$$

$$W_i = L^2(\Omega_i), \quad W = \bigoplus_{i=1}^{n_b} W_i = L^2(\Omega),$$

$$M_{ij} = H^{1/2}(\Gamma_{ij}), \quad \text{and } M = \bigoplus_{1 \le i < j \le n_b} M_{ij}.$$

Note that if non-zero flow boundary conditions were prescribed then the prescribed function needs to appear in the definition of the space $\mathbf{V}_i$. The weak form of the system (3.5a)–(3.5d) is given by seeking a map,
$\{(\tilde{\mathbf{u}}_\alpha \quad \hat{\mathbf{u}}_\alpha)^T, (p_\alpha \quad S_\alpha)^T, (\psi_\alpha \quad \sigma_\alpha)^T\} : J \to (\mathbf{V} \times \bar{\mathbf{V}}) \times W^2 \times M^2$, such that, for

$1 \leq i < j \leq n_b$, $\alpha = w$ and nw,

$$(\frac{\partial(\phi\rho_\alpha S_\alpha)}{\partial t}, w)_{\Omega_i} + (\nabla \cdot \hat{\mathbf{u}}_\alpha, w)_{\Omega_i} = (\hat{q}_\alpha, w)_{\Omega_i} \quad w \in W_i, \tag{3.6a}$$

$$(\mathbf{K}^{-1}\tilde{\mathbf{u}}_\alpha, \mathbf{v})_{\Omega_i} = (p_\alpha, \nabla \cdot \mathbf{v})_{\Omega_i} + (\rho_\alpha \mathbf{g}, \mathbf{v})_{\Omega_i} - \left\langle \psi_\alpha, \mathbf{v} \cdot \mathbf{n}_i \right\rangle_{\Gamma_i} \quad \mathbf{v} \in \mathbf{V}_i, \tag{3.6b}$$

$$(\hat{\mathbf{u}}_\alpha, \mathbf{v})_{\Omega_i} = (\frac{\rho_\alpha \kappa_{r\alpha}}{\mu_\alpha} \tilde{\mathbf{u}}_\alpha, \mathbf{v})_{\Omega_i} \quad \mathbf{v} \in \bar{\mathbf{V}}_i, \tag{3.6c}$$

$$\left\langle \zeta, [\hat{\mathbf{u}}_\alpha \cdot \mathbf{n}]_{ij} \right\rangle_{\Gamma_{ij}} = 0, \quad \zeta \in M_{ij}, \tag{3.6d}$$

with the initial conditions (3.4), where $\mathbf{n}_i$ is the unit outward normal to $\partial\Omega$. The unknowns ψ_α and σ_α represent the values of pressure and saturation, respectively, on the sub-domain interfaces; i.e., $\psi_\alpha = p_\alpha|_\Gamma$, $\sigma_\alpha = S_\alpha|_\Gamma$. Note that σ_α appears in (3.6d) through the relative permeability term, $\kappa_{r\alpha}(\sigma_\alpha)$ in (3.6c). Finally, different choices (i.e., different subspaces) of the space $\bar{\mathbf{V}}_i$ give rise to different methods. A common choice in many implementations is $\bar{\mathbf{V}}_i = \mathbf{V}_i$.

Let $\mathcal{T}_{h,i}$ be a conforming, quasi-uniform finite element partition of Ω_i , $1 \leq i \leq n_b$ and let h_i be its maximal element diameter. Define the mesh size $h = \max_{1 \leq i \leq n_b} h_i$. Note that the adjacent partitions $\mathcal{T}_{h,i}$ and $\mathcal{T}_{h,j}$ need not align on Γ_{ij}. Define $\mathcal{T}_h = \cup_{i=1}^{n_b} \mathcal{T}_{h,i}$ and let

$$\mathbf{V}_{h,i} \times W_{h,i} \subset \mathbf{V}_i \times W_i$$

be any of the usual mixed finite element spaces [96]. Similarly, let $\bar{\mathbf{V}}_{h,i} \subset \bar{\mathbf{V}}_i$. Then let

$$\mathbf{V}_h = \bigoplus_{i=1}^{n} V_{h,i}\ , \quad W_h = \bigoplus_{i=1}^{n} W_{h,i}\ , \quad \bar{\mathbf{V}}_h = \bigoplus_{i=1}^{n_b} \bar{\mathbf{V}}_{h,i}.$$

Let $\mathcal{T}_{H,ij}$ be a quasi-uniform finite element partition of Γ_{ij} with a maximal element diameter H_{ij} and let $H = \max_{1 \leq i < j \leq n_b} H_{ij}$. Define $\mathcal{T}_{\Gamma,H} = \cup_{1 \leq i < j \leq n_b} \mathcal{T}_{H,ij}$. Let $M_{H,ij} \subset L^2(\Gamma_{ij})$ be the "mortar" space on Γ_{ij}, containing either continuous or discontinuous piecewise polynomials of degree m on $\mathcal{T}_{H,ij}$, where $m \geq k + 1$; k being associated with the degree of polynomials in $\mathbf{V}_h \cdot \mathbf{n}$. Then let

$$M_H = \bigoplus_{1 \leq i < j \leq n_b} M_{H,ij}$$

be the mortar finite element space on Γ. The following condition is required in the analysis [91]. On each sub-domain, Ω_i, define a projection $\mathcal{Q}_{h,i} : L^2(\Gamma_i) \to \mathbf{v}_{h,i} \cdot \mathbf{n}_i|_{\Gamma_i}$ such that, for any $\phi \in L^2(\Gamma_i)$,

$$\left\langle \phi - \mathcal{Q}_{h,i}\phi, \mathbf{v} \cdot \mathbf{n}_i \right\rangle = 0, \quad \mathbf{v} \in \mathbf{V}_{h,i}. \tag{3.7}$$

Assumption 3.3.1. Assume that there exists a constant C, independent of h and H, such that

$$\|\zeta\|_{0,\Gamma_{ij}} \leq C \left(\|\mathcal{Q}_{h,i}\zeta\|_{0,\Gamma_{ij}} + \|\mathcal{Q}_{h,j}\zeta\|_{0,\Gamma_{ij}} \right), \quad \zeta \in M_H \,, 1 \leq i < j \leq n_b \tag{3.8}$$

Assumption 3.3.1 states that the mortar space cannot be too rich compared to the normal traces on the interface of the sub-domain velocity spaces. Note that $\mathcal{T}_{H,ij}$ need not be conforming if $M_{H,ij}$ is discontinuous.

Let $0 = t_0 < t_1 < t_2 < ...$, let $\Delta t^n = t_n - t_{n-1}$, and let $f^n = f(t_n)$, $\Delta f^n = f(t_n) - f(t_{n-1})$. Then, the backward Euler multiblock expanded mixed finite element method for the system (3.5a)-(3.5d) seeks for $1 \leq i < j \leq n_b$ and $n = 1, 2, 3...$, $\hat{\mathbf{u}}^n_\alpha|_{\Omega_i} \in \mathbf{V}_{h,i}$, $\tilde{\mathbf{u}}^n_{\alpha,h}|_{\Omega_i} \in \bar{\mathbf{V}}_{h,i}$, $p^n_h|_{\Omega_i} \in W_{h,i}$, $S^n_h|_{\Omega_i} \in W_{h,i}$, $p^n_H|_{\Gamma_{ij}} \in M_{H,ij}$, and $S^n_H|_{\Gamma_{ij}} \in M_{H,ij}$ such that, for $\alpha = w$ and nw, the equations

$$\left(\frac{\Delta(\phi\rho_{\alpha,h}S_{\alpha,h})^n}{\Delta t^n}, w \right)_{\Omega_i} + \left(\nabla \cdot \hat{\mathbf{u}}^n_{\alpha,h}, w \right)_{\Omega_i} = \left(q_\alpha^{n-\frac{1}{2}}, w \right)_{\Omega_i}, \quad w \in W_{h,i}, \tag{3.9a}$$

$$(\mathbf{K}^{-1}\tilde{\mathbf{u}}^n_{\alpha,h}, \mathbf{v})_{\Omega_i} = (p^n_{\alpha,h}, \nabla \cdot \mathbf{v})_{\Omega_i} + (\rho^n_{\alpha,h}\mathbf{g}, \mathbf{v})_{\Omega_i} - \left\langle p^n_{\alpha,H}, \mathbf{v} \cdot \mathbf{n}_i \right\rangle_{\Gamma_i}, \quad \mathbf{v} \in \mathbf{V}_{h,i}, \tag{3.9b}$$

$$(\hat{\mathbf{u}}^n_{\alpha,h}, \tilde{\mathbf{v}})_{\Omega_i} = \left(\frac{\rho^n_{\alpha,h}k^n_{r\alpha,h}}{\mu_{\alpha,h}} \tilde{\mathbf{u}}^n_{\alpha,h}, \tilde{\mathbf{v}} \right)_{\Omega_i}, \quad \tilde{\mathbf{v}} \in \bar{\mathbf{V}}_{h,i}, \tag{3.9c}$$

$$\left\langle \left[\hat{\mathbf{u}}^n_{\alpha,h} \cdot \mathbf{n} \right]_{i,j}, \zeta \right\rangle_{\Gamma_{ij}} = 0, \quad \zeta \in M_{H,ij} \tag{3.9d}$$

hold, together with the capillary pressure relation (2.1), the saturation constraint $\sum_\alpha S_\alpha = 1$ and initial conditions of the form $p_{\alpha,h}(0) = \hat{p}_{\alpha,0}$, $S_{\alpha,h}(0) = \hat{S}_{\alpha,0}$; i.e., the L^2 projections of $p_{\alpha,0}$ and $S_{\alpha,0}$ onto W_h. In (3.9), $\rho_{\alpha,h} = \rho_\alpha(p_{\alpha,h})$, $\mu_{\alpha,h} = \mu_\alpha(p_{\alpha,h})$ and $k_{r\alpha,h} = k_{r\alpha}(S_{\alpha,h})$ are known functions of the primary unknowns. In practice however, viscosity is usually assumed to be a constant. Note that (3.9) forms a non-linear parabolic system of partial differential equations because of the non-linear dependence of density and relative permeability on the primary unknowns. The unique solvability of system (3.9) for the case of single phase flow follows from assumption 3.3.1 and an argument as in [104].

Remark 3.3.2. Introducing the pressure gradient as a variable, $\tilde{\mathbf{u}}_{\alpha,h}$ in the expanded method allows for proper handling of the degenerate relative permeability $k_{r\alpha,h}(S_{\alpha,h})$. It also allows for handling a full permeability tensor $\mathbf{K}$ arising in the treatment of irregular domains [136], for accurate approximation of the mixed method on each sub-domain by cell-centered finite differences for $p_{\alpha,h}, S_{\alpha,h}$. This is achieved by approximating the vector integrals on the LHS of equations (3.9b) and (3.9c) and that on the RHS of equation (3.9c) by the trapezoidal-midpoint and trapezoidal quadrature rules respectively, thus eliminating $\tilde{\mathbf{u}}_{\alpha,h}$ and $\hat{\mathbf{u}}_{\alpha,h}$ (see Section 3.3.2).

3.3.1 Interface formulation

Let $\mathbf{M}_H = M_H \times M_H$ be the space of mortar primary variables. Then define a non-linear interface bivariate form $b^n : \mathbf{M}_H \times \mathbf{M}_H \to \mathbb{R}$ as follows. For $\eta = (p^n_{w,H}, S^n_{w,H}) \in \mathbf{M}_H$ and $\varsigma = (\varsigma_w, \varsigma_{nw}) \in \mathbf{M}_H$ (where the mortar primaries are chosen to be water phase pressure and saturation); let

$$b^n(\eta, \varsigma) = \sum_{1 \le i < j \le n_b} \int_{\Gamma_{ij}} \left(\left[\hat{\mathbf{u}}^n_{w,h}(\eta) \cdot \mathbf{n} \right]_{ij} \varsigma_w + \left[\hat{\mathbf{u}}^n_{nw,h}(\eta) \cdot \mathbf{n} \right]_{ij} \varsigma_{nw} \right) \mathrm{d}s, \tag{3.10}$$

where $\hat{\mathbf{u}}^n_{\alpha,h}$ is obtained from the solution to the sub-domain problems using mixed finite elements, given in (3.9), with Dirichlet boundary data $p^n_{\alpha,H}(\eta)$. Define a non-linear interface operator $\mathcal{B}^n : \mathbf{M}_H \to \mathbf{M}_H$ by

$$\left\langle \mathcal{B}^n \eta, \varsigma \right\rangle = b^n(\eta, \varsigma), \quad \forall \varsigma \in \mathbf{M}_H, \tag{3.11}$$

where $\left\langle \cdot, \cdot \right\rangle$ is the L^2 inner product in $\mathbf{M}_H$.

Then, it can be seen that $(\eta, p^n_{\alpha,h}(\eta), S^n_{\alpha,h}(\eta), \tilde{\mathbf{u}}^n_{\alpha,h}(\eta), \hat{\mathbf{u}}^n_{\alpha,h}(\eta))$ solves the system (3.9) when η is the solution of

$$\mathcal{B}^n(\eta) = 0. \tag{3.12}$$

The system of non-linear *interface* equations (3.12) is solved by an inexact Newton method [144, 145]. Each Newton step s is computed by a forward difference

GMRES iteration for solving $(\mathcal{B}^n)'(\eta)s = -\mathcal{B}^n(\eta)$. On each GMRES iteration, the action of the Jacobian $(\mathcal{B}^n)'(\eta)$ on a vector ς, is simply approximated by a forward difference approximation. It requires only one additional evaluation of the operator $\mathcal{B}^n$. It is also noted that the evaluation of $\mathcal{B}^n$ involves the solution of the sub-domain problems given by (3.9) in parallel and requires just two rather inexpensive projection steps from the mortar grid to the sub-domain grid and vice-versa. Further each sub-domain solve itself can be distributed among several processors. The sub-domain problems are also non-linear and are solved by a pre-conditioned Newton-Krylov method as detailed in [47].

3.3.2 Reduction to a cell-centered finite difference method

In this section, a finite difference stencil is derived for the primary unknowns in the case of the lowest order RTN (Raviart-Thomas-Nedelec) spaces on rectangles for the sub-domains [16]. The goal is to express $\tilde{\mathbf{u}}_{\alpha,h}$ and $\hat{\mathbf{u}}_{\alpha,h}$ in terms of $p_{\alpha,h}$, $S_{\alpha,h}$, $\psi_{\alpha,H}$ and $\sigma_{\alpha,H}$ so that (3.9a) results in an equation for the primary unknowns only. Toward this end, set $\bar{\mathbf{V}}_{h,i} = \mathbf{V}_{h,i}$ and define the following quadrature rules to evaluate the integrals in (3.9b) and (3.9c):

$$(\mathbf{K}^{-1}\tilde{\mathbf{u}}_{\alpha,h}, \mathbf{v})_{\Omega_i} \approx (\mathbf{K}^{-1}\tilde{\mathbf{u}}_{\alpha,h}, \mathbf{v})_{\Omega_i,TM}, \tag{3.13a}$$

$$(\hat{\mathbf{u}}_{\alpha,h}, \mathbf{v})_{\Omega_i} \approx (\hat{\mathbf{u}}_{\alpha,h}, \mathbf{v})_{\Omega_i,TM} \quad \text{and} \tag{3.13b}$$

$$(\frac{\rho_{\alpha,h}k_{r\alpha,h}}{\mu_{\alpha,h}}\tilde{\mathbf{u}}_{\alpha,h}, \mathbf{v})_{\Omega_i} \approx (\frac{\rho_{\alpha,h}k_{r\alpha,h}}{\mu_{\alpha,h}}\tilde{\mathbf{u}}_{\alpha,h}, \mathbf{v})_{\Omega_i,T}; \tag{3.13c}$$

where, as in [16], $(\cdot,\cdot)_M$ and $(\cdot,\cdot)_T$ represent an application of the mid-point and trapezoidal rules of integration respectively (in each co-ordinate direction). Then for $\mathbf{v}, \mathbf{q} \in \mathbb{R}^d$,

$$(\mathbf{v}, \mathbf{q})_{TM} = \begin{cases} (v_1, q_1)_{T\times M} + (v_2, q_2)_{M\times T} & \text{if } d = 2, \\ (v_1, q_1)_{T\times M\times M} + (v_2, q_2)_{M\times T\times M} + (v_3, q_3)_{M\times M\times T} & \text{if } d = 3. \end{cases}$$

In other words, the integral of the i^{th} components of the vectors is evaluated by applying the trapezoidal rules in the i^{th} direction and the mid-point rule in the other directions. Then, the rule (3.13a) when applied to (3.9b), basically expresses the normal component of the $\tilde{\mathbf{u}}_{\alpha,h}$ on the face of a given element, as the difference between the pressures at the mid- points of the two adjacent elements to that face. If the face is on a boundary; i.e., either a mortar interface or an external boundary, then the pressure considered on its exterior is $\psi_{\alpha,H}$ or the prescribed value, p_α^D, of phase pressure on $\partial\Omega^D$, the Dirchlet segment of $\partial\Omega$. This clearly corresponds to a finite difference approximation of $\tilde{\mathbf{u}}_\alpha = -\nabla p_\alpha$.

Similarly, the rules (3.13b) and (3.13c) when applied to (3.9c), express the normal component of $\hat{\mathbf{u}}_{\alpha,h}$ on the face of any given element in terms of the normal components of $\tilde{\mathbf{u}}_{\alpha,h}$ on the faces of the adjacent elements and the values of $K_{ij}, \rho_{\alpha,h}$ and $k_{r\alpha,h}$ at the mid-points of the adjacent elements. Note that the rule requires the value of K_{ij} on the face. This can be obtained by a number of averaging methods, the most popular of which is the harmonic averaging method; e.g., the value of K_{11}, K_{12} and K_{13} on a x-face is harmonically averaged across the neighboring elements of that face; K_{21}, K_{22} and K_{23} are harmonically averaged across y-faces and similarly K_{31}, K_{32} and K_{33} across the z-faces. This definition preserves the definition of the flux. Again, for an element face on a mortar or an external boundary, the primaries are obtained from $\psi_{\alpha,H}$ and $\sigma_{\alpha,H}$ or p_α^D and S_α^D respectively. Owing to a choice of the basis functions for $\mathbf{v} \in \mathbf{v}_{h,i}$, $\hat{\mathbf{u}}_{\alpha,h}$ does not depend on the values of $\tilde{\mathbf{u}}_{\alpha,h}$ on the far left and far right edges. For an illustration, the reader is referred to the Figure 4.1, [16].

It can be shown for steady incompressible flow (i.e., linear elliptic PDEs, see [16, 122]) that the finite difference approximation of (3.9a) reduces to 9-point stencil in the primary unknowns, $p_{\alpha,h}$ and $S_{\alpha,h}$ for $d = 2$ (and a 19-point stencil for $d = 3$). If $\mathbf{K}$ is a diagonal tensor, then this further reduces to a 5-point stencil for $d = 2$ and a 7-point stencil for $d = 3$. Further it can be shown that the resulting sparse matrix is positive semi-definite in the scalar unknowns, $p_{\alpha,h}, S_{\alpha,h}$. Optimal convergence at the rate of $O(h)$ is retained for the scalar unknowns as with existing finite element theory in suitable norms. A superconvergence rate of $O(h^2)$ is obtained in the strict interior of the domain for the scalars and $O(h^{3/2})$ for the fluxes.

3.4 Error analysis

In this section some *a priori* error estimates are derived for the case of multiscale mortar mixed methods applied to the problem of slightly compressible single phase Darcy flow with Dirichlet boundary conditions (assumed for convenience), governed by the equations

$$\frac{\partial}{\partial t}\phi\rho(p) - \nabla\cdot\mathbf{K}\rho(p)(\nabla p - \rho(p)\mathbf{g}) = f \qquad \text{in } \Omega\times J, \tag{3.14}$$

$$p = p_b \quad \text{on } \partial\Omega\times J, \tag{3.15}$$

$$p = p_0 \quad \text{in } \Omega\times\{0\}. \tag{3.16}$$

Thus it is assumed only one flowing phase exists, i.e., that, $\alpha = w$, say, and $S_\alpha \equiv 1$; for convenience, the phase suffix α is dropped. Keeping the basic notation of the preceding sections, the analysis presented below holds for the case of modeling slightly compressible single phase Darcy flow. For simplicity, the continuous in time solution is analysed here. Introducing the Darcy velocity $\mathbf{u} = -\rho\mathbf{K}(\nabla p - \rho\mathbf{g})$, the mixed weak form (3.14)–(3.16) is given by seeking a map $\{\mathbf{u}, p, \lambda\} : J \to \mathbf{V}\times W\times M$ such that, for $1 \le i \le n_b$,

$$\begin{aligned}
\left(\mathbf{K}^{-1}\rho^{-1}(p)\,\mathbf{u},\mathbf{v}\right)_{\Omega_i} &= (p,\nabla\cdot\mathbf{v})_{\Omega_i} - \left\langle\lambda,\mathbf{v}\cdot\mathbf{n}_i\right\rangle_{\Gamma_i} \\
&\quad - \left\langle p_b,\mathbf{v}\cdot\mathbf{n}_i\right\rangle_{\partial\Omega_i\setminus\Gamma} + (\rho(p)\mathbf{g},\mathbf{v})_{\Omega_i} && \mathbf{v}\in\mathbf{V}_i, && (3.17)\\
\left(\phi\frac{\partial}{\partial t}\rho(p), w\right)_{\Omega_i} + (\nabla\cdot\mathbf{u}, w)_{\Omega_i} &= (f, w)_{\Omega_i}, && w\in W_i, && (3.18)\\
\sum_{j=1}^{n_b}\left\langle\mu,\mathbf{u}\cdot\mathbf{n}_j\right\rangle_{\Gamma_j} &= 0, && \mu\in M, && (3.19)
\end{aligned}$$

with the initial condition $p = p_0$, where $\mathbf{n}_i$ is the outer unit normal to $\partial\Omega_i$. Note that λ is the pressure on the block interfaces Γ, i.e., $\lambda = p|_\Gamma$. Next, some projection operators are introduced that will be used later in the analysis.

3.4.1 Some projection operators

Let $\mathcal{I}_H^c$ be the nodal interpolant operator into the space M_H^c, which is the subset of continuous functions in M_H (where we may use the Scott-Zhang [124] operator to define the nodal values of ψ if ψ is not smooth enough to form $\mathcal{I}_H^c\psi$ directly). For any $\varphi \in L^2(\Omega)$, let $\hat{\varphi} \in W_h$ be its $L^2(\Omega)$ projection satisfying

$$(\varphi - \hat{\varphi}, w) = 0, \quad w \in W_h.$$

Recall that (3.7) defines the projection $\mathcal{Q}_{h,i} : L^2(\Gamma_i) \to \mathbf{V}_{h,i} \cdot \mathbf{n}_i|_{\Gamma_i}$. Also recall that, for any of the standard mixed spaces,

$$\nabla \cdot \mathbf{V}_{h,i} = W_{h,i},$$

and there exists a projection Π_i of $(H^\varepsilon(\Omega_i))^d \cap \mathbf{V}_i$ onto $\mathbf{V}_{h,i}$ (for any $\varepsilon > 0$), satisfying amongst other properties that for any $\mathbf{q} \in (H^\varepsilon(\Omega_i))^d \cap \mathbf{V}_i$,

$$\nabla \cdot \Pi_i \mathbf{q} = \widehat{\nabla \cdot \mathbf{q}}, \tag{3.20}$$

$$(\Pi_i \mathbf{q}) \cdot \mathbf{n}_i = \mathcal{Q}_{h,i}(\mathbf{q} \cdot \mathbf{n}_i). \tag{3.21}$$

Moreover from [12, 93],

$$\|\Pi_i \mathbf{q}\|_{0,\Omega_i} \le C(\|\mathbf{q}\|_{\varepsilon,\Omega_i} + \|\nabla \cdot \mathbf{q}\|_{0,\Omega_i}). \tag{3.22}$$

It is assumed that the order of approximation of $\mathbf{V}_{h,i}$ is $k+1$ and $W_{h,i}$ is $l+1$ (and recall that M_H approximates to order $m+1$). In all cases, $l = k$ or $l = k-1$, and for simplicity, it is assumed that the order of approximation is the same on every sub-domain. Then the projection operators have the following approximation properties:

$$\|\psi - \mathcal{I}_H^c \psi\|_{t,\Gamma_{ij}} \le C\|\psi\|_{s,\Gamma_{ij}} H^{s-t}, \qquad 0 \le s \le m+1,\ 0 \le t \le 1, \tag{3.23}$$

$$\|\psi - \mathcal{P}_H \psi\|_{-t,\Gamma_{ij}} \le C\|\psi\|_{s,\Gamma_{ij}} H^{s+t}, \qquad 0 \le s \le m+1,\ 0 \le t \le 1, \tag{3.24}$$

$$\|\varphi - \hat{\varphi}\| \le C\|\varphi\|_t h^t, \qquad 0 \le t \le l+1, \tag{3.25}$$

$$\|\nabla \cdot (\mathbf{q} - \Pi_i \mathbf{q})\|_{0,\Omega_i} \le C\|\nabla \cdot \mathbf{q}\|_{t,\Omega_i} h^t, \qquad 0 \le t \le l+1, \tag{3.26}$$

$$\|\mathbf{q} - \Pi_i \mathbf{q}\|_{0,\Omega_i} \le C\|\mathbf{q}\|_{r,\Omega_i} h^r, \qquad 1 \le r \le k+1, \tag{3.27}$$

$$\|\psi - \mathcal{Q}_{h,i}\psi\|_{-t,\Gamma_{ij}} \le C\|\psi\|_{r,\Gamma_{ij}} h^{r+t}, \qquad 0 \le r \le k+1,\ 0 \le t \le k+1, \tag{3.28}$$

$$\|(\mathbf{q} - \Pi_i \mathbf{q}) \cdot \mathbf{n}_i\|_{-t,\Gamma_{ij}} \le C\|\mathbf{q}\|_{r,\Gamma_{ij}} h^{r+t}, \qquad 0 \le r \le k+1,\ 0 \le t \le k+1, \tag{3.29}$$

where $\|\cdot\|_{-t}$ is the norm of H^{-t}, the dual of H^t (*not* H^t_0). The bounds stated in (3.25) and (3.26)–(3.29) are standard L^2-projection approximation results [39]; bound (3.27) can be found in [28, 120]; and (3.23) is a standard interpolation bound [39].

It is convenient to define the space of weakly continuous velocities, which is the space

$$\mathbf{V}_{h,0} = \left\{ \mathbf{v} \in \mathbf{V}_h : \sum_{i=1}^{n} \langle \mathbf{v}|_{\Omega_i} \cdot \mathbf{n}_i, \mu \rangle_{\Gamma_i} = 0 \ \ \forall \ \ \mu \in M_H \right\}.$$

The following lemma holds; see [12, 15].

Lemma 3.4.1. *Under hypothesis* (3.8)*, there exists a projection operator* $\Pi_0 : (H^{1/2+\varepsilon}(\Omega)) \cap \mathbf{V} \to \mathbf{V}_{h,0}$ *such that*

$$(\nabla \cdot (\Pi_0 \mathbf{q} - \mathbf{q}), w)_\Omega = 0, \quad w \in W_h, \tag{3.30}$$

and

$$\|\Pi_0 \mathbf{q} - \Pi \mathbf{q}\| \le C \sum_{i=1}^{n} \|\mathbf{q}\|_{r+1/2,\Omega_i} h^r H^{1/2}, \qquad 0 \le r \le k+1, \tag{3.31}$$

$$\|\Pi_0 \mathbf{q} - \mathbf{q}\| \le C \sum_{i=1}^{n} \left(\|\mathbf{q}\|_{r,\Omega_i} h^r + \|\mathbf{q}\|_{r+1/2,\Omega_i} h^r H^{1/2} \right), \quad 1 \le r \le k+1, \tag{3.32}$$

$$\|\Pi_0 \mathbf{q} - \mathbf{q}\| \le C \sum_{i=1}^{n} \|\mathbf{q}\|_{r,\Omega_i} h^{r-1/2} H^{1/2}, \qquad 1 \le r \le k+1, \tag{3.33}$$

wherein $\Pi \mathbf{q}|_{\Omega_i} = \Pi_i \mathbf{q}$*.*

The analysis also uses a nonstandard trace theorem (see [66, Theorem 1.5.2.1]).

$$\|q\|_{r,\Gamma_{ij}} \le C \|q\|_{r+1/2,\Omega_i} \tag{3.34}$$

Also, for any function $\mathbf{v} \in \mathbf{V}_{h,i}$ (see [28, 116])

$$\langle q, \mathbf{v} \cdot \mathbf{n} \rangle_{\partial\Omega_i} \le C \|q\|_{1/2,\partial\Omega_i} \|\mathbf{v}\|_{H(\mathrm{div};\Omega_i)}. \tag{3.35}$$

3.4.2 Elliptic projection

Let the solution $\{\mathbf{u}, p, \lambda\}$ be projected into the mixed finite element space by the "elliptic projection" map $\{\tilde{\mathbf{u}}, \tilde{p}, \tilde{\lambda}\} : J \to \mathbf{V}_h \times W_h \times M_H$ given by

$$\begin{aligned}
\big(\mathbf{K}^{-1}\rho^{-1}(p)\,\tilde{\mathbf{u}}, \mathbf{v}\big)_{\Omega_i} &= (\tilde{p}, \nabla\cdot\mathbf{v})_{\Omega_i} - \big\langle\tilde{\lambda}, \mathbf{v}\cdot\mathbf{n}_i\big\rangle_{\Gamma_i} && && (3.36)\\
&\quad - \big\langle p_b, \mathbf{v}\cdot\mathbf{n}_i\big\rangle_{\partial\Omega_i\setminus\Gamma} + (\rho(p)\mathbf{g}, \mathbf{v})_{\Omega_i} && \mathbf{v}\in\mathbf{V}_{h,i}, &&\\
(\phi\frac{\partial}{\partial t}\rho(p), w)_{\Omega_i} + (\nabla\cdot\tilde{\mathbf{u}}, w)_{\Omega_i} &= (f, w)_{\Omega_i}, && w\in W_{h,i}, && (3.37)\\
\sum_{j=1}^{n}\big\langle\mu, \tilde{\mathbf{u}}\cdot\mathbf{n}_j\big\rangle_{\Gamma_j} &= 0, && \mu\in M_H. && (3.38)
\end{aligned}$$

Subtracting (3.36)–(3.38) from (3.17)–(3.19), we see that the elliptic projection satisfies the following equations:

$$\begin{aligned}
\big(\mathbf{K}^{-1}\rho^{-1}(p)(\mathbf{u}-\tilde{\mathbf{u}}), \mathbf{v}\big)_{\Omega_i} &= (p-\tilde{p}, \nabla\cdot\mathbf{v})_{\Omega_i} && && (3.39)\\
&\quad - \big\langle p-\tilde{\lambda}, \mathbf{v}\cdot\mathbf{n}_i\big\rangle_{\Gamma_i}, && \mathbf{v}\in\mathbf{V}_{h,i}, &&\\
(\nabla\cdot(\mathbf{u}-\tilde{\mathbf{u}}), w)_{\Omega_i} &= 0, && w\in W_{h,i}, && (3.40)\\
\sum_{j=1}^{n_b}\big\langle\mu, (\mathbf{u}-\tilde{\mathbf{u}})\cdot\mathbf{n}_j\big\rangle_{\Gamma_j} &= 0, && \mu\in M_H. && (3.41)
\end{aligned}$$

It is noted that $\tilde{\lambda}$ can be eliminated from the mixed method (3.39)–(3.41) by restricting $\mathbf{V}_h$ to $\mathbf{V}_{h,0}$, the space of weakly continuous velocities; that is, the problem is equivalent to finding $\tilde{\mathbf{u}}\in\mathbf{V}_{h,0}$ and $\tilde{p}\in W_h$ such that

$$\begin{aligned}
\big(\mathbf{K}^{-1}\rho^{-1}(p)(\mathbf{u}-\tilde{\mathbf{u}}), \mathbf{v}\big) &= \sum_{i=1}^{n}((p-\tilde{p}, \nabla\cdot\mathbf{v})_{\Omega_i} && && (3.42)\\
&\quad - \big\langle p, \mathbf{v}\cdot\mathbf{n}_i\big\rangle_{\Gamma_i}), && \mathbf{v}\in\mathbf{V}_{h,0}, &&\\
\sum_{i=1}^{n}(\nabla\cdot(\mathbf{u}-\tilde{\mathbf{u}}), w)_{\Omega_i} &= 0, && w\in W_h. && (3.43)
\end{aligned}$$

Then, the following estimates are derived in [15].

Lemma 3.4.2. *For the velocity* $\tilde{\mathbf{u}}$ *and the pressure* $\tilde{p}$ *of the mixed elliptic projection* (3.36)–(3.38)*, if* (3.8) *holds, then there exists a positive constant* C *in-*

dependent of h and H such that

$$\|\nabla\cdot(\mathbf{u}-\tilde{\mathbf{u}})\| \le C\sum_{i=1}^{n}\|\nabla\cdot\mathbf{u}\|_{r,\Omega_i}h^r, \quad 1\le r\le l+1, \tag{3.44}$$

$$\|\mathbf{u}-\tilde{\mathbf{u}}\| \le C\sum_{i=1}^{n}\big(\|p\|_{s+1/2,\Omega_i}H^{s-1/2}+\|\mathbf{u}\|_{r,\Omega_i}h^r \tag{3.45}$$
$$+\|\mathbf{u}\|_{r+1/2,\Omega_i}h^rH^{1/2}\big), \quad 1\le r\le k+1,\ 1\le s\le m+1,$$

$$\|p-\tilde{p}\| \le C\sum_{i=1}^{n}\|p\|_{t,\Omega_i}h^t+\sum_{i=1}^{n}\big(\|p\|_{s+1/2,\Omega_i}H^{s+1/2} \tag{3.46}$$
$$+\|\nabla\cdot\mathbf{u}\|_{t,\Omega_i}h^tH+\|\mathbf{u}\|_{r,\Omega_i}h^rH+\|\mathbf{u}\|_{r+1/2,\Omega_i}h^rH^{3/2}\big),$$

where $1\le r\le k+1$*,* $1/2\le s\le m+1$*, and* $0\le t\le l+1$*.*

Note that it follows from the inverse inequality and Lemma 3.4.2 that

$$\|\tilde{\mathbf{u}}\|_{L^\infty(J;L^\infty(\Omega)^d)}\le C, \tag{3.47}$$

when $H=\mathcal{O}(h^{1/(s-1/2)})$, which at its limit is $H=\mathcal{O}(h^{1/(m+1/2)})$. This is not a restriction since it is the asymptotic scaling which maintains the optimal convergence rate for the lowest Raviart-Thomas-Nedelec space RTN_0, $k=0$. In what follows, estimates for $\frac{\partial}{\partial t}(\mathbf{u}-\tilde{\mathbf{u}})$ and $\frac{\partial}{\partial t}(p-\tilde{p})$ will be needed.

Lemma 3.4.3. *There exists a positive constant C independent of h and H such that*

$$\|\frac{\partial}{\partial t}(\mathbf{u}-\tilde{\mathbf{u}})\|_0 \le C\left[\|\frac{\partial}{\partial t}(\Pi_0\mathbf{u}-\mathbf{u})\|+\|\mathbf{u}-\tilde{\mathbf{u}}\|+\sum_{i=1}^{n}\|\frac{\partial p}{\partial t}\|_{s+1/2,\Omega_i}H^{s-1/2}\right].$$

Proof. Noting that $\sum_i\langle\mathcal{I}_H^c p,\mathbf{v}\cdot\mathbf{n}_i\rangle_{\Gamma_i}=0$ for any $\mathbf{v}\in\mathbf{V}_{h,0}$, (3.42)–(3.43) can be rewritten as follows:

$$\big(\mathbf{K}^{-1}\rho^{-1}(p)(\Pi_0\mathbf{u}-\tilde{\mathbf{u}}),\mathbf{v}\big)=\big(\mathbf{K}^{-1}\rho^{-1}(p)(\Pi_0\mathbf{u}-\mathbf{u}),\mathbf{v}\big) \tag{3.48}$$
$$+\sum_{i=1}^{n}((\hat{p}-\tilde{p},\nabla\cdot\mathbf{v})_{\Omega_i}-\big\langle p-\mathcal{I}_H^c p,\mathbf{v}\cdot\mathbf{n}_i\big\rangle_{\Gamma_i}), \qquad \mathbf{v}\in\mathbf{V}_{h,0},$$

$$\sum_{i=1}^{n}(\nabla\cdot(\Pi_0\mathbf{u}-\tilde{\mathbf{u}}),w)_{\Omega_i}=0, \qquad w\in W_h. \tag{3.49}$$

In what follows, time derivatives may be denoted by a suffix t to conserve space. Differentiating (3.48) and (3.49), substituting $\mathbf{v} = (\Pi_0\mathbf{u} - \tilde{\mathbf{u}})_t$ and $w = (\hat{p} - \tilde{p})_t$ and summing leads to the following equation.

$$\begin{aligned}\big(\mathbf{K}^{-1}\rho^{-1}(p)(\Pi_0\mathbf{u} - \tilde{\mathbf{u}})_t, (\Pi_0\mathbf{u} - \tilde{\mathbf{u}})_t\big) &= \big(\mathbf{K}^{-1}\rho^{-1}(p)(\Pi_0\mathbf{u} - \mathbf{u})_t, (\Pi_0\mathbf{u} - \tilde{\mathbf{u}})_t\big)\\ - \big(\big[\mathbf{K}^{-1}\rho^{-1}(p)\big]_t(\mathbf{u} - \tilde{\mathbf{u}}), (\Pi_0\mathbf{u} - \tilde{\mathbf{u}})_t\big) &+ \sum_{i=1}^{n} \big\langle (\mathcal{I}^c_H p - p)_t, (\Pi_0\mathbf{u} - \tilde{\mathbf{u}})_t \cdot \mathbf{n}_i \big\rangle_{\Gamma_i}.\end{aligned}$$

Next, using $\nabla \cdot (\Pi_0\mathbf{u} - \tilde{\mathbf{u}})_t = 0$ and $(\mathcal{I}^c_H p)_t = \mathcal{I}^c_H(p_t)$, yields [91]

$$\begin{aligned}\sum_{i=1}^{n} \big\langle (\mathcal{I}^c_H p - p)_t, (\Pi_0\mathbf{u} - \tilde{\mathbf{u}})_t \cdot \mathbf{n}_i \big\rangle_{\Gamma_i} &\le \sum_{i=1}^{n} \|\mathcal{I}^c_H p_t - p_t\|_{1/2,\partial\Omega_i} \|(\Pi_0\mathbf{u} - \tilde{\mathbf{u}})_t\|_{H(\mathrm{div};\Omega_i)}\\ &\le C\sum_{i=1}^{n} \|p_t\|_{s+1/2,\Omega_i} H^{s-1/2} \|(\Pi_0\mathbf{u} - \tilde{\mathbf{u}})_t\|_{0,\Omega_i}.\end{aligned}$$

Therefore, it follows from assumptions (A2)–(A3) that

$$\|(\Pi_0\mathbf{u} - \tilde{\mathbf{u}})_t\| \le C\left[\|(\Pi_0\mathbf{u} - \mathbf{u})_t\| + \|\mathbf{u} - \tilde{\mathbf{u}}\| + \sum_{i=1}^{n} \|p_t\|_{s+1/2,\Omega_i} H^{s-1/2}\right],$$

where upon noticing $(\Pi_0\mathbf{u})_t = \Pi_0\mathbf{u}_t$ and applying the triangle inequality completes the proof. □

Lemma 3.4.4. *There exists a positive constant C independent of h and H such that*

$$\|\frac{\partial}{\partial t}(p - \tilde{p})\|_0 \le C\left(\|\frac{\partial}{\partial t}(\mathbf{u} - \tilde{\mathbf{u}})\| + \|\mathbf{u} - \tilde{\mathbf{u}}\| + \sum_{i=1}^{n} \|\frac{\partial p}{\partial t}\|_{s+1/2,\Omega_i} H^{s+1/2}\right).$$

Proof. A duality argument is applied. Let φ be the solution of

$$\begin{aligned} -\Delta\varphi &= -(\hat{p} - \tilde{p})_t \quad &&\text{in } \Omega,\\ \varphi &= 0 &&\text{on } \partial\Omega,\end{aligned}$$

satisfying elliptic regularity,

$$\|\varphi\|_2 \le C\|(\hat{p} - \tilde{p})_t\|. \tag{3.50}$$

Differentiating (3.42) with respect to t, taking $\mathbf{v} = \Pi_0 \nabla \varphi$ and using the weak continuity of $\mathbf{v}$ shows that

$$\begin{aligned}
\|(\hat{p}-\tilde{p})_t\|^2 &= \sum_{i=1}^{n} ((\hat{p}-\tilde{p})_t, \nabla\cdot\Pi_0\nabla\varphi)_{\Omega_i} \\
&= \sum_{i=1}^{n} \Big(\big([\mathbf{K}^{-1}\rho^{-1}(p)(\mathbf{u}-\tilde{\mathbf{u}})]_t, \Pi_0\nabla\varphi\big)_{\Omega_i} \\
&\qquad + \big\langle p_t - \mathcal{I}_H^c p_t, \Pi_0\nabla\varphi\cdot\mathbf{n}_i \big\rangle_{\Gamma_i} \Big). \qquad (3.51)
\end{aligned}$$

Using assumptions (A2)–(A3), the first term on the right is estimated as

$$\sum_{i=1}^{n} \big([\mathbf{K}^{-1}\rho^{-1}(p)(\mathbf{u}-\tilde{\mathbf{u}})]_t, \Pi_0\nabla\varphi\big)_{\Omega_i} \le C\left(\|(\mathbf{u}-\tilde{\mathbf{u}})_t\| + \|\mathbf{u}-\tilde{\mathbf{u}}\|\right)\|\varphi\|_2. \quad (3.52)$$

For the second term on the right in (3.51), it can be shown that

$$\begin{aligned}
&\big\langle p_t - \mathcal{I}_H^c p_t, \Pi_0\nabla\varphi\cdot\mathbf{n}_i\big\rangle_{\Gamma_i} \\
&\quad = \big\langle p_t - \mathcal{I}_H^c p_t, (\Pi_0\nabla\varphi - \Pi_i\nabla\varphi)\cdot\mathbf{n}_i + (\Pi_i\nabla\varphi - \nabla\varphi)\cdot\mathbf{n}_i + \nabla\varphi\cdot\mathbf{n}_i\big\rangle_{\Gamma_i} \\
&\quad \le \sum_j \|p_t - \mathcal{I}_H^c p_t\|_{0,\Gamma_{ij}} \big(\|(\Pi_0\nabla\varphi - \Pi_i\nabla\varphi)\cdot\mathbf{n}_i\|_{0,\Gamma_{ij}} \\
&\quad + \|(\Pi_i\nabla\varphi - \nabla\varphi)\cdot\mathbf{n}_i\|_{0,\Gamma_{ij}}\big) + \sum_j \|p_t - \mathcal{I}_H^c p_t\|_{-1/2,\Gamma_{ij}} \|\nabla\varphi\cdot\mathbf{n}_i\|_{1/2,\Gamma_{ij}} \\
&\quad \le C H^{s+1/2} \|p_t\|_{s+1/2,\Omega_i} \|\varphi\|_{2,\Omega_i}, \quad 0 \le s \le m+1, \qquad (3.53)
\end{aligned}$$

wherein the inequalities (3.23), (3.31), and (3.29) have been used. □

Note that the inverse inequality and Lemma 3.4.4 imply that

$$\|\tilde{p}_t\|_{L^\infty(J;L^\infty(\Omega))} \le C. \qquad (3.54)$$

3.4.3 Some *a priori* error estimates

In this section, *a priori* error estimates are derived for the pressure and velocity unknowns using the results from the preceding sections. Recall that the mixed finite element approximation of (3.17)–(3.18) is given by seeking a map $\{\mathbf{u}_h, p_h, \lambda_H\} : J \to \mathbf{V}_h \times W_h \times M_H$ such that, for $1 \le i \le n$,

$$\begin{aligned}
&\big(\mathbf{K}^{-1}\rho^{-1}(p_h)\,\mathbf{u}_h, \mathbf{v}\big)_{\Omega_i} = (p_h, \nabla\cdot\mathbf{v})_{\Omega_i} - \big\langle \lambda_H, \mathbf{v}\cdot\mathbf{n}_i\big\rangle_{\Gamma_i} && \quad (3.55)\\
&\qquad\qquad - \big\langle p_b, \mathbf{v}\cdot\mathbf{n}_i\big\rangle_{\partial\Omega_i\setminus\Gamma} + (\rho(p_h)\mathbf{g}, \mathbf{v})_{\Omega_i} \qquad\qquad \mathbf{v}\in\mathbf{V}_{h,i}, &&\\
&(\phi\frac{\partial}{\partial t}\rho(p_h), w)_{\Omega_i} + (\nabla\cdot\mathbf{u}_h, w)_{\Omega_i} = (f, w)_{\Omega_i}, \qquad\qquad w\in W_{h,i}, && \quad (3.56)\\
&\sum_{j=1}^{n}\big\langle \mu, \mathbf{u}_h\cdot\mathbf{n}_j\big\rangle_{\Gamma_j} = 0, \qquad\qquad \mu\in M_H, && \quad (3.57)
\end{aligned}$$

with the initial condition $p_h(0) = \widehat{p(\rho_0)}$, its $L^2(\Omega)$ projection onto W_h. Then, the following result holds.

Theorem 3.4.5. *There exists a positive constant C independent of h and H such that*

$$\begin{aligned}
&\|p - p_h\|_{L^\infty(J;L^2(\Omega))} + \|\mathbf{u} - \mathbf{u}_h\|_{L^2(J;L^2(\Omega)^d)}\\
&\qquad\qquad \le C\left[\|p - \tilde{p}\|_{W^{1,\infty}(J;L^2(\Omega))} + \|\mathbf{u} - \tilde{\mathbf{u}}\|_{L^2(J;L^2(\Omega)^d)}\right].
\end{aligned}$$

Proof. Subtracting (3.55)–(3.57) from (3.36)–(3.38) gives the following equations for the error:

$$\begin{aligned}
&\big(\mathbf{K}^{-1}\rho^{-1}(p_h)(\tilde{\mathbf{u}} - \mathbf{u}_h), \mathbf{v}\big)_{\Omega_i} = (\tilde{p} - p_h, \nabla\cdot\mathbf{v})_{\Omega_i} - \big\langle \tilde{\lambda} - \lambda_H, \mathbf{v}\cdot\mathbf{n}_i\big\rangle_{\Gamma_i}\\
&\qquad + \big(\mathbf{K}^{-1}(\rho^{-1}(p) - \rho^{-1}(p_h))\tilde{\mathbf{u}}, \mathbf{v}\big)_{\Omega_i} + ((\rho(p) - \rho(p_h))\mathbf{g}, \mathbf{v})_{\Omega_i} \quad \mathbf{v}\in\mathbf{V}_{h,i},\\
&(\phi(\rho(\tilde{p}) - \rho(p_h))_t, w)_{\Omega_i} + (\nabla\cdot(\tilde{\mathbf{u}} - \mathbf{u}_h), w)_{\Omega_i}\\
&\qquad\qquad\qquad\qquad = (\phi(\rho(\tilde{p}) - \rho(p))_t, w)_{\Omega_i}, \quad w\in W_{h,i},\\
&\sum_{j=1}^{n}\big\langle \mu, (\tilde{\mathbf{u}} - \mathbf{u}_h)\cdot\mathbf{n}_j\big\rangle_{\Gamma_j} = 0, \quad \mu\in M_h. \qquad\qquad (3.58)
\end{aligned}$$

Let $\mathbf{v} = \tilde{\mathbf{u}} - \mathbf{u}_h$, $w = \tilde{p} - p_h$, and $\mu = \tilde{\lambda} - \lambda_H$. Then adding the resulting equations yields

$$\begin{aligned}
&\big(\mathbf{K}^{-1}\rho^{-1}(p_h)(\tilde{\mathbf{u}} - \mathbf{u}_h), \tilde{\mathbf{u}} - \mathbf{u}_h\big) + (\phi(\rho(\tilde{p}) - \rho(p_h))_t, \tilde{p} - p_h)_{\Omega_i}\\
&\quad = \big(\mathbf{K}^{-1}(\rho^{-1}(p) - \rho^{-1}(p_h))\tilde{\mathbf{u}}, \tilde{\mathbf{u}} - \mathbf{u}_h\big)_{\Omega_i} + ((\rho(p) - \rho(p_h))\mathbf{g}, \mathbf{u} - \mathbf{u}_h)_{\Omega_i}\\
&\quad + (\phi(\rho(\tilde{p}) - \rho(p))_t, \tilde{p} - p_h)_{\Omega_i}\,. \qquad\qquad (3.59)
\end{aligned}$$

Note that [104, 137]

$$\left(\phi\frac{\partial}{\partial t}\big[\rho(\tilde{p})-\rho(p_h)\big],\tilde{p}-p_h\right)_{\Omega_i} \geq \frac{d}{dt}\int_{\Omega_i}\phi\int_0^{\tilde{p}-p_h}\rho'(p_h+\xi)\xi\,d\xi\,dx - C\|\tilde{p}-p_h\|^2 \tag{3.60}$$

and

$$\int_{\Omega_i}\phi\int_0^{\tilde{p}-p_h}\rho'(p_h+\xi)\xi\,d\xi\,dx \geq \frac{1}{2\alpha^2}\|\tilde{p}-p_h\|^2, \tag{3.61}$$

for ρ' is bounded below positively due to assumptions (A1)–(A2). Also, note that by assumptions (A2)–(A3),

$$\big(\mathbf{K}^{-1}\rho^{-1}(p_h)(\tilde{\mathbf{u}}-\mathbf{u}_h),\tilde{\mathbf{u}}-\mathbf{u}_h\big) \geq \frac{1}{\alpha^2}\|\tilde{\mathbf{u}}-\mathbf{u}_h\|^2. \tag{3.62}$$

Hence using the mean-value theorem, the chain rule, and assumptions (A1)–(A2), (3.59) results in

$$\begin{aligned}&\frac{d}{dt}\int_{\Omega_i}\phi\int_0^{\tilde{p}-p_h}\rho'(p_h+\xi)\xi\,\mathrm{d}\xi\,\mathrm{dx}+\frac{1}{\alpha^2}\|\tilde{\mathbf{u}}-\mathbf{u}_h\|^2\\ &\leq C[\|\tilde{p}-p_h\|\|\tilde{\mathbf{u}}\|_{0,\infty}\|\tilde{\mathbf{u}}-\mathbf{u}_h\|+\|p-p_h\|\|\mathbf{u}-\mathbf{u}_h\|\\ &+(\|p-\tilde{p}\|\|\frac{\partial\tilde{p}}{\partial t}\|_{0,\infty}+\|\frac{\partial}{\partial t}(p-\tilde{p})\|)\|\tilde{p}-p_h\|].\end{aligned}$$

Next, using (3.47), (3.54), the triangle inequality, and Young's inequality (i.e., $ab \leq \varepsilon a^2 + \frac{b^2}{4\varepsilon}$) yields

$$\begin{aligned}&\frac{d}{dt}\int_{\Omega_i}\phi\int_0^{\tilde{p}-p_h}\rho'(p_h+\xi)\xi\,\mathrm{d}\xi\,\mathrm{dx}+\frac{1}{\alpha^2}\|\tilde{\mathbf{u}}-\mathbf{u}_h\|^2\\ &\leq C\left[|\tilde{p}-p_h\|^2+\|p-\tilde{p}\|^2+\|(p-\tilde{p})_t\|^2+\|\mathbf{u}-\tilde{\mathbf{u}}\|^2\right].\end{aligned}$$

Integrating in time, then using (3.61), and applying Gronwall's inequality gives

$$\begin{aligned}&\|\tilde{p}-p_h\|_{L^\infty(J;L^2(\Omega))}+\|\tilde{\mathbf{u}}-\mathbf{u}_h\|_{L^2(J;L^2(\Omega)^d)}\\ &\leq C\left[\|p-\tilde{p}\|_{L^2(J;L^2(\Omega))}+\|(p-\tilde{p})_t\|_{L^2(J;L^2(\Omega))}+\|\mathbf{u}-\tilde{\mathbf{u}}\|_{L^2(J;L^2(\Omega)^d)}\right].\end{aligned}$$

A final application of the triangle inequality and the Lemmas 3.4.2–3.4.4 results in the desired error estimates. □

Numerical examples demonstrating the convergence results are presented in Section 3.6.

3.5 The reactive transport problem

Consider the reactive transport problem described by the equations for miscible displacement in Chapter 2. In this section, an operator-splitting approach is presented for approximations to the solution of the system (2.14)-(2.16), thus separating the flow and transport components [13, 113]. To speed up the computation, the mortar method is currently applied only to solve the flow problem. Further a time-split scheme is adopted for the transport component. In what follows, the flow is assumed to be independent of the transport. Thus the flow equations can be solved as detailed in (3.9) and Section 3.3.1 and the solution is assumed known by this point. For clarity, the solute transport equations are repeated here in a more general setting than the single-species in a single phase set-up of Section 2.2.2.

In what follows, no-flow boundary conditions as in (2.22) are assumed to hold with $\partial\Omega^N = \partial\Omega$, although more general boundary conditions can also be treated. For a multi-species in a multiphase flow field, the combined equations for species i in phase α is written as,

$$\frac{\partial(\phi c_{i\alpha} S_\alpha)}{\partial t} + \nabla \cdot (c_{i\alpha}\mathbf{u}_\alpha - \phi S_\alpha \mathbf{D}_{i\alpha}\nabla c_{i\alpha}) = r(c_{i\alpha}) \quad \text{in } \Omega \times J, \tag{3.63a}$$

$$\mathbf{D}_{i\alpha}\nabla c_{i\alpha} \cdot \mathbf{n} = 0 \quad \text{on } \partial\Omega \times J, \tag{3.63b}$$

$$c_{i\alpha} = c^0_{i\alpha} \quad \text{in } \Omega \times \{0\}. \tag{3.63c}$$

It is noted that the diffusion-dispersion tensor for species i in phase α is expressed as a sum of *molecular diffusion* and *hydrodynamic dispersion* components; i.e., $\mathbf{D}_{i\alpha} = \mathbf{D}^{\text{diff}}_{i\alpha} + \mathbf{D}^{\text{hyd}}_{i\alpha}$, where,

$$\mathbf{D}^{\text{diff}}_{i\alpha} = \tau_\alpha d_{\text{mol},i\alpha}\mathbf{I} \tag{3.64a}$$

$$\phi S_\alpha \mathbf{D}^{\text{hyd}}_{i\alpha} = d_{t,\alpha}|\mathbf{u}_\alpha|\mathbf{I} + (d_{l,\alpha} - d_{t,\alpha})\frac{\mathbf{u}_\alpha \mathbf{u}_\alpha^T}{|\mathbf{u}_\alpha|} \tag{3.64b}$$

Here τ_α is a constant that measures the "tortuousity" of the flow of phase α while $d_{\text{m},i\alpha}$, $d_{l,\alpha}$, and $d_{t,\alpha}$ are the *molecular diffusion*, *longitudinal*, and *transverse dispersion coefficients*, respectively. Note that the diffusion-dispersion tensor $\mathbf{D}$ is positive definite and symmetric. Hence, the problem (3.63) is not degenerate parabolic like the two phase immiscible problem of Section 3.2. Finally, the source term $r(c_{i\alpha})$ takes the general form,

$$r(c_{i\alpha}) = r^I_{i\alpha} + \phi S_\alpha r^C_{i\alpha} + q_{i\alpha} \tag{3.65}$$

where the terms $r^I_{i\alpha}$ and $r^C_{i\alpha}$ model the influx (or efflux) from other phases and the chemical rate of decay (or formation) of species i in phase α, resp. The term $q_{i\alpha}$ models a source (or sink) for species i in phase α. Further, note that the net interchange of species between phases is zero; i.e.,

$$\sum_\alpha r_{i\alpha} + r_{iR} = 0. \tag{3.66}$$

In (3.66), the sum is on flowing phases and r_{iR} is the influx (efflux) of species i into the stationary phases (for e.g., the rock matrix). If there is no adsorption, $r_{iR} \equiv 0$.

3.5.1 A time-split scheme

In the time-split scheme for solving the reactive-transport equations (3.63), advection, reaction and diffusion are solved successively and separately from each other. The solution at each stage contributes to an increment (or decrement) in the concentration. In order to develop this scheme, a “phase-summed” formulation is first derived to simplify the problem. Further, an instantaneous equilibrium partitioning of the species among the phases is assumed. This is given by a constant $\theta_{i\alpha}$ for species i in phase

$$c_{i_\alpha} = \theta_{i\alpha} c_{i\alpha_R}, \tag{3.67}$$

where α_R is a reference phase, say, the water phase. This assumption is justified by the fact that the rate of exchange of species between phases occurs much more rapidly than the rate at which the concentration of individual species changes with time. Then summing (3.63a)–(3.63b) over α, for a given species

i, reduces it to

$$\frac{\partial(\phi_i^* c_{iw})}{\partial t} + \nabla \cdot (c_{iw}\mathbf{u}_i^* - \mathbf{D}_i^* \nabla c_{iw}) = r^*(c_{iw}) \quad \text{in } \Omega \times J, \tag{3.68a}$$

$$\mathbf{D}_i^* \nabla c_{iw} \cdot \mathbf{n} = 0 \quad \text{on } \partial\Omega \times J, \tag{3.68b}$$

$$c_{iw} = c_{iw}^0 \quad \text{in } \Omega \times \{0\}. \tag{3.68c}$$

The asterisked (*) phase-summed terms in (3.68) terms are defined as follows:

$$\phi_i^* = \phi \sum_\alpha \theta_{i\alpha} S_\alpha \tag{3.69a}$$

$$\mathbf{u}_i^* = \sum_\alpha \theta_{i\alpha} \mathbf{u}_\alpha \tag{3.69b}$$

$$\mathbf{D}_i^* = \phi \sum_\alpha S_\alpha \theta_{i\alpha} \mathbf{D}_{i\alpha} \tag{3.69c}$$

$$r^*(c_{iw}) = \phi \sum_\alpha r_{i\alpha}^C + r_{iR} + \sum_\alpha q_{i\alpha}. \tag{3.69d}$$

Note that (3.68) is in fact a system for all the species i. While it is used to solve for c_{iw}, concetrations in the other phases can be calculated from the equilibrium partitioning relationship (3.67). Assume that at time $t = \tau_m$, the concentrations of all species are known. Assume also that $(\tau_m, \tau_{m+1}) \subset (t_n, t_{n+1})$ and that the values of $\mathbf{u}_i^*$ and ϕ_i^* are known at the old and new flow time-steps, i.e., t_n and t_{n+1}. The concentration time step is in general smaller owing to the explicit nature of the advection and reaction components. This is given by a suitably defined CFL criterion. A direct discretization of (3.68a) then yields,

$$\frac{T_i^{m+1} - T_i^m}{\Delta\tau^{m+1}} + \nabla \cdot (c_{iw}^m \mathbf{u}_i^{*,m+1/2} - \mathbf{D}_i^{*,m} \nabla c_{iw}^{m+1}) = r^*(c_{iw}^{m+1/2}). \tag{3.70}$$

In (3.70) $\Delta\tau^{m+1} = \tau_{m+1} - \tau_m$ and $T_i = \phi_i^* c_{iw}$. Note also that the phase-summed properties, ϕ_i^* and $\mathbf{u}_i^*$ are evaluated at time $t \in (\tau_m, \tau_{m+1})$ by linear interpolation between the known values at t_n and t_{n+1}. Direct solution of (3.70) is impractical. Thus, a time-split algorithm is applied wherein the advection, chemical reaction and diffusion-dispersion components are solved "independently" of each other. Each component delivers intermediate values for T_i, labelled $\bar{T}_i$, $\hat{T}_i$ and T_i^{m+1}. The individual steps of this algorithm are described below.

3.5.2 Advection

Let the true and approximate solution spaces for species concentration be the same as those defined for pressure (or saturation) defined in in Section 3.3; i.e., piecewise constants in each element of partitions $\mathcal{T}_{h,j}$. The equation solved in the advection step is then given (in the weak form) for sub-domains $1 \leq j \leq n_b$ by

$$\left(\frac{\partial \phi_i^* c_{iw}}{\partial t}, w\right)_{\Omega_j} + (\nabla \cdot (c_{iw}\mathbf{u}_i^*), w)_{\Omega_j} = \left(\sum_\alpha q_{i\alpha}, w\right)_{\Omega_j} \qquad w \in W_j. \tag{3.71}$$

Notice that only the last term of the right hand side given by (3.69d) is included as the source term in (3.71). The advection problem (3.71) is solved by applying a higher order Godunov scheme using upstream weighted concentrations in computing the "fluxes" in the resulting Riemann problem. This eliminates any instability in the solution (see Appendix A) owing to the convection term, $\nabla \cdot (c_{iw}\mathbf{u}_i^*)$ in (3.71) that is known (see [32]) to introduce spatial oscillations into the numerical scheme that are undesirable. This is especially true if $|\mathbf{u}_i^*|$ is much larger than $\|\mathbf{D}_i^*\|$, specifically when the Peclet number is greater than 2. The Peclet number is the "normal-to-face" velocity times the inter-node distance divided by the diffusivity, i.e. for a constant scalar diffusivity, in one dimension, this takes the form $Pe = (\mathbf{u}_i^* \cdot \mathbf{n})\Delta x/D$. Hence, there is a need to suitably treat this term to remove this spatial instability in the numerical solution.

Consider then the following upwinding scheme. Let the finite element approximation of the solution to (3.71) be $c_{h,iw}$. It is first observed that the term $(\nabla\cdot(c_{h,iw}\mathbf{u}_{h,i}^{*,m+1/2}), w)_{\Omega_j}$ arising in the finite element approximation of(3.71) may be expanded as

$$(\nabla \cdot (c_{h,iw}\mathbf{u}_{h,i}^{*,m+1/2}), w)_{\Omega_j} = (\nabla c_{h,iw} \cdot \mathbf{u}_{h,i}^{*,m+1/2}, w)_{\Omega_j} + (c_{h,iw}\nabla \cdot \mathbf{u}_{h,i}^{*,m+1/2}, w)_{\Omega_j}$$

upon applying the differentiation by parts identity $\nabla \cdot (c\mathbf{u}) \equiv \nabla c \cdot \mathbf{u} + c\nabla \cdot \mathbf{u}$. Then, summing over all the elements in $\mathcal{T}_{h,j}$, integrating by parts and recalling that $c_{h,iw} \in W_h$ (so that $\nabla c_{h,iw}|_E = 0$) yields

$$(\nabla \cdot (c_{h,iw}\mathbf{u}_{h,i}^{*,m+1/2}), w)_{\Omega_j} = \sum_{E\in\mathcal{T}_{h,j}} (c_{h,iw}\nabla \cdot \mathbf{u}_{h,i}^{*,m+1/2}, w)_E$$

$$= \sum_{E\in\mathcal{T}_{h,j}} \left\langle c_{h,iw}\mathbf{u}_{h,i}^{*,m+1/2} \cdot \mathbf{n}_E, w\right\rangle_{\partial E} - \sum_{E\in\mathcal{T}_{h,j}} (\mathbf{u}_{h,i}^{*,m+1/2}, \nabla(c_{h,iw}w))_E.$$

The latter term, $(\mathbf{u}_{h,i}^{*,m+1/2}, \nabla(c_{h,iw}w))_E$, vanishes on each element E, since $c_{h,iw}w \in W_h$, the space of piecewise constants on each element of $\mathcal{T}_h$. Here, note that $\mathbf{n}_E$ is the unit outward normal to E. Thus the convection term reduces to

$$(\nabla \cdot (c_{h,iw}\mathbf{u}_{h,i}^{*,m+1/2}), w)_{\Omega_j} = \sum_{E\in\mathcal{T}_{h,j}} \left\langle c_{h,iw}\mathbf{u}_{h,i}^{*,m+1/2} \cdot \mathbf{n}_E, w\right\rangle_{\partial E}. \tag{3.72}$$

Let ∂E_{jk} be the interface between elements E_j and E_k and recall that $c_{h,iw}$ is discontinuous along ∂E_{jk}, since it is piecewise constant over each element E of $\mathcal{T}_h$. The upwinding scheme is then applied to the element E_j along the interface; i.e., for $\mathbf{x} \in \partial E_{jk}$, gives,

$$\left\langle c_{h,iw}\mathbf{u}_{h,i}^{*,m+1/2} \cdot \mathbf{n}_{E_j}, w\right\rangle_{\partial E_{jk}} = \begin{cases} \left\langle c_{h,iw}|_{E_j}\mathbf{u}_{h,i}^{*,m+1/2} \cdot \mathbf{n}_{E_j}, w\right\rangle_{\partial E_{jk}} & \text{if } \mathbf{u}_{h,i}^{*,m+1/2} \cdot \mathbf{n}_{E_j} > 0 \\ \left\langle c_{h,iw}|_{E_k}\mathbf{u}_{h,i}^{*,m+1/2} \cdot \mathbf{n}_{E_j}, w\right\rangle_{\partial E_{jk}} & \text{if } \mathbf{u}_{h,i}^{*,m+1/2} \cdot \mathbf{n}_{E_j} < 0. \end{cases}$$

This basically states that $c_{h,iw}$ assumes the "upwind" value (denoted by $c_{h,iw}^{\text{upw}}$) on the interface ∂E_{jk}; i.e., if the fluid is flowing out from element j into element k, then $c_{h,iw}$ assumes the value in E_j on the interface and if the fluid enters element j from element k, then $c_{h,iw}$ assumes the value in E_k. It can be shown that this simple method ensures that the resulting numerical scheme is stable; (see [60, 81]). At the interfaces between sub-domains with non-matching grids, the upwind value (in the case when fluid is entering the element under consideration) is the L^2 projection from the adjacent sub-domain.

Setting $T_i^m = \phi_i^{*,m}c_{h,iw}^m$, an explicit approximation of the time derivative in (3.71) yields the following weak form for a first-order Godunov method,

$$\left(\frac{\bar{T}_i - T_i^m}{\Delta\tau^{m+1}}, w\right)_{\Omega_j} + \sum_{E\in\mathcal{T}_{h,j}} \left\langle c_{h,iw}^{m,\text{upw}}\mathbf{u}_{h,i}^{*,m+1/2} \cdot \mathbf{n}_E, w\right\rangle_{\partial E} = (\sum_\alpha q_{i\alpha}, w)_{\Omega_j}, \quad w \in W_{h,j}$$

for $\bar{T}_i$ from which the intermediate value of concentration, $\bar{c}_{h,iw}$ can be calculated using $\bar{c}_{h,iw} = \bar{T}_i/\phi_i^{*,m+1}$. For higher-order Godunov methods, the implementation presented in [44, 59] can be followed. The basic idea is to construct a numerical flux approximation from a piecewise linear re-construction of the scalar variable, $c_{h,iw}$ using the element slopes from different slope calculation methods [24]. The numerical flux approximation on the boundary of each element consists of calculating left and right states, and solving a Riemann problem in one-dimension (normal to the boundary).

Given left and right states c^L and c^R, the Riemann solution is determined by the Godunov flux [64]. For a given flux function $\omega(c)$, the Godunov flux $H_\omega(c^L, c^R)$ is given by

$$H_\omega(c^L, c^R) = \begin{cases} \min_{c^L \le c \le c^R} \omega(c) & \text{if } c^L \le c^R \\ \max_{c^R \le c \le c^L} \omega(c) & \text{otherwise.} \end{cases}$$

The calculation of left and right states follows from a Taylor expansion about the element centers in each direction as presented in [44]. It can also be shown that H_ω is Lipschitz in its arguments if ω is Lipschitz in c, and H_ω is consistent, that is $H_\omega(c, c) = \omega(c)$. Finally, for monotone increasing positive coefficients such as c_{iw} in (3.71), the numerical flux is simply the upwinded flux evaluated at either c^L or c^R depending on the direction of the flux as described for the first-order upwinded scheme.

3.5.3 Chemical reaction

After the advection step is completed, the next step is to solve the chemical reaction component of (3.70) given by

$$\frac{\partial \phi_i^* c_{iw}}{\partial t} = \phi \sum_\alpha r_{i\alpha}^C \tag{3.73}$$

which can be expressed as a system of non-linear ODEs in the vector of concentrations $\mathbf{c} \equiv \{c_{iw}\}_{i=1}^{n_c}$. Then, the right hand side is the vector of reaction rates $\mathbf{r}(\mathbf{c})$ and the resulting system is given by

$$\frac{\mathrm{d}\mathbf{c}}{\mathrm{d}t} = \mathbf{r}(\mathbf{c}). \tag{3.74}$$

In (3.73), the adsorption term is assumed to be identically zero. Explicit ODE integration can be used to solve (3.73), even exactly in some cases (depending on the right hand side). Approximations can be obtained by numerical integration; for e.g., with the first order forward-Euler scheme, (3.73) reduces to

$$\frac{\hat{T}_i - \bar{T}}{\Delta t} = \phi \sum_{\alpha} r^C_{i\alpha} \tag{3.75}$$

for the intermediate value of concentrations, $\hat{T}$ which is then used as an initial condition for the diffusion-dispersion step to be discussed in Section 3.5.4.

For more accurate approximations, higher-order Runge-Kutta integration schemes are used in the numerical implementation. For example, suppose $\Delta\tau_l \equiv \tau_{l+1} - \tau_l$ to be the time step at which the chemical reaction step is performed, where $\tau_l, \tau_{l+1} \in [\tau_m, \tau_{m+1}]$. Note that chemical reaction time steps are nested within the transport step, which is in itself nested within the flow step. This is required because the reaction rates can become large and thus smaller time steps are needed in order to maintain stability of the solution of the ODE system. An explicit second-order Runge-Kutta integration scheme is then given by the predictor-corrector steps

$$\begin{aligned} \delta c_{1,i} &= \Delta\tau^l r_i\left(\mathbf{c}\right) \\ \delta c_{2,i} &= \Delta\tau^l r_i\left(\mathbf{c} + \frac{1}{2}\delta\mathbf{c}_1\right) \\ \hat{\mathbf{c}} &= \mathbf{c} + \delta\mathbf{c}_2. \end{aligned}$$

The exact form of the right-hand side depends on the nature of the chemical reaction. It is noted here that for all first order reactions governed by a *radioactive decay* law, as in (3.80), this term is treated in the diffusion-dispersion component. This is because the negative exponent, $-\lambda_d$, which denotes the rate at which the species decays with time, when moved to the left-hand side, adds to the diagonal of the resulting matrix in the finite element approximation. This results in stronger diagonal dominance which makes the diffusion step more stable.

The right-hand side of (3.75) will be denoted by R_i^C, where, for simplicity the phase subscript, α has been dropped. Assume there are N_C components that react to form N_R products, of which N_R^Q have reached an equilibrium concentration and N_R^K are kinetic. The rate at which the kinetic products are formed is given by the classical kinetic reaction law,

$$R_i^C = k_i^f \prod_{j=1}^{N_C} c_j^{p_{ji}} - k_i^b c_{N_C+i}. \tag{3.76}$$

In (3.76), k_i^f and k_i^b are the *forward* and *backward* rate constants that model the rates at which the product is formed and lost, respectively in a given phase. Recall that most chemical reactions proceed in both directions. Finally, $\mathbf{P} = \{p_{ji}\} \in \mathbb{R}^{N_C \times N_R^K}$ is the matrix of *powers* on the concentrations of the components in the rate law.

The "Monod" style rate law is often used instead of the classical rate law to model the growth of microbes at a concentration X, on a substrate at a concentration S, and is given by

$$\frac{\mathrm{d}X}{\mathrm{d}t} = kX\frac{S}{K+S}, \tag{3.77}$$

where, the constant K is referred to as the *half saturation* constant. The Monod rate equation (3.77) is widely used to model biologically mediated reactions. A more general form of (3.77) is used in the numerical experiment presented in Section 3.6.3, given by,

$$R_i^C = k_i^f \prod_{j=1}^{N_C} c_j^{p_{ji}} \prod_{j=1}^{N_C} \frac{c_j}{K_{ij}^{\text{half}} + c_j} - k_i^b c_{N_C+i}. \tag{3.78}$$

Note that (3.78) is applied to each of the N_R^M products modeled using the Monod style law. Typically these reactions are irreversible and so k_i^b is set to zero.

Equilibrium controlled reactions are governed by equations that take the form,

$$c_{N_C+i} = K_i \prod_{j=1}^{N_C} c_j^{a_{ji}}, \quad i = 1, \ldots, N_R^Q. \tag{3.79}$$

where, K_i is the equilibrium constants of these reactions. Recall that the equilibrium constant of a chemical reaction is equal to the ratio of the forward and backward rate constants. This is referred to as the *mass action* law. The matrix $\mathbf{A} = \{a_{ji}\}$ is called the *stoichiometric* matrix. For more details on the different types of chemical reactions and rate laws, the reader is referred to [113]

Radioactive decay (and in general, any first-order reaction) is governed by the equation,

$$R_i^C = -\lambda_d c_i = -\frac{\ln 2}{\tau_i^{\text{half}}} c_i, \tag{3.80}$$

where $\lambda_d > 0$, is a radioactive-decay constant and τ_i^{half} is called the *half-life period* of species i. Finally, linear adsorption is modelled by the equation,

$$c_{is} = K_{is}^A c_{iw}, \tag{3.81}$$

where c_{is} is the concentration of species i in the the rock (solid) phase and c_{iw} is the concentration in the reference (water) phase. The constant, K_{is}^A, represents an adsorption factor.

3.5.4 Diffusion-Dispersion

After the advection and chemical reaction steps are solved, the next step is to solve the diffusion-dispersion equation. This takes the form,

$$\frac{\partial(\phi_i^* c_{iw})}{\partial t} - \nabla \cdot \mathbf{D}_i^* \nabla c_{iw} = 0. \tag{3.82}$$

This is solved fully implicitly using an expanded mixed finite element formulation with the full-tensor $\mathbf{D}$ as discussed earlier in Section 3.2. The only difference is that, mortars are not used. Instead the problem is solved on the whole domain by applying L^2 projections to account for the non-matching grids. Once again, the quadrature rules defined in [16], reduces the problem to a cell-centered finite difference method for the unknowns; i.e., concentrations of the species.

Consider the discretized form of (3.82) and introduce concentration gradient terms, $\hat{\mathbf{z}} = -\nabla c$ and $\mathbf{z} = \mathbf{D}^* \hat{\mathbf{z}}$. Then, the weak form of (3.82) in an expanded mixed finite element setting, seeks $\hat{\mathbf{z}}_{h,iw}^{m+1}|_{\Omega_j} \in \bar{\mathbf{V}}_{h,j}$, $\mathbf{z}_{h,iw}^{m+1}|_{\Omega_j} \in \mathbf{V}_{h,j}$, $c_{h,iw}^{m+1}|_{\Omega_j} \in W_{h,j}$, such that, for $1 \leq j \leq n_b$,

$$\left(\frac{\phi_i^{*,m+1} c_{h,iw}^{m+1} - \phi_i^{*,m} c_{h,iw}^{m}}{\Delta\tau^{m+1}}, w\right)_{\Omega_j} + \left(\nabla \cdot \hat{\mathbf{z}}_{h,iw}^{m+1}, w\right)_{\Omega_j} = 0, \quad w \in W_{h,j}, \tag{3.83a}$$

$$(\hat{\mathbf{z}}_{h,iw}^{m+1}, \mathbf{v})_{\Omega_j} = (c_{h,iw}^{m+1}, \nabla \cdot \mathbf{v})_{\Omega_j} - \left\langle \mathcal{P}_j c_{h,iw}, \mathbf{v} \cdot \mathbf{n}_j \right\rangle_{\Gamma_j}, \quad \mathbf{v} \in \mathbf{V}_{h,j}, \tag{3.83b}$$

$$(\mathbf{z}_{h,iw}^{m+1}, \tilde{\mathbf{v}})_{\Omega_j} = (\mathbf{D}_i^{*,m+1} \hat{\mathbf{z}}_{h,iw}^{m+1}, \tilde{\mathbf{v}})_{\Omega_j}, \quad \tilde{\mathbf{v}} \in \bar{\mathbf{V}}_{h,i}. \tag{3.83c}$$

Here, $\mathcal{P}_j : L^2(\Gamma_j) \to L^2(\Gamma_k)$ is an L^2-orthogonal projection satisfying $\forall \phi \in L^2(\Gamma_j)$

$$\langle \phi - \mathcal{P}_j \phi, \mathbf{v} \cdot \mathbf{n}_j \rangle_{\Gamma_{kj}} = 0, \quad \forall \mathbf{v} \in \mathbf{V}_{h,i}, \forall k \text{ such that } \overline{\Omega}_k \cap \overline{\Omega}_j \neq \emptyset.$$

It is noted that if this concentration is chosen at time t^{m+1}, then the method is *implicit* in nature. An alternative is to compute projections of concentrations at time t^m resulting in an *explicit* form of the system (3.83). These projections are illustrated for a simple problem with two sub-domains in Figure 3.2 below.

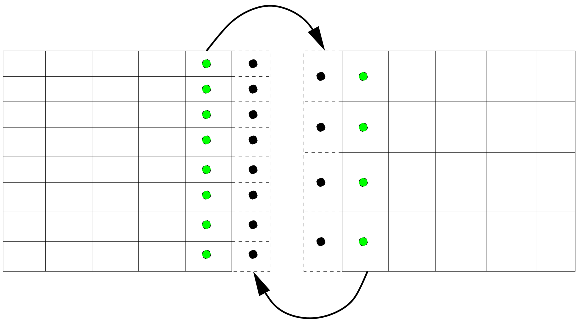

Figure 3.2: Accounting for non-matching grids by L^2 projections.

Consider once again the lowest order RTN spaces for rectangular elements. A difficulty associated with solving the system (3.83) is the large number of unknowns. As in Section 3.3.2, suitable quadrature rules can be defined to approximate the integrals appearing in (3.83), thereby eliminating $\tilde{\mathbf{z}}_{h,iw}$ and $\hat{\mathbf{z}}_{h,iw}$ in terms of $c_{h,iw}$. Depending on the quadrature rules applied, (3.83) can be reduced to a suitable finite difference formulation in $c_{h,iw}$ that is much easier to solve. The quadrature rules for the concentration gradient terms are given as follows.

$$(\hat{\mathbf{z}}_{h,iw}, \mathbf{v})_{\Omega_j} \approx (\hat{\mathbf{z}}_{h,iw}, \mathbf{v})_{\Omega_j,TM}, \tag{3.84a}$$

$$(\mathbf{z}_{h,iw}, \mathbf{v})_{\Omega_j} \approx (\mathbf{z}_{h,iw}, \mathbf{v})_{\Omega_j,TM}, \tag{3.84b}$$

$$(\mathbf{D}_i^* \hat{\mathbf{z}}_{h,iw}, \mathbf{v})_{\Omega_j} \approx (\mathbf{D}_i^* \hat{\mathbf{z}}_{h,iw}, \mathbf{v})_{\Omega_j,T}. \tag{3.84c}$$

In (3.84), as in Section 3.3.2, the concentration gradient on a cell edge is expressed in terms of the adjacent cell concentrations. Thus, for elements on an interface between two sub-domains, the projection $\mathcal{P}$ is used to project concentrations from the elements on the interface of the adjacent sub-domain into an extra (ghost) layer, as illustrated by Figure 3.2. In this manner, the gradients are completely eliminated from the system (3.83), resulting in a linear system for concentrations with a 19-point stencil in three dimensions. Typically this system is non-symmetric and is solved by a preconditioned GMRES solver.

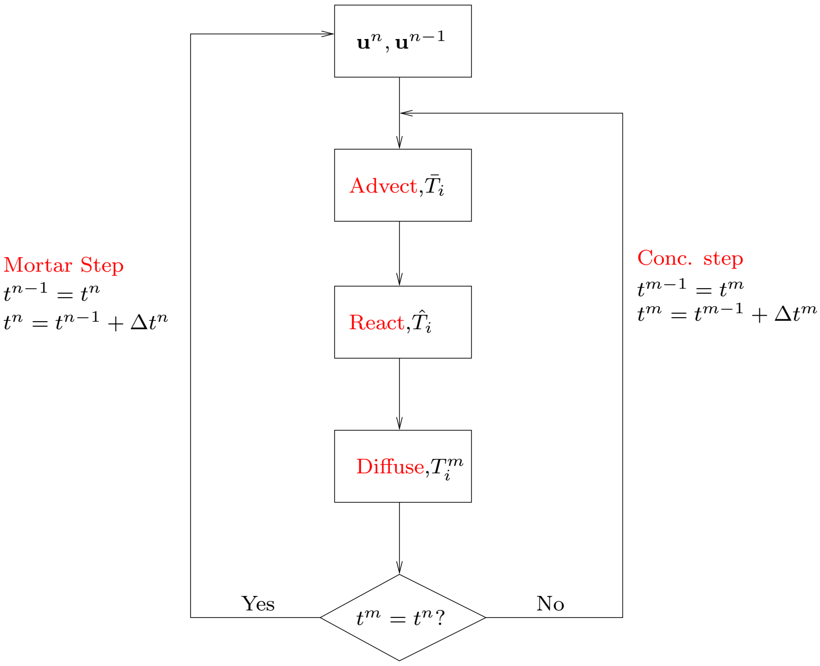

Figure 3.3: Algorithm for time-split scheme

3.6 Numerical results

In this section, some numerical examples are presented that demonstrate the efficiency and effectiveness of the mortar finite element method for some benchmark problems in transient multiscale flow in porous media applications. The advantage of using higher order mortar spaces is also demonstrated. The examples presented here cover four basic types of problems:

(1) Transient single phase applications,

(2) Transient two phase applications, and

(3) Reactive transport applications.

3.6.1 Transient single phase applications

Consider flow of a slightly compressible fluid through a porous medium. The flow problem is governed by (2.15)–(2.16) of Section 2.2.1. This section is divided into two parts. The first part demonstrates numerical convergence results of the mortar multiscale finite element method for slightly compressible single phase flow. To this end, two 3-d two-block test problems are presented with known analytic solutions $p = p(\mathbf{x}, t)$. The errors in the pressure p and velocity u are shown for varying mesh element and time step sizes. For ease of computation and input, the gravity term is ignored in the calculation by assuming $g \equiv 0$ but it does not in any way affect the calculation of errors or the final result. Optimal order rates of convergence are observed for the pressure variable in both cases, but sub-optimal rates are observed for the velocity variable. The sub-optimal rates observed for velocity could be due to the post-processing for velocity in the computation as well as the discrete-in-time approximation of the time integrals.

The second part considers two slightly harder problems that have proved challenging to multiscale methods [74]: the idealized diagonal channel problem and the fluvial reservoir problem (the latter represents the 85th layer of the 10th

SPE comparative project on upscaling methods). Solutions obtained for these problems by applying the mortar mixed finite element method were found to compare favorably to the results presented by Aarnes *et al* [74] for the incompressible case. The results shown here are of $\ln |\mathbf{u}|$ for slightly compressible flow. A compressibility factor of 4.0×10^{-5} psi^{-1} was assumed for the fluid phase in the calculations. The latter computations were performed on upto 16 processors on the Bevo cluster at the Center for Subsurface Modeling at the University of Texas at Austin.

3.6.1.1 Convergence tests

For the first example, an isotropic and homogeneous reservoir with an identity permeability field, $\mathbf{K} = \mathbf{I}$ (mD) is considered. An analytic true solution for the pressure field given by

$$p(\mathbf{x}, t) \equiv x_1^2 + x_2^2 + x_3^2 + t^2$$

is prescribed in the domain which is a cube of side 1 ft in $\mathbb{R}^3$ described by the co-ordinates $[0, 1]^3$. The solution is computed numerically using the mortar multiscale mixed finite element method developed in Sections 3.3–3.3.1. In order to reproduce an appoximation to the analytic solution, IPARS was suitably modified to accept boundary conditions by means of arbitrary user-defined analytical functions. Further, to facilitate the computation of errors in pressure and velocity, a provision was made to accept any analytic true solution, velocity and source (right hand side) term. In this particular case, the velocity components are clearly given by the Darcy law (2.16) to be

$$u_1(\mathbf{x}, t) \equiv -\frac{2x_1}{\mu}, \quad u_2(\mathbf{x}, t) \equiv -\frac{2x_2}{\mu}, \text{ and } u_3(\mathbf{x}, t) \equiv -\frac{2x_3}{\mu}.$$

A constant fluid viscosity $\mu \equiv 2$ cp and porosity of 0.2 are assumed. The fluid density is assumed to vary as $\rho = \rho_0 \exp(cp)$ and the source term is obtained by direct substitution of ρ, p and $\mathbf{u}$ into the continuity equation (2.15). The simulation end time $T = 8$ days. Figure 3.4 shows snapshots of the pressure solution at $t = 2,\ 4,\ 6$ and 8 days on the fourth level of refinement (see

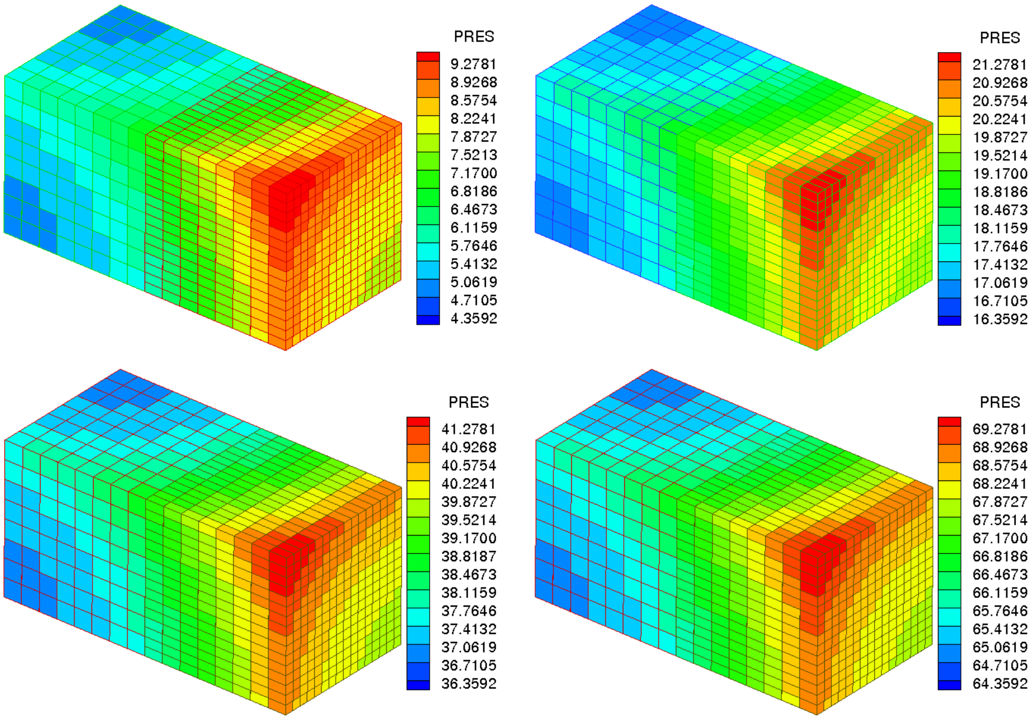

Figure 3.4: Convergence test 1: Snapshots of pressure at $t = 2, 4, 6$ and 8 days.

Table 3.2). Table 3.1 shows plots of errors in pressure, p and velocity, $\mathbf{u}$ i.e., the quantities $\|p - p_h\|_{L^\infty(J;L^2(\Omega))}$ and $\|\mathbf{u} - \mathbf{u}_h\|_{L^2(J;L^2(\Omega)^d)}$ for the case of continuous linear mortar functions, over varying levels of sub-domain grid refinements starting from coarsest grids of 1×1×1 upto finest grids of 32×32×32 on either sub-domain. With each level, the time step has been decreased by the same factor as the mesh element size (in this case a factor 2). Similar data for the case of non-matching grids in the two sub-domains is presented in Table 3.2.

Level	Sub-domain grids	Mortar grid	p_{err}	$\mathbf{u}_{\text{err}}$
0	1×1×1	0×0	3.5060E-01	2.9224E-02
1	2×2×2	1×1	8.8036E-02	2.0668E-02
2	4×4×4	2×2	2.2101E-02	1.4614E-02
3	8×8×8	4×4	5.5260E-03	1.0334E-02
4	16×16×16	8×8	1.3602E-03	7.3083E-03
5	32×32×32	16×16	3.0681E-04	5.1685E-03

Table 3.1: Convergence test 1: Pressure and velocity error using continuous linear mortars, matching grids

Level	Sub-domain grids	Mortar grid	p_{err}	$\mathbf{u}_{\text{err}}$
1	1×1×1, 2×1×2	1×1	2.2728E-01	2.7379E-02
2	2×2×2, 4×2×4	1×1	5.9797E-02	1.9418E-02
3	4×4×4, 8×4×8	2×2	1.5492E-02	1.3693E-02
4	8×8×8, 16×8×16	4×4	3.9567E-03	9.6730E-03
5	16×16×16, 32×16×32	8×8	9.9162E-04	6.8370E-03

Table 3.2: Convergence test 1: Pressure and velocity error using continuous linear mortars, non-matching grids

For the second example, an anisotropic, heterogenous and diagonal permeability field given by the diagonal elements $K_{11} = \sin(x_2 x_3)$, $K_{22} = x_1^2 + x_3^2$ and $K_{33} = 1 - \cos(x_1 x_2)$. As in the case of the previous example, an analytic true solution for the pressure field given by

$$p(\mathbf{x}, t) \equiv x_2^2 + x_3^2 + x_1 x_2 \cos(t)$$

is prescribed in the domain which is once again the cube $[0, 1]^3$. The velocity components of flow for this pressure field are given by

$$u_1(\mathbf{x}, t) \equiv -\frac{x_2 \sin(x_2 x_3) \cos t}{\mu}, \quad u_2(\mathbf{x}, t) \equiv -\frac{(x_1^2 + x_3^2)(2x_2 + x_1 \cos t)}{\mu}, \text{ and}$$
$$u_3(\mathbf{x}, t) \equiv -\frac{2\,[1 - \cos(x_1 x_2)]\, x_3}{\mu}.$$

Clearly the permeability field is spatially heterogenous and the true pressure is oscillatory in time while the true velocity is oscillatory in both space and time. Thus, this problem poses more challenges to the mortar method especially during the interface Newton iterations. But once again, similar convergence rates are observed as in the case of the previous example.

The fluid properties (viscosity), constitutive equations (for fluid density in terms of pressure) and simulation end time ($T = 8$ days) are the same as in the previous example. Figure 3.5 shows snapshots of the pressure solution at $t = 2$, 4, 6 and 8 days on the fourth level of refinement (see Table 3.4). Table 3.3 shows plots of errors in pressure, p and velocity, $\mathbf{u}$ i.e., the quantities $\|p - p_h\|_{L^\infty(J;L^2(\Omega))}$ and $\|\mathbf{u} - \mathbf{u}_h\|_{L^2(J;L^2(\Omega)^d)}$ for the case of continuous quadratic mortar functions, over varying levels of sub-domain grid refinements starting

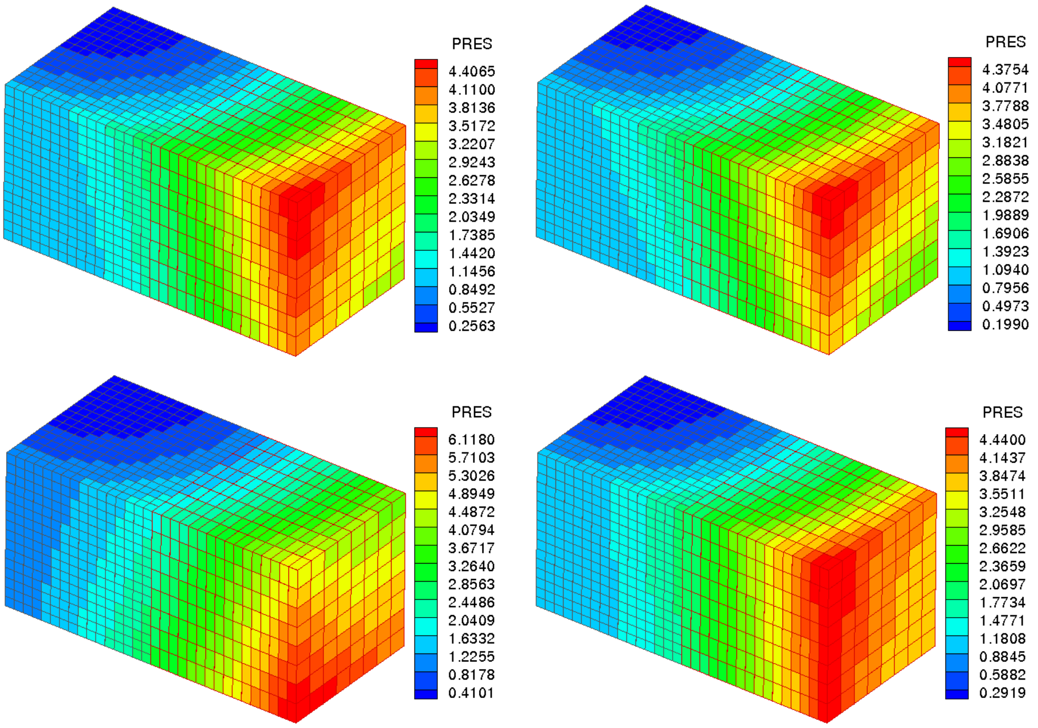

Figure 3.5: Convergence test 2: Snapshots of pressure at $t = 2, 4, 6$ and 8 days.

from coarsest grids of 1×1×1 upto upto finest grids of 32×32×32 on either sub-domain. Once again, with each increasing level, the time step has been decreased by the same factor as the mesh element size (in this case a factor 2). Similar data for the case of non-matching grids in the two sub-domains is presented in Table 3.4.

It is observed from Tables 3.3 and 3.4 that the rate of convergence of the pressure variable is slightly higher for the case of continuous quadratic moratrs

Level	Sub-domain grids	Mortar grid	p_{err}	$\mathbf{u}_{\text{err}}$
0	1×2×1	1×1	1.7221E-01	1.4775E-02
1	2×2×2,	1×1	4.3295E-02	1.0843E-02
2	4×4×4,	1×1	1.0372E-02	7.6064E-03
3	8×8×8,	2×2	2.5073E-03	5.3191E-03
4	16×16×16,	3×3	5.8309E-04	3.7196E-03
5	32×32×32,	4×4	1.3601E-04	2.5866E-03

Table 3.3: Convergence test 2: Pressure and velocity error using continuous quadratic mortars, matching grids

Level	Sub-domain grids	Mortar grid	p_{err}	$\mathbf{u}_{\text{err}}$
1	2×2×2, 1×2×1	1×1	2.6288E-01	1.0781E-02
2	4×4×4, 2×4×2	1×1	4.2737E-02	9.0668E-03
3	8×8×8, 4×8×4	2×2	8.2127E-03	6.8452E-03
4	16×16×16, 8×16×8	3×3	1.8084E-03	4.8870E-03
5	32×32×32, 16×32×16	4×4	4.0186E-04	3.4549E-03

Table 3.4: Convergence test 2: Pressure and velocity error using continuous quadratic mortars, non-matching grids

than for linear mortars. It is also noted that the number of interface iterations before convergence is achieved is smaller for quadratic mortars.

3.6.1.2 Diagonal channel flow

This problem has proved quite challenging to most multiscale methods. Here, a single high-permeability channel goes diagonally across the (square) domain, from source at the lower left corner to the sink at the upper right corner. The domain measures 64 × 64 units. The permeability is 100 units along the main diagonal (connecting the source and the sink) and unity elsewhere. A unit source and sink are located at either end of the high permeable layer (which is 3 elements thick away from the corners). The domain is partitioned into 64 sub- domains; i.e., an 8×8 coarse grid. Each sub-domain is further sub-divided into an 8×8 fine grid. Thus on the fine scale, an element size is 1 unit, while on the coarse scale it is 8 units. The solution profiles shown here are snapshots at $t = 20$ days.

Figure 3.6 shows the reference solution on the left, on a single-domain (64 x 64 fine mesh) and the mortar solution on the right on an 8×8 sub-domain partition with 4×4 continuous linear mortars. Further, by applying *a posteriori* error estimates based on the work of Wheeler and Yotov [146], the mortar degrees of freedom can be chosen to be coarser away from the regions where the error in the solution is high, while preserving the overall accuracy of the solution. This is illustrated in Figure 3.7 on a 4×4 coarse mesh domain partitioning (sub-domains are 16×16) with 2×2 mortars everywhere; but 4×4 mortars around corner elements.

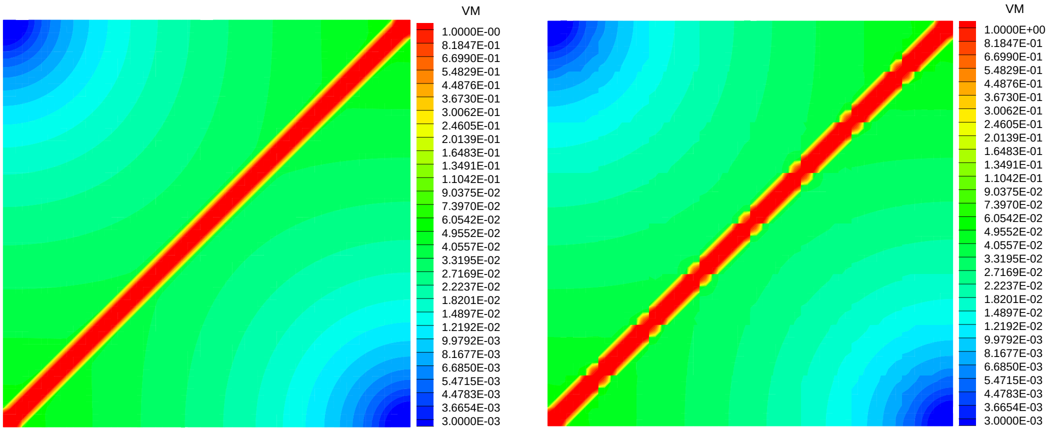

Figure 3.6: Diagonal channel: Reference (left) and mortar (right) solutions.

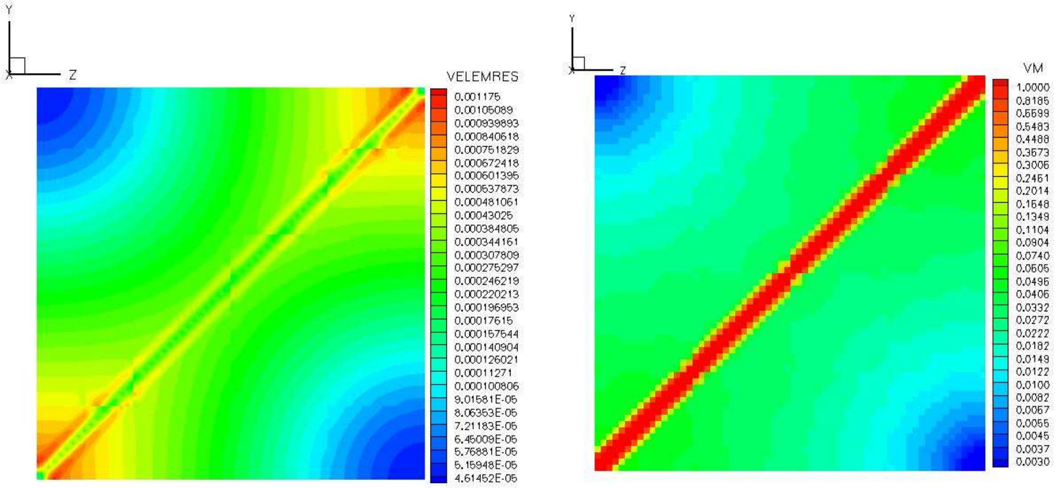

Figure 3.7: Diagonal channel: Residual based errors (left) and coarse-mortar solution (right).

3.6.1.3 Fluvial reservoir flow

As a second example, a more realistic fluvial reservoir problem is considered, where the permeability field contains many narrow high flow "channels". The permeability data for this problem was taken from the 85th layer of the 10th SPE comparative project [38]. The fine grid consists of 60 × 220 elements. Sources and sinks are placed in a five-spot pattern, with a unit source in the center and sinks of equal strength ($\frac{1}{4}^{\text{th}}$ that of the source) at each of the four corners of the domain. The permeability field varies across seven orders of magnitude. The permeability and reference solution on a single domain (60×220 mesh) are shown in Figure 3.8 while the residual based *a posteriori* error estimates for the velocity field and the mortar finite element solution on the 5×11 coarse mesh (55 sub-domains, each with a 12×20 mesh) are shown in 3.9. Again, the mortar elements were chosen coarse where the errors were small. The error was highest at the lower left and upper right corners of the domain because despite extremely low permeabilities, the flow rates specified at the sinks in these corners is equal to the sinks at the higher permeability corners.

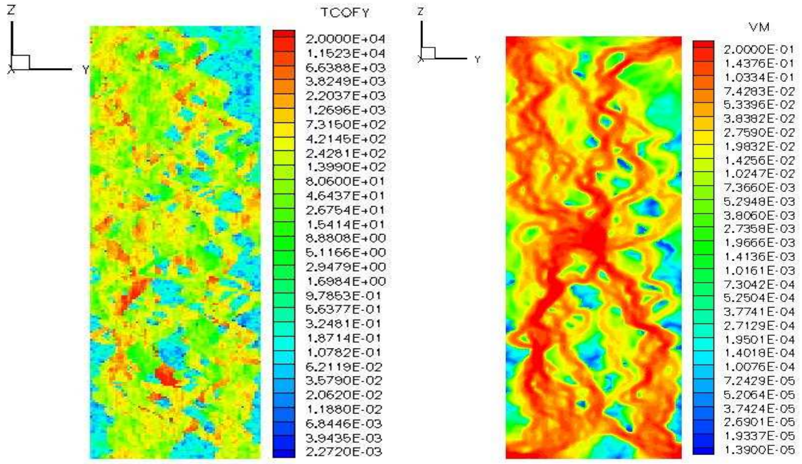

Figure 3.8: Fluvial Reservoir: Permeability and reference solution.

Remark 3.6.1. It is noted here that *a posteriori* error estimates in [146] were derived for elliptic problems (steady single phase flow through porous medium).

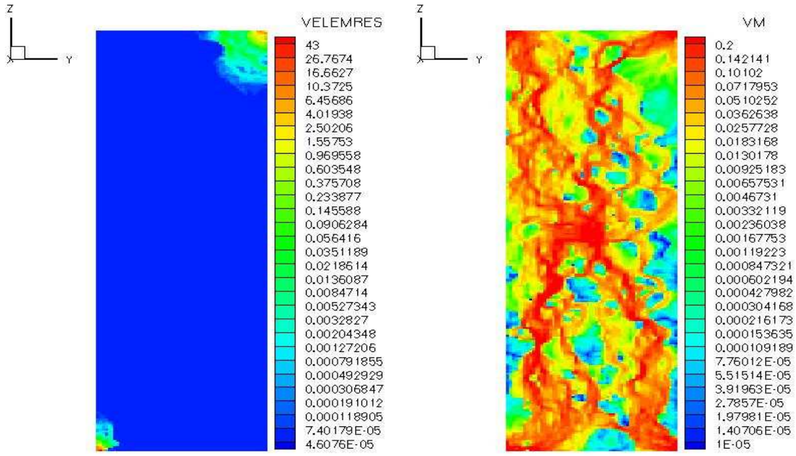

Figure 3.9: Fluvial Reservoir: Residual-based errors and coarse mortar solution.

Hence, they are applied here to the elliptic projection of the mortar finite element solution $p_h, \mathbf{u}_h, \lambda_H$, where λ_H is the pressure on the sub-domain interfaces. Formally stated, this is the solution $p_h^e, \mathbf{u}_h^e, \lambda_H^e$, for $1 \le i \le n$, to the problem,

$$
\begin{aligned}
(\nabla \cdot \mathbf{u}_h^e, w)_{\Omega_i} =& (\hat{q}, w)_{\Omega_i} - (\frac{\partial}{\partial t}(\phi \rho_h), w)_{\Omega_i} && w \in W_{h,i}, \\
(\mathbf{K}^{-1} \rho_h^{-1} \mathbf{u}_h^e, \mathbf{v})_{\Omega_i} =& (p_h^e, \nabla \cdot \mathbf{v})_{\Omega_i} - \langle \lambda_H^e, \mathbf{v} \cdot \mathbf{n}_i \rangle_{\Gamma_i} \\
& - \langle p^D, \mathbf{v} \cdot \mathbf{n}_i \rangle_{\partial \Omega_i \setminus \Gamma} + (\rho_h \mathbf{g}, \mathbf{v})_{\Omega_i} && \mathbf{v} \in \mathbf{V}_{h,i}, \\
\sum_{j=1}^{n} \langle \zeta, \mathbf{u}_h^e \cdot \mathbf{n}_j \rangle_{\Gamma_j} =& 0, && \zeta \in M_H.
\end{aligned}
$$

3.6.2 Transient two phase applications

Consider now the immiscible flow of two phases through a porous medium discussed in Chapters 2 and 3. The phases considered here are oil and water, a very common model in the petroleum industry. The problem considered here used permeability data from the 6th SPE comparative project. In this section, in addition to solution profiles, some comparisons are presented between the continuous piecewise linear and piecewise quadratic mortar space choices [15]. The domain is a 2x2 coarse mesh (i.e., 4 sub-domains) and the computations are performed on different levels with successively finer sub-domain meshes. Theoretical results for optimal convergence rates derived for the single phase (elliptic) problem, provide a means to select the size of the corresponding mortar elements on each level.

3.6.2.1 SPE Case 6

Multiblock multiscale methodology has been implemented in IPARSv2 (Integrate Parallel and Accurate Reservoir Simulator) [70]. In this section, the simulation result is presented for an oil-water immiscible displacement problem in a horizontal cross-section of a heterogeneous reservoir. The simulation domain has dimensions of 6144 ft ×6144 ft. The permeability field and the sub-domain grids on the coarsest level are shown in Figure 3.10. Initial oil pressure is 500 psi and initial water saturation is 0.22, which is close to its residual value. Then water is injected at the upper left corner at a pressure that increases from 505 psi to 5000 psi in the first 100 days (and remains constant thereafter).

The simulation was run on four different levels of refinement. The grids for linear mortars are chosen proportional to the sub-domain grids; more precisely, the grid on a given mortar is taken to be a coarsening by a factor of 2 of the coarser adjacent sub-domain grid. This choice ensures the error is uniform in h everywhere in the domain [142]. The choice for the number of degrees of freedom for quadratic mortars is motivated by a result for single phase flow (see [148], Theorem 2.1 and Remark 2.1). Thus, for quadratic mortars, it is assumed that $N_H = \sqrt{N_h}$, where, N_h and N_H are the number of mortar elements for continuous linear and quadratic mortars respectively. This choice ensures optimal convergence at the rate of $\mathcal{O}(h)$ in the pressure for single phase flow.

The simulations for piecewise continuous linear and quadratic mortars produce almost identical results. Oil pressure and water saturation profiles are shown at $t = 851$ days on the third level of refinement in Figure 3.11 only for quadratics.

The comparison of oil recovery curves in Figure 3.12 also shows that the solutions with linear and quadratic mortars agree almost identically. However the multiscale method using quadratic mortars is more efficient as Table 3.5

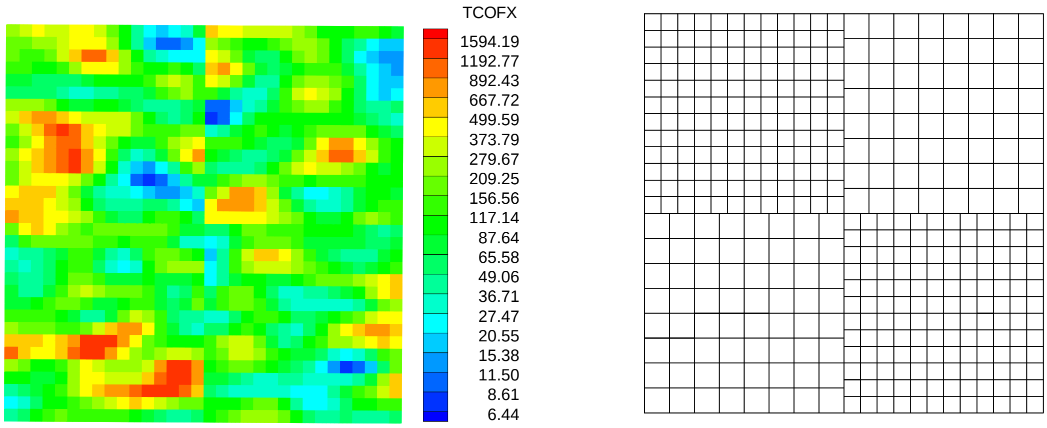

Figure 3.10: Permeability field (left) and grids (right) on the coarsest level.

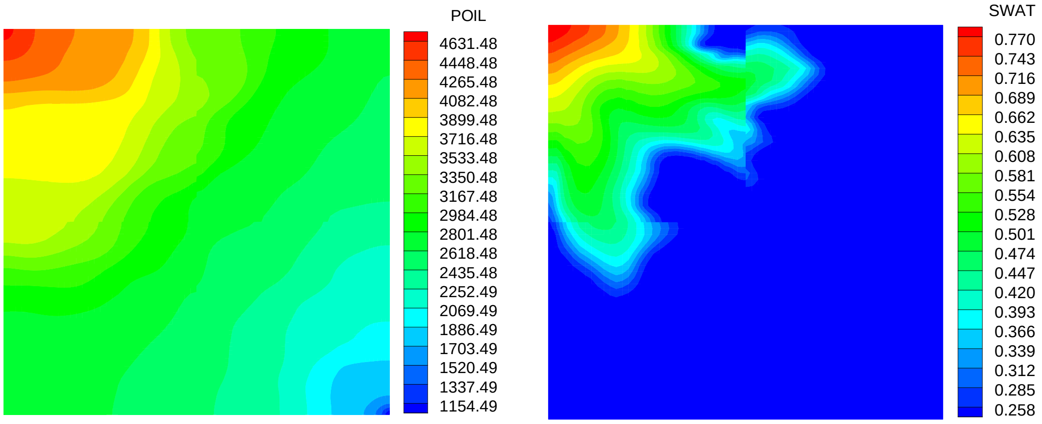

Figure 3.11: Computed solution at 851 days with piecewise quadratic mortars on the third grid level.

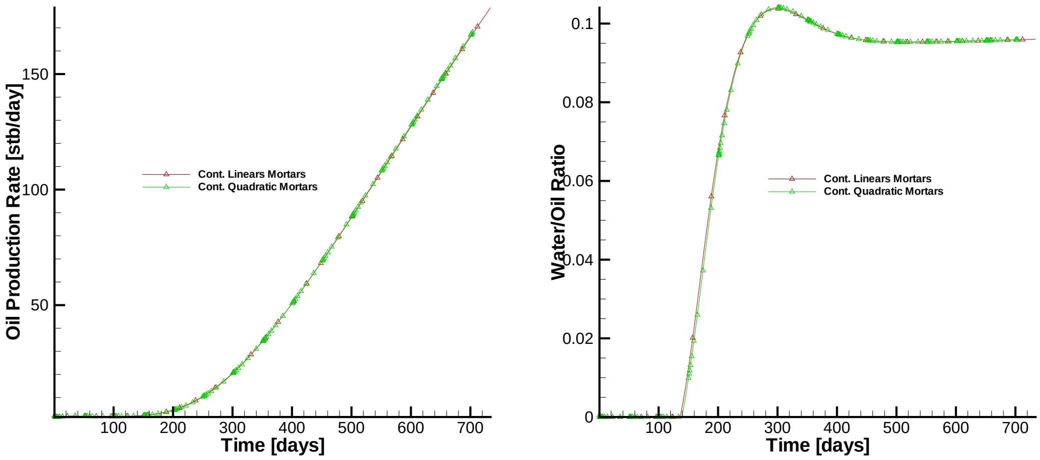

Figure 3.12: Comparison of oil recovery curves for linear and quadratic mortars on the third refinement level.

Level	Sub-domain grids	Linear mortars		Quadratic mortars	
		grids	itns.	grids	itns.
1	8×8, 12×12	4	51.2	2	42.3
2	16×16, 24×24	8	72.7	3	54.4
3	32×32, 48×48	16	92.6	4	63.9
4	64×64, 96×96	32	155.2	6	75.9

Table 3.5: Interface GMRES iterations for linear and quadratic mortars

indicates. There, the average number of interface GMRES iterations per time step are displayed for linears and quadratics at every level of refinement. It is noted that the number is smaller per time step, for the quadratic case and increases at a smaller rate as the grids are refined. All of these computations were performed in parallel on upto 36 processors at CSM's bevo cluster.

3.6.3 Reactive transport applications

In this section, results are presented on numerical solutions to the miscible displacement problem discussed in Section 3.5. Specifically a NAPL remediation application is considered. Microbial bio-degradation (i.e., the decomposition of contaminants by micro-organisms) plays an important role in rendering certain kinds of contaminants harmless. It is a naturally occurring process that can be accelerated to protect potable water supply. Unfortunately, microbial bio-degradation is a physically and chemically complex process. It involves flow and transport. The transport is often characterized by advection, reaction and diffusion. The reaction stage involves chemical interaction between hydrocarbons, microbes, oxygen, nitrogen and various other compounds. Thus, the numerical simulation of these processes is of critical importance in understanding them and designing bio-restoration mechanisms.

In all the examples presented here, a square-shaped domain is considered for simplicity, with dimensions 20 ft×400 ft×400 ft. There are two wells arranged in a quarter-five spot pattern that inject and produce the phase (in this case, water) thus driving the flow of the species. The permeability field and phase summed flux are as shown in Figure 3.13. It has two low permeabil-

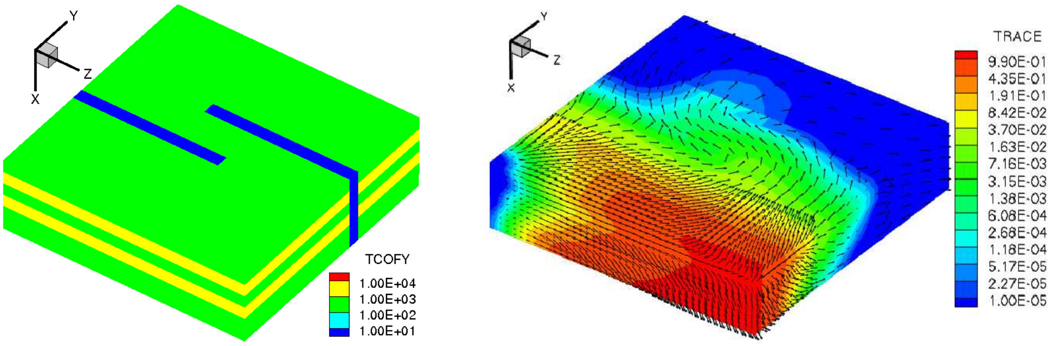

Figure 3.13: Permeability and flow fields for NAPL remediation problem.

ity barriers obstructing the flow, which makes it a hard problem for coupled flow and transport. There are 10 species in this problem. The first and second examples presented here model the species transport in single and two phase flow respectively. The interacting species in both these problems are toluene (C_7H_8; flowing and stationary denoted by the formulae C_7H_8(f) and C_7H_8(s), respectively), oxygen (O_2), nitrogen (N_2), microbes (living and dead, denoted by M_l and M_d, respectively), complex organic bio-degraded products (denoted by P_1 and P_2) and a non-radioactive tracer. The species undergo the following chemical reactions:

$$\begin{array}{ccc} \mathrm{C_7H_8}(f) & \rightleftharpoons & \mathrm{C_7H_8}(s) \\ 10.87\ \mathrm{C_7H_8}(f) + 62.5\ \mathrm{O_2} & \rightleftharpoons & 0.5\ \mathrm{M}_l + \mathrm{P}_1 \\ 10.87\ \mathrm{C_7H_8}(f) + 92.8571\ \mathrm{N_2} & \rightleftharpoons & 0.5\ \mathrm{M}_l + \mathrm{P}_2 \\ \mathrm{M}_l & \rightleftharpoons & \mathrm{M}_d. \end{array}$$

The pertinent data for the first two problems is presented in Table 3.6. No-flow and zero diffusive flux boundary conditions are assumed in these problems. The last example of this section presents a comparison between first- and second-order Godunov schemes applied to the advection component of the transport problem for the case of single species in single phase flow.

3.6.3.1 Species transport in single phase flow

At initial time, the tracer, toluene and the microbes occupy a thin strip on the left-end of the domain, i.e., $0 \leq y \leq y_0$ in Figure 3.13, at concentrations

Property	Value
Simulation end time	101.0 days
Physical dimensions	400.0 ft×400.0 ft×20.0 ft
Depth below surface	1120.0 ft
Vertical/Horizontal perm ratio	5.0
Min/max horizontal perm	10.0 mD, 10000.0 mD
Average porosity	0.2
Initial oil pressure	500.00 psi
Initial water saturation	0.2
Molecular diffusivity	1.0 sq-ft/day
Dispersivity (d_l, d_t)	1.0, 0.2 ft
Oil/water compressibility	4.0E-05, 3.3E-06
Maximum injection bhp	510.0 psi
Minimum producion bhp	350.0 psi

Table 3.6: Reactive transport problems: Summary of test data

Species	Water	Oil
Tracer	1.0	1.0
C_7H_8(f,s)	1.0E-04	1.0
O_2	50.0	1.0
N_2	50.0	1.0
M_l, M_d	1.0	1.E-03
P_1, P_2	1.0	1.E-03

Table 3.7: Equilibrium partitioning coefficents

of 1.0 lbM/cu-ft, 3.0 lbM/cu-ft and 6.12 lbM/cu-ft, respectively. The oxygen and nitrogen occupy the rest of the domain $y_0 \leq y \leq L$ at concentrations of 7.485×10^{-3} lbM/cu-ft and 1.459×10^{-2} lbM/cu-ft, respectively. Here $y_0 = 40$ ft and $L = 400$ ft. A specified hydrostatic phase pressure is used to initialize the flow problem. The problem is first solved, assuming a single-domain with a fine grid ($10 \times 40 \times 40$, with the x-axis pointing in direction of gravity depth).

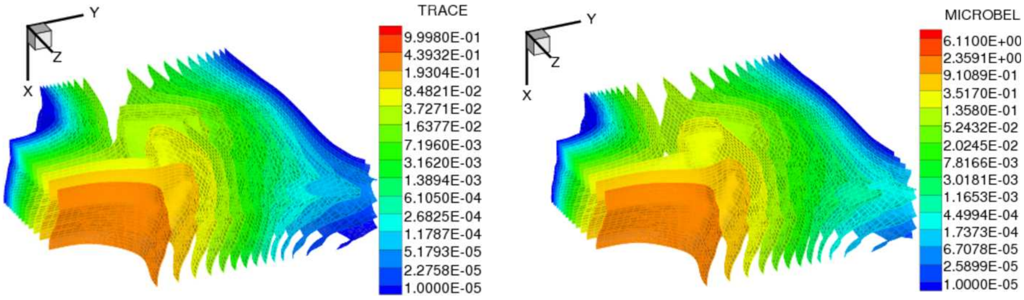

Figure 3.14: Tracer and microbe concentration at $t = 100$ days.

Then the problem is repeated by partitioning the domain into three sub-domains (one fine and two coarse) along the $y-$ direction. This is done in three different ways by positioning the sub-domain with the fine grid differently in each case. The solutions to the single-domain "fine-everywhere" are then compared to the multiblock case. Figure 3.14 shows the tracer and microbe concentrations at time $t = 100$ days for the single-domain problem. Figure 3.15 shows similar profiles for NAPL and bio-degraded product.

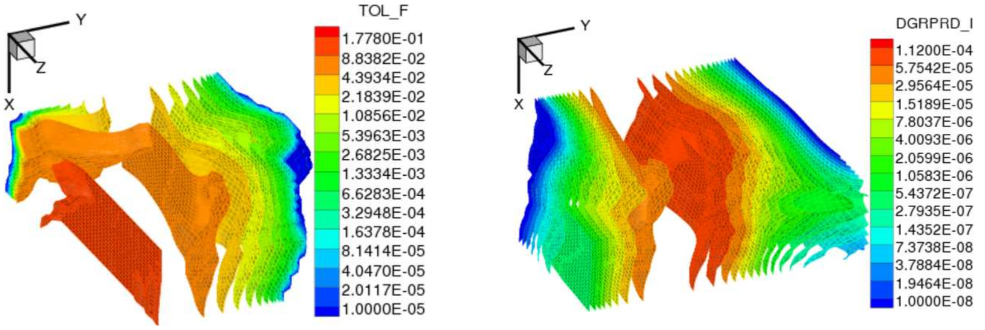

Figure 3.15: NAPL and bio-degraded product concentration at $t = 100$ days.

Figure 3.16 shows the profile of the tracer concentration at times $t = 5, 50$ and 100 days. This demonstrates how the tracer flows with time. The last panel in the figure can be used to compare with the reference solution at the same time in Figure 3.14.

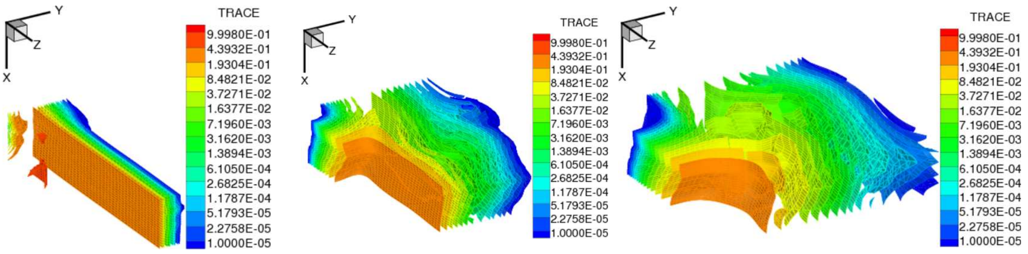

Figure 3.16: Mortars - Tracer concentration at $t = 5, 50$ and 100 days.

Similarly, Figure 3.17 shows the profile of the microbe concentration at similar times with the last panel being the one of interest for comparison. It is also observed that the tracer and the microbe have almost similar profiles with time.

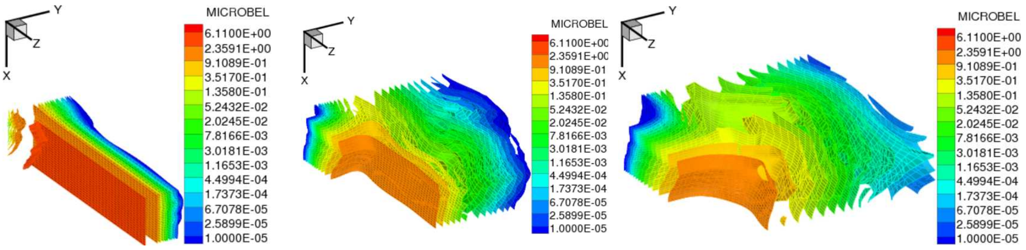

Figure 3.17: Mortars - Microbe concentration at $t = 5, 50$ and 100 days.

Figure 3.18 shows the profile of the NAPL concentration at similar times. From this figure it is observed that the flow and spread of NAPL has been checked to some extent by the reaction with the microbes. Finally, Figure 3.19 shows the profile of concentrations of one of the bio-degraded products at similar times.

In the numerical experiments described, it was observed that variably refined sub-domains (one fine and two coarse with the fine sub-domain located differently in each case) performed up to 50% faster than the single domain fine-everywhere case. This justifies the use of mortars in such problems.

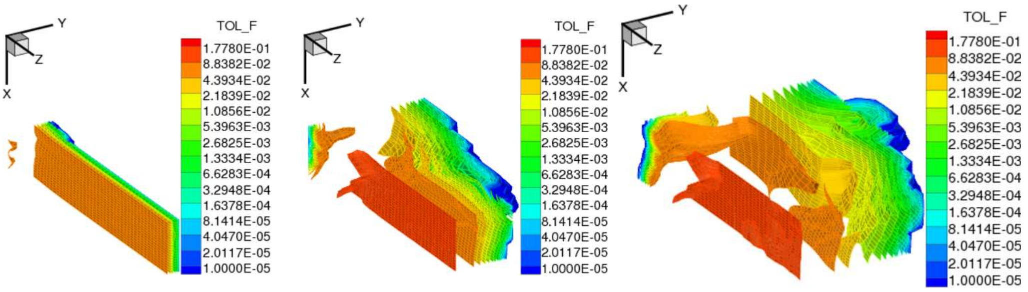

Figure 3.18: Mortars - NAPL concentration at $t = 5, 50$ and 100 days.

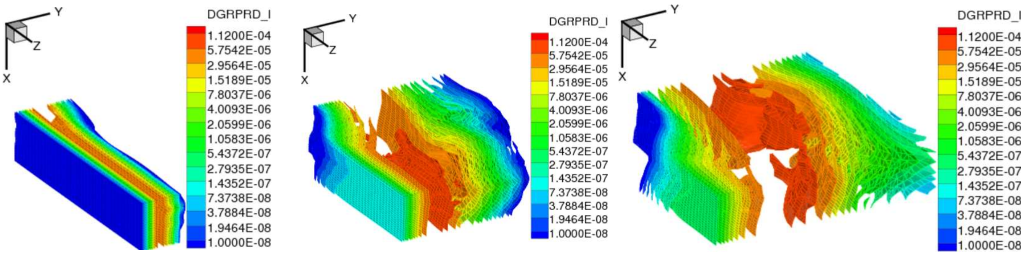

Figure 3.19: Mortars - By-product concentration at $t = 5, 50$ and 100 days.

3.6.3.2 Species transport in two phase flow

In this section, the assumptions of Sections 3.6.3 and 3.6.3.1 still hold but the species are assumed to be transported in two flowing phases (say, water and oil) with initial conditions expressed in the aqueous phase. The equilibrium partitioning coefficients of the species in the phases is given in Table 3.7. It is also assumed that the phases do not enter into chemical reactions with the species. Comparison of the microbe concentration at time $t = 40$ days for the single-domain and a multiblock case is shown in Figure 3.20. It is noted that the front has crossed $y = 280$ ft (Γ_{23}).

Similar comparison at $t = 40$ days is shown in Figure 3.21 for the NAPL concentration. Once again, it is observed that the spread of NAPL has been checked to some extent by the reaction with the microbes. The microbes “feed” on the NAPL in the presence of O_2 and N_2 (a form of aerobic respiration), reducing them to relatively harmless by-products (CO_2 and water). This illustrates the importance of using bio-remediation methods in treating hazardous wastes.

In the numerical experiments described, it was observed that variably

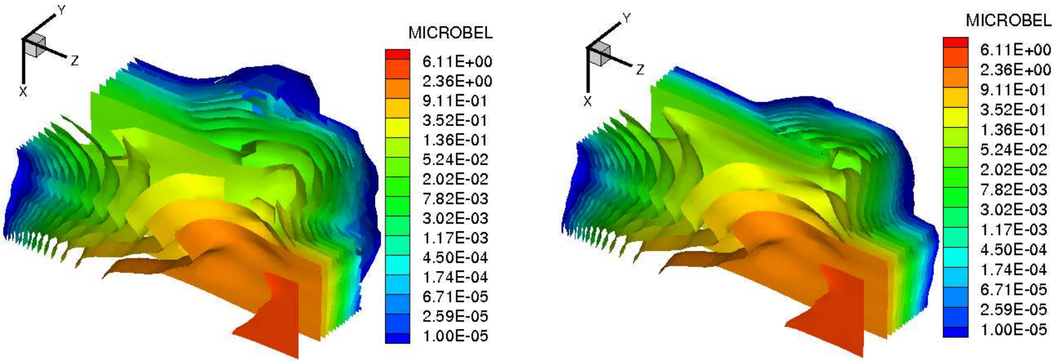

Figure 3.20: Microbe conc. at t = 40 days: multiblock (left) and single block (right).

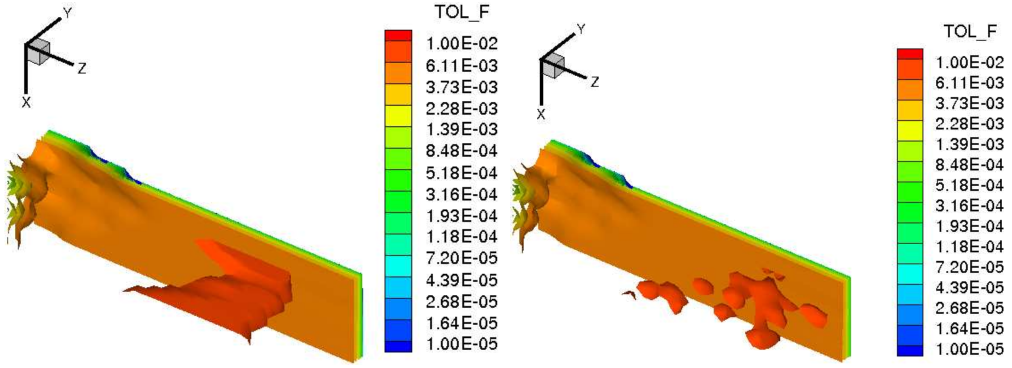

Figure 3.21: NAPL conc. at t = 40 days: multiblock (left) and single block (right).

refined sub-domains (one fine and two coarse with the fine sub-domain located differently in each case) performed upto 50% faster than the single domain “fine-everywhere” case. This justifies the use of mortars in such problems. However, it is noted that coarser sub-domain grid results in increased grid dispersion effects and hence, a dynamic meshing strategy is recommended. Further, appropriate error estimators (for coupled flow and transport) are needed in order to decide where to put the fine grid. This is especially hard in a multi-species example as the one described in this section if the species are scattered in different parts of the domain.

3.6.3.3 Comparison of first- and higher-order Godunov methods

In this section, a comparison of first and higher-order Godunov methods (abbreviated as F.O.G. and H.O.G. respectively) is presented for case of single species transport in single phase flow. The problem is solved on a fine grid of 4×80×80 (with the positive x- axis pointing in the direction of increasing depth). The two wells described earlier in Section 3.6.3 drive the flow. The initial concentration of the species is 1 lbM/cu-ft, located at the $[1, 1, 1]$ element.

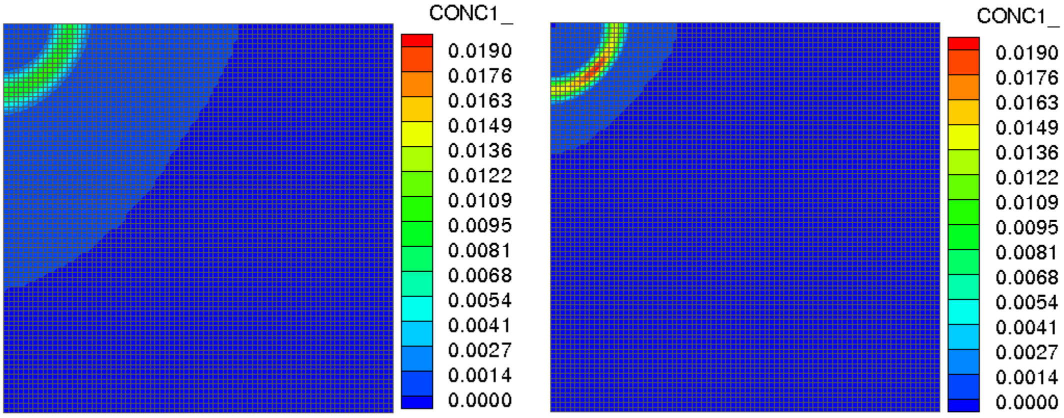

Figure 3.22: Comparison of F.O.G. and H.O.G. methods at 15 days.

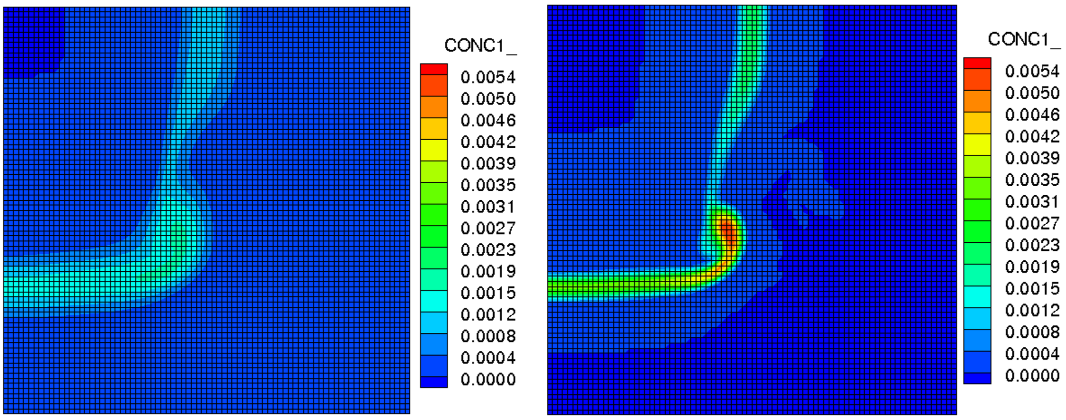

Figure 3.23: Comparison of F.O.G. and H.O.G. methods at 90 days.

The Figures 3.22–3.24 show the concentration of the species at 15, 90 and 140 days using the first- (left) and second-order (right) Godunov methods respectively. Clearly, numerical dispersion is greatly reduced using the higher-order Godunov method.

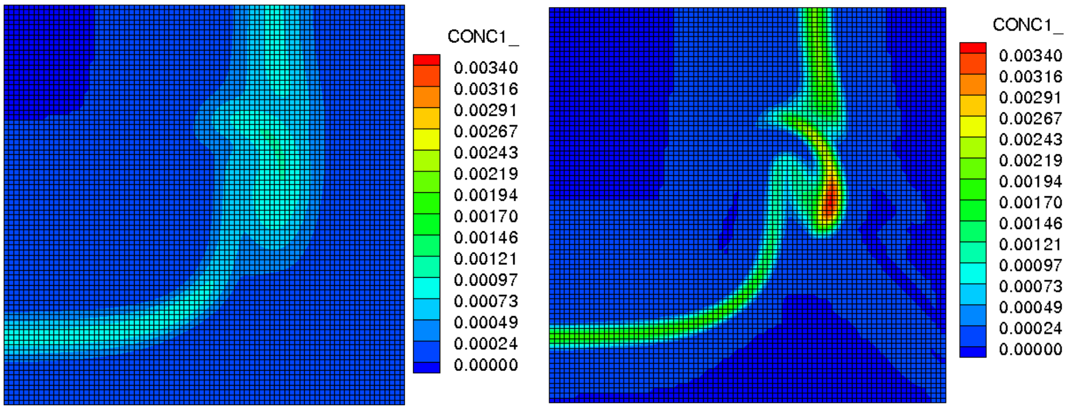

Figure 3.24: Comparison of F.O.G. and H.O.G. methods at 140 days.

Chapter 4

Enhanced velocity mixed FEM for coupling multiphase flow and species transport on non-matching multiblock grids

In the previous chapter, the mortar mixed finite element method was presented to solve the problem of coupling flow and transport on non-matching multiblock grids. In this chapter, a non-mortar method (the enhanced velocity mixed FEM) is presented as an efficient alternative to solving the same problem. The method is locally mass conservative and H-div conforming unlike the mortar method. In addition, the need to perform often expensive interface iterations to solve the non-linear interface problem is completely eliminated. Furthermore, unlike the case of the mortar method, in the case of identical number of elements in problems using single- and multiblock grids, the cost of the non-mortar approach is comparable to the single-block method and if coarser blocks are used, the computational cost is greatly reduced which is a great benefit to using this method.

The enhanced velocity mixed FEM was first introduced for flow problems in [136]. It derives its name from the enhanced velocity spaces along the interfaces, introduced to maintain flux continuity by design. Thus no additional matching conditions (such as pressure or flux matching conditions) are required to be met. In [136], the authors prove convergence of the method in the pressure and velocity variables for the case of steady (incompressible) single phase flow (linear elliptic PDE). For the sake of completeness, the main ideas of these proofs are reproduced here for a similar problem with more general boundary conditions in the presence of gravity. The error analysis is also extended to the case of slightly compressible single phase flow in the presence of gravity and a proof is presented here. Most importantly, this work extends the theory and implementation in [136] to the coupled flow-transport problem which is of significance in many real world applications as mentioned in Section 1.1. In addition, convergence of the method is proved for the species transport problem on non-matching multiblock grids and some numerical examples are presented.

4.1 Enhanced velocity mixed FEM (EV-MFEM) for flow

The motivation for using mixed FEM on non-matching multiblock grids was presented in Section 1.1. These methods are especially useful for modeling flow through porous media because of their local mass conservation property as well as their accurate approximation of the flux variable. The latter is a matter of great significance in such applications as for example, the coupling of flow with transport since the solution to the solute transport problem is dependent on the flux from the flow problem. The theory, implementation and application (via numerical examples) will be discussed later in this chapter. The flow equations hold with their usual meaning in every sub-domain (sometimes referred to as "fault-block") with some physically meaningful boundary conditions on the fault-block interfaces. These boundary conditions are the continuity of phase pressures and phase fluxes. The grids on each block can be non-matching along the interfaces between fault-blocks lending to the flexibility of the method as well as a ready extension to such applications as multimodel, multiphysics and multinumerics couplings.

The mortar method has been detailed in Chapter 3. More complete references include [12, 142]. It is now well understood that these methods lead to a non-conforming discretization scheme with the flux matching condition imposed weakly through Lagrange multipliers (or mortar function spaces). This section aims to introduce an efficient alternative which by construction (of an enhanced velocity space along fault-block interfaces), yields a flux-continuous velocity apoximation space and is therefore also H-div conforming. Thus no interface problem (with underlying sub-domain problems) is required to be solved. The enhanced velocity method was originally implemented in IPARS [136] for solving 3-d parallel, multiphase porous media flow problems and has since been extended for the coupling of multiphase flow and transport in this work. It was already shown that the method was about an order of magnitude faster than the current implementation of the mortar mixed method in IPARS [136] while providing similar accuracy. As expected, a similar trend is also observed in the case of coupled flow and transport applications (see Section 4.8).

4.1.1 Formulation of EV-MFEM

For convenience of analysis, attention is restricted to the case of steady (incompressible) single phase flow in the presence of gravity. Extensions to the non-linear transient flow problem and implementation details will be briefly discussed in subsequent subsections. Steady single phase flow written in a mixed form is governed by the equations of the form

$$\mathbf{u} = -\mathbf{K}(\nabla p - \rho_0 \mathbf{g}) \quad \text{in } \Omega \tag{4.1a}$$

$$\nabla \cdot \mathbf{u} = f \quad \text{in } \Omega \tag{4.1b}$$

$$p = p_b \quad \text{on } \Gamma^D. \tag{4.1c}$$

$$\mathbf{u} \cdot \mathbf{n} = u_b \quad \text{on } \Gamma^N. \tag{4.1d}$$

General boundary conditions have been prescribed on $\partial\Omega = \bar{\Gamma}^D \cup \bar{\Gamma}^N$. As in Chapter 3, $\Omega = \cup_{i=1}^{n_b} \Omega_i \subset \mathbb{R}^d$ with $d = 2$ or 3 represents a multiblock domain Ω with n_b sub-domains Ω_i. The permeability tensor $\mathbf{K}$ is assumed to be symmetric and positive definite (with the density divided by viscosity term, absorbed in it). Further, all the definitions and assumptions of Section 3.1 are assumed to hold. Functional spaces for the mixed weak formulation of (4.1a)–(4.1d) are defined as usual to be

$$\begin{aligned}
\mathbf{V} &= H(\text{div}; \Omega) \equiv \left\{ \mathbf{v} \in (L^2(\Omega))^d : \nabla \cdot \mathbf{v} \in L^2(\Omega) \right\}, \\
\mathbf{V}^0 &= \mathbf{V} \cap \left\{ \mathbf{v} : \mathbf{v} \cdot \mathbf{n} = 0 \text{ on } \Gamma^N \right\}, \\
\mathbf{V}^N &= \mathbf{V} \cap \left\{ \mathbf{v} : \mathbf{v} \cdot \mathbf{n} = u_b \text{ on } \Gamma^N \right\}, \\
W &= L^2(\Omega).
\end{aligned}$$

The notations used here for Sobelev spaces, norms and inner products and duality pairings are the same as in Section 3.1. With this notation, the H-div norm of $\mathbf{v}$ may be defined as

$$\|\mathbf{v}\|_{\mathbf{V}} \equiv \|\mathbf{v}\|_{H(\text{div};\Omega)} \equiv \left(\|\mathbf{v}\|^2 + \|\nabla \cdot \mathbf{v}\|^2\right)^{1/2}$$

and the L^2 norm of $w \in W$ is defined as detailed before in Section 3.1. Then a weak solution of the fluid flow problem (4.1a)–(4.1d) is the pair $\mathbf{u} \in \mathbf{V}^N$ and $w \in W$ that satisfy the weak formulation

$$(\mathbf{K}^{-1}\mathbf{u}, \mathbf{v}) = (p, \nabla \cdot \mathbf{v}) + (\rho_0 \mathbf{g}, \mathbf{v}) - \left\langle p_b, \mathbf{v} \cdot \mathbf{n} \right\rangle_{\Gamma^D}, \quad \mathbf{v} \in \mathbf{V}^0 \tag{4.2}$$

$$(\nabla \cdot \mathbf{u}, w) = (f, w), \quad w \in W. \tag{4.3}$$

Existence and uniqueness for the system (4.3) has been shown for example in [28, 120]. Consider next the finite element discretization of (4.3). Although the weak formulation can be defined for all the usual mixed FEM spaces on orthogonal (brick) as well as simplicial elements, attention is restricted here to the most commonly used lowest order Raviart-Thomas space, RT_0 [96, 116] on rectangles (in 2-d) and bricks (in 3-d).

Further, let $h, \mathcal{T}_{h,i}, \mathcal{T}_h$ have the same meanings of mesh size, fault-block discretizations and union of fault-block discretizations respectively as in Section 3.1. Note that $\mathcal{T}_{h,i}$ and $\mathcal{T}_{h,j}$ need not match on Γ_{ij}. The RT_0 space for any element $E \in \mathcal{T}_h$ is defined by

$$\begin{aligned} &\mathbf{V}_h(E) \equiv \{\mathbf{v} \in \mathbb{R}^d : v_k = \alpha_k + \beta_k x_k;\, \alpha_k, \beta_k \in \mathbb{R},\, k = 1, 2 \ldots d\} \\ &W_h(E) \equiv \{w = \text{constant}\} \end{aligned}$$

It is well-known that a vector function $\mathbf{v} \in \mathbf{V}_h(E)$ can be uniquely identified by its normal components $\mathbf{v} \cdot \mathbf{n}$ at the mid-points of all the edges (in 2-d) or faces (in 3-d) of E, where $\mathbf{n}$ is the unit outward normal to ∂E. These normal components constitute the degrees of freedom of $\mathbf{v} \in \mathbf{V}_h(E)$. Similarly, the degree of freedom of the scalar function $w \in W_h(E)$ is its value at the center of

E. The pressure finite element approximation space on Ω is then defined in the usual manner (see Section 3.1) as

$$W_h \equiv \{w \in L^2(\Omega) : w|_E \in W_h(E) \, \forall \, E \in \mathcal{T}_h\}$$

The next step is to construct a finite element approximation space for velocity on Ω. This is where the formulation differs from the usual mortar mixed FEM or mixed-hybrid FEM schemes. Recall the sub-domain velocity approximation space $\mathbf{V}_{h,i}$ defined as

$$\mathbf{V}_{h,i} \equiv \{\mathbf{v} \in H(\text{div}; \Omega_i) : \mathbf{v}|_E \in \mathbf{V}_h(E), \, \forall \, \mathcal{E} \in \mathcal{T}_{h,i}\}$$

from Section 3.1. The reader may recognize this as the usual RT_0 space on Ω_i. It is also known that the space formed by the direct sum of all the sub-domain velocity approximation spaces, viz.,

$$\mathbf{V}_h \equiv \bigoplus_{i=1}^{n_b} \mathbf{V}_{h,i}$$

is *not* a subspace of $H(\text{div}; \Omega)$ since the normal components of the velocity vector do not match up on the sub-domain interfaces Γ. This is what motivated the introduction of the mortar finite element space (of Lagrange multipliers) which allowed a weak continuity in the fluxes across the sub-domain interfaces. The enhanced velocity mixed method modifies the degrees of freedom on Γ instead. To this end, let $\mathcal{T}_{h,ij}$ denote the intersection of the traces of $\mathcal{T}_{h,i}$ and $\mathcal{T}_{h,j}$ and let $\mathcal{T}_h^\Gamma \equiv \cup_{1 \le i \le j \le n_b} \mathcal{T}_{h,ij}$. Fluxes are then forced to match on each element $e \in \mathcal{T}_h^\Gamma$. Consider then any element $E \in \mathcal{T}_{h,i}$ sharing a face with the interface between blocks i and j (where $1 \le i, j \le n_b$), i.e., where $E \cap \Gamma_{ij} \neq \emptyset$. Then the newly defined interface grid, $\mathcal{T}_{h,ij}$ introduces a partition of the face of E adjacent to Γ_{ij}, i.e., on $\partial E \cap \Gamma_{ij}$. This partition may be extended into the element E as shown in Figure 4.1.

On each sub-element E_k induced by extending the partition formed by $\partial E \cap \Gamma_{ij}$, a basis function $\mathbf{v}_{E_k}$ is defined in the RT_0 space $\mathbf{V}_h(E_k)$ whose normal component $\mathbf{v}_{E_k} \cdot \mathbf{n}$ is unity on e_k, and zero on all other edges (or faces) of E_k. Let

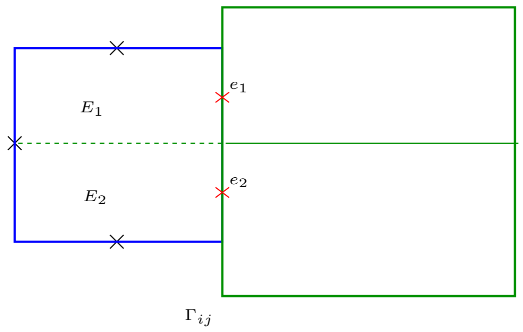

Figure 4.1: Degrees of freedom for the enhanced velocity space

$\mathbf{V}_h^\Gamma$ be the span of all such basis functions defined on all sub-elements induced by the interface discretization $\mathcal{T}_{h,ij}$. Then the enhanced velocity space, $\mathbf{V}_h^*$ is defined by

$$\mathbf{V}_h^* \equiv \bigoplus_{i=1}^{n_b} \mathbf{V}_{h,i}^0 \bigoplus \mathbf{V}_h^\Gamma \cap H(\mathrm{div};\Omega), \tag{4.4}$$

where $\mathbf{V}_{h,i}^0 \equiv \{\mathbf{v} \in \mathbf{V}_{h,i} : \mathbf{v}\cdot\mathbf{n} = 0 \text{ on } \Gamma_i\} \subset \mathbf{V}_{h,i}$, is the subspace of $\mathbf{V}_{h,i}$ with zero normal traces on Γ_i. The addition of extra interface degrees of freedom allows for constructing a flux continuous velocity approximation on the interface and thus rendering the velocity space H-div conforming. The drawback is that this modifies the usual RT_0 definition of the velocity space on all elements adjacent to fault-block interfaces and therefore, this introduces difficulties in the analysis and implementation of a robust linear solver. With the enhanced velocity space $\mathbf{V}_h^*$ defined in (4.4), and $\mathbf{V}_h^{*,0} \equiv \mathbf{V}_h^* \cap \left\{\mathbf{v} : \mathbf{v}\cdot\mathbf{n} = 0 \text{ on } \Gamma^N\right\}$ and $\mathbf{V}_h^{*,N} \equiv \mathbf{V}_h^* \cap \left\{\mathbf{v} : \mathbf{v}\cdot\mathbf{n} = u_b \text{ on } \Gamma^N\right\}$ (where the fluxes are assigned weakly), the mixed finite element approximation of the weak formulation (4.3) seeks $\mathbf{u}_h \in \mathbf{V}_h^{*,N}$ and $p_h \in W_h$ such that

$$(\mathbf{K}^{-1}\mathbf{u}_h, \mathbf{v}) = (p_h, \nabla\cdot\mathbf{v}) + (\rho_0 \mathbf{g}, \mathbf{v}) - \left\langle p_b, \mathbf{v}\cdot\mathbf{n}\right\rangle_{\Gamma^D}, \quad \mathbf{v} \in \mathbf{V}_h^{*,0} \tag{4.5}$$

$$(\nabla\cdot\mathbf{u}_h, w) = (f, w), \quad w \in W_h. \tag{4.6}$$

4.2 Analysis of EV-MFEM for steady single phase flow

In this section, some mathematical theory is developed prior to proving convergence of the method for steady single phase flow. Let Π^* be a projection operator that maps $\left(H^1(\Omega)\right)^d$ onto $\mathbf{V}_h^*$, defined locally for any element $E \in \mathcal{T}_h$ and $\mathbf{q} \in \left(H^1(E)\right)^d$ by

$$\int_e (\Pi^* \mathbf{q} - \mathbf{q}) \cdot \mathbf{n} \mathrm{ds} = 0,$$

where e is either any edge (in 2-d) or face (in 3-d) of E not lying on Γ or an edge (in 2-d) or face (in 3-d) of a sub-element, E_k (as in Figure 4.1) induced by the interface discretization $\mathcal{T}_h^\Gamma$ (recall from Section 4.1.1). An application of the divergence theorem yields

$$(\nabla \cdot (\Pi^* \mathbf{q} - \mathbf{q}), w) = 0, \quad \forall\, w \in W_h. \tag{4.7}$$

Further, since $\mathbf{V}_h(E) \subset \mathbf{V}_h^*(E)$, the enhanced velocity space can be expected to have at least as good approximation properties as the original RT_0 space. Thus, it is assumed [28, 116] that

$$\|\mathbf{q} - \Pi^* \mathbf{q}\| \leq C \|\mathbf{q}\|_1 h, \quad \forall\, \mathbf{q} \in \left(H^1(\Omega)\right)^d. \tag{4.8}$$

Note however that for arbitrary $\mathbf{v} \in \mathbf{V}_h^*$, $\nabla\cdot\mathbf{v}$ may be a piecewise constant function (not identically constant) on elements E that share an edge (in 2-d) or face (in 3-d) with the interface Γ. This follows from the definition of $\mathbf{V}_h^*$ (see for example Figure 4.1). Therefore, it follows that

$$\nabla \cdot \mathbf{V}_h^* \supset W_h;$$

but the two spaces may be different. This results in two consequences. First, $\nabla \cdot \Pi^* \mathbf{q}$ does not equal the L^2 projection of $\nabla \cdot \mathbf{q}$ onto W_h. Thus, no direct approximation properties exist for $\nabla \cdot \Pi^* \mathbf{q}$, unlike the usual mixed FEM projector Π defined on the RT_0 space $\mathbf{V}_{h,i}$ that satisfies for any $\mathbf{q} \in \left(H^1(\Omega_i)\right)^d$,

$$\|\mathbf{q} - \Pi \mathbf{q}\|_{\Omega_i} \leq C \|\mathbf{q}\|_{1,\Omega_i} h, \text{ and} \tag{4.9}$$

$$\|\nabla \cdot (\mathbf{q} - \Pi \mathbf{q})\|_{\Omega_i} \leq C \|\nabla \cdot \mathbf{q}\|_{r,\Omega_i} h^r, \quad 0 \leq r \leq 1. \tag{4.10}$$

Secondly, if $\mathbf{v} \in \mathbf{V}_h^*$ is a discrete divergence free vector, i.e., $\mathbf{v} \in \mathbf{Z}_h$ where

$$\mathbf{Z}_h \equiv \{\mathbf{v} \in \mathbf{V}_h^* : (\nabla \cdot \mathbf{v}, w) = 0,\, \forall\, w \in W_h\},$$

then, it does not follow that $\nabla \cdot \mathbf{v} = 0$. In fact, this can be seen by taking $\nabla \cdot \mathbf{v} = 1$ on sub-element E_1 and $\nabla \cdot \mathbf{v} = -1$ on sub-element E_2 of Figure 4.1. Hence, even though one may show that an inf-sup condition given by

$$\inf_{w \in W_h \setminus \{0\}} \sup_{\mathbf{v} \in \mathbf{V}_h^* \setminus \{\mathbf{0}\}} \frac{(\nabla \cdot \mathbf{v}, w)}{\|\mathbf{v}\|_{\mathbf{V}} \|w\|_W} \geq \beta \tag{4.11}$$

holds for the pair $(\mathbf{V}_h^*, W_h)$ for saddle-point problems (such as those given by (4.5)–(4.6)), a second condition, needed in the general saddle-point theory, i.e., the coercivity of $(\mathbf{K}^{-1}\mathbf{v}, \mathbf{v})$ in $\mathbf{Z}_h$, is not satisfied. Hence, the general saddle-point theory is not applied here. Instead a more direct approach is used to prove solvability and convergence.

Lemma 4.2.1. *Assume that Γ^D has non-zero measure so that compatibility problems arising due to all Neumann conditions are avoided. Then there exists a unique solution to the system* (4.5)–(4.6).

Proof. Since (4.5)–(4.6) forms a square system, it suffices to show uniqueness which in turn, implies existence. This is accomplished by showing that the solution is given by $p_h \equiv 0, \mathbf{u}_h \equiv \mathbf{0}$ when the right hand side vanishes. To this end, let $f = 0$, $p_b = 0$, $u_b = 0$ and $\mathbf{g} = \mathbf{0}$. Then taking $\mathbf{v} = \mathbf{u}_h$ and $w = p_h$ leads to $\mathbf{u}_h = \mathbf{0}$. Thus, $(p_h, \nabla \cdot \mathbf{v}) = 0$ for any $\mathbf{v} \in \mathbf{V}_h^{*,0}$. Starting from a Dirichlet boundary element, i.e., any $E : E \cap \Gamma^D \neq \emptyset$ one can show easily (by choosing a local basis function $\mathbf{v} \in \mathbf{V}_h^{*,0}$ satisfying $\mathbf{v} \cdot \mathbf{n} \neq 0$ on $\partial E \cap \Gamma^D$ and zero elsewhere) that for any such element $p_h|_E = 0$. Then propagating out in pairs of elements, using the divergence theorem, and the fact that $\mathbf{v} \cdot \mathbf{n}$ is a constant on all (sub-)faces and continuous across inter-element (sub-)faces, it follows that indeed $p_h = 0$. □

For the analysis that follows, another common L^2 projection operator will be required. For any $\varphi \in L^2(\Omega)$, let $\hat{\varphi} \in W_h$ be its $L^2(\Omega)$ projection satisfying

$$(\varphi - \hat{\varphi}, w) = 0, \quad \forall\, w \in W_h.$$

This ("hat projection") operator satisfies the standard L^2 approximation property

$$\|\varphi - \hat{\varphi}\| \leq C\|\varphi\|_r h^r, \quad 0 \leq r \leq 1. \tag{4.12}$$

The following bound on $\nabla \cdot \Pi^* \mathbf{q}$ is derived in [136] and is stated here without proof.

Lemma 4.2.2. *For any* $\mathbf{q} \in H^1(\Omega)$*, there exists a constant* C *independent of* h *such that*

$$\|\nabla \cdot \Pi^* \mathbf{q}\| \leq C\|\mathbf{q}\|_1. \tag{4.13}$$

4.3 Some *a priori* error estimates for EV-MFEM applied to steady single phase flow

Subtracting (4.5)–(4.6) from (4.2)–(4.3), yields the error equations

$$\big(\mathbf{K}^{-1}(\mathbf{u} - \mathbf{u}_h), \mathbf{v}\big) = (p - p_h, \nabla \cdot \mathbf{v}), \quad \forall\, \mathbf{v} \in \mathbf{V}_h^{*,0}, \tag{4.14}$$

$$(\nabla \cdot (\mathbf{u} - \mathbf{u}_h), w) = 0, \quad \forall\, w \in W_h. \tag{4.15}$$

From the property (4.7) of the projection operator Π^*, (4.15) can be re-written as

$$(\nabla \cdot (\Pi^* \mathbf{u} - \mathbf{u}_h), w) = 0, \quad w \in W_h. \tag{4.16}$$

Let $\mathbf{v} = \Pi^* \mathbf{u} - \mathbf{u}_h$ and $w = p - p_h$. Then, (4.14) yields (after some manipulation by adding and subtracting terms)

$$\begin{aligned} &\big(\mathbf{K}^{-1}(\Pi^* \mathbf{u} - \mathbf{u}_h), \Pi^* \mathbf{u} - \mathbf{u}_h\big) = \\ &\quad \big(\mathbf{K}^{-1}(\Pi^* \mathbf{u} - \mathbf{u}), \Pi^* \mathbf{u} - \mathbf{u}_h\big) + (p - \hat{p}, \nabla \cdot \mathbf{v}). \end{aligned} \tag{4.17}$$

The second term on the right hand side of (4.17) can be bounded by noting that from (4.17),

$$\nabla \cdot (\Pi^* \mathbf{u} - \mathbf{u}_h)|_E = 0, \, \forall\, E \in \mathcal{T}_h : E \cap \Gamma = \emptyset.$$

This can be seen by simply taking $w = \nabla \cdot (\Pi^* \mathbf{u} - \mathbf{u}_h)$ in the interior and observing that in the interior $\nabla \cdot (\Pi^* \mathbf{u} - \mathbf{u}_h) \in W_h$. Then, let all other elements

E sharing an edge (in 2-d) or face (in 3-d) with Γ comprise a new triangulation, Ω^*. In other words, let $\Omega^* = \cup\{E \in \mathcal{T}_h : E \cap \Gamma \neq \emptyset\}$. Then, it follows that

$$\begin{aligned}(p - \hat{p}, \nabla \cdot (\Pi^*\mathbf{u} - \mathbf{u}_h)) &= (p - \hat{p}, \nabla \cdot (\Pi^*\mathbf{u} - \mathbf{u}_h))_{\Omega^*} \\ &\leq Ch\|p\|_{1,\Omega^*} h^{-1}\|\Pi^*\mathbf{u} - \mathbf{u}_h\|_{\Omega^*} \\ &\leq Ch^{1/2}\|p\|_{1,\infty,\Omega^*}\|\Pi^*\mathbf{u} - \mathbf{u}_h\|. \qquad (4.18)\end{aligned}$$

The first inequality in (4.18) is derived from the Cauchy-Schwartz inequality, (4.12) and an inverse inequality to bound $\nabla \cdot (\Pi^*\mathbf{u} - \mathbf{u}_h)$. The second inequality uses the fact that there exists a constant C such that $|\Omega^*| \leq Ch$. Finally, the bounds (4.8), (4.17), (4.18) lead to the following estimate for velocity.

Theorem 4.3.1. *For the velocity* $\mathbf{u}_h$ *of the mixed method* (4.6)*, there exists a positive constant* C *dependent on* Ω *and* $\|\mathbf{K}\|_{0,\infty}$*, but independent of* h *such that*

$$\|\mathbf{u} - \mathbf{u}_h\| \leq C\left(\|p\|_{1,\infty,\Omega^*} h^{1/2} + \|\mathbf{u}\|_{1,\Omega} h\right). \qquad (4.19)$$

To derive a pressure error estimate in the L^2 norm, a duality argument is applied. To this end, let φ be a solution of

$$\begin{aligned} -\nabla \cdot \mathbf{K}\nabla\varphi &= -(\hat{p} - p_h) && \text{in } \Omega, \\ \varphi &= 0 && \text{on } \Gamma^D \\ -\mathbf{K}\nabla\varphi \cdot \mathbf{n} &= u_b && \text{on } \Gamma^N. \end{aligned}$$

Assuming elliptic regularity (which holds for smooth convex domains Ω; for other cases less strong estimates may be derived),

$$\|\varphi\|_2 \leq C\|\hat{p} - p_h\|. \qquad (4.20)$$

Next, take $\mathbf{v} = \Pi^*\mathbf{K}\nabla\varphi$ in (4.14) to get

$$\begin{aligned}\|\hat{p} - p_h\|^2 &= (\hat{p} - p_h, \nabla \cdot \Pi^*\mathbf{K}\nabla\varphi) \\ &= \left(\mathbf{K}^{-1}(\mathbf{u} - \mathbf{u}_h), \Pi^*\mathbf{K}\nabla\varphi\right) + (\hat{p} - p, \nabla \cdot \Pi^*\mathbf{K}\nabla\varphi) \qquad (4.21)\end{aligned}$$

Using the bounds (4.12) and (4.13), the second term on the right hand side of (4.21) (following the second equality) can be bounded as

$$(\hat{p} - p, \nabla \cdot \Pi^* \mathbf{K} \nabla \varphi) \le Ch \|p\|_1 \|\varphi\|_2 \tag{4.22}$$

where C is (here, and in the following) a constant that may depend on $\|\mathbf{K}\|_{1,\infty}$. The first term on the right hand side following the second equality of (4.21) is bounded using the estimate (4.8) as follows.

$$\begin{aligned}\big(\mathbf{K}^{-1}(\mathbf{u} - \mathbf{u}_h), \Pi^* \mathbf{K} \nabla \varphi\big) &= \big(\mathbf{K}^{-1}(\mathbf{u} - \mathbf{u}_h), \Pi^* \mathbf{K} \nabla \varphi - \mathbf{K} \nabla \varphi\big) + (\mathbf{u} - \mathbf{u}_h, \nabla \varphi) \\ &\le Ch \|\mathbf{u} - \mathbf{u}_h\| \|\varphi\|_2 + (\mathbf{u} - \mathbf{u}_h, \nabla \varphi). \end{aligned} \tag{4.23}$$

The second term of estimate (4.23), (on the right hand side of the inequality) can be re-written using (4.13), (4.15), and (4.22) as

$$\begin{aligned}(\mathbf{u} - \mathbf{u}_h, \nabla \varphi) &= (\nabla \cdot (\mathbf{u} - \mathbf{u}_h), \varphi - \hat{\varphi}) \\ &= (\nabla \cdot (\mathbf{u} - \Pi^* \mathbf{u}), \varphi - \hat{\varphi}) + (\nabla \cdot (\Pi^* \mathbf{u} - \mathbf{u}_h), \varphi - \hat{\varphi}) \\ &\le Ch \|\mathbf{u}\|_1 \|\varphi\|_1 + (\nabla \cdot (\Pi^* \mathbf{u} - \mathbf{u}_h), \varphi - \hat{\varphi})_{\Omega^*} \end{aligned} \tag{4.24}$$

where the argument used to derive the bound (4.18) is used to arrive at the last term on the right hand side of the bound (4.24). Finally, this term can be further bounded by employing the Sobelev embedding inequality [6]

$$\|\varphi\|_{1,q} \le C \|\varphi\|_2, \quad \begin{array}{ll} 2 \le q \le \frac{2d}{d-2} = 6, & d = 3 \\ 2 \le q \le \infty, & d = 2. \end{array} \tag{4.25}$$

Let $\frac{1}{p} + \frac{1}{q} = 1$. The last term in (4.24) is then bounded using Hölder's inequality as follows:

$$\begin{aligned}(\nabla \cdot (\Pi^* \mathbf{u} - \mathbf{u}_h), \varphi - \hat{\varphi})_{\Omega^*} &\le \|\nabla \cdot (\Pi^* \mathbf{u} - \mathbf{u}_h)\|_{L^p(\Omega^*)} \|\varphi - \hat{\varphi}\|_{L^q(\Omega^*)} \\ &\le C \|\nabla \cdot (\Pi^* \mathbf{u} - \mathbf{u}_h)\|_{L^p(\Omega^*)} h \|\varphi\|_{1,q,\Omega^*} \\ &\le C \|\nabla \cdot (\Pi^* \mathbf{u} - \mathbf{u}_h)\|_{L^p(\Omega^*)} h \|\varphi\|_2, \end{aligned} \tag{4.26}$$

wherein a L^q-version of the L^2 projection error (4.12) and the Sobelev embedding result (4.25) has been used. Finally, employing Hölder's inequality again, yields for any $1 < s < \infty$,

$$\|\phi\|_{L^s(G)} \leq \left\{ \left(\int_G \phi^2 \mathrm{dx} \right)^{s/2} \left(\int_G 1 \mathrm{dx} \right)^{1-s/2} \right\}^{1/s} = \|\phi\|_{L^2(G)} |G|^{\frac{2-s}{2s}}, \qquad (4.27)$$

wherein, substituting $\phi = \nabla \cdot (\Pi^* \mathbf{u} - \mathbf{u}_h)$, $G = \Omega^*$, and $s = p$ gives

$$\|\nabla \cdot (\Pi^* \mathbf{u} - \mathbf{u}_h)\|_{L^p(G)} \leq C \|\nabla \cdot (\Pi^* \mathbf{u} - \mathbf{u}_h)\|_{L^2(\Omega^*)} h^{1/p-1/2}. \qquad (4.28)$$

Finally, substituting this last bound in the error estimate (4.26) and using the enhanced velocity error estimate (4.19) results in

$$\begin{aligned} (\nabla \cdot (\Pi^* \mathbf{u} - \mathbf{u}_h), \varphi - \hat{\varphi})_{\Omega^*} &\leq C h^{-1} \|\Pi^* \mathbf{u} - \mathbf{u}_h\| h^{1/p-1/2} h \|\varphi\|_2 \\ &\leq C h^{1/p} (\|p\|_{1,\infty,\Omega^*} + \|\mathbf{u}\|_1 h^{1/2}) \|\varphi\|_2. \qquad (4.29) \end{aligned}$$

Note that for $d = 2$, q can be arbitrarily large, so that we can take $p = 1 + \varepsilon$. For $d = 3$, we can take $q = 6$ and $p = \frac{6}{5}$. The results (4.20)–(4.26), and (4.29) combined with the L^2 projection error estimate (4.12), then lead to the following theorem.

Theorem 4.3.2. *For the pressure p_h of the mixed method* (4.6)*, there exists a positive constant C dependent on $\Omega \subset \mathbb{R}^d$ and $\|\mathbf{K}\|_{1,\infty}$, but independent of h such that*

$$\|p - p_h\| \leq C \left(\|p\|_{1,\infty,\Omega^*} + \|\mathbf{u}\|_1 h^{1/2} \right) h^r, \qquad (4.30)$$

where $r = 1$ if $d = 2$ and $r = 5/6$ if $d = 3$.

For interior error bounds, the reader is referred to [136].

4.4 Analysis of EV-MFEM for transient, slightly (non-linear) compressible single phase flow

In this section, the theory presented in [136] and repeated in Sections 4.2–4.3 is extended to the case of transient, slightly non-linear (compressible) single phase flow through porous media. It also holds for the case of linear parabolic PDEs governing single phase flow. The equations governing non-linear slightly compressible flow was presented in Chapter 3, (3.14)–(3.16). They are repeated here for the reader's convenience:

$$\frac{\partial}{\partial t}\phi\rho(p) - \nabla\cdot\mathbf{K}\rho(p)(\nabla p - \rho(p)\mathbf{g}) = f \qquad \text{in } \Omega\times J, \tag{4.31}$$

$$p = p_b \quad \text{on } \Gamma^D\times J, \tag{4.32}$$

$$-\mathbf{K}\rho(p)(\nabla p - \rho(p)\mathbf{g})\cdot\mathbf{n} = u_b \quad \text{on } \Gamma^N\times J, \tag{4.33}$$

$$p = p_0 \quad \text{in } \Omega\times\{0\}. \tag{4.34}$$

As in Chapter 3, let $J = [0, T]$ be the simulation time period of interest. Introducing the mass velocity variable $\mathbf{u} = -\mathbf{K}\rho(p)(\nabla p - \rho\mathbf{g})$, the problem can be stated in a mixed form to seek $\{\mathbf{u}, p\}$ that satisfies

$$\mathbf{K}^{-1}\rho^{-1}(p)\,\mathbf{u} = -\nabla p + \rho(p)\mathbf{g} \qquad \text{in } \Omega\times J, \tag{4.35}$$

$$\frac{\partial}{\partial t}\phi\rho(p) + \nabla\cdot\mathbf{u} = f \qquad \text{in } \Omega\times J, \tag{4.36}$$

$$p = p_b \quad \text{on } \partial\Omega\times J, \tag{4.37}$$

$$\mathbf{u}\cdot\mathbf{n} = u_b \quad \text{on } \Gamma^N\times J, \tag{4.38}$$

$$p = p_0 \quad \text{on } \Omega\times\{0\}. \tag{4.39}$$

For the analysis that follows, suppose that ϕ is a constant, $\rho \approx \rho_0(1+cp)$, where c is the fluid compressibility and ρ_0 is the reference density (measured at some reference pressure). Then, $\frac{\partial\rho}{\partial t} = \rho_0 c\frac{\partial p}{\partial t}$. Also, let $c_0 = \rho_0 c$. Then, following the analysis of Sections 4.2–4.3, the weak formulation of the system (4.35)–(4.39) is given by seeking $\{\mathbf{u}, p\} : J \to H(\mathrm{div};\Omega)\times L^2(\Omega)$ that satisfies (weakly) (4.38) and

$$\begin{aligned}(\mathbf{K}^{-1}\rho^{-1}(p)\mathbf{u}, \mathbf{v}) &= (p, \nabla\cdot\mathbf{v}) - \langle p_b, \mathbf{v}\cdot\mathbf{n}\rangle_{\Gamma^D} \\ &\quad + (\rho(p)\mathbf{g}, \mathbf{v}) \qquad\qquad \mathbf{v}\in\mathbf{V}^0,\end{aligned} \tag{4.40}$$

$$(\phi c_0\frac{\partial p}{\partial t}, w) + (\nabla\cdot\mathbf{u}, w) = (f, w), \qquad w\in L^2(\Omega). \tag{4.41}$$

Next, the enhanced velocity mixed finite element approximation of the weak solution $\{\mathbf{u}, p\}$ is given by seeking $\{\mathbf{u}_h, p_h\} : J \to \mathbf{V}_h^{*,N} \times W_h$ that satisfies

$$\begin{aligned}
(\mathbf{K}^{-1}\rho^{-1}(p_h)\,\mathbf{u}_h, \mathbf{v}) &= (p_h, \nabla\cdot\mathbf{v}) - \langle p_b, \mathbf{v}\cdot\mathbf{n}\rangle_{\Gamma^D} \\
&\quad + (\rho(p_h)\mathbf{g}, \mathbf{v}) \qquad\qquad \mathbf{v} \in \mathbf{V}_h^{*,0}, \qquad (4.42)\\
(\phi c_0 \frac{\partial p_h}{\partial t}, w) + (\nabla\cdot\mathbf{u}_h, w) &= (f, w), \qquad\qquad w \in W_h. \qquad (4.43)
\end{aligned}$$

4.4.1 Error estimates for EV-MFEM applied to transient, non-linear single phase flow

Subtracting (4.42) from (4.40) yields (after adding and subtracting $\Pi^*\mathbf{u}$ terms and manipulating),

$$\begin{aligned}
&\big(\mathbf{K}^{-1}\rho^{-1}(p_h)(\Pi^*\mathbf{u}-\mathbf{u}_h), \mathbf{v}\big) - (p - p_h, \nabla\cdot\mathbf{v}) = \big(\mathbf{K}^{-1}\rho^{-1}(p_h)(\Pi^*\mathbf{u}-\mathbf{u}), \mathbf{v}\big)\\
&\quad - \big(\mathbf{K}^{-1}(\rho^{-1}(p)-\rho^{-1}(p_h))\mathbf{u}, \mathbf{v}\big) + ((\rho(p)-\rho(p_h))\mathbf{g}, \mathbf{v}) \quad \mathbf{v} \in \mathbf{V}_h^{*,0}. \quad (4.44)
\end{aligned}$$

Taking $\mathbf{v} = \Pi^*\mathbf{u} - \mathbf{u}_h$ in (4.44) gives

$$\begin{aligned}
&\big(\mathbf{K}^{-1}\rho^{-1}(p_h)(\Pi^*\mathbf{u}-\mathbf{u}_h), \Pi^*\mathbf{u}-\mathbf{u}_h\big) - (\hat{p} - p_h + p - \hat{p}, \nabla\cdot(\Pi^*\mathbf{u}-\mathbf{u}_h))\\
&\quad = \big(\mathbf{K}^{-1}\rho^{-1}(p_h)(\Pi^*\mathbf{u}-\mathbf{u}), \Pi^*\mathbf{u}-\mathbf{u}_h\big)\\
&\quad - \big(\mathbf{K}^{-1}(\rho^{-1}(p)-\rho^{-1}(p_h))\mathbf{u}, \Pi^*\mathbf{u}-\mathbf{u}_h\big)\\
&\quad + ((\rho(p)-\rho(p_h))\mathbf{g}, \Pi^*\mathbf{u}-\mathbf{u}_h). \qquad (4.45)
\end{aligned}$$

Next, subtracting (4.43) from (4.41), adding and subtracting $\hat{p}$, $\Pi^*\mathbf{u}$ terms and using (4.7) yields

$$\left(\phi c_0 \frac{\partial(\hat{p}-p_h)}{\partial t}, w\right) + (\nabla\cdot(\Pi^*\mathbf{u}-\mathbf{u}_h), w) = 0, \quad w \in W_h, \qquad (4.46)$$

Setting $w = \hat{p} - p_h$ and adding (4.45) and (4.46) leads to

$$\begin{aligned}
&\big(\mathbf{K}^{-1}\rho^{-1}(p_h)(\Pi^*\mathbf{u}-\mathbf{u}_h), \Pi^*\mathbf{u}-\mathbf{u}_h\big) + \left(\phi c_0 \frac{\partial(\hat{p}-p_h)}{\partial t}, \hat{p}-p_h\right)\\
&\quad = -(\hat{p}-p, \nabla\cdot(\Pi^*\mathbf{u}-\mathbf{u}_h)) + \big(\mathbf{K}^{-1}\rho^{-1}(p_h)(\Pi^*\mathbf{u}-\mathbf{u}), \Pi^*\mathbf{u}-\mathbf{u}_h\big)\\
&\quad - \big(\mathbf{K}^{-1}(\rho^{-1}(p)-\rho^{-1}(p_h))\mathbf{u}, \Pi^*\mathbf{u}-\mathbf{u}_h\big)\\
&\quad + ((\rho(p)-\rho(p_h))\mathbf{g}, \Pi^*\mathbf{u}-\mathbf{u}_h). \qquad (4.47)
\end{aligned}$$

Then, applying the arguments used to arrive at (4.18), the Lipschitz continuity of ρ and ρ^{-1}, Young's inequality for products, the essential boundedness of $\mathbf{u}$, and assumptions (A1)–(A3) of Chapter 3 leads to

$$\begin{aligned}
&\gamma_1\|\Pi^*\mathbf{u}-\mathbf{u}_h\|^2+\phi c_0\frac{1}{2}\frac{\partial}{\partial t}\|\hat{p}-p_h\|^2 \\
&\quad\le c_1\|p\|_{1,\infty,\Omega^*}\|\Pi^*\mathbf{u}-\mathbf{u}_h\|h^{1/2}+\frac{\varepsilon_1}{2}\|\Pi^*\mathbf{u}-\mathbf{u}_h\|^2+\frac{1}{2\varepsilon_1}\|\Pi^*\mathbf{u}-\mathbf{u}\|^2 \\
&\quad+c_2(L_{\rho^{-1}},\|\mathbf{u}\|_\infty,\gamma)\|p-p_h\|\|\Pi^*\mathbf{u}-\mathbf{u}_h\|+c_3(L_\rho,\|\mathbf{g}\|)\|p-p_h\|\|\Pi^*\mathbf{u}-\mathbf{u}_h\|.
\end{aligned} \tag{4.48}$$

In (4.48) L is used to denote the Lipschitz constant; and c_1, c_2 and c_3 are all constants. Applying the triangle inquality, $\|p-p_h\|\le\|p-\hat{p}\|+\|\hat{p}-p_h\|$ and Young's inequality to the first and the last two terms on the right hand side of (4.48) yields

$$\begin{aligned}
&\gamma_1\|\Pi^*\mathbf{u}-\mathbf{u}_h\|^2+\phi c_0\frac{1}{2}\frac{\partial}{\partial t}\|\hat{p}-p_h\|^2\le c_1\frac{\varepsilon_0}{2}\|p\|^2_{1,\infty,\Omega^*}h+c_1\frac{1}{2\varepsilon_0}\|\Pi^*\mathbf{u}-\mathbf{u}_h\|^2 \\
&+\frac{\varepsilon_1}{2}\|\Pi^*\mathbf{u}-\mathbf{u}_h\|^2+\frac{1}{2\varepsilon_1}\|\Pi^*\mathbf{u}-\mathbf{u}\|^2+c_2\frac{\varepsilon_2}{2}\|\Pi^*\mathbf{u}-\mathbf{u}_h\|^2+c_2\frac{1}{2\varepsilon_2}\|p-\hat{p}\|^2 \\
&+c_2\frac{\varepsilon_3}{2}\|\Pi^*\mathbf{u}-\mathbf{u}_h\|^2+c_2\frac{1}{2\varepsilon_3}\|\hat{p}-p_h\|^2+c_3\frac{\varepsilon_4}{2}\|\Pi^*\mathbf{u}-\mathbf{u}_h\|^2+c_3\frac{1}{2\varepsilon_4}\|p-\hat{p}\|^2 \\
&+c_3\frac{\varepsilon_5}{2}\|\Pi^*\mathbf{u}-\mathbf{u}_h\|^2+c_3\frac{1}{2\varepsilon_5}\|\hat{p}-p_h\|^2.
\end{aligned} \tag{4.49}$$

Note that γ_1 and the coefficients ε_i, $i=0,\ldots,5$ are constants arising from boundedness of $\mathbf{K},\rho$ and ρ^{-1} and the Young's inequality, respectively. Finally, choosing ε_i small enough so that the $\|\Pi^*\mathbf{u}-\mathbf{u}_h\|^2$ terms on the right hand side of (4.49) can be absorbed into the corresponding term on the left hand side, yields

$$\begin{aligned}
\gamma_2\|\Pi^*\mathbf{u}-\mathbf{u}_h\|^2+\phi c_0\frac{1}{2}\frac{\partial}{\partial t}\|\hat{p}-p_h\|^2&\le c_4\|p\|^2_{1,\infty,\Omega^*}h \\
&+c_5\left(\|\mathbf{u}\|_1^2+\|p\|_1^2\right)h^2+c_6\|\hat{p}-p_h\|^2.
\end{aligned} \tag{4.50}$$

Integrating (4.50), assuming for convenience that $p_h(0)=\hat{p}(0)$ and applying Gronwall's inequality in the integral form, leads to the following important result.

Theorem 4.4.1. *There exists constants C_1, C_2 depending on the final time T and on other properties such as the Lipschitz constants L on ρ, the bounds on $\phi, \rho, \rho^{-1}, \mathbf{K}$, and $\mathbf{K}^{-1}$, but not depending on h, such that*

$$\begin{aligned}\|\Pi^*\mathbf{u} - \mathbf{u}_h\|^2_{L^2(J;L^2(\Omega))} + \|\hat{p} - p_h\|^2_{L^\infty(J;L^2(\Omega))} &\leq C_1\|p\|^2_{L^2(J;W^1_\infty(\Omega^*))}h \\ &+ C_2\left(\|\mathbf{u}\|^2_{L^2(J;H^1(\Omega))} + \|p\|^2_{L^2(J;H^1(\Omega))}\right)h^2. \qquad (4.51)\end{aligned}$$

Finally, an application of the triangle inequality and the bounds derived for $\|p - \hat{p}\|$ and $\|\Pi^*\mathbf{u} - \mathbf{u}\|$ from (4.12) and (4.8) results in estimates of the order of $h^{1/2}$ for the pressure error, $\|p - p_h\|_{L^\infty(J;L^2(\Omega))}$ and velocity error, $\|\mathbf{u} - \mathbf{u}_h\|_{L^2(J;L^2(\Omega))}$. Hence, better steady state estimates (presently, order $h^{1/2}$) are required in order to get improved error estimates.

4.5 Extension of EV-MFEM to multiphase flow

The method introduced in the preceding sections has been extended to model multiphase flow through porous media [136]. The basic idea is to use an expanded-mixed finite element method in conjunction with the enhanced velocity method discussed previously. The mass balance equations are given by

$$\frac{\partial\left(\phi S_\alpha \rho_\alpha\right)}{\partial t} + \nabla \cdot \hat{\mathbf{u}}_\alpha = \hat{q}_\alpha, \ \alpha = \ w, nw \quad \text{in} \quad \Omega \times J, \qquad (4.52)$$

where the notation used is the same as in Section 2.1.2, Chapter 2. Recall therein, the definition of the extensive version of Darcy velocity, $\hat{\mathbf{u}}_\alpha$ is given by

$$\hat{\mathbf{u}}_\alpha = -\frac{\rho_\alpha \mathbf{K} \kappa_{r\alpha}}{\mu_\alpha}\left[\nabla p_\alpha - \rho_\alpha \mathbf{g}\right], \ \alpha = \ w, nw \quad \text{in} \quad \Omega \times J. \qquad (4.53)$$

The system of equations is finally closed by the capillary pressure relation and saturation constraint,

$$p_n - p_w = p_c(S_w), \quad \sum_\alpha S_\alpha = 1. \qquad (4.54)$$

As in Section 3.2 of Chapter 3, a pressure gradient term is introduced as an intermediate velocity variable, $\tilde{\mathbf{u}}_\alpha$ for $\alpha = w, nw$ given by

$$\tilde{\mathbf{u}}_\alpha = -\mathbf{K}(\nabla p_\alpha - \rho_\alpha \mathbf{g}). \qquad (4.55)$$

For a detailed motivation for the introduction of this new variable, the reader is referred to [16]. For multiphase flow, this term allows proper treatment of the degeneracies that arise in the diffusion term at $S_\alpha = 0$ when $\kappa_{r\alpha}(S_\alpha) = 0$. It also allows an easy treatment of full permeability tensors $\mathbf{K}$ in the context of usual mixed finite element methods and by appropriate quadrature rules, reduces the method to a simple and well-known cell-centered finite difference scheme. Then, with (4.55), the extensive Darcy velocity can be written as

$$\hat{\mathbf{u}}_\alpha = \frac{\rho_\alpha \kappa_{r\alpha}}{\mu_\alpha}\tilde{\mathbf{u}}_\alpha. \tag{4.56}$$

Suppose further for convenience that Dirichlet boundary conditions in the form of phase pressures are given by

$$p_\alpha = p_\alpha^b,\ \alpha = \ w, nw \quad \text{in} \quad \partial\Omega \times J. \tag{4.57}$$

Then, let $0 = t_0 < t_1 < t_2 < ...$, $\Delta t^n = t_n - t_{n-1}$, and let $f^n = f(t_n)$, $\Delta f^n = f(t_n) - f(t_{n-1})$. The backward Euler multiblock expanded enhanced mixed finite element method for the system (4.52)-(4.56) seeks for $n = 1, 2, 3...$, $\hat{\mathbf{u}}_\alpha^n \in \mathbf{V}_h^*$, $\tilde{\mathbf{u}}_{\alpha,h}^n \in \mathbf{V}_h^*$, $p_{\alpha,h}^n \in W_h$, $S_{\alpha,h}^n \in W_h$, such that, for $\alpha = w$ and nw,

$$\left(\frac{\Delta(\varphi\rho_{\alpha,h}S_{\alpha,h})^n}{\Delta t^n}, w\right) + \left(\nabla\cdot\hat{\mathbf{u}}_{\alpha,h}^n, w\right) = \left(q_\alpha^{n-\frac{1}{2}}, w\right), \qquad w \in W_{h,i}, \tag{4.58a}$$

$$(\mathbf{K}^{-1}\tilde{\mathbf{u}}_{\alpha,h}^n, \mathbf{v}) = (p_{\alpha,h}^n, \nabla\cdot\mathbf{v}) + (\rho_\alpha\mathbf{g}, \mathbf{v}) - \langle p_{\alpha,h}^{n,b}, \mathbf{v}\cdot\mathbf{n}\rangle_{\partial\Omega}, \quad \mathbf{v} \in \mathbf{V}_h^*, \tag{4.58b}$$

$$(\hat{\mathbf{u}}_{\alpha,h}^n, \tilde{\mathbf{v}}) = \left(\frac{\rho_{\alpha,h}^n k_{r\alpha,h}^n}{\mu_{\alpha,h}}\tilde{\mathbf{u}}_{\alpha,h}^n, \tilde{\mathbf{v}}\right), \qquad \tilde{\mathbf{v}} \in \mathbf{V}_h^*, \tag{4.58c}$$

Owing to the non-linearities in the density, relative permeability and capillary pressure terms, (4.58) is typically written out (after integration over a time-step) in a residual form and the resulting non-linear residual equation solved using Newton's method.

Consider the implementation of the scheme for steady single phase flow with a diagonal permeability field. Then, let the transimissibility across an edge (in 2-d) or face (in 3-d), e_i be given by (see for example, Figure 4.2)

$$T_i \equiv \frac{2|e_i|}{\frac{h_a}{K_a} + \frac{h_{b,i}}{K_{b,i}}}. \tag{4.59}$$

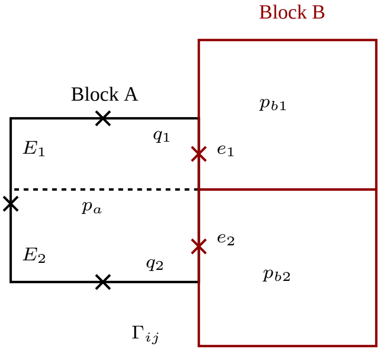

Figure 4.2: Finite differences across the fault-block interface

Then, applying the special quadrature rules of [16] to the (4.5)–(4.6), it can be seen that the flux q_i on the edge (face) e_i is given by

$$q_i = -T_i \left(p_{b,i} - p_a\right), \; i = 1, 2, ..., N_a, \tag{4.60}$$

where N_a is the number of interfacial couplings associated with the element a of fault block A. The flux on the edge (face) $e \equiv \cup_{i=1}^{N_a} e_i$ is then given by

$$q = \sum_{i=1}^{N_a} q_i. \tag{4.61}$$

The element mass balance (4.6) serve to couple the pressure in the element a of fault block A with the pressures in the elements b_i of fault block B that share a common face with it (see Figure 4.2). Thus, this increases the size of the stencil for the cell-centered finite difference approximation for elements $E \in \Omega^*$. Hence, the resulting algebraic problem is more challenging to solve. To overcome this difficulty, a ghost layer of unknown pressures can be introduced adjacent to fault block interfaces (one associated with each fault block). The pressures in the ghost layer can then be expressed in terms of the adjacent block pressures across the interface. In other words, the flux q may be written as

$$q = -T(p_a^e - p_a), \tag{4.62}$$

where $T = \sum_{i=1}^{N_a} T_i$ is the total transmissibility across the face e. Then from (4.59)–(4.62), the "effective pressure" in the ghost cell is given by

$$p_a^e = \frac{\sum_{i=1}^{N_a} T_i p_{b,i}}{T}. \tag{4.63}$$

In non-linear problems such as the case of transient, slightly compressible flow or multiphase flow through porous media, a similar method is followed by consolidating the contributions (to the ghost layer coefficients of primary unknowns) arising from each interfacial intersection e_i. Within each Newton iteration the ghost layers are then updated by solving a local system on the interface as described by equation (4.63).

4.6 Modeling coupled flow and transport using EV-MFEM

As in Section 3.5 of Chapter 3, an operator-splitting method is used to solve the problem of flow coupled to species transport. A phase-summed time-split formulation is used as before to determine the concentrations in a reference phase from which concentrations in all other phases can be determined using the phase equilibrium partitioning coefficients. The equations governing species transport as well as the phase-summed formulation are exactly the same as in Section 3.5. In addition, the advection and chemical reaction equations and implementation are exactly similar to those described in Sections 3.5.2–3.5.3 and hence these will not be repeated here in great detail. The boundary conditions considered are as specified by (2.22) in Section 2.2.1, Chapter 2; so that $\Gamma^N = \partial\Omega$ in the context of transport.

Advection is solved using a higher-order Godunov scheme as described in Section 3.5.2 within the sub-domains. For advection across fault-block interfaces, the EV-MFEM flux is taken advantage of, with the necessary modifications for determining slopes of species concentrations for elements $E \in \Omega^*$. Chemical reactions are solved as usual using a higher-order Runge-Kutta integration scheme. Since chemical reactions are completely local phenomenon, i.e., they depend only on quantities such as rate constants, concentrations, temperature within the element under consideration, they are of little interest from the point of view of the performance of EV-MFEM. Advection and diffusion on the other hand are both transport phenomena and thus play an important role in deciding the performance of the EV-MFEM.

The diffusion-dispersion step is solved using a backward-Euler in time and EV-MFEM in space discretizations. The problem is solved on the whole domain by employing test functions in the normal trace-free enhanced velocity approximation space $\mathbf{V}_h^{*,0}$ that satisfies flux continuity and local mass balance by construction. The phase-summed equations for diffusion-dispersion takes the form (for each component i)

$$\frac{\partial(\phi_i^* c_{iw})}{\partial t} - \nabla \cdot \mathbf{D}_i^* \nabla c_{iw} = 0, \quad 1 \leq i \leq n_c. \tag{4.64}$$

where the terms ϕ_i^*, $\mathbf{D}_i^*$ and c_{iw} have the same meaning as in Section 3.5.4.

Consider the discretized form of (4.64) and let $\mathbf{z} = \mathbf{D}^* \nabla c$. Then, the weak form of (4.64) in an EV-MFEM setting, seeks $\mathbf{z}_{h,iw}^{m+1} \in \mathbf{V}_h^{*,0}$, $c_{h,iw}^{m+1} \in W_h$, such that

$$\left(\frac{\phi_i^{*,m+1} c_{h,iw}^{m+1} - \phi_i^{*,m} c_{h,iw}^{m}}{\Delta \tau^{m+1}}, w \right) + \left(\nabla \cdot \mathbf{z}_{h,iw}^{m+1}, w \right) = 0, \quad w \in W_h, \tag{4.65a}$$

$$\left((\mathbf{D}_i^{*,m+1})^{-1} \mathbf{z}_{h,iw}^{m+1}, \mathbf{v} \right) = \left(c_{h,iw}^{m+1}, \nabla \cdot \mathbf{v} \right), \quad \mathbf{v} \in \mathbf{V}_h^{*,0}. \tag{4.65b}$$

For (4.65b) to make sense, the molecular diffusion is assumed to be non-singular (for cases when phase velocity dependent physical dispersion vanishes). This is often the case. In the current numerical implementation, only diagonal diffusion tensors (arising due to molecular diffusion) are considered. Using the quadrature rules (3.84) in Chapter 3, the concentration gradient on a cell edge is expressed in terms of the adjacent cell concentrations. Thus, for elements on an interface between two fault blocks the scheme described in Section 4.5 completely eliminates any gradients and velocity terms from (3.83), resulting in a linear system for concentrations. In general this system can be non-symmetric and is solved in IPARS by a BiCGS (stabilized bi-conjugate gradient) solver using a geometric multigrid preconditioner.

4.7 Some *a priori* error estimates for EV-MFEM applied to coupled single phase flow and transport problems

In this section *a priori* error estimates are derived for the species concentration solution obtained using the time-split scheme of Section 3.5.1, Chapter 3 with the enhanced velocity method (EV-MFEM) employed for the diffusion step. It is also recalled for the reader's convenience, from the same section, that a phase-summed formulation of species transport is given by

$$\frac{\partial(\phi_i^* c_{iw})}{\partial t} + \nabla\cdot(c_{iw}\mathbf{u}_i^* - \mathbf{D}_i^*\nabla c_{iw}) = r^*(c_{iw}) \quad \text{in } \Omega\times J, \tag{4.66a}$$

$$\mathbf{D}_i^*\nabla c_{iw}\cdot\mathbf{n} = 0 \quad \text{on } \partial\Omega\times J, \tag{4.66b}$$

$$c_{iw} = c_{iw}^0 \quad \text{in } \Omega\times\{0\}, \tag{4.66c}$$

and that a direct discretization of (4.66a) over the time interval $(\tau_m, \tau_{m+1}) \subset (t_n, t_{n+1})$ results in the approximation scheme

$$\frac{T_i^{m+1} - T_i^m}{\Delta\tau^{m+1}} + \nabla\cdot(c_{iw}^m\mathbf{u}_i^{*,m+1/2} - \mathbf{D}_i^{*,m}\nabla c_{iw}^{m+1}) = r^*(c_{iw}^{m+1/2}), \tag{4.67}$$

where $\Delta\tau^{m+1} = \tau_{m+1} - \tau_m$, $T_i = \phi_i^* c_{iw}$ and ϕ_i^*, $\mathbf{u}_i^*$ are evaluated at time $t \in (\tau_m, \tau_{m+1})$ (the concentration step) by linear interpolation in (t_n, t_{n+1}) (the flow step) using the known values at t_n and t_{n+1}.

For convenience of analysis as well as to ease the burden of notation, the problem is re-formulated here assuming a single species flowing in a single phase. Only advection and diffusion are considered. The extension that includes reactions is based on ODE theory and error estimates can be derived for it based on the arguments in [49]. Thus in this case $r^*(c_{iw}) = q_{i\alpha}$. The case of multiple species in single phase flow follows, since equations (4.67) for all species $i = 1, 2, \ldots n_c$, are independent of each other. In what follows, let the symbols c, ϕ, $\mathbf{u}$, $\mathbf{D}$ and q be used to denote c_{iw}, ϕ_i^*, $\mathbf{u}_i^*$, $\mathbf{D}_i^*$ and $\sum_\alpha q_{i\alpha}$ respectively, since this is more appropriate for single phase flow. The proof of the desired error estimates follows the arguments presented in [44]. Thus, let $0 = \tau_0 < \tau_1 < \ldots \tau_M = T$, $\Delta\tau^m = \tau_m - \tau_{m-1}$, and for any function $f = f(t)$, let

$$\partial_t f^m \equiv \frac{f(\tau_m) - f(\tau_{m-1})}{\Delta\tau^m}$$

At each discrete time-level, the solution values and fluxes $\mathbf{z}$ are approximated using the EV-MFEM spaces defined on $\mathcal{T}_h$. Further let $c_h^n \in W_h$, $\mathbf{z}_h^n \in \mathbf{V}_h^{*,0}$ denote the approximate solutions for the concentration and the "concentration velocity" obtained using the EV-MFEM method on non-matching multiblock grids. Also, let $\mathbf{w} \equiv c\mathbf{u}$ denote the advective velocity in the analysis.

Then, given $c_h^{m-1} \in W_h$, the time-split scheme is applied to first solve the advection equation

$$(\phi \bar{c})_t + \nabla \cdot \mathbf{w}(\mathbf{x}, t, \bar{c}) = q \quad \text{in } \Omega \times (\tau_{m-1}, \tau_m], \tag{4.68}$$

with initial condition c_h^{m-1}. The solution obtained at the end of this step will be denoted by $\bar{c}_h^m$. Next, the diffusion equation given by

$$(\phi c)_t + \nabla \cdot \mathbf{z}(\mathbf{x}, t, c) = 0 \quad \text{in } \Omega \times (\tau_{m-1}, \tau_m] \tag{4.69}$$

is solved with an initial condition $\bar{c}_h^m$. The solution at the conclusion of this step will be denoted c_h^m and approximates c^m. For any element $E \in \mathcal{T}_h$, integrating (4.68) over $E \times [\tau_{m-1}, \tau_m]$ yields

$$\int_E (\phi \bar{c})^m \mathrm{dx} = \int_E (\phi c_h)^{m-1} \mathrm{dx} + \int_E q \mathrm{dx} - \int_{\tau_{m-1}}^{\tau_m} \int_{\partial E} \mathbf{w}(\mathbf{x}, t, \bar{c}) \cdot \mathbf{n} \mathrm{ds}, \tag{4.70}$$

where $\mathbf{n}$ is the unit outer normal to ∂E.

It follows from (4.70), that accurate approximations of the advective flux $\int_{\partial E} \mathbf{w}(\mathbf{x}, t, \bar{c}) \cdot \mathbf{n} \mathrm{ds}$, yield accurate approximations, $\bar{c}_h^m$ of $\bar{c}^m$. It can be shown that the explicit higher-order Godunov scheme satisfies some of the accuracy requirements in the analysis [44]. Next, let $\mathbf{w}_h^{m-1}(\mathbf{x}, c_h^{m-1}) \in \mathbf{V}_h^{*,0}$ be an approximation to $\mathbf{w}$. Then, the solution $\bar{c}_h^m$ is given by the explicit advective update

$$(\phi \bar{c}_h)^m|_E = (\phi c_h)^{m-1}|_E + \int_E q \mathrm{dx} - \frac{\Delta \tau^m}{|E|} \int_{\partial E} \mathbf{w}_h^{m-1}(\mathbf{x}, t, \bar{c}) \cdot \mathbf{n} \mathrm{ds}, \tag{4.71}$$

where $|E|$ denotes the measure of element E. Next, the EV-MFEM is applied to the system

$$\begin{aligned} \mathbf{z} &= -\mathbf{D} \nabla c && \text{in } \Omega \times (\tau_{m-1}, \tau_m], \\ (\phi c)_t + \nabla \cdot \mathbf{z} &= 0 && \text{in } \Omega \times (\tau_{m-1}, \tau_m], \end{aligned}$$

with initial condition $\bar{c}_h^m \in W_h$. A backward-Euler in time scheme using (4.71) yields approximations c_h^m, $\mathbf{z}_h^m \in \mathbf{V}_h^{*,0}$ to c^m and $\mathbf{z}^m$ upon solving the system of equations resulting from the weak-form

$$\big((\mathbf{D}^{-1}\mathbf{z}_h)^m, \mathbf{v}\big) - (c_h^m, \nabla\cdot\mathbf{v}) = 0 \qquad \mathbf{v} \in \mathbf{V}_h^{*,0} \tag{4.72}$$

$$(\partial_t(\phi c_h)^m, w) + (\nabla\cdot\mathbf{z}_h^m, w) = (q, w) - (\nabla\cdot\mathbf{w}_h^{m-1}, w), \qquad w \in W_h. \tag{4.73}$$

It is also observed that the true solution-pair $\{c, \mathbf{z}\}$ satisfies the weak form

$$\big((\mathbf{D}^{-1}\mathbf{z})^m, \mathbf{v}\big) - (c^m, \nabla\cdot\mathbf{v}) = 0 \qquad \mathbf{v} \in \mathbf{V}_h^{*,0} \tag{4.74}$$

$$((\phi c)_t^m, w) + (\nabla\cdot\mathbf{z}^m, w) = (q, w) - (\nabla\cdot\mathbf{w}^{m-1}, w), \qquad w \in W_h. \tag{4.75}$$

Following [44], let $c_h^0 \equiv \hat{c^0}$ be the usual L^2 projection of the true initial condition. Hence, c_h^0 satisfies

$$(c_h^0, w) = (c^0, w) \quad \forall\, w \in W_h. \tag{4.76}$$

It is also noted from Remark 1, [44] that the special quadrature rules of [16] (see Section 3.5.4, Chapter 3) for rectangular elements, serve to eliminate $\mathbf{z}_h^m$ from the system (4.72)–(4.78) and thus effectively reducing it to a cell centered finite difference scheme. As in Section 3.4.3 (based on [137]), the standard technique (for time dependent problems), of comparing the approximate solution to an elliptic projection is employed. To this end, let $\tilde{c}(\cdot, t)$, $\tilde{\mathbf{z}}(\cdot, t)$ denote the solution to the EV-MFEM formulation of the elliptic projection of the solution of (4.66a). Then for each $\tau \in [0, T]$,

$$\big(\mathbf{D}^{-1}(\cdot, t)\tilde{\mathbf{z}}(\cdot, t), \mathbf{v}\big) - (\tilde{c}(\cdot, t), \nabla\cdot\mathbf{v}) = 0 \qquad \mathbf{v} \in \mathbf{V}_h^{*,0} \tag{4.77}$$

$$(\nabla\cdot\tilde{\mathbf{z}}(\cdot, t), w) = (\nabla\cdot\mathbf{z}(\cdot, t), w) \qquad w \in W_h, \tag{4.78}$$

where the right-hand side of (4.78) is given by

$$(\nabla\cdot\mathbf{z}(\cdot, t), w) = (q, w) - ((\phi c)_t(\cdot, t), w) - (\nabla\cdot\mathbf{w}(\cdot, t), w)\,.$$

In Section 4.3, *a priori* error estimates were derived for the EV-MFEM formulation described by the weak form given in (4.6). It is noted that the property of $\mathbf{K}$, given by assumption (A3) of Section 3.1 in Chapter 3 is assumed to hold even for $\mathbf{D}$ (namely that it is uniformly positive definite). Then, it follows that there exists a constant C dependent on $\Omega \subset \mathbb{R}^d$ and $\|\mathbf{D}\|_{1,\infty}$, but independent of h such that

$$\|\mathbf{z} - \tilde{\mathbf{z}}\| \leq C \left(\|c\|_{1,\infty,\Omega^*} h^{1/2} + \|\mathbf{z}\|_{1,\Omega} h \right), \tag{4.79}$$

$$\|c - \tilde{c}\| \leq C \left(\|c\|_{1,\infty,\Omega^*} + \|\mathbf{z}\|_1 h^{1/2} \right) h^r, \tag{4.80}$$

where $r = 1$ if $d = 2$ and $r = 5/6$ if $d = 3$. Similarly, for interior bounds, the reader is referred to [136]. Having these results, it is possible to derive error estimates for the method given by (4.72)–(4.76). To that end, let $\tilde{\mathbf{w}} \in \mathbf{V}_h^{*,0}$ satisfy the property that $\tilde{\mathbf{w}} \cdot \mathbf{n}$ at the mid-point of every interior edge (in 2-d) or face (in 3-d) is equal to the integral average of $\mathbf{w} \cdot \mathbf{n}$ on that edge or face. For edges or faces formed by intersections of fault-block interfacial elements, $\tilde{\mathbf{w}}$ satisfies the property that $\tilde{\mathbf{w}} \cdot \mathbf{n}$ at the mid-point of each interfacial sub-face equals the integral average of $\mathbf{w} \cdot \mathbf{n}$ on that sub-face. Thus, $\tilde{\mathbf{w}}$ satisfies

$$(\nabla \cdot (\tilde{\mathbf{w}} - \mathbf{w})(\cdot, t), w) = 0, \quad w \in W_h. \tag{4.81}$$

Following [44], let $\xi \equiv c_h - \tilde{c}$, $\boldsymbol{\eta} \equiv \mathbf{z}_h - \tilde{\mathbf{z}}$ and $\beta \equiv \hat{c} - \tilde{c}$. It is assumed that the numerical advection velocity approximation resulting from the use of explicit higher-order Godunov methods, $\mathbf{w}_h^{m-1}(\mathbf{x}, c_h^{m-1})$ satisfies the error estimate

$$\|\mathbf{w}_h^{m-1}(\cdot, c_h^{m-1}) - \tilde{\mathbf{w}}^{m-1}\| \leq C \left[\|\xi^{m-1}\| + \|\beta^{m-1}\| + h^s + \Delta t \right], \tag{4.82}$$

for c and the data sufficiently smooth and where $s \geq 1$. For a motivation of the proof of this result, the reader is referred to [44] (see also Appendix C). The preceding results of this section lead to the following important theorem.

Theorem 4.7.1. *For the given data and solution pair $\{c, \mathbf{z}\}$ sufficiently smooth, an advective velocity approximation of $\mathbf{w}$, satisfying inequality (4.82), and assuming the positve-definiteness property (A3) from Section 3.1, Chapter 3 holds for $\mathbf{D}^{-1}$, i.e. $\exists \gamma > 0$ such that $0 < \frac{1}{\gamma} \leq \mathbf{y}^T \mathbf{D}^{-1} \mathbf{y} \leq \gamma$ for every $\mathbf{y} \in \mathbb{R}^d$, the* *following error estimate applies:*

$$\max_m \|\xi^m\| + \left(\sum_{m=0}^{M} \|\mathbf{D}^{-1/2}\boldsymbol{\eta}\|^2 \Delta\tau^m\right)^{1/2} \tag{4.83}$$
$$\leq C(\gamma)\left(h^r + \Delta\tau + \|\beta^0\| + \left[\sum_{m=0}^{M} \|\beta^m\|^2 \Delta\tau^m\right]^{1/2} + \left[\int_0^T \|\beta_t(\cdot,t)\|^2 \mathrm{dt}\right]^{1/2}\right),$$

where $\Delta\tau = \max_m \Delta\tau^m$ *and* $C(\gamma) > 0$ *is a constant independent of* h *and* $\Delta\tau$*, but dependent only on* γ*.*

Proof. An observation is first in order. From an analysis analogous to Section 3.4.2, Chapter 3, note that the error $\|\beta_t\|$ can be bounded using the triangle inequality and standard L^2-projection error estimates. Then, subtracting (4.77)–(4.78) for the elliptic projection from (4.72)–(4.73) respectively, and applying (4.81) yields,

$$\big((\mathbf{D}^{-1}\boldsymbol{\eta})^m, \mathbf{v}\big) - (\xi^m, \nabla\cdot\mathbf{v}) = 0, \quad \mathbf{v} \in \mathbf{V}_h^{*,0} \tag{4.84}$$

$$\begin{aligned}(\partial_t(\phi\xi)^m, w) + (\nabla\cdot\boldsymbol{\eta}^m, w) &= -(\partial_t(\phi\tilde{c})^m, w) + ((\phi c)_t^m, w) \\ &\quad -(\nabla\cdot\mathbf{w}_h^m - 1, w) + (\nabla\cdot\tilde{\mathbf{w}}^m, w) \\ &= (\partial_t(\phi\beta)^m, w) + ((\phi c)_t^m - \partial_t(\phi c)^m, w) \\ &\quad + \big(\nabla\cdot(\tilde{\mathbf{w}}^m - \mathbf{w}_h^{m-1}), w\big), \quad w \in W_h.\end{aligned} \tag{4.85}$$

Selecting test functions $\mathbf{v} = \boldsymbol{\eta}^m$, $w = \xi^m$ and adding (4.84)–(4.85) yields

$$\begin{aligned}(\partial_t(\phi\xi)^m, \xi^m) + \big((\mathbf{D}^{-1}\boldsymbol{\eta})^m, \boldsymbol{\eta}^m\big) &= (\partial_t(\phi\beta)^m, \xi^m) + ((\phi c)_t^m - \partial_t(\phi c)^m, \xi^m) \\ &\quad + \big(\nabla\cdot(\tilde{\mathbf{w}}^m - \mathbf{w}_h^{m-1}), \xi^m\big).\end{aligned} \tag{4.86}$$

From (4.84) and inequality (4.82), it follows that

$$\begin{aligned}(\nabla\cdot(\tilde{\mathbf{w}}^m - \mathbf{w}_h), \xi^m) &= \big((\mathbf{D}^{-1}\boldsymbol{\eta})^m, \tilde{\mathbf{w}}^m - \mathbf{w}_h^{m-1}\big) \\ &\leq \frac{1}{2}\|(\mathbf{D}^{-1/2}\boldsymbol{\eta})^m\|^2 + \frac{1}{2}\|(\mathbf{D}^{-1/2})^m(\tilde{\mathbf{w}}^m - \mathbf{w}_h^{m-1})\|^2 \\ &\leq \frac{1}{2}\|(\mathbf{D}^{-1/2}\boldsymbol{\eta})^m\|^2 + C(\gamma)\|\tilde{\mathbf{w}}^m - \tilde{\mathbf{w}}^{m-1}\|^2 \\ &\quad + C(\gamma)\|\tilde{\mathbf{w}}^{m-1} - \mathbf{w}_h^{m-1}\|^2 \\ &\leq \frac{1}{2}\|(\mathbf{D}^{-1/2}\boldsymbol{\eta})^m\|^2 + C(\gamma)\left[\|\xi^{m-1}\|^2 + \|\beta^{m-1}\|^2 + h^{2r} + \Delta\tau^2\right].\end{aligned} \tag{4.87}$$

Also, it can be readily verified that

$$(\partial_t(\phi\beta)^m + (\phi c)_t^m - \partial_t(\phi c)^m, \xi^m) \leq \frac{C}{\Delta\tau^m}\left(\int_{\tau_{m-1}}^{\tau_m} \|(\phi\beta)_t(\cdot,t)\|^2 \mathrm{dt} + \Delta\tau^2\right) + \|\xi^m\|^2 \tag{4.88}$$

Substituting bounds (4.87) and (4.88) into (4.86) and applying assumption (A1) on the property of the porosity function ϕ from Section 3.1 in Chapter 3, yields

$$\begin{aligned}(\partial_t\xi^m, \xi^m) &+ \frac{1}{2}\|(\mathbf{D}^{-1/2}\boldsymbol{\eta})^m\|^2 \\ &\leq C(\gamma)\left(h^2r + \Delta\tau^2 + \|\xi^m\|^2 + \|\xi^{m-1}\|^2 + \|\beta^{m-1}\|^2\right) \\ &\quad + \frac{C}{\Delta\tau^m}\int_{\tau_{m-1}}^{\tau_m} \|\beta_t(\cdot,t)\|^2 \mathrm{dt}.\end{aligned} \tag{4.89}$$

Then, using the fact that

$$(\partial_t\xi^m, \xi^m) = \frac{1}{2}\left[\|\xi^m\|^2 - \|\xi^{m-1}\|^2 + \|\xi^m - \xi^{m-1}\|^2\right], \tag{4.90}$$

multiplying both sides of the inequality (4.89) by $2\Delta\tau^m$, summing on m and applying the discrete Gronwall lemma, completes the proof. □

A final application of the triangle inequality yields desired error bounds for $c - c_h$, $\mathbf{z} - \mathbf{z}_h$, and $\mathbf{w} - \mathbf{w}_h$.

4.8 Computational results

In this section numerical results are presented that demonstrate the application of EV-MFEM to challenging problems that couple flow and transport on non-matching multiblock grids. Results are shown for species transport in both single phase and two phase flow. First, a model verification problem is presented that shows that the method works - in other words, that the flow and transport solutions on a single fine-grid domain agrees with a multiblock equivalent with matching grids. The choice of matching grids is made here because as mass is transported across fault-block interfaces separating non-matching grids (where the solution is expressed in different approximating spaces), the solution of such intensive variables as those that are used in the calculation of extensive variables (for e.g., saturation for volumes and concentrations for mass) can differ greatly. Hence, comparison of solutions to matching grid and non-matching grid problems for such variables does not serve any purpose. On the other hand, it is entirely reasonable to compare intensive variables such as pressure across the interfaces separating fault-blocks with non-matching grids. Following this, computational results are presented for problems involving species transport in single- and multiphase flow.

4.8.1 Verification of EV-MFEM

To verify the EV-MFEM scheme, a fairly general and challenging problem modeling transport (advection-diffusion) of a species in two phase flow through a highly heterogeneous porous medium is considered. The problem is first solved in a single-block fine-grid configuration. The resulting solution is then compared to that obtained using a 4-block matching-grid configuration with exactly the same number of elements as in the 1-block case. It is expected that the solutions should match exactly in this case and this is indeed found to be the case. The data for this problem is briefly summarized in Table 4.1 for the single-block case. There are two wells that drive the flow - an injection well pumps water at a bottom-hole pressure (bhp) gradually increasing from 505.0 psi to 1000.0 psi during the time interval $t \in [0, 50]$ days; a production well produces oil at a bhp also gradually decreasing from 480 psi to 450 psi over the the time interval $t \in [0, 30]$ days. A standard Brooks-Corey type relative permeability relationship is applied to model the flow. A higher-order Godnov method is used to model the advection step of the species transport and a backward Euler in time and EV-MFEM in space for the diffusion step.

The permeability profiles of the medium (specifically the y-direction permeability) is shown in a top-view in Figure 4.3. The z-direction permeability is similar to it, while the x-direction permeability is $\frac{1}{5}^{\text{th}}$ of the y- and z-permeabilities. A physically meaningful projection algorithm is used to project the single-block permeability onto (non-)matching multiblock grids. The multiblock permeability field is also shown in Figure 4.3.

Property	Value
Simulation end time	101.0 days
Physical dimensions	400.0 ft×400.0 ft×24.0 ft
Depth below surface	1120.0 ft
Vertical/Horizontal perm ratio	5.0
Min/max horizontal perm	32.20 mD, 7970.95 mD
Average porosity	0.2
Grid dimensions	12×32×32
Initial oil pressure	500.00 psi
Initial water saturation	0.2
Initial species concentration	100.0 lbM/cu-ft
Molecular diffusivity	0.1 sq-ft/day
Equilibrium partitioning in oil/water	1.0, 1.0
Oil/water compressibility	4.0E-05, 3.3E-06
Maximum injection bhp	1000.0 psi
Minimum producion bhp	450.0 psi

Table 4.1: EV-MFEM verification: Summary of test data

The initial concentration of the species in the domain is 100 lbM/cu-ft at the location specified by the $[1, 1, 1]$ grid element. The EV-MFEM scheme is the applied to solve both the two phase flow equations as well as the component transport equations and the solution compared to the single-block fine-grid solution. Figure 4.4 shows oil phase pressures at t =50 and 100 days for the single-block case. Similarly, Figure 4.5 shows the pressures at the same time instants for the multiblock case.

Figure 4.6 shows the water phase saturation profiles at t =50 and 100 days, while Figure 4.7 shows the water phase saturation profile for the multiblock matching grid case at identical time instants. It is observed that the water front has crossed all mortars at the time instants of these solutions. Also the shape of the water front is indicative of the low and high permeability regions.

Finally, Figure 4.8 shows the species concentration profiles at t =50 and 100 days, while Figure 4.9 shows the species concentration profile for the multiblock matching grid case at the same time instants. Once again the shape and position of the concentration front is indicative of the flow of the water phase. Further since there is no source or sink of the species, the species grad-

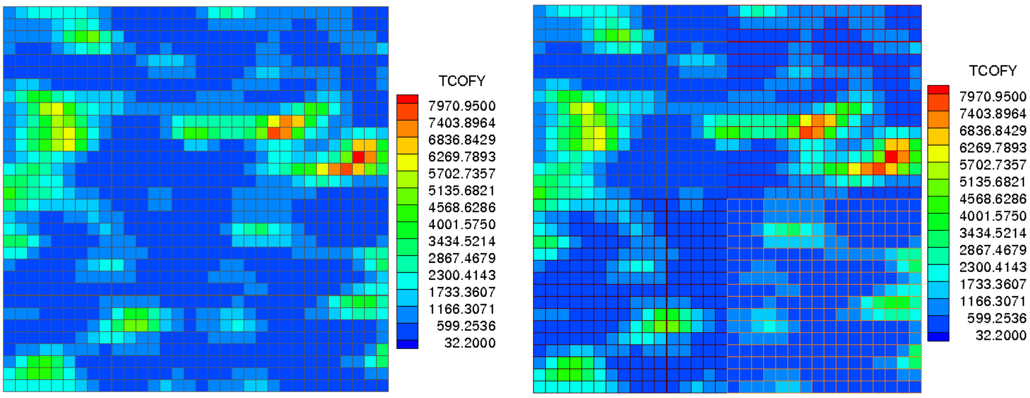

Figure 4.3: EV-MFEM verification: SPE6 Permeability field - single-block (left), 4-block matching grids (right)

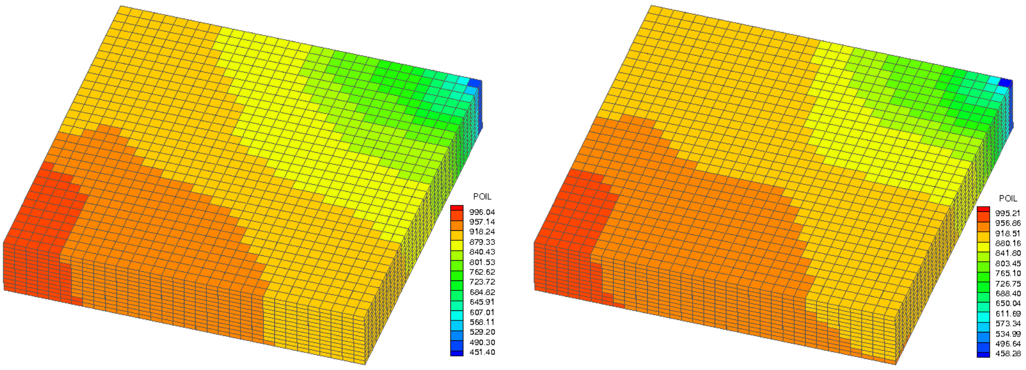

Figure 4.4: EV-MFEM verification: Oil phase pressure, single-block (left: 50 days, right: 100 days)

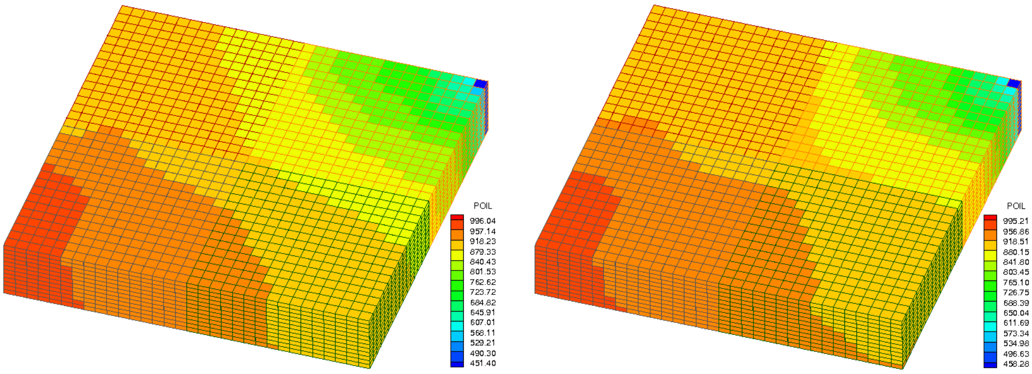

Figure 4.5: EV-MFEM verification: Oil phase pressure, 4-block matching grid (left: 50 days, right: 100 days)

ually diffuses over the entire domain (as can be seen by a rapid decrease in the concentration) while being transported by the phase velocity.

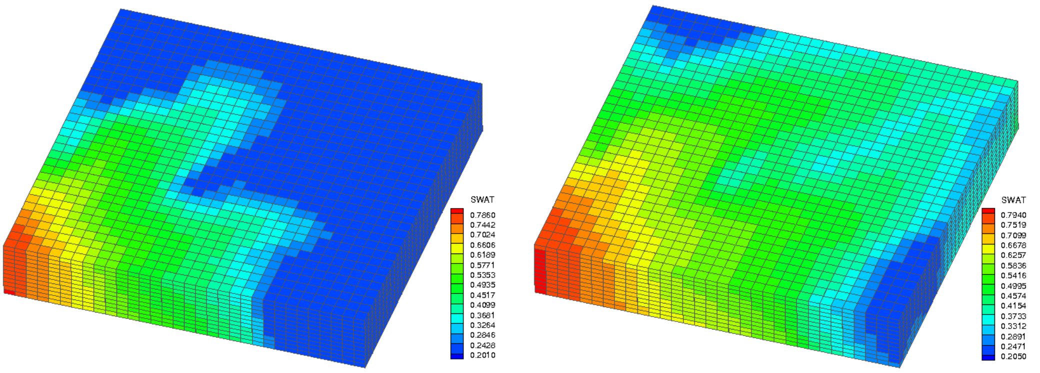

Figure 4.6: EV-MFEM verification: Water phase saturation, single-block (left: 50 days, right: 100 days)

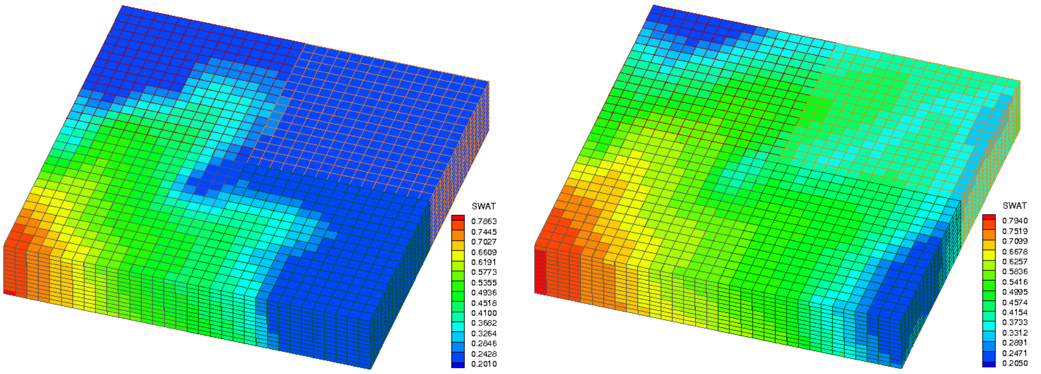

Figure 4.7: EV-MFEM verification: Water phase saturation, 4-block matching grid (left: 50 days, right: 100 days)

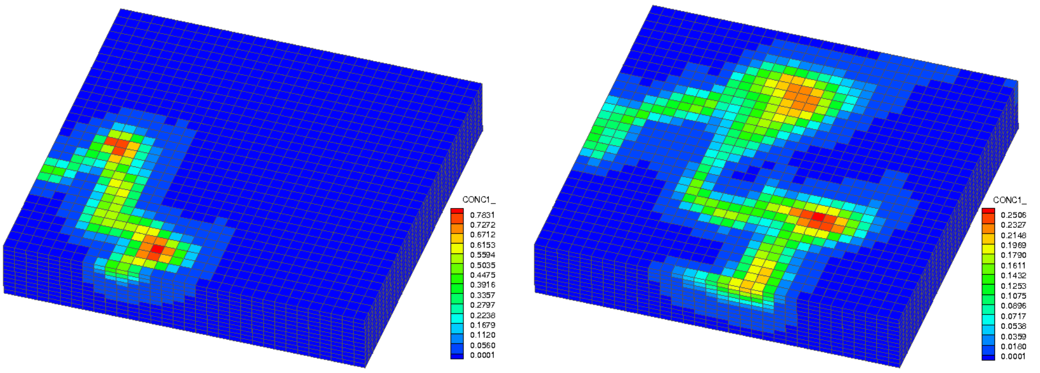

Figure 4.8: EV-MFEM verification: Species concentration, single-block (left: 50 days, right: 100 days)

It can be seen from the results in this section that the solutions for identical problems in single- and multiblock configurations agree completely

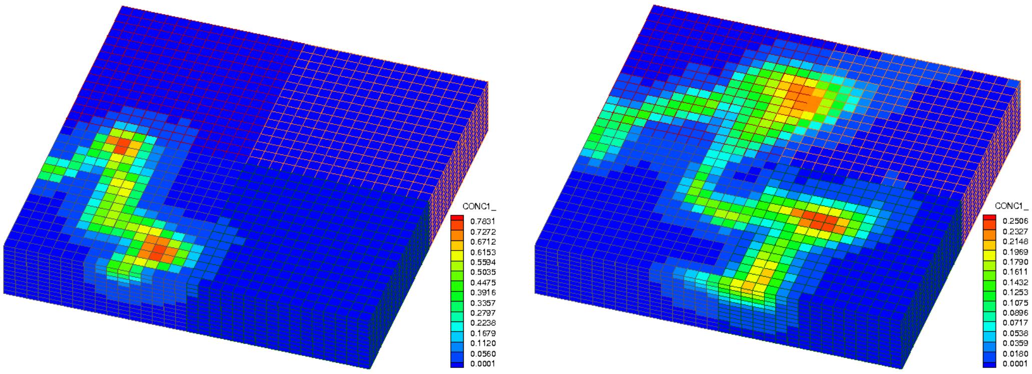

Figure 4.9: EV-MFEM verification: Species concentration, 4-block matching grid (left: 50 days, right: 100 days)

with each other and therefore verifies the implementation. It is also noted that the actual computational time for the coupled problem using matching grid and identical number of elements as the single-block configuration was observed to be comparable (only about 10% higher) to the single-block computation time on identical CPUs, for the simulation coupling flow and transport described above upto an end time of 101 days. Comparisons of the computational time for the mortar method described in Chapter 3 to single-block computational times shows that the mortar method takes in excess of 100% more time than the single-block method for identical and complex problems as the one described in this section.

4.8.2 Transport in multiphase flow

In this section, solutions to two interesting problems using EV-MFEM on non-matching multiblock grids, are presented. In the first problem, a species is transported across a barrier permeability field as described in Section 3.6.3 of Chapter 3. In order to restrict attention to the performance of EV-MFEM described earlier in this chapter, only transport (advection-diffusion) of a single species is considered. Non-matching grids play no role in affecting the modeling of phenomena such as chemical reactions which are completely local and hence, they are disregarded here. Table 4.2 summarizes the data for this problem. A 2-block configuration is assumed for this problem. As in the previous section,

Property	Value
Simulation end time	101.0 days
Physical dimensions	200.0 ft×200.0 ft×20.0 ft
Depth below surface	1120.0 ft
Vertical/Horizontal perm ratio	5.0
Min/max horizontal perm	10.0 mD, 2000.0 mD
Average porosity	0.2
Grid dimensions in blocks	10×9×20, 5×11×10
Initial oil pressure	500.00 psi
Initial water saturation	0.22
Initial species concentration	100.0 lbM/cu-ft
Molecular diffusivity	0.1 sq-ft/day
Equilibrium partitioning in oil/water	1.0, 1.0
Oil/water compressibility	4.0E-05, 3.3E-06
Maximum injection bhp	510.0 psi
Minimum producion bhp	350.0 psi

Table 4.2: EV-MFEM Flow around a barrier: Summary of data

two wells drive the flow as given in the data. A standard Brooks-Corey type relative permeability is used and advection and diffusion are modeled as before.

The y-direction permeability and the oil phase pressure at the end of t =101 days is shown in Figure 4.10.

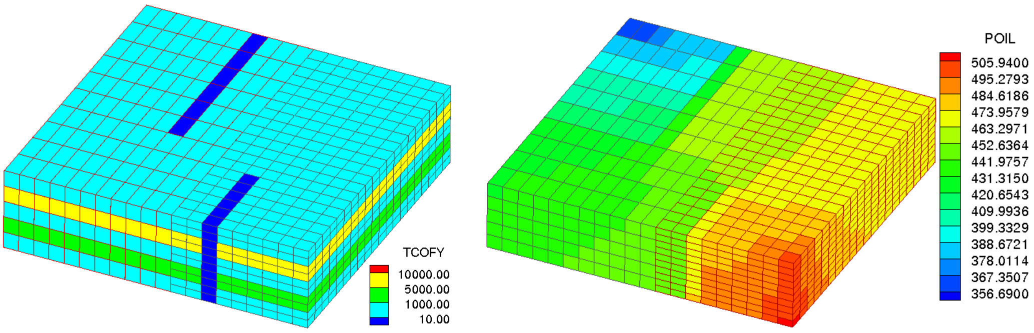

Figure 4.10: EV-MFEM Barrier case: Permeability field (left) and oil phase pressure at 101.0 days (right)

Figure 4.11 shows the water saturation profile at time instants t =5, 46, 76 and 101 days.

Finally, Figure 4.12 shows the species concentration profile at the same

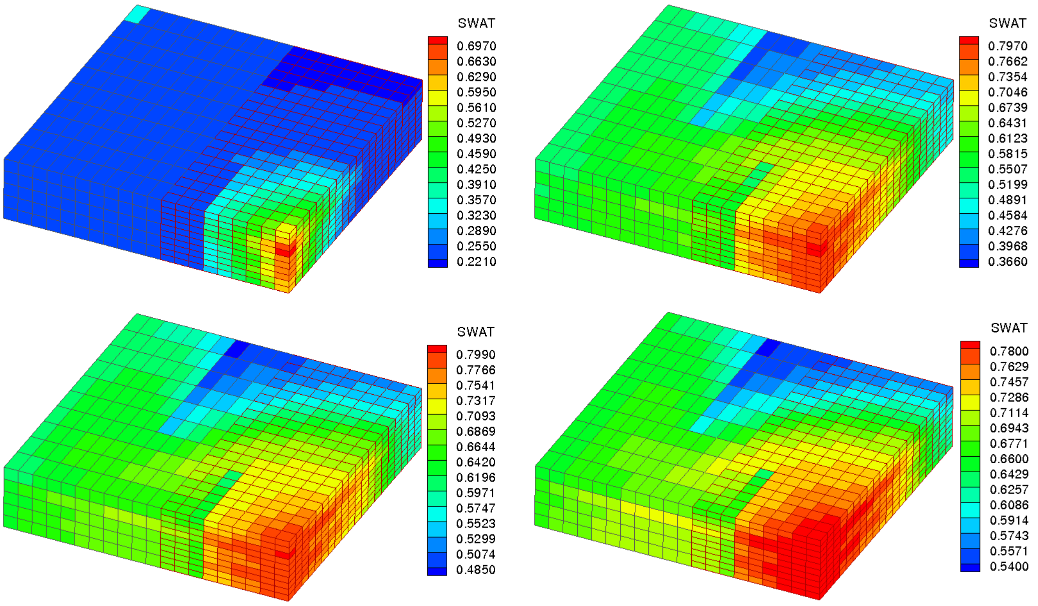

Figure 4.11: EV-MFEM Barrier case: Water phase saturation profile at 5, 46, 76, and 101 days (clockwise from top left)

time instants t =5, 46, 76 and 101 days. The scale of display is the same at all times in order to show the concentration as it diffused to very small amounts rapidly.

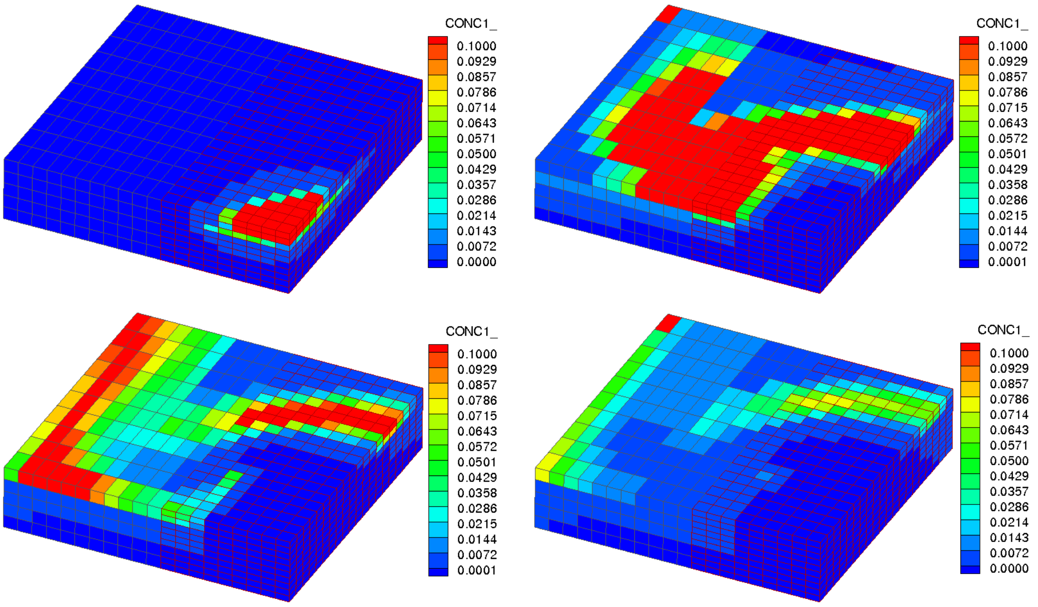

Figure 4.12: EV-MFEM Barrier case: Species concentration profile at 5, 46, 76, and 101 days (clockwise from top left)

In this example, the 2-block example using EV-MFEM takes about 10 times less computational time than an identical problem set-up and computed using the mortar MFEM method of Chapter 3. These results are not entirely unexpected as they were reported for the flow problem in [136]. Hence similar trends are to be expected (infact, even greater savings in time) for the coupled flow and transport problem. As a final example in this section, a 4-block non-matching grid version of the problem in Section 4.8.1 to demonstrate the huge savings in computational time that can be achieved. The fault-blocks are coarsened away from the injection well (where the species is initially resident). The permeability for the single-block fine everywhere and the 4-block case are shown in Figure 4.13 As indicated clearly by Figure 4.13, there are small but potentially significant differences in the permeability due to the projection onto different grids. Hence, this is another reason why a blind comparison of solution of a single-block problem to an arbitrary multiblock (equivalent) problem is unwarranted.

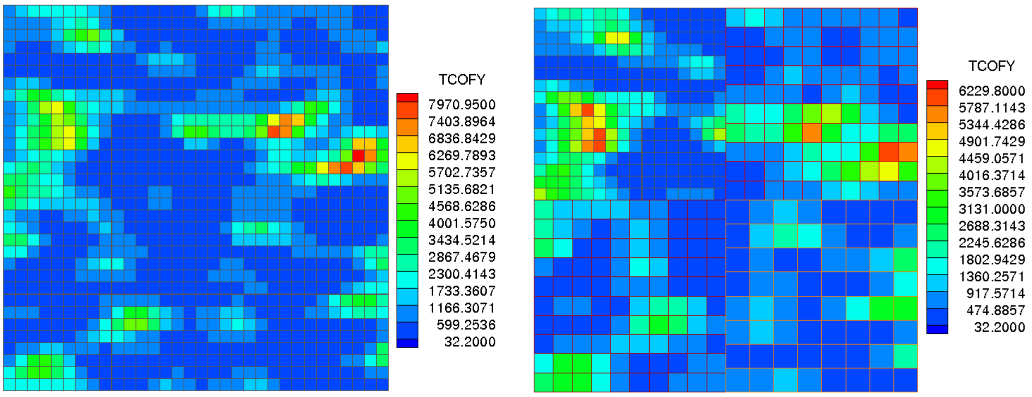

Figure 4.13: EV-MFEM SPE6 Example 2: Permeability field - single-block (left), 4-block non-matching grids (right)

Figure 4.14 shows the water phase saturation as well as the species concentration at time instants t =50, 100 days.

Finally, it is observed that the 4-block configuration, with non-matching grids employed for the computation in this section, takes less than about $\frac{1}{5}^{\text{th}}$ of the computational time of the single-block fine-grid problem presented in Sec-

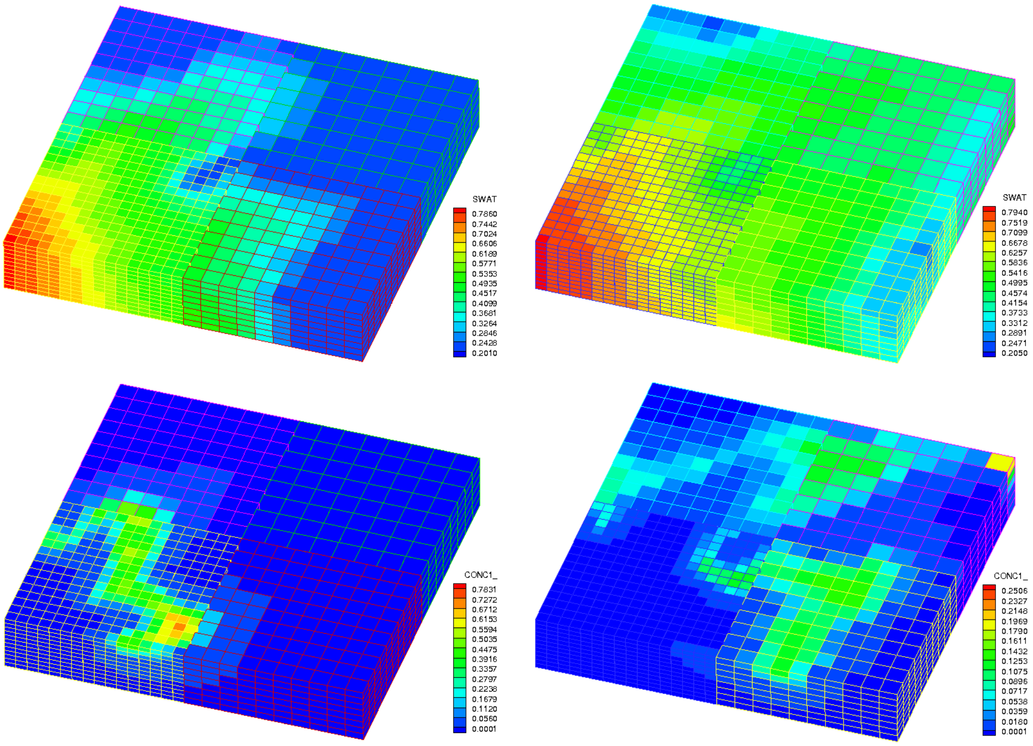

Figure 4.14: EV-MFEM SPE6 Example 2: Water phase saturation and species concentration profile at 50 and 100 days (clockwise from top left)

tion 4.8.1! This represents an extremely huge savings (81.5%) in computational time that is worthwhile even at the cost of some accuracy for such applications as in groundwater contaminant transport. Moreover, the multiblock implementation using the EV-MFEM applied to this problem took less than 0.1 of the computational time for the identical problem using mortar MFEM.

Chapter 5

Coupling of mixed FEM and discontinuous Galerkin methods using mortar finite element spaces

In modeling flow in porous media it is essential to employ physics preserving algorithms; namely, discretizations should be locally mass conservative and fluxes should be continuous. In addition, geological media exhibits a high level of spatial variability at a multiplicity of scales, from the size of grains or pores, to facies, stratigraphic and hydrologic units, up to sizes of formations. Hence numerical methods to solve sub-surface flow should be able to treat highly heterogeneous permeabilities. Two methods that are well suited to subsurface modeling are the mixed finite element (MFE) methods and discontinuous Galerkin (DG). The common features of these methods are local conservation of mass and accurate treatment of rough coefficients and grids.

MFE can be considered as a family of methods that differ mainly in the choice of numerical quadrature applied. They include the widely used cell-centered finite differences on structured rectangular grids and more recent formulations for general corner point or unstructured grids such as mimetic finite differences and multipoint flux approximation methods (MPFA). The advantage of the MFE methods is that they provide accurate approximation for both the pressure and the velocity and flux continuity is preserved.

DG methods are finite element methods that use discontinuous approximations. Examples of these schemes include the Bassy and Rebay method [22], the Local Discontinuous Galerkin (LDG) [8, 41] methods, the Oden-Babuška-Baumann (OBB-DG) [99] method and interior penalty Galerkin methods [48, 119, 138]. DG methods are of particular interest for multiscale problems because they have several appealing properties: local mass conservation, support of higher order approximations and tensor permeabilities, implementability on non-conforming grids, and capable of delivering exponential rates of convergence with appropriate meshing. On the other hand, because of the number of unknowns, DG solvers can be expensive.

It is well known that non-overlapping domain decomposition (DD) is a useful approach for obtaining robust and efficient parallel solvers for finite element/finite difference discretizations of elliptic equations [63]. A DD example that allows for spatial coupling/decoupling is the mortar multiblock method [114, 140]. Here the governing equations hold locally on the sub-domains and physically driven matching conditions are imposed on block interfaces in a numerically stable and accurate way using mortar finite element spaces. Major advantages in applying a mortar multiblock approach include the ability to treat multiphysics, multinumerics, multidomains, and multiscale resolution and adaptivity. Domain decomposition solvers and preconditioners for mortar discretizations have been developed in [3, 4, 65, 79, 110].

In [15] the multiscale mortar mixed finite element discretizations for second order elliptic equations was developed. The continuity of flux is imposed via a mortar finite element space on a coarse grid scale, while the equations in the coarse elements (or sub-domains) are discretized on a fine grid scale. The polynomial degree of the mortar and sub-domain approximation spaces may differ; in fact, the mortar space achieves approximation comparable to the fine scale on its coarse grid by using higher order polynomials. This formulation can be viewed as a variational multiscale method. In [62] this approach was extended to include the coupling of DG and MFE using mortar finite elements.

In this chapter, the mortar couplings of DG with DG/MFE methods is presented. The possibility of different scales in the mortar and sub-domain grids is allowed. Such couplings allow for **(1)** the flexibility of applying DG to sub-domains where general grids are required for treating pinchouts, discrete faults and fractures, and highly heterogeneous non-diagonal permeability tensors; **(2)**

developing a mortar domain decomposition parallel DG solver via reduction to an interface problem and employing conjugate gradient or GMRES for the solution of each Newton step; in this regard, efficient interface preconditioners such as balancing could be developed [43, 92, 110]; **(3)** applying the MFE method, which has substantially fewer unknowns than DG, in regions with relatively smooth or structured grids; **(4)** achieving model reduction through multiscale approximations.

This chapter is organized as follows. The slightly compressible single phase model problem is first briefly described. A multiblock formulation allowing for a general multidomain coupling of MFE and DG using coarse mortar spaces is then defined. The solution of these multinumeric discretizations using a non-overlapping DD algorithm and corresponding interface problem are introduced. Computational results illustrating the effectiveness of the mortar coupling are presented. Conclusions are given in the last section.

5.1 Slightly compressible single phase flow in porous media

Consider the following nonlinear second order parabolic equation, which can be used to model a time-dependent single phase slightly compressible flow in porous media:

$$\frac{\partial(\varphi\rho(p))}{\partial t} - \nabla\cdot(\rho(p)\mathbf{K}(\nabla p - \rho(p)\mathbf{g})) = f \quad \text{in } \Omega\times[0,T], \tag{5.1}$$

$$\rho(p)\mathbf{K}(\nabla p - \rho(p)\mathbf{g})\cdot\mathbf{n} = 0 \quad \text{on } \partial\Omega\times[0,T], \tag{5.2}$$

$$p = p_0 \quad \text{in } \Omega\times\{0\}. \tag{5.3}$$

The above system can also be written in a mixed form:

$$\mathbf{u} = -\rho(p)\mathbf{K}(\nabla p - \rho(p)\mathbf{g}) \quad \text{in } \Omega\times[0,T], \tag{5.4}$$

$$\frac{\partial(\varphi\rho(p))}{\partial t} + \nabla\cdot\mathbf{u} = f \quad \text{in } \Omega\times[0,T], \tag{5.5}$$

$$\mathbf{u}\cdot\mathbf{n} = 0 \quad \text{on } \partial\Omega\times\{0\}, \tag{5.6}$$

$$p = p_0 \quad \text{in } \Omega\times\{0\}. \tag{5.7}$$

Here, $\Omega \subset \mathbf{R}^d$, $d = 2$ or 3, is the flow domain with $\mathbf{n}$ being the unit outward normal vector to $\partial\Omega$; p, $\mathbf{u}$, and ρ are the fluid pressure, Darcy velocity, and density, respectively; φ is the rock porosity, $\mathbf{K}$ is a symmetric, uniformly positive definite tensor representing the rock permeability divided by the fluid viscosity, f is the source term, g is the gravitational constant, and D is the depth. The equation of state is given by

$$\frac{d\rho}{\rho} = c_f dp,$$

where c_f is the fluid compressibility constant.

The homogeneous Neumann boundary conditions are considered merely for simplicity and the results have been generalized to more general boundary conditions.

5.2 The multiblock method revisited

For convenience, the multiblock mortar method is revisited in this section in the context of coupling mixed FEM and DG in adjacent sub-domains. Let the domain Ω be decomposed into a finite number of non-overlapping sub-domain blocks Ω_i so that $\overline{\Omega} = \cup_{i=1}^{n_b} \overline{\Omega}_i$. The blocks may form a geometrically nonconforming partition. Let $\Gamma_{i,j} = \partial\Omega_i \cap \partial\Omega_j$, $\Gamma = \cup_{1 \le i < j \le n_b} \Gamma_{i,j}$, and $\Gamma_i = \partial\Omega_i \cap \Gamma = \partial\Omega_i \backslash \partial\Omega$. The unit outer normal vector to $\partial\Omega_i$ is denoted by $\mathbf{n}_i$. Let the set of block indices be divided into two groups: one, denoted by I_{DG}, uses DG as discretization method; the other, which will be denoted by I_{MFE}, uses MFE. Next, assume that $I_{\mathrm{DG}} \neq \emptyset$ but note that I_{MFE} might be empty. For the case where only MFE is used, the reader is referred to [12, 15, 91, 142].

Let $\mathcal{T}_{h,i}$ be a non-degenerate (quasi-uniform) finite element partition of Ω_i for $i \in I_{\mathrm{DG}}(I_{\mathrm{MFE}})$. Also, note that $\mathcal{T}_{h,i}$ and $\mathcal{T}_{h,j}$ to be non-matching on $\Gamma_{i,j}$. The set of all interior edges/faces within $\mathcal{T}_{h,i}$ is denoted by $\mathcal{E}_{h,i}$. On each $e \in \mathcal{E}_{h,i}$, a unit normal vector $\mathbf{n}_e$ is chosen once and for all. Consider a given $e \in \mathcal{E}_{h,i}$ with $e = \partial E_m \cap \partial E_n$ where $E_m, E_n \in \mathcal{T}_{h,j}$ and $\mathbf{n}_e$ exterior to E_m. The average and jump on e of an element-wise smooth function χ is given by

$$\{\chi\} := \frac{1}{2}\left(\chi|_{E_m} + \chi|_{E_n}\right), \quad [\chi] := \chi|_{E_m} - \chi|_{E_n}.$$

Let $\mathcal{T}_{H,i,j}$ be a quasi-uniform finite element partition of $\Gamma_{i,j}$. Define $\mathcal{T}^{\Gamma,H} = \cup_{1\le i<j\le n_b}\mathcal{T}_{H,i,j}$ and $\mathcal{T}_{H,i} = \cup\{\mathcal{T}_{H,i,j} : 1 \le j \le n_b, \Gamma_{i,j} \neq \emptyset\}$. The following functional spaces were used in the weak formulation of the problem:

$$\begin{aligned} X_i &:= \left\{q \in L^2(\Omega_i) : \forall E \in \mathcal{T}_{h,i}, q|_E \in H^s(E)\right\}, \ s > \frac{3}{2}, \quad i \in I_{\mathrm{DG}}, \\ \mathbf{V}_i &:= \{\mathbf{v} \in H(\mathrm{div};\Omega_i) : \mathbf{v}\cdot\mathbf{n} = 0 \text{ on } \partial\Omega_i \cap \partial\Omega\}, \quad W_i := L^2(\Omega_i), \quad i \in I_{\mathrm{MFE}}, \\ \Lambda_{i,j} &:= H^{\frac{1}{2}}(\Gamma_{i,j}). \end{aligned}$$

For the discrete problem, the following finite element space is used for DG domains:

$$X_{h,i} := \left\{q_h \in L^2(\Omega_i) : \forall E \in \mathcal{T}_{h,i}, q_h|_E \in \mathbb{P}_r(E)\right\}, \quad r \ge 1, \quad i \in I_{\mathrm{DG}}.$$

For the MFE domains, let $\mathbf{V}_{h,i} \times W_{h,i} \subset \mathbf{V}_i \times W_i$ be any of the usual mixed finite element spaces defined on $\mathcal{T}_{h,i}$ (see [28], Section III.3). The most commonly used mixed spaces are the Raviart-Thomas spaces of order k, RT_k [96, 116]. The IPARS (Integrated Parallel and Accurate Reservoir Simulator) code base that is used to implement the results in this work, uses RT_0 space on rectangular partitions.

On the interface a mortar finite element space is used to approximate the pressure and impose weakly continuity of flux and pressure. Let $M_{H,i,j} \subset L^2(\Gamma_{i,j})$ be the mortar space on $\Gamma_{i,j}$, containing at least either the continuous or discontinuous piecewise polynomials of degree m on $\mathcal{T}_{H,i,j}$. The numerical experiments presented here use either $m = 0$ or $m = 1$ as choices for the polynomical degrees. Then, the mortar finite element space on Γ is defined as

$$M_H = \bigoplus_{1\le i<j\le n_b} M_{H,i,j}.$$

5.3 A weak formulation

Let $0 = t_0 < t_1 < t_2 < ...$, $\Delta t^n = t_n - t_{n-1}$, and $f^n = f(t_n)$. Define bivariate forms and nonlinear functionals for the DG scheme in Ω_i, $i \in I_{\text{DG}}$ as:

$$
\begin{aligned}
B_i(p^n, q) :=& \sum_{E \in \mathfrak{T}_{h,i}} \int_E \frac{(\phi\rho)^n - (\phi\rho)^{n-1}}{\Delta t^n} q\,dx + \sum_{E \in \mathfrak{T}_{h,i}} \int_E \rho^n \mathbf{K}(\nabla p^n - \rho^n \mathbf{g}) \cdot \nabla q\,dx \\
&- \sum_{e \in \mathcal{E}_{h,i}} \int_e \{\rho^n \mathbf{K}(\nabla p^n - \rho^n \mathbf{g}) \cdot \mathbf{n}_e\}\,[q]\; ds \\
&+ \sum_{e \in \mathcal{E}_{h,i}} \int_e \{\rho(q) \mathbf{K}(\nabla q - \rho(q) \mathbf{g}) \cdot \mathbf{n}_e\}\,[p^n]\; ds \\
&- \int_{\Gamma_i} \rho^n \mathbf{K}(\nabla p^n - \rho^n \mathbf{g}) \cdot \mathbf{n}_i q|_{\Omega_i}\,ds \\
&+ \int_{\Gamma_i} \rho(q) \mathbf{K}(\nabla q - \rho(q) \mathbf{g}) \cdot \mathbf{n}_i p^n|_{\Omega_i}\,ds \\
&+ \sum_{e \in \mathcal{E}_{h,i}} \frac{\sigma_e}{h_e} \int_e [p^n]\,[q]\; ds + \sum_{\tau \in \mathfrak{T}_{H,i}} \frac{\sigma_\tau}{H_\tau} \int_\tau p^n|_{\Omega_i} q|_{\Omega_i}\,ds, \\
L_i(q; \lambda^n) :=& \int_{\Omega_i} f\,q\,dx + \int_{\Gamma_i} \rho(q) \mathbf{K}(\nabla q - \rho(q) \mathbf{g}) \cdot \mathbf{n}_i \lambda^n\,ds \\
&+ \sum_{\tau \in \mathfrak{T}_{H,i}} \frac{\sigma_\tau}{H_\tau} \int_\tau q|_{\Omega_i} \lambda^n\,ds.
\end{aligned}
$$

Assume $0 < \sigma_\gamma^0 \leq \sigma_\gamma \leq \sigma_\gamma^1$, $0 < \sigma_\tau^0 \leq \sigma_\tau \leq \sigma_\tau^1$.

The discrete-in-time weak formulation of the problem (5.1)–(5.3) for $i \in I_{\text{DG}}$ and (5.4)–(5.7) for $i \in I_{\text{MFE}}$ is to find $p_h^n|_{\Omega_i} \in X_{h,i}$ for $i \in I_{\text{DG}}$, $(\mathbf{u}_h^n, p_h^n)|_{\Omega_i} \in$

$\mathbf{V}_{h,i} \times W_{h,i}$ for $i \in I_{\text{MFE}}$, and $\lambda_H^n \in M_H$, for $n = 1, 2, 3...$, such that

$$B_i(p_h^n, q) = L_i(q; \lambda_H^n), \quad \forall\, q \in X_{h,i},\ i \in I_{\text{DG}}, \tag{5.8}$$

$$\begin{aligned}\int_{\Omega_i} \mathbf{K}^{-1}(\rho_h^n)^{-1}\mathbf{u}_h^n \cdot \mathbf{v}\, dx = \int_{\Omega_i} p_h^n\, \nabla \cdot \mathbf{v}\, dx - \int_{\Gamma_i} \mathbf{v} \cdot \mathbf{n}_i \lambda_H^n\, ds \\ + \int_{\Omega_i} \rho_h^n \mathbf{g} \cdot \mathbf{v}\, dx, \quad \forall\, \mathbf{v} \in \mathbf{V}_{h,i},\ i \in I_{\text{MFE}},\end{aligned} \tag{5.9}$$

$$\int_{\Omega_i} \frac{(\phi\rho_h)^n - (\phi\rho_h)^{n-1}}{\Delta t^n}\, w\, dx + \int_{\Omega_i} \nabla \cdot \mathbf{u}_h^n\, w\, dx = \int_{\Omega_i} f^n\, w\, dx, \quad \forall\, w \in W_{h,i},\ i \in I_{\text{MFE}}, \tag{5.10}$$

$$\begin{aligned}\sum_{i \in I_{\text{DG}}} \left(- \int_{\Gamma_i} \rho_h^n \mathbf{K}(\nabla p_h^n - \rho_h^n \mathbf{g})|_{\Omega_i} \cdot \mathbf{n}_i \mu\, ds + \sum_{\tau \in \mathcal{T}_{H,i}} \frac{\sigma_\tau}{H_\tau} \int_\tau (p_h^n|_{\Omega_i} - \lambda_H^n)\, \mu\, ds \right) \\ + \sum_{i \in I_{\text{MFE}}} \int_{\Gamma_i} \mathbf{u}_h^n|_{\Omega_i} \cdot \mathbf{n}_i \mu\, ds = 0, \quad \forall \mu \in M_H.\end{aligned} \tag{5.11}$$

5.4 Domain decomposition

The discrete system (5.8)–(5.11) can be solved on each time step by reducing it to an interface problem in the (coarse) mortar space. To this end, let $b^n : M_H \times M_H \to \mathbf{R}$ define a non-linear interface bivariate form as follows. For $\psi = \lambda_H^n \in M_H$ and $\mu \in M_H$, let

$$\begin{aligned}b^n(\psi, \mu) = \sum_{i \in I_{\text{DG}}} \left(- \int_{\Gamma_i} \rho_h^n \mathbf{K}(\nabla p_h^n - \rho_h^n \mathbf{g})|_{\Omega_i} \cdot \mathbf{n}_i \mu\, ds + \sum_{\tau \in \mathcal{T}_{H,i}} \frac{\sigma_\tau}{H_\tau} \int_\tau (p_h^n|_{\Omega_i} - \psi)\, \mu\, ds \right) \\ + \sum_{i \in I_{\text{MFE}}} \int_{\Gamma_i} \mathbf{u}_h^n|_{\Omega_i} \cdot \mathbf{n}_i \mu\, ds,\end{aligned}$$

where $p_h^n = p_h^n(\psi)$, $\mathbf{u}_h^n = \mathbf{u}_h^n(\psi)$ are obtained from the solution of (5.8)–(5.10) with Dirichlet boundary data ψ.

Next, let $\mathcal{B}^n : M_H \to M_H$ define a non-linear interface operator by

$$\langle \mathcal{B}^n \psi, \mu \rangle = b^n(\psi, \mu), \quad \forall \mu \in M_H,$$

where $\langle \cdot, \cdot \rangle$ is the L^2-inner product in M_H. Then, it can be shown that $(\psi, p_h^n(\psi), \mathbf{u}_h^n(\psi))$ is the solution to (5.8)–(5.11), when $\psi \in M_H$ solves

$$\mathcal{B}^n(\psi) = 0. \tag{5.12}$$

The system of nonlinear equations (5.12) on the interface is solved by an inexact Newton method. Each Newton step s is computed by a forward difference GMRES iteration for solving $(\mathcal{B}^n)'(\psi)s = -\mathcal{B}^n(\psi)$. On each GMRES iteration the action of the Jacobian $(\mathcal{B}^n)'(\psi)$ on a vector μ is approximated by a forward difference which requires only one evaluation of the nonlinear operator $\mathcal{B}^n$. The evaluation of $\mathcal{B}^n$ involves solving sub-domain problems (5.8)–(5.10) in parallel and two inexpensive projection steps - from the mortar grid onto the local sub-domain grids and from the local grids onto the mortar grid. Since each block can be distributed among a number of processors, the sub-domain solvers are parallel themselves. The sub-domain problems are also nonlinear and are solved by a preconditioned Newton-Krylov solver [47, 80] for the MFE domains and an iterative coupling approach [111] for the DG domains.

5.5 Computational results

Solutions of numerical experiments performed on simple test cases are first presented to validate the method. Then, additional results of some challenging problems in reservoir simulation are shown to motivate the future application of the theory. For all the tests presented, degrees of approximation used were $r = 2$ (p.w. quadratics for DG domains) and $k = 0$ (RT_0 spaces for MFE domains). The mortar spaces are chosen to be either piecewise constants or piecewise continuous linear functions for all tests.

5.5.1 DG-DG, Two-block problem

The first problem models single phase slightly compressible flow in a domain with physical dimensions of 200 ft × 100 ft × 100 ft and a constant porosity of 0.2. A two-block configuration with DG discretizations in either block and using matching grids is applied as shown in Fig. 5.1. Both blocks have an 8×8×8 grid with cuboidal elements of side 1 ft each, split into prisms (for a total of 1024 elements in each block). A uniform permeability of 100 mD is assumed in either block. Dirichlet boundary conditions (BC's) of 300 and

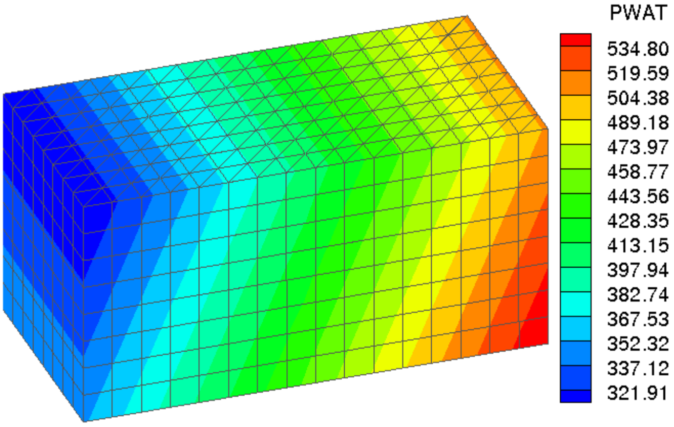

Figure 5.1: 2-block DG-DG problem with matching grids

550 psi are respectively specified on the surfaces $x = 0$ft and $x = 200$ ft at a reference depth, $z = 0$ft. Hence, the effect of gravity is taken into consideration here. Note that in this example the negative z-axis is aligned with the direction of gravity. No-flow BC is assumed elsewhere. One of the main objectives of this test was to validate the implementation in IPARS. The degrees of approximation used for this test case were $r = 2, k = 0$ and $m = 0$. Figure 5.1 also shows the pressure profile at a reasonably "steady state" corresponding to $t = 40$ days.

In the next test, the previous case is re-considered with non-matching grids. This time, the blocks have cuboidal elements split into prisms (again) in an 8×8×8 grid in one block and a 10×10 ×10 grid in the other as shown in Fig. 5.1. Thus the blocks have 1024 and 2000 prismatic elements respectively. The properties of the porous medium and the initial and boundary conditions are assumed to be the same as in the previous test case. The degrees of approximation used for this test case were $r = 2, k = 0$ and $m = 1$. Figure 5.2 shows the pressure and velocity profiles at a "steady state", $t = 40$ days. This test validates the implementation for the case of non-matching grids. Tests were performed for mortars in other directions as well, but are not shown here for brevity.

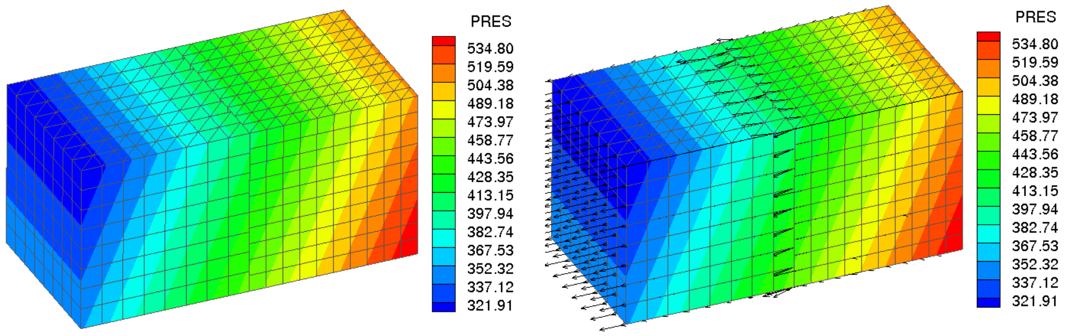

Figure 5.2: 2-block DG-DG problem with non-matching grids (left: grid, pressure right: grid, velocity profile)

5.5.2 DG-MFE, Quarter-five spot matching grid problem

The second problem models single phase slightly compressible flow in a domain with physical dimensions of 200 ft × 200 ft × 100 ft and a constant porosity of 0.2. A four-block configuration with DG and MFE discretizations using matching grids is applied in diagonally opposite blocks as shown in Fig. 5.3. The MFE domains are assigned an $8{\times}8{\times}8$ grid while the DG grid has twice the number of elements. The permeability is uniform in each block but is discontinuous across block 2 interfaces (1 mD in block 2 and 100 mD in the remaining blocks). Two BHP specified wells with pressure of 550 and 300 psi are located at the diagonally opposite corners in the DG domains. No-flow BC is assumed elsewhere. The degrees of approximation used for this test case were $r = 2, k = 0$ and $m = 1$. Figure 5.3 also shows the pressure and velocity profile at a “steady state” corresponding to $t = 40$ days.

5.5.3 DG-MFE, 7 blocks with 2 wells

The third problem models flow in a domain with physical dimensions 120 ft × 120 ft × 30 ft. A constant porosity of 0.2 and permeability of 100 mD are assumed. This problem motivates the idea of using DG around wells and MFE elsewhere in modeling flow driven by wells. The DG domains that contain the wells are assigned a finer grid than the MFE domains. A 7-block configuration is assumed with 2 wells located in DG domains at the diagonally

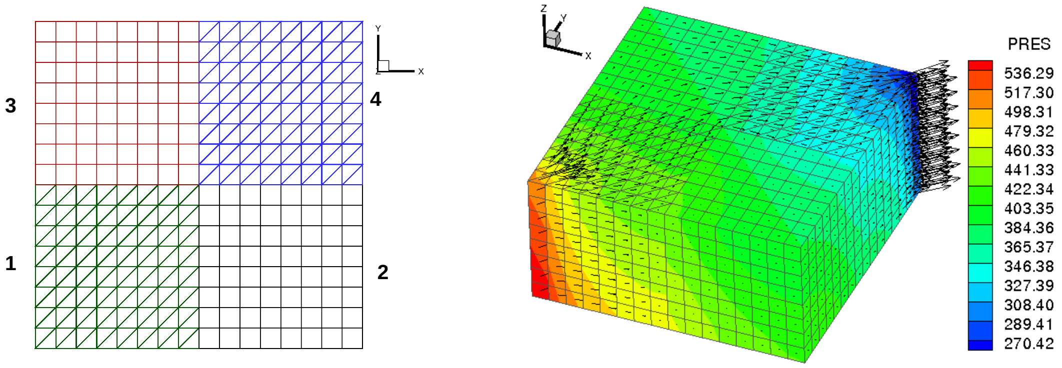

Figure 5.3: 4-block DG-MFE quarter-five spot problem (left: grid, right: solution)

opposite corners as shown in Fig. 5.4. A bottom-hole pressure of 550 psi and 300 psi is specified at these wells. No-flow BC is assumed elsewhere. The degrees of approximation used were $r = 2, k = 0$ and $m = 1$. The solution profile is also shown in Fig. 5.3.

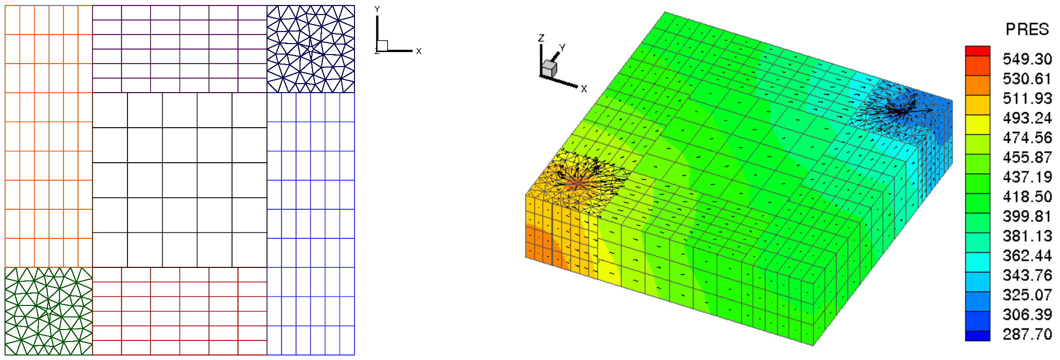

Figure 5.4: 7-block DG-MFE problem with DG around wells (left: grid, right: solution)

Chapter 6

Coupling of porescale network models and continuum scale models of flow using mortar finite element spaces

porescale models are becoming increasingly useful as predictive tools for modeling flow and transport in porous media. These models can accurately represent the 3-D pore-structure of real media. Currently first-principles modeling methods are being employed for obtaining qualitative and quantitative behavior. Generally, artificial and simple boundary conditions are imposed on a model which is the used as a stand alone tool for extracting macroscopic parameters. However, realistic boundary conditions, reflecting flow and transport in surrounding media, may be necessary for behavior that occurs over larger length scales or including porescale models in a multiscale setting.

In this chapter, porescale network models are coupled to adjacent media (additional porescale or continuum-scale models) using mortar finite element spaces introduced in Chapter 3. While mortars have been used in the past to couple sub-domains of different models, physics, and meshes, they are extended here for the first time to porescale models. The approach is demonstrated by modeling single phase flow in coupled porescale models, but the methodology can be utilized to model dynamic processes and perform multiscale modeling in 3-D continuum simulators for flow and transport.

6.1 Overview of porescale network modeling

Flow and transport in porous media are typically modeled at the continuum scale by solving the continuity equation together with momentum, energy, and/or species balances. Constitutive equations, such as Darcy's law, are substituted into these equations for velocity. Quantitative values of empirical parameters, such as permeability, relative permeability, and capillary pressure are needed as inputs for the model which are dependent on the media morphology and/or the fluids in the pore space. Experimental measurements are commonly used to estimate the parameters used for direct substitution into continuum simulators, but recently, porescale models have become a popular and efficient method for parameter estimation. Network modeling is a porescale technique in which the porous medium is approximated as an interconnected network of pores and pore throats.

Network models have long been used to study important behavior regarding flow and transport in porous media, but were limited to qualitative studies because simple 2-D or 3-D lattices were used. More recently, quantitative techniques have been developed to model certain behavior in porous media including single phase Newtonian flow [31], multiphase flow [20], and non-Newtonian flow [87, 128]. Physically-representative network models [31] are often mapped directly from a rigorous description of some original well described porous medium and therefore they retain important morphology and spatial correlations that are necessary for obtaining quantitative and predictive results. In order to make network modeling as predictive as possible, advancements continue to be made in two specific areas: (1) characterization of the 3D pore structure and transformation into a physically-representative network model, and (2) accurate flow modeling in the resulting network using a first-principles approach.

The first step in characterizing the pore structure is to obtain an accurate, numerical description of the porous medium. X-ray computed microtomography [82, 84, 141] is a technique used to extract the 3D pore structure of real, naturally occurring porous media. The high-resolution images obtained through XMT are digitally represented as voxels which (in a binary image) define the pore and grain space. Computer-generated methods offer an alternative to high-resolution imaging of porous media. These methods can include stochastic approaches [7, 82] in which the porous medium is reconstructed using statistical properties and process based approaches that attempt to simulate the geological process in which the medium is formed. For example, in [20], Baake and Oren created computer-generated sandstones by modeling sedimentation, compaction, and diagenesis.

Regardless of the method used to digitally represent the medium, the second step is conversion to a network model of pores and throats. Grain-based methods are usually tied to approaches that represent grain positions in porous media. In [31], Bryant *et al* used a Delaunay tessellation to determine the pores and interconnected throats to create a physically-representative network model. Al-Raoush *et al* [9] extended that work by using a modified Delaunay tessellation, which allowed the pore interconnectivity to vary. For voxel data obtained from imaging, the medial-axis [83, 125] can be used to thin the void space, from which one can map out the pores and throats in the network. Recently, a grain based reconstruction algorithm [131] was created to generate network models from voxel data. Advantages of this method include its insensitivity to image resolution and the mapping of the network from fundamental building blocks in the material (i.e., the grains).

6.2 Recent trends in pore-continuum scale coupling

Once the network model is generated, it can be used to model a wide range of flow and transport problems by forcing mass conservation at every pore and solving fundamental equations of momentum, mass, and heat transfer in the connecting throats. Early network modeling assumed throats were simple capillary tubes or transformed the throats into equivalent capillaries [31, 87] so that the Navier-Stokes equations, etc. could be solved in a straightforward manner. Advancements continue to be made to account for the actual irregular geometry of these throats. Balhoff and Thompson [128, 129] have developed closed-form empirical flow equations for non-Newtonian fluids in converging/diverging ducts (which are more representative of the true throat geometry) by solving the momentum equations numerically.

The recent improvements in these two areas (characterization of the pore structure and flow modeling) has allowed network modeling to become more of a predictive tool for obtaining upscaled, macroscopic parameters. Despite these advancements, simple boundary conditions (usually a pressure gradient in one-dimension) are almost always imposed when flow modeling is performed. Since the porescale model often represents a portion of a much larger medium, the true boundary conditions should depend on flow behavior in the surrounding media. Imposing artificial boundary conditions can lead to misleading upscaled values, whereas choosing appropriate boundary conditions on the network require direct coupling to adjacent media (additional porescale or continuum-scale models). The latter procedure is not straightforward because the models are independent and the boundary pores may not be naturally connected to the adjacent model.

Recently, Balhoff *et al* [130] developed a domain-decomposition method for coupling a porescale model to an adjacent continuum model. In that approach, a pressure field is determined iteratively at the interface such that flow in/out of every boundary pore of the network model matches the total flow out/in of the continuum region (integrated over an area corresponding to each specific pore). The resulting interface boundary conditions were very complex due to the heterogeneity captured in the porescale models. It was shown that the boundary conditions could be significantly different for two similar realizations (with identical macroscopic properties such as grain diameter, porosity, and permeability) because the pore structure is different. Implementing a simple boundary condition (such as a constant pressure, linear pressure profile, or one obtained by approximating the porescale region as a continuum) was also shown to result in incorrect qualitative and quantitative results.

While this multiscale approach provides a motivation for determining realistic boundary conditions by coupling to adjacent media, it has limited practicality. First, the continuum model in that work was simple and amenable to an analytical solution, so fluxes could be evaluated easily at discrete points corresponding to the boundary pore positions in the adjacent network model. The method would not be applicable for coupling two discrete network models because the boundary pore positions would not match in general. Second, the approach can be very inefficient because it involves solving M simultaneous equations (M being the number of boundary pores). Each sub-domain must be solved M times to generate the Jacobian for the interface problem and it becomes obvious that this is not computationally efficient, especially for nonlinear and transient problems.

In this chapter, a domain decomposition approach using mortars has been developed following [12], to model flow and transport in porous media. This has been implemented in the IPARS academic/research code base. The decomposed sub-domains can model different physics, contain different models, [114, 139] or implement different finite difference or finite element meshes [12, 15, 62, 91]. The sub-domains are solved independently and the interface boundary conditions are determined using mortar spaces. The mortar space is a 2-D, finite element space that is used to project primary variables (e.g. pressure) onto the sub-domain faces. The projected pressure field must be chosen so that the jump in secondary variables (e.g. fluxes) is zero, thus maintaining continuity. Accuracy can be improved by utilizing finer meshes on the mortar space or using higher-order mortars such as linear or quadratic basis functions [15]. Since the sub-domains in the mortar method are solved independently, they can be viewed as “black boxes” and thus could be models at different scales. However, the mortar coupling method has not yet been extended to include porescale models. The method would have some advantages over the method used in [130] for that application in that each element would contain several pores and therefore a significantly fewer number of interface equations would have to be solved. Zhodi and Wriggers [149] did use a novel domain decomposition approach to couple microscale models, but the interface boundary conditions were not chosen rigorously. They modeled mechanics at a continuum scale and then used the solution to impose boundary conditions at the sub-domain interfaces. In [130] some of the limitations of utilizing boundary conditions in this manner is shown.

A number of other methods have been developed to perform multiscale modeling in solid mechanics by coupling atomistic and continuum approaches. Kohloff *et al* [78] modeled mechanics in an atomistic domain surrounded by a continuum finite-element mesh. Boundary conditions at the interface were determined by ensuring consistency in strains in a small overlap region. Broughton *et al* [30] extended the work of Kohloff *et al* using molecular-atomistic-ab initio dynamics (MAAD) by refining the continuum, finite element mesh to the atomic scale in the overlap region. Wagner and Liu [134] have developed a bridging scale technique in which the atomistic and continuum scales completely overlap. More information on these multiscale methods can be found in the review by Rudd and Broughton [121] as well as in an introduction by Klein and Zimmerman [75].

The objective of the current work is to model flow in porous media by coupling porescale network models to other porescale or continuum-scale models using mortars at the interface. The mortars provide a method for determining realistic boundary conditions on predictive porescale models, since they are intended to represent a portion of a much larger porous medium. The outline of the chapter is as follows. Section 6.3 presents the mathematical approach for network modeling. The equations for mortar coupling these porescale models to other porescale or continuum-scale models are derived. Next, Section 6.4 presents numerical results. There, the implementation is validated by coupling two identical, periodic porescale models and comparing this unique case to the actual interface pressure field. Next, different porescale models are coupled together; both qualitative and quantitative results are discussed. Finally, a porescale model is coupled to surrounding continuum-scale models and some interesting results and applications are presented.

6.3 Mathematical model

The equations governing the coupling of porescale and continuum scale are presented in detail in [21] and are repeated here for clarity. A mixed finite element (MFE) formulation is assumed in the continuum sub-domains and a "network" model in the porescale sub-domains. The network model is also referred to as a "ball and stick" model where the balls represent pores and the sticks represent the throats connecting pores. Analogous to the description in Chapter 3, let $\Omega = \cup_{i=1}^{n_b} \Omega_i^{s_i}$ be a domain decomposed into n_b sub-domains (blocks), $\Omega_i^{s_i}$ where $s_i = p$ or c depending on whether the i^{th} sub-domain is governed by a porescale or a continuum-scale model. Further, let Γ_i, Γ_{ij} and Γ denote the block interfaces as in Chapter 3. For the present case, their definitions are given by

$$\Gamma_{ij} \equiv \partial\Omega_i^{s_i} \bigcap \partial\Omega_j^{s_j},\ \Gamma \equiv \bigcup_{1 \le i < j \le n_b} \Gamma_{ij}, \text{ and } \quad \Gamma_i \equiv \partial\Omega_i^{s_i} \bigcap \Gamma = \partial\Omega_i^{s_i} \backslash \partial\Omega.$$

Further, let the finite element approximation spaces be as introduced in Chapter 3. Formally then, the problem is to find a solution $(\mathbf{u}_{h,i}^c, p_{h,i}^c) \in \mathbf{V}_{h,i}(\Omega_i^c) \times W_{h,i}(\Omega_i^c)$, $\{p^p(\mathbf{x}_{i,k}) : \mathbf{x}_{i,k} \in \Omega_k^p\} \in \mathbb{R}^{N_{\Omega_k^p}}$ and $\lambda_H \in M_H(\Gamma)$ such that, for $1 \le i \le N_c$, the following weak form is satisfied:

$$\begin{aligned}
&(\nabla \cdot \mathbf{u}_{h,i}^c, w)_{\Omega_i^c} = (\hat{q}, w)_{\Omega_i^c} && w \in W_{h,i}, && \text{(6.1a)}\\
&(\mathbf{K}^{-1}\mathbf{u}_{h,i}^c, \mathbf{v})_{\Omega_i^c} = (p_{h,i}^c, \nabla \cdot \mathbf{v})_{\Omega_i^c} - \left\langle \lambda_H, \mathbf{v} \cdot \mathbf{n}_i \right\rangle_{\Gamma_i} && && \\
&\qquad\qquad - \left\langle g^c, \mathbf{v} \cdot \mathbf{n} \right\rangle_{\partial\Omega_i^c \backslash \Gamma} && \mathbf{v} \in \mathbf{V}_{h,i} && \text{(6.1b)}
\end{aligned}$$

and for $1 \le k \le N_p$,

$$\begin{aligned}
&\sum_{j=1}^{n_i} q_{ij,k}^p = 0 && 1 \le i \le N_{\Omega_k^p}, && \text{(6.2a)}\\
&q_{ij,k}^p = \gamma_{ij,k}(p_{i,k}^p - p_{j,k}^p), && && \text{(6.2b)}\\
&p_{i,k}^p = \begin{cases} g^p(\mathbf{x}_i), & \mathbf{x}_i \in \partial\Omega_{k,D}^p \\ (\Pi\lambda_H)(\mathbf{x}_i), & \mathbf{x}_i \in \partial\Omega_k^p \cap \Gamma \end{cases} && && \text{(6.2c)}
\end{aligned}$$

with the interface condition

$$\sum_{j=1}^{n} \left\langle \zeta, \mathbf{u}_{h,j}^{s_j} \cdot \mathbf{n}_j \right\rangle_{\Gamma_j} \quad \zeta \in M_H(\Gamma). \tag{6.3}$$

In (6.1)–(6.2), g^c, g^p are the (Dirichlet) boundary conditions on the continuum and porescale boundaries, respectively. More general boundary conditions have been treated in the implementation as will be presented in the subsequent section. The multiplicity of continuum and porescale sub-domains is represented by N_c, N_p, respectively so that $n_b = N_c + N_p$. Next, $N_{\Omega_k^p}$ represents the number of pores in the porescale sub-domain Ω_k^p and n_i is the number of pores neighboring the i^{th} pore in that sub-domain. Finally, $q_{ij,k}^p$ represents the flow through the throat connecting pores i and j in the k^{th} porescale sub-domain while $\gamma_{ij,k}$ denotes the "conductivity" of the same throat (analogous to the conductivity derived from absolute permeability in continuous porous media). The source term for the continuum-scale domains is given by $\hat{q}$. It is assumed that $\gamma_{ij,k}$ is given from measurements or otherwise. In (6.3), s_j can be substituted by p or c (i.e., a porescale or a continuum sub-domain). The symbol Π is the standard L^2-projection operator that maps pressure from the mortar space onto an adjacent sub-domain face (see for e.g., Equation (2.13) in [12]). The vector $\mathbf{n}_j$ is the unit outward normal to Γ_j and $\mathbf{u}_{h,j}^{s_i}$ is the sub-domain flux on the interface(s) associated with the j^{th} sub-domain. This coincides with the usual notion of sub-domain face flux for the continuum sub-domains. For the porescale sub-domains however, it is computed by first defining $\mathcal{T}(\Gamma_k)$, a discretization of the face Γ_k and then defining the flux as

$$\mathbf{u}_{h,k}^p \cdot \mathbf{n}_k|_e \equiv \sum_{i,j} q_{ij,k}^p : \mathbf{x}_{i(j)} \in e, \forall\, e \in \mathcal{T}(\Gamma_k).$$

Thus, $\mathbf{u}_{h,k}^p \cdot \mathbf{n}_k|_e$ is approximated by summing the fluxes across all throats that intersect the face $e \in \mathcal{T}(\Gamma_k)$ as shown in Figure 6.1.

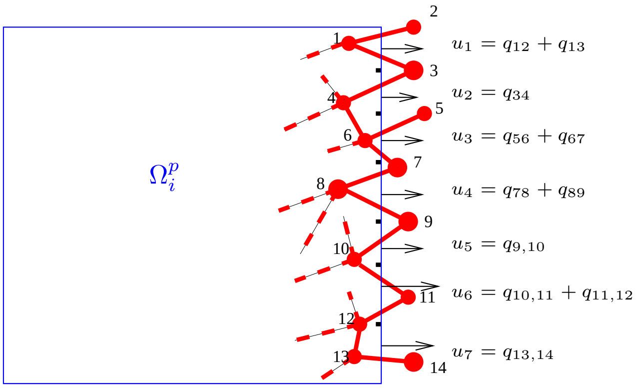

Figure 6.1: Fluxes across porescale sub-domain faces.

It can be shown (see for e.g., [12, 15] for a proof) that the system (6.1)–(6.3) can be reduced to an interface formulation in λ_H just as in Section 3.3.1. The resulting system is much simpler to solve than the scheme described in Section 6.2 due to Balhoff *et al*, since the mesh on the mortar interface can be made as coarse as desirable by using a higher order polynomial function space. Further, this method does not suffer from limitations such as requiring pores on adjacent porescale sub-domains to match up or known analytic solutions for continuum sub-domains. Further it clearly becomes more amenable to solution as the number of sub-domains increases. In the numerical results presented, a Newton-GMRES (inexact Newton) scheme has been applied to solve the resulting interface equation. Proofs of convergence or existence and uniqueness are beyond the scope of the current work and may form the subject of a future work. Numerous computational results are presented to demonstrate the validity of the model.

6.4 Numerical results

In this section, several numerical results are presented to validate the coupling of porescale network models with other porescale network models as well as with continuum models in adjacent sub-domains for the case of single phase Darcy flow. First, a model verification experiment is designed for validating the coupling of different porescale network models to demonstrate the effectiveness of the method. Next, the method is extended by integrating it into the reservoir simulator, IPARS and testing the performance on a number of problems. In this context, an example is presented with porescale network models used to model the flow around a wells and single phase flow elsewhere. In some examples, a variety of porescale network models are placed adjacent to each other (representing different sand-types) to simulate heterogeneity in real reservoirs. Additionally, the effect of boundary conditions on such problems is also examined. Finally, experimental convergence results are presented in the pressure and flux variables.

6.4.1 Model verification experiment

As a first step, a model verification test is designed and solved that compares the "averaged" pore pressure on the mid-section of a single porescale network domain to the phase pressures on the interface when the porescale network is split in two at the mid-section throats and coupled using the method of Section 6.3. Each individual medium has $10,000$ uniform sized spheres with a porosity of 38%, and particle diameter of 0.049 cm. The resulting network has $41,273$ interior pores, 826 and 847 boundary pores on their left and right faces, respectively (these two sets of boundary pores are adjacent at the interface when the network is coupled to its replica) as shown in Figure 6.2 (right). The network has a permeability of approximately 2.4×10^{-6} cm^2. Constant pressure boundary conditions were assigned to each side of the domain, viz., $p = 0.3$ Pa and $p = 0.1$ Pa) as indicated in Figure 6.2. All other faces were assigned no-flow boundary conditions. First, the flow is simulated for the single-domain porescale network model by solving the resulting system of equations from (6.2).

Next the problem is solved as two porescale network domains coupled using (6.1)–(6.3). Since the two domains are identical and have the same macroscopic permeability, a constant interface pressure of 0.2 Pa would seem reasonable. In fact, that boundary condition results in a total flowrate exiting the first sub-domain that matches the flowrate entering the second sub-domain. However, a closer inspection of reveals that this interface boundary condition is not correct and the phase fluxes match poorly at a smaller scale as shown in Figure 6.3. In fact, the pressure on the mid-section of the single-block ("true") case was found to vary from approximately $p = 0.195$ to $p = 0.209$ at the interface (see Figure 6.2, left), which is significant given the total pressure difference specified across the boundary faces. It is apparent that the pressure is significantly higher (on average) in the area of the lower left quadrant. Higher pressures are required because of some relatively low-conducting throats in that region. It is obvious that utilizing an average pressure of $p = 0.2$ would not be able to

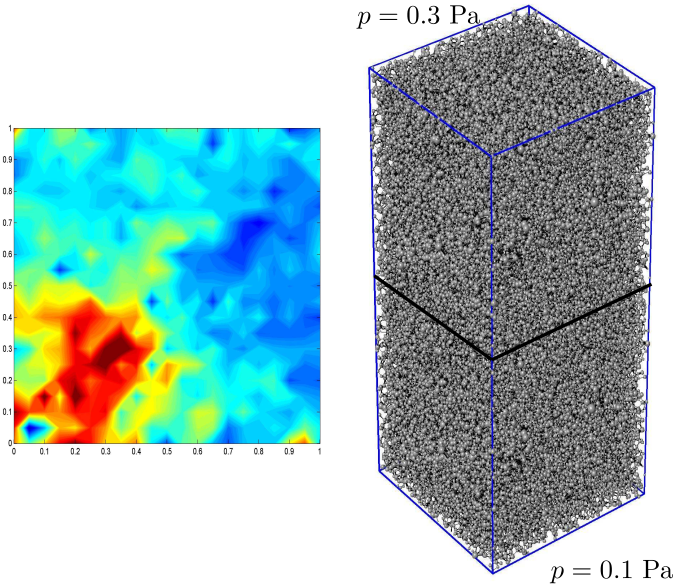

Figure 6.2: A single porescale network model split in two and solved using the mortar method.

correctly capture this behavior and it is not surprising that the simple constant pressure boundary condition results in a poor flux-match.

Next, computations are performed on increasing levels of refinement for constant, continuous linear and continuous quadratic mortar spaces as described in the preceding section. It is observed that the coupled solutions on successively finer scale converge to the "true" solution on the mid-section of the single block. Figure 6.4 shows a series of pressure contours for varying degree of refinements and polynomial types on the mortars and Figure 6.5 shows the pressure contours on the mid-section of the single porescale network model compared with the best mortar-coupled pressure solution.

The flux match obtained after convergence using an 8×8 quadratic mortar space and a 32× 32 sub-domain face grid is demonstrated in Figure 6.6. The fluxes are averaged on an 8×8 grid on the sub-domain faces (as in Figure 6.3

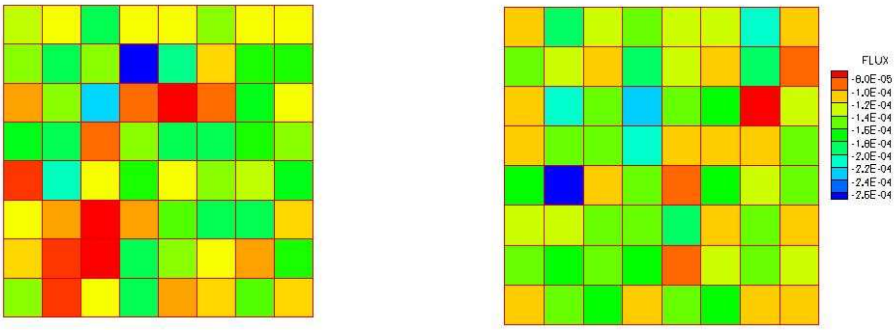

Figure 6.3: Mis-match of fluxes averaged on sub-domain faces using $p = 0.2$ Pa on interface.

Mortar Grids	Constants	Linears	Quadratics
1× 1	1.08×10^{-2}	1.03×10^{-2}	$1.0\ \times10^{-2}$
2× 2	1.03×10^{-2}	1.0×10^{-2}	$9.69\ \times10^{-3}$
4× 4	1.0×10^{-2}	9.69×10^{-3}	$7.7\ \times10^{-3}$
8× 8	9.12×10^{-3}	7.72×10^{-3}	$3.29\ \times10^{-3}$

Table 6.1: Comparison of flux error with mortar h- and p- refinements

for convenience.

Table 6.1 presents a suitable measure of the error in the flux across the interface for various mortar degrees of freedom and polynomial orders as described above. The flux error is determined by calculating the difference between the "true" flux at the interface (which is obtained by projecting the flux on a sufficiently fine discretization K, of the mid-section of the "naturally" coupled single porescale network onto the finest mortar space in each case, i.e., 8 ×8 constants, continuous linears and continuous quadratics) and the corresponding flux obtained using the mortar finite element approach. The resulting error is then normalized by the value of the "true" flux at the interface. Thus, letting $\mathbf{u}$ represent the "true" flux and $\mathbf{u}_h$, the approximate flux obtained by the mortar method, the flux error is given by

$$e_{\mathbf{u}_h} \equiv \frac{\mid \int_\Gamma (\mathbf{u} - \mathbf{u}_h) \cdot \mathbf{n} \mathrm{ds} \mid}{\mid \int_\Gamma \mathbf{u} \cdot \mathbf{n} \mathrm{ds} \mid}$$

Next, a comparison of the normalized errors in the pore-pressure is pre-

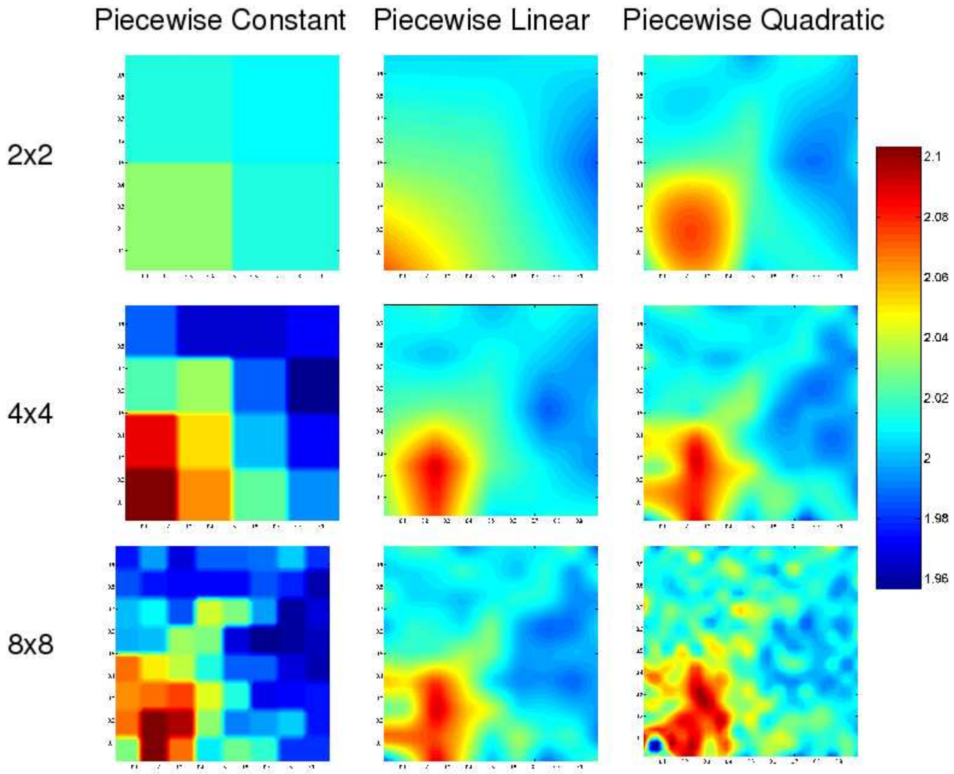

Figure 6.4: Pressure profile on mortar interface between two porescale networks for varying refinement levels and polynomial types.

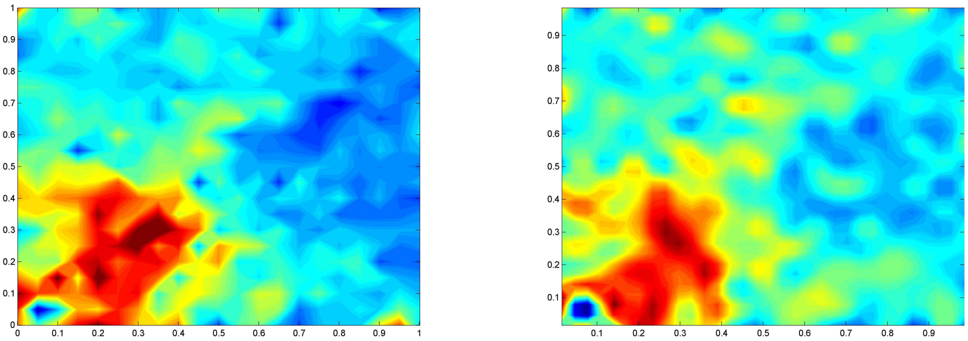

Figure 6.5: Comparison of true and mortar-coupled pressures.

sented in Table 6.2. The normalized error, e_p^k in the k^{th} porescale sub-domain is defined as

$$e_p^k \equiv \frac{\sum_{i=1}^{N_{\Omega_k^p}} |p_i^{\text{act}} - p_i^{\text{mort}}|}{N_{\Omega_k^p} \Delta p},$$

where $N_{\Omega_k^p}$ is the total number of pores, ΔP represents the total pressure drop

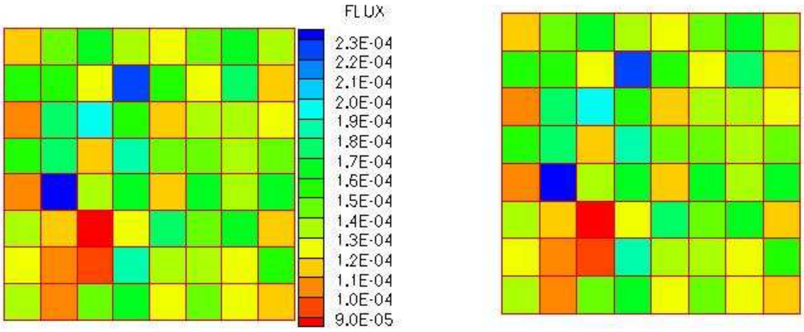

Figure 6.6: Flux match on sub-domain faces using an 8×8 grid quadratic mortar space.

Mortar Grids	Constants	Linears	Quadratics
2× 2	8.35×10^{-3}	7.02×10^{-3}	$5.93\ \times10^{-3}$
4× 4	7.38×10^{-3}	5.81×10^{-3}	$5.51\ \times10^{-3}$
8× 8	6.54×10^{-3}	5.51×10^{-3}	$6.11\ \times10^{-3}$

Table 6.2: Comparison of pressure error with mortar h- and p- refinements

across the faces where the boundary conditions are specified and p_i^{act} , p_i^{mort} are the "true" and mortar pressure solutions respectively. A general trend of decreasing error with mortar mesh size and polynomial degree is observed from the table. But it is important to note that too fine mortar meshes imply very fine sub-domain refinement (for porescale sub-domains this means fine partitions $\mathcal{T}(\Gamma_k)$). Also pore-pressure error may not be the quantity analogous to the pressure variable in continuum models. When the mesh $\mathcal{T}(\Gamma_k)$ becomes so fine that no throats cut across some of the elements, the accuracy of the solution begins to suffer. A remedy to this problem is to use non-uniform sub-domain and mortar meshes.

6.4.2 Coupling different porescale models

Figure 6.7 shows four different porescale models coupled in a 2×2 block pattern. The statistics of the blocks are given in Table 6.3; block 1 is a computer-

Block	Type	# Grains	Pores	Grain dia	Permeability	Dimensions
1	CG	1000	4094	0.053 cm	1.0E-05 cm^2	1×1×1
2	CG	10000	41273	0.025 cm	2.4E-06 cm^2	1×1×1
3	SS	2487	9463	0.020 cm	9.0E-08 cm^2	1×1×1
4	CG	10000	32496	0.014 cm	3.0E-06 cm^2	1×1×1

Table 6.3: Summary of network statistics used in coupling simulations

generated sphere packing with 1000 uniform spheres, block 2 is a computer-generated sphere packing with 10000 uniform spheres, block 3 is a sandstone with 2487 grains taken from the Wall Creek Member of the Cretaceous Frontier Formation, Wyoming, USA [131], and block 4 is a sphere packing with 10000 spheres with a size distribution and a spatial correlation. A one-dimensional pressure gradient is imposed on the porous media by imposing a constant pressure on the lateral boundary faces ($p = 0.3$ and $p = 0.1$ Pa) and no-flow boundaries on the other four boundary faces. The exterior boundary conditions are artificial; but in reality they would be determined from additional coupling to other models. The porescale models are coupled at each interface using mortar spaces with 4×4 grids and quadratic basis functions.

In Table 6.3, network type CG stands for networks built from "computer-generated" porous medium, while SS denotes sandstones obtained from X-ray microtomography (XMT) measurements. Figure 6.8 is a 2-d contour plot of pressure for the 4-block porescale pattern (the 3D data is collapsed into 2D by an averaging method for clarity). The points represent the location of pore centers in the network model and the color scales the pressure in the pores. The white background is the grain space (the figures do not in any way represent the actual porosity and the denser blocks simply have more pores). A few observations can be made from this figure. First, a continuity of pressure is observed along all of the mortar boundaries, enforced in the interface formulation of the mortar method. Second, the results show heterogeneity in the pressure field which would not be observed if continuum models were used.

The total flow through the domain in Figure 6.8 can be calculated as 2.26×10^{-}3 cm3/s. The results can be compared to a continuum simulation

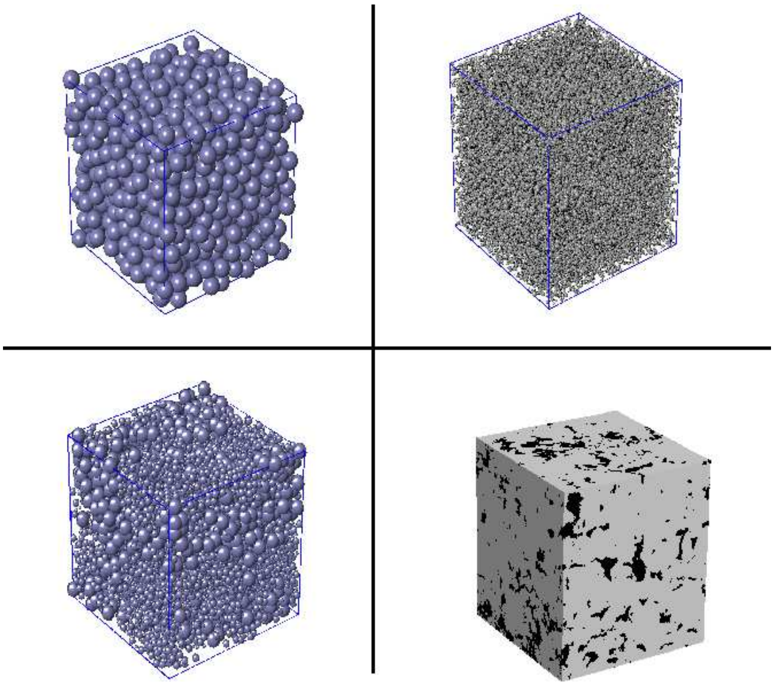

Figure 6.7: Schematic of coupling different porescale network models in a 2×2 block pattern.

by using the upscaled permeabilities for each model listed in Table 3. The resulting flowrate is 1.35×10−3 cm3/s, which underestimates the actual flowrate by approximately 40%. Further, Figure 6.9 shows the pressure field for the same four porescale models arranged in a different pattern (from Table 6.3, network #3 is placed in the lower-left block, network #2 placed in the lower-right block, network #4 placed in the the upper-right block, and network #1 placed in the upper-left block). In this second simulation, the flowrate using the porescale models is 1.31×10^{-3} cm^3/s. For this case, the continuum simulation resulted in a 40% overestimation (1.88×10^{-3} cm^3/s). The examples demonstrate the limitations of upscaling macroscopic properties directly by using the porescale models as stand-alone tools. Direct upscaling can severely under or overestimate behavior when coupled to surrounding media.

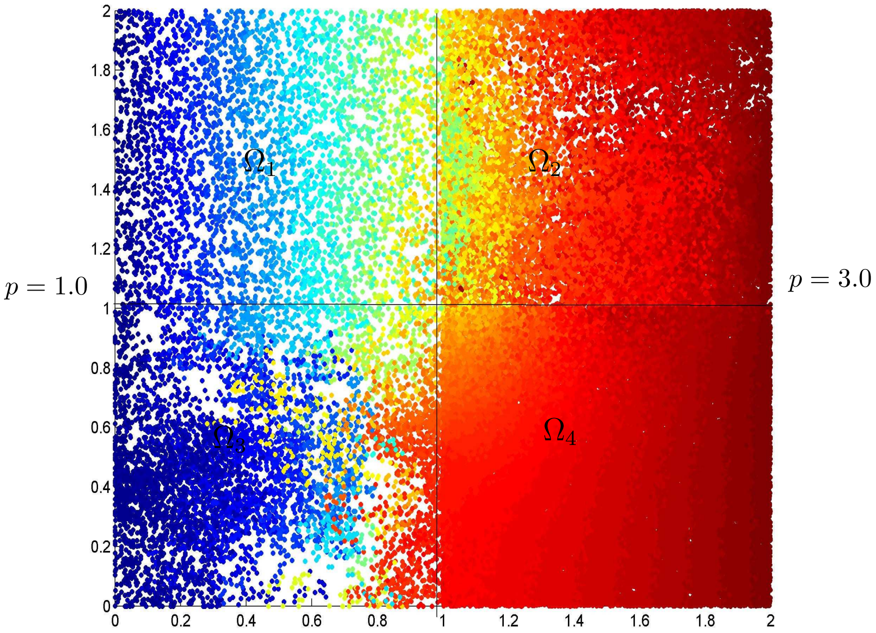

Figure 6.8: Contour plot of pressure when 4 different porescale networks are coupled using mortar spaces.

6.4.3 Coupling porescale with continuum models

The mortar method presented here is not limited to coupling only porescale models to each other. It can be easily extended to couple porescale models to continuum-scale, Darcy models. This application of the mortars is very useful for multiscale modeling, in which the domain is primarily modeled at the continuum scale, but specific regions are modeled at the porescale to capture important fundamental behavior. The porescale network model #3 of Table 6.3 is coupled to surrounding continuum models. The continuum models used here employ a 4×4×4 grid in each block and utilizing Darcy's law. All three blocks are given a uniform permeability, equal to the upscaled values for network model #3 shown in Table 6.3. A 1-d pressure gradient is imposed from right to left for this "simple" problem. The four blocks are coupled using 1×1 quadratic mortars at the interfaces to ensure continuity of pressures and fluxes. It is to be noted that the axis is rotated in this simulation so that the flow is actually

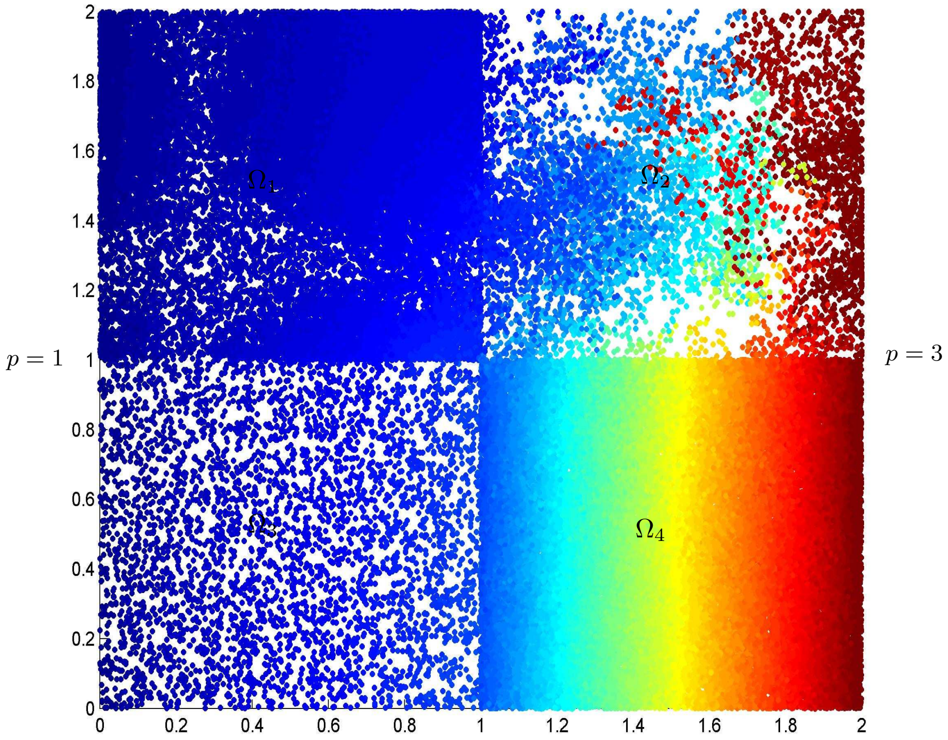

Figure 6.9: Contour plot of pressure when 4 different porescale networks are coupled using mortar spaces - case 2.

in the y-direction.

Figure 6.10 is the contour plot of pressure in the domain for the continuum and porescale regions and it is clear that pressure is continuous at the interfaces. If the entire domain had been modeled at the continuum scale (with the permeability also being uniform in the current porescale region), then the solution would have been trivial. The pressure would increase linearly from left to right and the streamlines would be straight. In the simulation here, the heterogeneity in the porescale region results in a more complicated solution, not only in the porescale region, but the continuum region as well where the permeability is uniform. In Figure 6.10, it can be seen that velocity has a vertical component even in the continuum region as a result of the non-uniform boundary conditions resulting from the coupling to the porescale region.

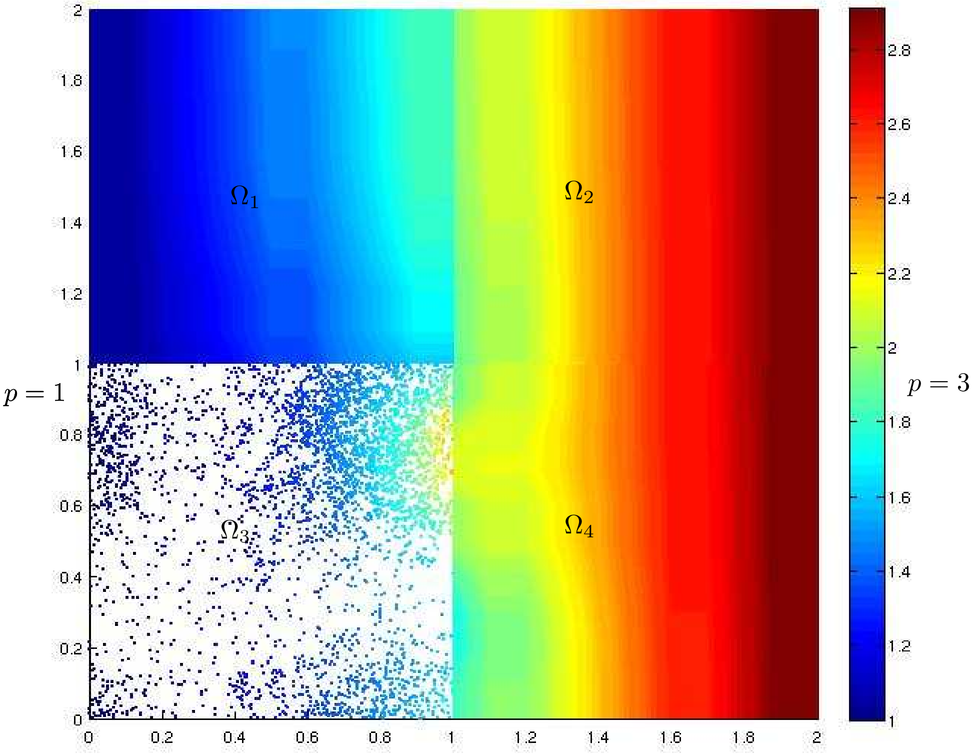

Figure 6.10: Contour plot of pressure when one porescale network is coupled to 3 continuum-scale models using mortar spaces.

The total flow through the domain is 7.90×10^{-5} cm^3 which is about 15% higher than the flowrate (6.76×10^{-5} cm^3/s) obtained from utilizing Darcy's law and the uniform permeability of $K_{yy} = 1.015 \times 10^{-7}$ cm^2. Moreover, the flow exiting the porescale region (block #3 of Figure 6.10) is 50% higher than the continuum block (#1) directly above it. Although the average, upscaled permeability in the porescale region is the same as the other blocks, the natural heterogeneity allows for preferential pathways for flow and the model acts as a "sink" for fluid to enter from the surrounding blocks. The pressure field in Figure shows the contour lines bend to allow for flow to enter the porescale region. This is another demonstration of the limitations of simple upscaling without imposing realistic boundary conditions on the network model.

6.4.4 Well modeling example

Finally, the solution to a harder problem is presented in Figure 6.11, which simulates the flow around a well (assumed square in computations). The figure shows a near well-bore steady state solution profile. The eight blocks immediately surrounding the central well-bore (the square hole in the figure) are porescale networks that were formed using three different kinds of sands with varying degrees of heterogeneity and grain sizes (and consequently permeability). These were arranged so that sands of a given grain size were placed next to each other. It is noted that the voids in the porescale sub-domains denotes the rock matrix and so clearly, the three porescale networks in the upper-right quadrant of the well-bore is less permeable, while that in the rest of the quadrants is more permeable. Around the porescale "ring" are larger continuum blocks that are modeled using mixed finite elements for single phase steady flow.

A total of 12 blocks are present in the domain decomposition for the computation in Figure 6.11. The boundary conditions are Dirichlet (pressure specified wells and a constant pressure on the external domain boundaries). It is interesting to note that the flow is preferential as indicated by the non-symmetric location of the light blue shade (the "halo") around the porescale sub-domains. This is because porescale networks with different grain sizes were used and arranged so as to induce such a behavior, as a test that verifies that the solution agrees with intuition. A similar example run with just one network used for all eight porescale sub-domains exhibited almost perfect symmetry, barring small heterogeneities. The solution for that problem is not presented here. Finally, it is remarked that similar computations were performed with no-flow boundary conditions specified on some of the external domain boundaries and pressure on the others. The solutions to all such problems agreed completely with those expected from intuition.

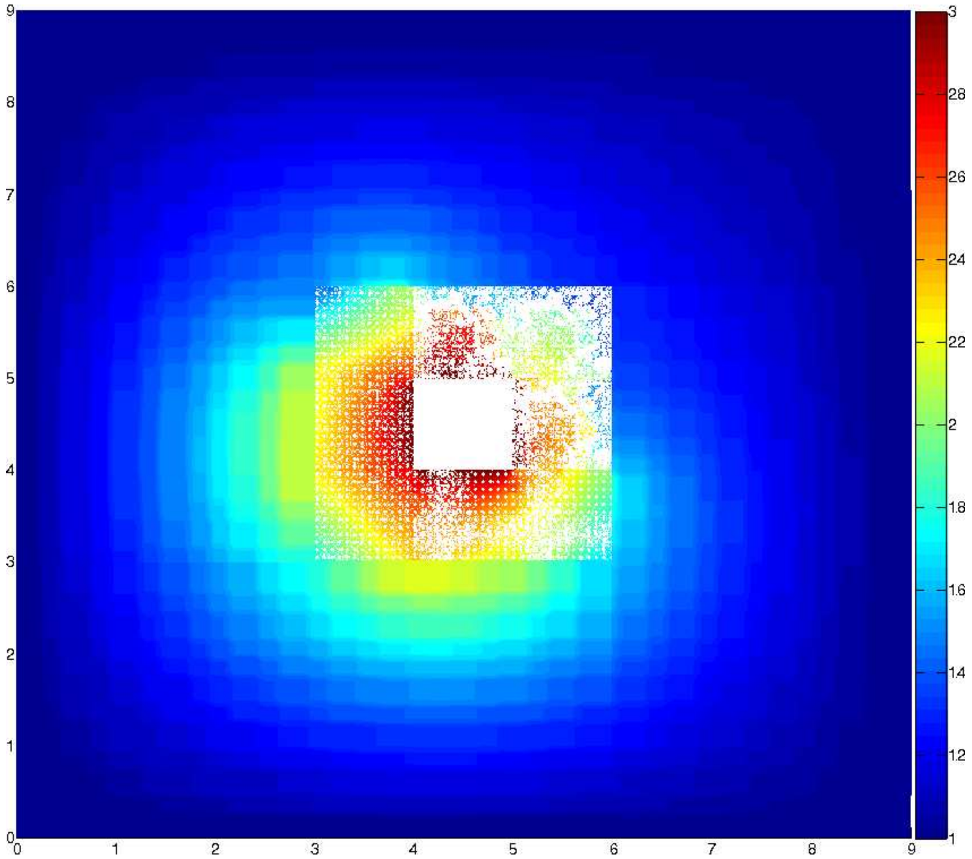

Figure 6.11: Steady-state pressure profile immediately around a well-bore

Chapter 7

An iteratively coupled non-isothermal pressure concentration formulation (IMPEC) with geochemistry

Most real-world applications in sub-surface flow are rarely confined to single- or two-phase regimes. For example, the production of oil is a multicomponent, multiphase flow problem where several hydro-carbon components can exist in the non-aqueous liquid ("oleic") or vapor (gas) phases. The non-aqueous phase properties can then be regarded as a mole-fraction weighted function of the component properties. The component properties themselves are typically characterized by an equation of state (EOS) for the molar specific volumes as a function of the pressure and temperature, while viscosities are given by a separate constitutive equation. In addition, components can enter into chemical reactions with the aqueous phase or with the minerals in the surrounding rock-matrix. Infact, such reactions with rock minerals can affect the geomechanical properties of the rock matrix as well as properties such as porosity and permeability which in turn alters the flow and transport behavior. Further the rates of these reactions are a function of the local reservoir temperature. Thus, it is clear that there is a complex interplay between multiphase flow, transport, chemistry and thermal effects in such problems.

This chapter describes an efficient and parallel numerical scheme for non-isothermal multiphase compositional flow coupled to geochemical reactions. The underlying theory is first presented followed by a brief description of the equation of state (EOS) and the two-phase flash implementation. An "implicit-pressure, explicit-concentrations"(IMPEC) algorithm is then applied iteratively to enforce a non-linear volume balance (saturation) constraint. The pressure system is solved using a mixed FEM discretization in space and a backward-Euler discretization in time, while the concentrations are updated explicitly in a manner that preserves local mass balance of every component. A major application of this scheme is in the modeling of field scale CO_2 sequestration, as an enhanced oil recovery (EOR) process or for storage in deep saline aquifers as mentioned in Section 1.2.

Thermal energy transfer also plays an important role in such problems since it can effect the phase properties and component reaction rates significantly. Hence, accurate and locally conservative methods are desirable to model the thermal effects. To this end, a time-split scheme for modeling thermal energy transfer is presented, which is sequentially coupled to the flow model. As with the transport model presented in Section 3.5, thermal advection is solved using a higher-order Godunov method while thermal conduction is solved using a backward-Euler in-time, mixed FEM scheme. Following this, a chemical reaction model is also sequentially coupled to the flow-thermal steps to update the molar concentrations of components entering into chemical reactions. Finally, some numerical results are presented for challenging benchmark problems.

7.1 Compositional flow model

The notation employed in this section is mostly consistent with that used in earlier chapters (for example Chapter 2). But for convenience, terms are redefined here as they are used in a more general multiphase, multicomponent flow formulation. Let i and α represent component and phase indices respectively. In the IPARS simulator $i = 1$ refers to the water component. Component mass balances for n_c components, $i = 1, \ldots n_c$ are then given by the system of partial differential equations

$$\frac{\partial(\phi N_i)}{\partial t} + \nabla \cdot (\sum_{\alpha} \mathbf{J}_i^{\alpha}) = q_i. \tag{7.1}$$

In (7.1), ϕ denotes the medium porosity while N_i and q_i represent the molar concentration and injection (production) rates at sources (sinks) of component i, respectively. $\mathbf{J}_i^{\alpha}$ is the “net mass velocity” of component i in phase α given by

$$\mathbf{J}_i^\alpha = \rho_\alpha \xi_i^\alpha \mathbf{u}_\alpha - \phi \rho_\alpha S_\alpha \mathbf{D}_i^\alpha \nabla \xi_i^\alpha. \tag{7.2}$$

The definition of the diffusion-dispersion tensor, $\mathbf{D}_i^\alpha$ can be found in [36]. Since, the current implementation assumes a diagonal tensor, only molecular diffusion is considered in this context. This renders $\mathbf{D}_i^\alpha$ a diagonal tensor. In (7.2), ρ_α, S_α and $\mathbf{u}_\alpha$ represent the density, saturation and velocity, respectively of phase α and ξ_i^α is the mole fraction of component i in phase α. The velocity $\mathbf{u}_\alpha$ is given by the well known Darcy's constitutive law

$$\mathbf{u}_\alpha = -\frac{\kappa_{r\alpha}}{\mu_\alpha} \mathbf{K}(\nabla p_\alpha - \rho_\alpha \mathbf{g}). \tag{7.3}$$

The phase pressures p_α may be eliminated in terms of a "reference" phase pressure p (usually assumed to be the non-aqueous liquid, i.e., the oleic phase pressure) by the capillary pressure relations which is assumed to be a known function of phase saturations, given by equations

$$p_\alpha = p + p_{c\alpha}(S_\alpha). \tag{7.4}$$

In (7.4), α runs through all phase indices except that of the reference phase. Also, in the expression of Darcy velocity, (7.3), $\mathbf{K}$ is the absolute permeability of the medium and μ_α and $\kappa_{r\alpha}$ denote the α-phase viscosity and relative permeability, respectively. It is assumed that $\kappa_{r\alpha}$ is a function of the phase saturations, $\{S_\alpha\}$ given, for example, by Stone's model of 3-phase relative peremeability curves derived from 2-phase relative permeability curves (see for example, [89]). The reference phase pressure is used in the flash, well and geomechanical calculations. After linearization, the porosity may be expressed as

$$\phi = \phi_0\{1 + c_r(p - p_0)\}, \tag{7.5}$$

where c_r is the (constant) rock compressibility factor and ϕ_0 is the porosity at the prescribed standard pressure, p_0.

In what follows, pure component properties are expressed in terms of state variables p and T and their mole-fractions ξ_i^α determined using thermodynamic equations for phase equilibrium (also termed the "fugacity or flash" equations) which in turn yield phase properties from appropriate mixing rules. Phase saturations are expressed in terms of the state variables $[p, \mathbf{N}, \{\xi_i^\alpha\}, T]^T$ (detailed in Section 7.1.1). Then it remains to decouple the system and solve for the reference phase pressure p, the component molar concentrations N_i, phase compositions $\{\xi_i^\alpha\}$ and the reservoir temperature T. To this end, an Arrhenius exponential temperature correlation of the form $\mu_w = \mu_{w,\text{ref}} \exp b_w(\frac{1}{T} - \frac{1}{T_{\text{ref}}})$ is assumed to describe the water phase viscosities μ_w where $\mu_{w,\text{ref}}$ is the reference viscosity of water prescribed at T_{ref} and b_w is a constant.

Similarly, the non-aqueous phase viscosities μ_α in (7.3) are calculated using a Lohrenz-Bray-Clark correlation (see for example, [40]). In this method, at low pressures, component viscosities are estimated using a Stiel and Thodos correlation in the form, $\mu_i^{\text{low}} = \frac{\beta_i}{\lambda_i}$, where β_i is a function of $T_{i,r}$ and λ_i is a function of $T_{i,\text{cr}}$ and $p_{i,\text{cr}}$. At higher pressures, a slightly different correlation is used to obtain μ_i^{high}. Using the component values and an appropriate mixing rule, phase viscosities are calculated. The terms $T_{i,\text{cr}}, p_{i,\text{cr}}$ and $T_{i,r}$ are explained in more detail in Section 7.1.1. Non-aqueous phase molar specific volumes, i.e., $\nu_\alpha \equiv 1/\rho_\alpha$, are given by the gas law

$$\nu_\alpha = \frac{RTZ_\alpha}{p_\alpha} \tag{7.6}$$

where R is the Universal gas constant and Z_α is the "Z-factor" (also called "compressibility factor") of phase α, obtained by solving the equation of state. The aqueous phase, molar specific volume is given by

$$\nu_w = \frac{\nu_w^0 B_w^0}{1 + c_w(p_w - p^0)} \tag{7.7}$$

where c_w is the water phase compressibility and p_w^0 is the standard water phase pressure (usually, one atmosphere) at which the values ν_w^0, B_w^0 of the molar specific volume and the "formation volume factor", respectively, are prescribed. The phase saturations are then expressed in terms of the state variables, viz., $[p, \mathbf{N}, \{\xi_i^\alpha\}, T]^T$ by the equations,

$$S_w = \nu_w N_w,\ S_l = (1 - v)\nu_l \sum_{i=2}^{n_c} N_i,\ S_g = v\nu_g \sum_{i=2}^{n_c} N_i \tag{7.8}$$

where v is the vapor fraction and the subscripts w, l and g stand for the aqueous, oleic and gaseous phases, respectively. The saturations calculated in (7.8) will not, in general, sum to unity due to the decoupling of the pressure-component equations and therefore the iterative IMPEC method needs an additional constraint,

$$S_T \equiv \sum_{\alpha} S_\alpha = 1. \tag{7.9}$$

S_T denotes the total saturation in (7.9) (the volume balance criterion) which forms the convergence condition for the iterative IMPEC method.

7.1.1 EOS and Flash implementation

The IPARS simulator uses the Peng-Robinson EOS [112] to determine the non-aqueous molar specific volumes of (7.6) in terms of the "Z-factors" which are functions of p and T. It can be shown [33] that this reduces to solving a cubic equation for $\bar{Z}_\alpha$, which includes a volumetric shift parameter C_α so that, $Z_\alpha = \bar{Z}_\alpha - C_\alpha$. The cubic EOS for phase α then takes the form

$$\bar{Z}_\alpha^3 + h_1(B_\alpha)\bar{Z}_\alpha^2 + h_2(A_\alpha, B_\alpha)\bar{Z}_\alpha + h_3(A_\alpha, B_\alpha) = 0. \tag{7.10}$$

The parameters A_α, B_α appearing in the coefficients h_j of the cubic Eqquation of state (7.10), and the volumetric shift, C_α, in the definition of $\bar{Z}_\alpha$ are functions of the component "reduced" pressures and temperatures, $\{p_{i,r}\}$ and $\{T_{i,r}\}$, where $p_{i,r} = p_i/p_{i,\mathrm{cr}}, T_{i,r} = T/T_{i,\mathrm{cr}}$. They are also functions of the composition of that phase (via an appropriate mixing rule involving component mole fractions $\{\xi_i^\alpha\}$). It is noted that p_i is the partial pressure of the component i in the phase α given by Dalton's law of partial pressures and $p_{i,\mathrm{cr}}, T_{i,\mathrm{cr}}$ represent the component critical pressures and temperatures which are thermodynamic properties unique to every chemical component. For a detailed discussion on these and related thermodynamic concepts, the interested reader is referred to [33]. The Newton-Raphson method for non-linear equations is used to solve (7.10) until the change in $\bar{Z}_\alpha$ is less than a prescribled tolerance. When multiple real roots exits, the root resulting in lowest Gibbs free energy is taken.

The component mole fractions, $\{\xi_i^\alpha\}$ in non-aqueous phases are determined by solving the "flash" equations, which are a set of thermodynamic equilibrium equations. To this end, some auxiliary variables are required in the calculation. Vapor fractions, denoted v, (i.e., the fraction of total non-aqueous moles in the gas phase) are determined using the Rachford-Rice equation. It is given by

$$\mathcal{R}_v \equiv \sum_i \frac{(K_i - 1)z_i}{1 + (K_i - 1)v} = 0. \tag{7.11}$$

In (7.11), z_i is the total non-aqueous mole fraction of component i and K_i is defined in (7.12). The fluid is a single-phase liquid when $v = 0$ and is a single-phase vapor when $v = 1$. Once v is determined using (7.11), the component mole fractions in the liquid and vapor phases are calculated from

$$\xi_i^l = \frac{z_i}{1 + (K_i - 1)v}, \quad \xi_i^g = K_i \xi_i^l. \tag{7.12}$$

For any given state, the equibrium phase composition $\{\xi_i^\alpha\}$ is determined using the "flash" algorithm. From thermodynamic principles, phase equilibrium at constant pressure and temperature requires that component fugacities in each of the non-aqueous phases be equal, i.e., for $i = 2, \ldots, n_c$,

$$f_i^g = f_i^l. \tag{7.13}$$

Instead of solving (7.13) for component fugacities, the simulator solves for $\ln(K_i)$, working with fugacity coefficients, $\Phi_i^\alpha \equiv \frac{f_i^\alpha}{\xi_i^\alpha p}$ instead of fugacities. This modifies (7.13) to

$$R_i \equiv \ln(\Phi_i^l) - \ln(\Phi_i^g) - \ln(K_i) = 0. \tag{7.14}$$

The $\ln(\Phi_i^\alpha)$ term in (7.14) is a function of Z_α, $\{\xi_i^\alpha\}$ and p_α for the case of the Peng-Robinson EOS. The flash algorithm then applies the Newton-Raphson method to find the root of (7.14). The basic steps of the flash algorithm are summarized below. For additional details, the reader is referred to [33, 40, 50, 97].

1. $p_\alpha(p), T$ and z_i are assumed known at the start of the time step and remain constant during the flash calculation. A starting value of K_i is assumed given. The Rachford-Rice equation (7.11) is then solved for vapor fraction, v.

2. Next, component mole fractions, $\{\xi_i^\alpha\}$, in non-aqueous phases are determined using (7.12). Note that $\xi_w^l = \xi_w^g \equiv 0$ and $\xi_w^w \equiv 1$ are not of interest here, since water is treated as a separate phase and is not involved in the flash calculations.

3. The cubic Peng-Robinson EOS (7.10) is then solved to obtain the phase Z-factors, Z_α. Then using the p_α given and the Z_α and $\{\xi_i^\alpha\}$ just obtained, the logarithm of the fugacity coefficients $\ln(\Phi_i^\alpha)$ are calculated from their functional form $\ln \Phi_i^\alpha \equiv f(Z_\alpha, \{\xi_i^\alpha\}, p_\alpha)$.

4. Equation (7.14) is checked for convergence and expanded in terms of $\delta[\ln(K_i)]$ to get an update for $\ln(K_i)$. The flash algorithm stops here if converged (or in case the trivial solution is encountered, i.e., when for all i, $K_i \equiv 1$ within a tolerance); otherwise it continues from step 1.

7.1.2 Iterative IMPEC method

As indicated by (7.8), phase saturations are functions of the state variables $[p, \mathbf{N}, T, \{\xi_i^\alpha\}]^T$. The volume balance condition at the $(k+1)^{\text{th}}$ iteration of the n^{th} time step is written as

$$S_T^{k+1} \equiv \sum_\alpha S_\alpha{}^{k+1} = 1. \tag{7.15}$$

Expanding S_T^{k+1} in a Taylor series about S_T^k upto the first order terms, yields the approximation

$$\frac{\partial S_T}{\partial p}\delta p + \sum_{i=1}^{n_c} \frac{\partial S_T}{\partial N_i}\delta N_i + \sum_{i=2}^{n_c} \frac{\partial S_T}{\partial(\ln K_i)}\delta(\ln K_i) = 1 - S_T^k. \tag{7.16}$$

It can be shown that the fugacity equations (7.13) can be expanded in terms of $\delta p, \delta N_i$ and $\delta(\ln K_i)$ and this expansion may be rearranged to express

$\delta(\ln K_i)$ in terms of δp and δN_i. This expression is then substituted in (7.16) resulting in an equation in terms of δp and δN_i. Finally, the component mass balance (7.1) is then expanded to express δN_i in terms of δp which results in a single system in cell pressure changes of the form

$$\mathbf{A}\delta p = \mathbf{b} \tag{7.17}$$

which is the linear pressure system and can be solved using any standard linear solver.

After the pressure is updated, the change in porosity is calculated using (7.5) and the component accumulation term (denoted $\mathcal{A}_i$) in the mass balance (7.1)) is calculated from

$$\mathcal{A}_i^{k+1} = \frac{\phi N_i^k + N_i^k \delta\phi + \phi^k \delta N_i - \phi^n N_i^n}{\Delta t}. \tag{7.18}$$

In (7.18), δN_i has been expressed in terms of δp using the mass balance (2.4). Then the $(k+1)^{\text{th}}$ iteration concentrations are obtained using the equation

$$N_i^{k+1} = \frac{\Delta t \mathcal{A}_i^{k+1} + \phi^n N_i^n}{\phi^{k+1}}. \tag{7.19}$$

Naturally, component material balance errors arise due to the product of N_i^{k+1} and ϕ^{k+1}. These are avoided by the correction in (7.19). The explicit-in-time concentration update of (7.19) can cause the IMPEC calculations to become unstable if time steps become too large. To limit time step sizes, the simulator currently uses a saturation-type control to limit time step sizes for the iterative IMPEC implementation. For a given component, saturation change is defined as

$$(\Delta S_T)_i = \frac{\partial S_T}{\partial N_i} \Delta N_i. \tag{7.20}$$

where ΔN_i is the change in concentration of the i^{th} component. The simulator then requires that $\mid (\Delta S_T)_i \mid \leq \Delta S_{\max}$ for all components i during a timestep where $\Delta S_{\max}$ is a user specified input.

After the $(k+1)^{\text{th}}$ level iteration solution for p and N_i are available, the simulator returns to check if the volume balance (convergence) condition given in (7.15) is satisfied. If not, it repeats the process described between(7.16) and (7.19) until (7.15) holds upto a tolerance or until a maximum number of iterations is exceeded. At each iteration the solution from the most recently available iteration (or previous time step in the case $k = 1$) is used. For additional details on the compositional model, the interested reader is referred to Appendix B.

7.2 Thermal energy balance model

The IPARS compositional model implements a "weak" or "sequential" coupling between the flow and thermal steps. For many real-world subsurface applications, especially the CO_2 sequestration processes mentioned in the introduction, this is justifiable since the temperature changes encountered are typically relatively small. In this section, the equations governing thermal energy transfer and the time-split solution scheme to solve them are presented. Thermal energy balance is described by the PDE

$$\frac{\partial U_T T}{\partial t} + \nabla \cdot (\sum_\alpha \rho_\alpha C_{p\alpha} T \mathbf{u}_\alpha - \lambda \nabla T) = q_H \tag{7.21}$$

in the unknown reservoir temperature T. Note that an instantaneous thermal equilibrium assumption is made so that the only unknown is T, the reservoir temperature field. This is justifiable for many of the applications in sub-surface flow where temperature changes are much slower than the rate of thermal energy transfer between fluids and the rock matrix. But it probably does not hold locally for cases such as high rates of injection of super-heated steam in the regions immediately surrounding the injection well-bores. Here U_T is the "effective isochoric specific heat capacity" (in thermodynamics, this is nothing but $\partial U/\partial T$). It is given by

$$U_T = (1 - \phi)\rho_s C_{vs} + \phi \sum_\alpha \rho_\alpha S_\alpha C_{v\alpha}. \tag{7.22}$$

In (7.21)–(7.22), $C_{p\alpha}$ and $C_{v\alpha}$ are the isobaric and isochoric molar specific heat capacities of the phase α computed from their respective component counterparts using an appropriate mixing rule. The effective reservoir thermal conductivity is denoted by λ and q_H is the "heat source/sink per unit volume" given by

$$q_H = \sum_{\alpha} C_{p\alpha} q_\alpha T_{\text{src}} \tag{7.23}$$

where q_α is the injection or production flow rates of the phase α per unit volume, once again calculated from their component counterparts, q_i in (2.4)) and the component mole fractions. It is noted that T_{src} is the temperature of the injected fluid T_{inj} at source points and equals the resident temperature T at the sink points. The subscript s in (7.22) represents the rock phase.

7.2.1 Time-Split Scheme

The time-split scheme used to solve for the reservoir temperature T is completely analogous to the time-split scheme for component molar concentrations presented in Section 3.5.1 but is presented here very briefly for completeness. Let $t^{m+1} \in [t^n, t^{n+1}]$ be the time at which the thermal step is solved. In general, the simulator allows for multiple thermal steps nested within a flow step. As in Section 3.5.1, the basic idea of the *time-split* scheme is to successively account for (by accumulation) the advection and diffusion (or thermal conduction, in this case) in time. Hence, it can be regarded as an operator-splitting method. For theoretical details of the method, the interested reader is referred to [49, 113]. Accordingly, the thermal energy balance (7.21) is split into a thermal advection and a thermal conduction step. The advection step is given by the equation

$$\frac{\partial (U_T T)}{\partial t} + \nabla \cdot \left(\sum_{\alpha} \rho_\alpha C_{p\alpha} T \mathbf{u}_\alpha\right) = q_H. \tag{7.24}$$

A higher order Godunov method has been implemented using element slopes of the scalar variables in the advection term and carefully chosen slope limiters [44, 59, 85]. The first order scheme is presented here. For an overview of the higher-order method, see Section 3.5.2. Let E be any element of the finite element mesh and $H_E^m \equiv \int_E U_T^m T^m \, dx$ be the local thermal energy content in E

at time step m of the thermal algorithm. Integration over E of (7.24) against the characteristic function on E, gives the weak form of the advection step,

$$\frac{\bar{H} - H_E^m}{\Delta t^m} + \int_E \sum_\alpha \bar{\mathbf{u}}_\alpha \cdot \mathbf{n} \mathrm{ds} = \int_E q_H^{m+1/2} \mathrm{dx}. \tag{7.25}$$

In (7.25), $\Delta t^m = t^{m+1} - t^m$, $\mathbf{n}$ is the unit outward normal to element E and $\bar{H}$ denotes the intermediate value of the local thermal energy content H_E^{m+1} (which is sought to obtain T_E^{m+1}) from the contribution due to advection only and becomes the initial condition for the conduction step. Further, the quantity $\bar{\mathbf{u}}_\alpha = (C_{p\alpha}T)^{m,\mathrm{upw}}(\rho_\alpha^{\mathrm{upw}}\mathbf{u}_\alpha)^{m+1/2}$, where $(C_{p\alpha}T)^{m,\mathrm{upw}}$ represents the upwinded value of $(C_{p\alpha}T)^m$ based on the sign of $\mathbf{u}_\alpha^{m+1/2} \cdot \mathbf{n}$. Similarly, $\rho_\alpha^{m+1/2,\mathrm{upw}}$ denotes the upwinded value of $\rho_\alpha^{m+1/2}$ based on the sign of $\mathbf{u}_\alpha^{m+1/2} \cdot \mathbf{n}$. It is noted that the values of ρ_α and $\mathbf{u}_\alpha$ are known at flow time steps t^n and t^{n+1}. Thus, $(\rho_\alpha \mathbf{u}_\alpha)^{m+1/2}$ is the linear interpolant computed at $t^{m+1/2}$.

Once $\bar{H}$ is determined, the conduction step is solved, given by

$$\frac{\partial(U_T T)}{\partial t} - \nabla \cdot (\lambda \nabla T) = 0. \tag{7.26}$$

In the weak form, upon integration by the characteristic function on E, this becomes

$$\frac{H_E^{m+1} - \bar{H}}{\Delta t^m} - \int_E \nabla \cdot (\lambda \nabla T^{m+1}) = 0. \tag{7.27}$$

Eq. (7.27) is solved using the backward-Euler and mixed finite element methods for time and space discretizations respectively. The lowest order RT_0 approximation space in conjunction with the trapezoidal quadrature rule for the flux term $\lambda \nabla T^{m+1}$ reduces it to a cell-centered finite difference approximation [122]. The accumulation term H^{m+1} is linearized about the current value of temperature.

7.3 Chemistry model

After the flow and thermal steps are completed, the chemical reactions are performed. For this purpose the chemistry component from a separate transport chemistry model (TRCHEM) [113] in IPARS was coupled to the thermal-compositional model. At present the simulator can only treat chemical reactions occuring in the aqueous phase which are the most commonly occurring reactions in sub-surface flow applications. First the ordinary differential equations governing chemical reactions are presented. Different types of chemical reactions can be modelled and are briefly described in this section.

Let c_i^α represent the concentration of species i in phase α, where $c_i^\alpha = \xi_i^\alpha \rho_\alpha S_\alpha$. It is noted that c_i^α is related to the total concentration N_i by $N_i = \sum_\alpha c_i^\alpha$. For the chemistry part, α is assumed to be the index corresponding to water phase since only aqueous chemical reactions are considered. Then let $\mathbf{c} \equiv \{c_{iw}\}_{i=1}^{n_c}$ denote the vector of species concentrations in the aqueous phase. Next suppose that the vector of reaction rates is denoted by $\mathbf{r}(\mathbf{c})$ then, the system of non-linear ODEs governing chemical reaction is given by

$$\frac{\mathrm{d}\mathbf{c}}{\mathrm{d}t} = \mathbf{r}(\mathbf{c}). \tag{7.28}$$

Multiple chemical reaction time steps are allowed in the simulator and are also assumed nested within the flow time step. The time step is adjusted when rates of reactions become very large for stability of the solution. Let $\Delta\tau^l \equiv t^{l+1} - t^l$ be the time step of the chemical reaction where $t^l, t^{l+1} \in [t^n, t^{n+1}]$. A higher order explicit Runge-Kutta (RK) method of numerical integration is used to solve the system (7.28). The simulator has second and fourth order explicit RK methods currently available. For example, using the second order method (RK2) the formula to update the concentrations of species $i = 1, \ldots, n_c$ from the value $\mathbf{c}$ before the chemistry to $\hat{\mathbf{c}}$ after the chemistry step is given by

$$\begin{aligned} \mathbf{k}_{1,i} &= \Delta\tau^l \mathbf{r}_i(\mathbf{c}) \\ \mathbf{k}_{2,i} &= \Delta\tau^l \mathbf{r}_i\left(\mathbf{c} + \frac{1}{2}\mathbf{k}_1\right) \\ \hat{\mathbf{c}} &= \mathbf{c} + \mathbf{k}_2. \end{aligned} \tag{7.29}$$

The types of chemical reactions that can be handled by the simulator have already been discussed in Section 3.5.3 and will not be repeated here.

The coupled flow-thermal-chemistry algorithm is depicted in the flow chart shown in Figure 7.1.

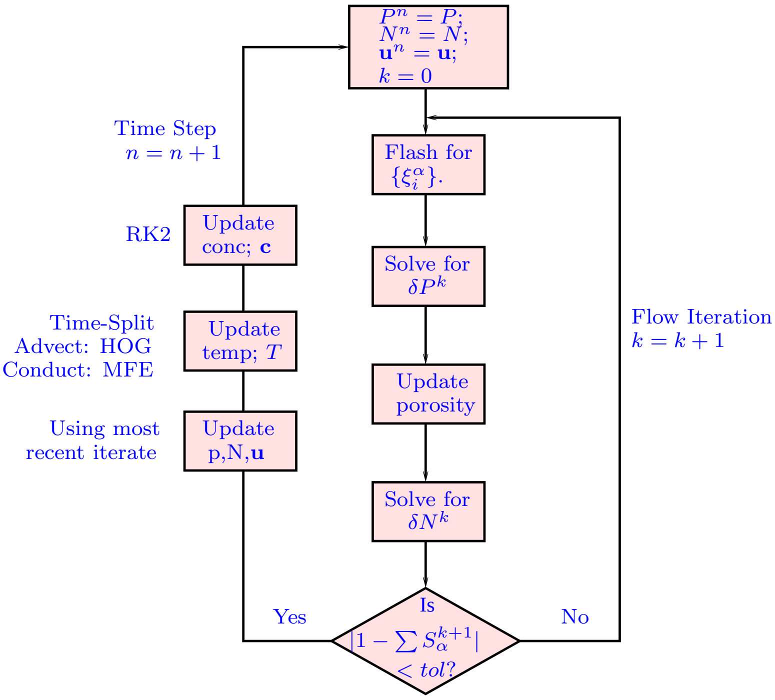

Figure 7.1: Coupled flow-thermal-chemistry algorithm

7.4 Computational results

In this section some model verification tests for isothermal as well as non-isothermal flow problems are presented. More details can be found in [52–54]. Further, the numerical model presented in the preceding sections is also tested on some challenging problems. The first problem is designed to illustrate the parallel performance of the flow model on extremely fine grids and heterogeneous permeability fields. It also motivates the use of an iteratively coupled flow model for multiphase, multicomponent EOR applications as opposed to a fully implicit method. The second problem demonstrates the application of the coupled flow and thermal model to solve the problem of CO_2 flow and leakage when injected close to an abandoned leaky well. The final example presents the coupling of flow, thermal and chemistry applied to CO_2 injection in a deep heterogeneous aquifer.

7.4.1 Model verification tests

The first example is based on the 5th SPE project [**?**]. In this test a quarter of a five spot water-alternating-gas (or WAG) injection cycle is used for oil production. Primary production is carried out during the first year followed by water injection at 12000 stb/day alternated with gas injection at 12000 scf/day thereafter with a period of one year each. The non-aqueous phases are assumed to consist of 6 components, viz., the n-alkanes C1, C3, C6, C15 and C20. The composition of the injected gas is 77% methane, 20% propane and 3% hexane. A coarse 7×7×3 grid is assumed. The permeability is layered along the depth as follows: $K_{xx} = K_{yy} = \{200, 50, 500\}$ mD and $K_{zz} = \{25, 50, 50\}$ mD. The global dimension of the reservoir is 3500 m × 3500 m × 100 m. The simulation time is 20 years. Some comparisons of solutions were made with a commercial simulator, GEM developed by The Computer Modeling Group, Canada [97]. Figure 7.2 shows the comparison of cumulative oil produced and cumulative gas injected and produced.

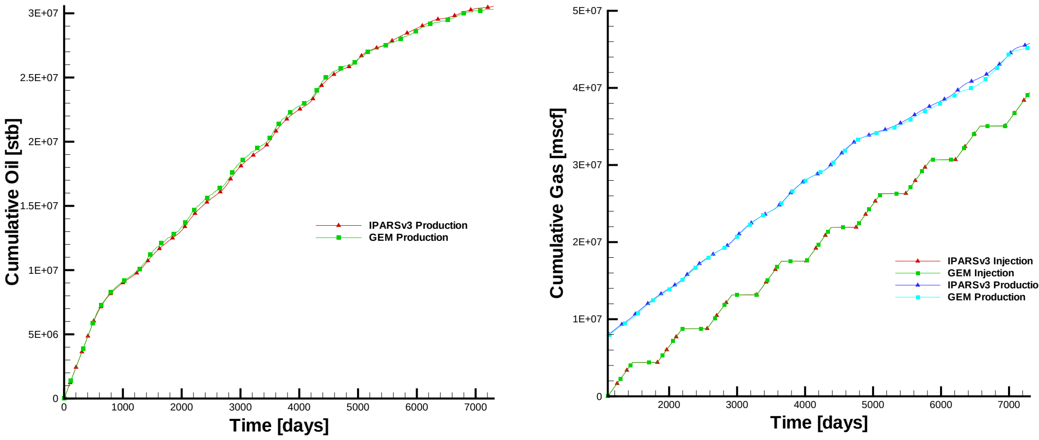

Figure 7.2: SPE 5, WAG Injection example.

The second example is a 1-d, "hot water pulse" injection problem in which water at 100 F is injected for 100 days into a reservoir saturated with water initially at 60 F. Thereafter water is injected at 60 F for another 300 days. Heat conduction is ignored in this example. This example clearly illustrates the advantage of the higher order Godunov scheme. Figures 7.3a and 7.3b show the

Property	Value
Length of reservoir, ft	2500.0
Width of reservoir, ft	10.0
Height of reservoir, ft	10.0
Vertical/Horizontal permeability ratio	1.0
Average horizontal permeability, mD	400.0
Average porosity	0.2
Grid dimensions	1×100×1
Rock density, lb/cu-ft	165.0
Rock isochoric sp. heat, Btu/lb-F	0.2
Initial water pressure, psi	5000.0
Initial reservoir temperature, F	60.0
Maximum injection pressure, psi	5200.0
Minimum production pressure, psi	3000.0

Table 7.1: 1-d hot water pulse injection: Summary of data

reservoir temperature profiles at $t = 3, 28, 100, 200, 300$ and 400 days using the first order Godunov scheme (upwind differences) and a higher order Godunov scheme respectively. The pulse solution is preserved in the latter, while the solution is highly smeared in the former as one may expect due to numerical diffusion. A rock density of 165 lb/cu-ft and rock isochoric specific heat capacity of 0.2 Btu/lb-F is assumed in all the thermal examples considered. A maximum time step of 1 day was chosen for this simulation. Data for this example is summarized in Table 7.1.

The third example considered is the case of cold water injection in a heterogeneous reservoir. This is a single phase (water) flow example solved within the compositional model framework. It served as a means of verifying the thermal implementation. The permeability and porosity are in general higher at greater depths. A 2-d domain is first assumed with a coarse 26×8 grid with global dimensions of 1318.2 ft × 26 ft. Standard values of rock density (165 lb/cu-ft) and effective thermal conductivity (44.0 Btu/ft-lb-d) were assumed. There are two wells, one injecting water at a constant pressure of 4121 psi and temperature of 60 F. The production well is held at 3771 psi. The reservoir is initially at 3771 psi and 86 F. Figures 7.4a–7.4b show the comparison on the coarse grid, between the temperature profiles (all shown on a scale ranging from

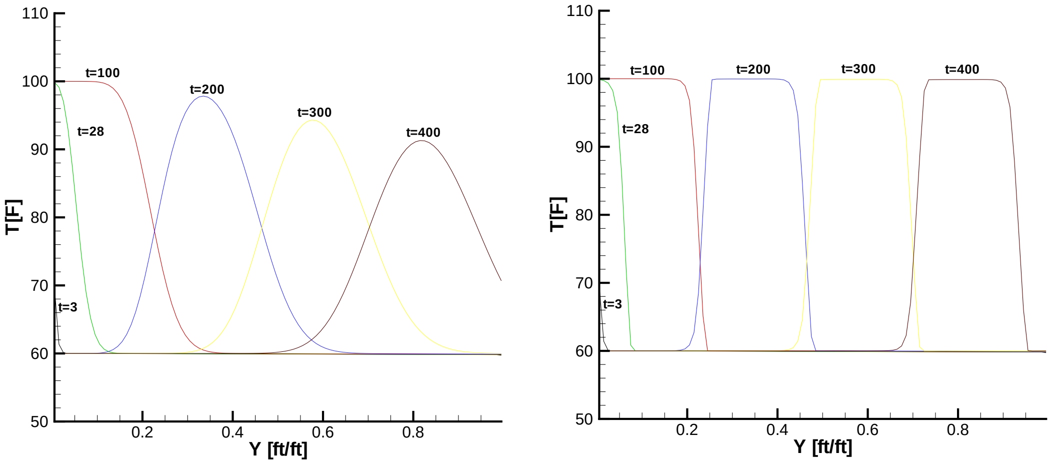

a. *First order Godunov* b. *Higher order Godunov*

Figure 7.3: "Hot water pulse" injection problem

60 F to 86 F) at a simulation time of 100 days obtained by IPARS (Figure 7.4b) and another widely used and reliable simulator UTCHEM (Figure 7.4a) developed at the Center for Petroleum and Geosystems Engineering, UT Austin [51]. Figures 7.4c and 7.4d show the solutions (both from IPARS) to the same problem solved on a much finer grid of 16×100 using the first order Godunov scheme and a higher order Godunov scheme respectively. It is noted that the first order scheme described here exhibited much more numerical diffusion on the same fine grid.

7.4.2 Parallel computations

The first example in this section simulates a multiphase flow scenario in which a "five-spot" water-alternating-gas (WAG) injection cycle with the injection well located at the center of the domain and the production wells at the 4 corners is employed for oil production. Primary production is carried out during the first year followed by water injection at 12000 stb/day alternated with gas injection at 12000 scf/day thereafter with a period of one year each. The non-aqueous phases are assumed to consist of 6 components, viz., the n-alkanes C1, C3, C6, C15 and C20. Gas injection is proportioned among the first 3 components as 77% methane, 20% propane and 3% hexane. An extremely heterogeneous reservoir with permeabilities varying by 6 orders of magnitude

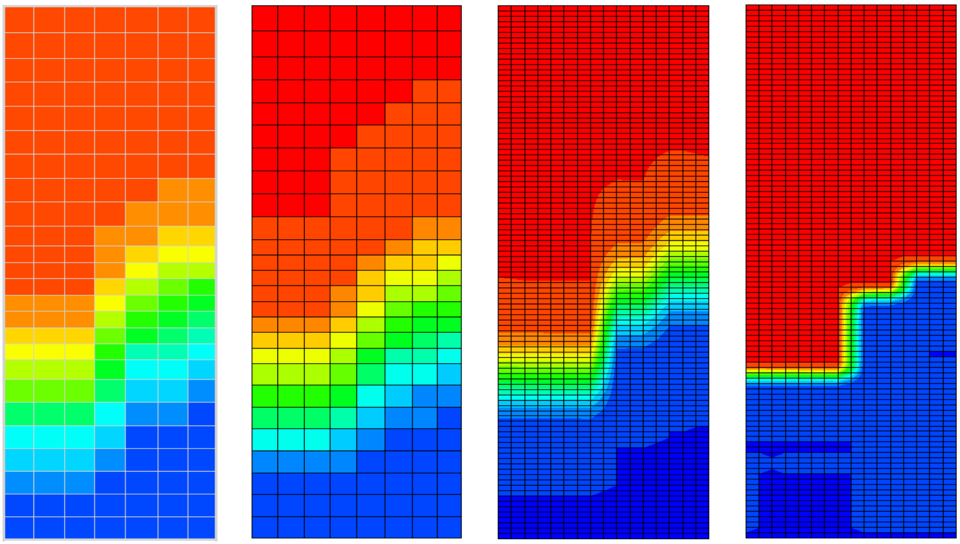

a b c d

Figure 7.4: Temperature profile comparisons: Cold water injection in a heterogenous reservoir.

and derived from the 10^{th} SPE project is assumed [38] after projecting onto a very fine grid of 100 × 100× 40. The global dimensions of the reservoir are 3500 m × 3500 m × 100 m. The simulation time is 3 years. A coarser version of this problem using a more uniform permeability was verified against a commercial simulator and the solutions agreed very well.

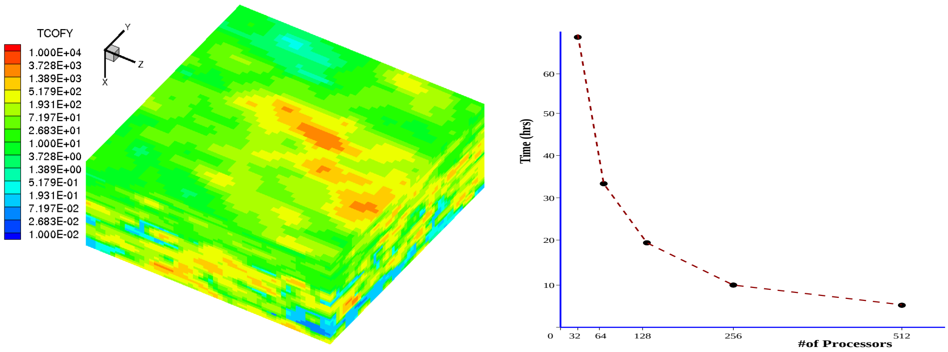

a b

Figure 7.5: Permeability field and parallel performance

For a fully implicit implementation, the number of unknowns for this problem per element is 7; i.e., one for the reference phase pressure and one for each of the 6 component molar concentrations and hence the Jacobian computations are excessively expensive. On extremely fine grids as used in this simulation, this could potentially become very difficult to solve using codes that implement a fully implicit compositional model. This problem was tested on 32, 64, 128, 256 and 512 cores on the parallel distributed memory architecture of the Lonestar cluster at the TACC facility, UT Austin. A parallel efficiency of about 80% was observed. Figures 7.5a and 7.5b show the K_{yy} permeability field in mD and the parallel performance (plot of actual computational time versus number of cores) respectively. The gas saturation and molar concentration of a component (propane) at the completion of one complete WAG cycle (i.e., 3 years) are shown in Figures 7.6a and 7.6b respectively

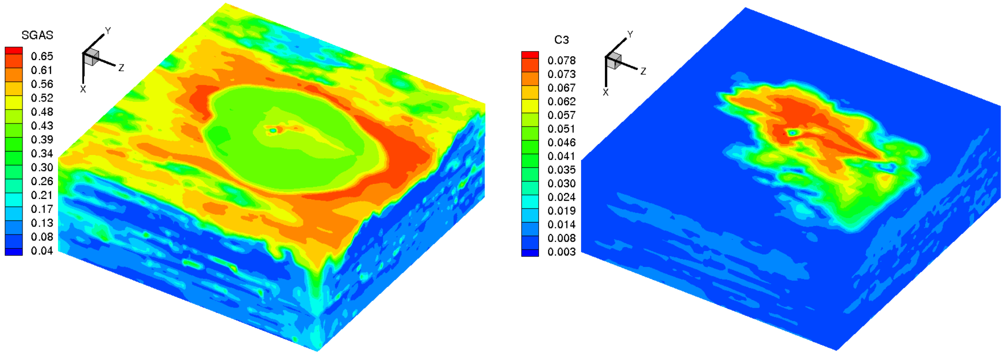

a b

Figure 7.6: Gas saturation and C3 molar concentration

7.4.3 CO_2 sequestration

The first example of this section simulates the leakage of CO_2 when injected near an abandoned leaky well. The physical reservoir is a domain of dimensions 1000 m × 1000m × 160 m. There are two aquifers of permeability approximately 20 mD each, separated by an impermeable aquitard. A leaky well modeled as a porous medium with a permeability of about 1000 mD is located at the center of the domain and an injection well is 100 m away. CO_2 is injected at a rate of 8.8 kg/s at 92.48 °F. The reservoir is initially saturated with brine and is at a depth of 640 m. An initial geothermal gradient of 0.054 F °/m is specified with a bottom temperature of 93.2 ° F. The outputs of interest were the CO_2 leakage rate at the mid-section of the leaky well (as a percent of the injection rate), the CO_2 plume shape as it approached the leaky well as well as the arrival time and the peak leakage value. The boundary conditions were no-flow on the vertical surfaces and equal to the initial conditions on the lateral surfaces. Figure 7.7 presents a schematic of this problem. For details as well as problem data, the reader is referred to [1].

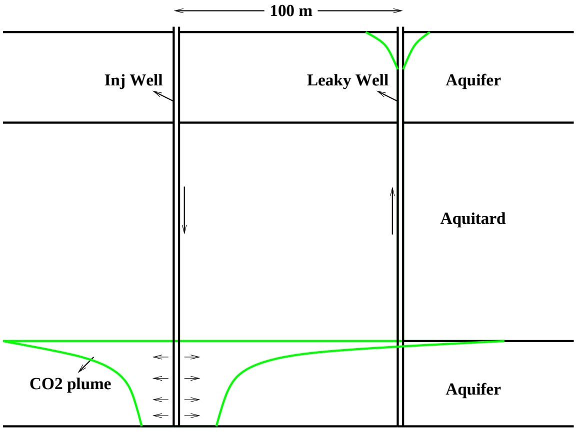

Figure 7.7: CO_2 injected near and abandoned leaky well.

Due to the shallow depth of the reservoir, the critical pressure and temperature of CO_2 happen to lie along the mid-plane passing through the aquitard. As a result of this, when CO_2 rises, it experiences large change in properties which combined with varying spatial and temporal reservoir temperature in turn have a strong influence on the leakage rate. Brooks-Corey [29] relative permeability and capillary pressure curves are assumed. Figure 7.8a and 7.8b show the CO_2 leakage rate and temperature in the leaky well respectively. The sudden drop in temperature when CO_2 initially reaches the leaky well is due to the displacement of warmer brine and abrupt change in properties upon crossing the critical point.

An arrival time of close to 50 days is observed which agreed reasonably well with other comparable commercial and academic research codes. A simulation on a similar problem with a greater reservoir depth of 2840 m, isothermal conditions and a linear relative permeability and capillary pressure produced

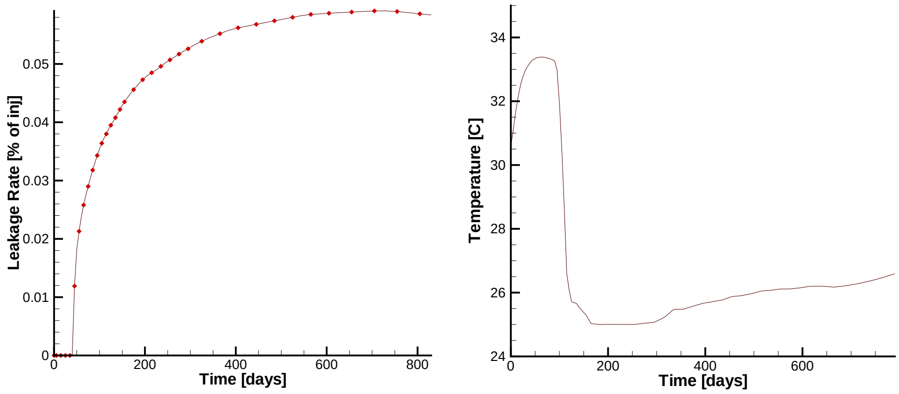

a b

Figure 7.8: CO_2 leakage rate and temperature profile (C) in leaky well

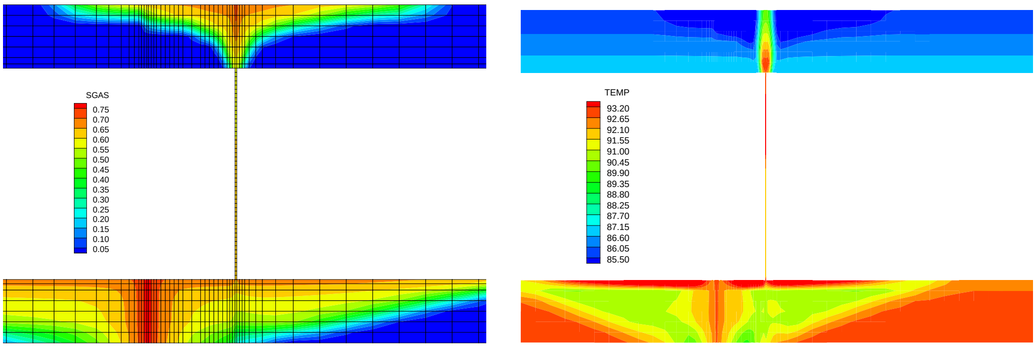

a b

Figure 7.9: CO_2 saturation and reservoir temperature (F) across a section through wells

earlier arrival time and higher leakage rates. Figure 7.9a and 7.9b shows the CO_2 gas saturation and reservoir temperature profile across a section passing through the wells at $t = 705$ days. This problem was solved using a computational grid of 66×45×64 on upto 96 processors on the Ranger cluster at TACC and Bevo2 cluster at ICES, UT Austin.

The second example studies the storage capacity of CO_2 when injected in a naturally faulted geological formation. The major challenge with this problem was in accurately modeling the geometry of the domain with the faults. A stair-stepped approximation was employed to treat the geometry in keeping with the stencil resulting from mixed FEM that is implemented in the compositional flow model. The domain in this problem models the Johansen formation off the coast of Norway. The lateral dimensions of the domain are 9600 m × 8600 m and the thickness varies between 90 m and 140 m. A detailed problem description including the geometry, porosity and permeability information can be downloaded from the web [1]. CO_2 was injected at a constant rate of 15 kg/s for a period of 25 years into the lower 50 m of an injection well located at y =3300 m and z =5440 m. The geometry and permeability obtained from the actual data is shown in Figure 7.10a while the stair stepped fine grid approximation of the same is shown in Figure 7.10b. Similarly, Figures 7.11a and 7.11b show the porosity for the actual and approximated geometries respectively (without the grid superimposed). In Figure 7.11b, the well location indicated by an arrow.

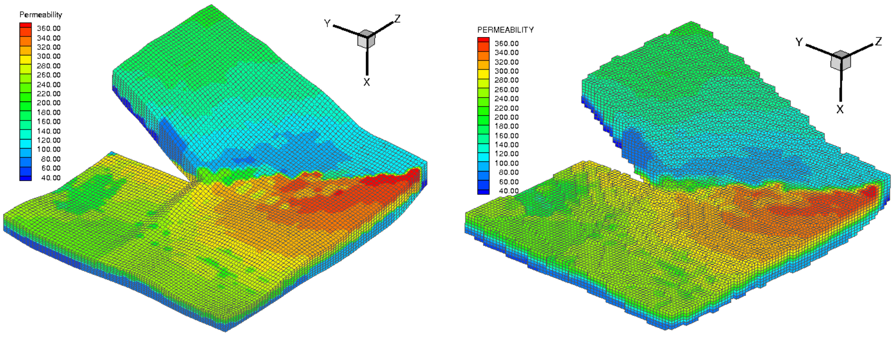

a b

Figure 7.10: CO_2 injection in faulted formation: Permeability in mD

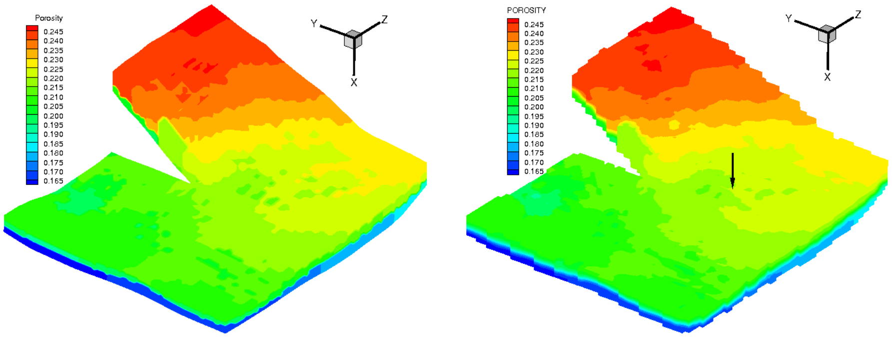

a b

Figure 7.11: CO_2 injection in faulted formation: Porosity

A fine grid of 45×80×80 was used for the outer bounding box and suitably interpolated to get values of the properties at corners of the box that intersect with the actual domain. For all other points, negative values are assigned and these are used to keyout the elements that are actually inactive in the bounding box (i.e., the corners that do not intersect the actual domain). A finer grid for the outer bounding box therefore yields a better stair stepped approximation to the real geometry. Temperature also played a role in this problem. The formation was initially saturated with brine at 0.1 salinity. A temperature of 100 ° C and a pressure based on the density of brine at these conditions was specified at the reference depth of 3000 m. The highest point in the formation was at a depth of about 2500 m. For this problem, a higher-order Godunov thermal advection scheme was applied.

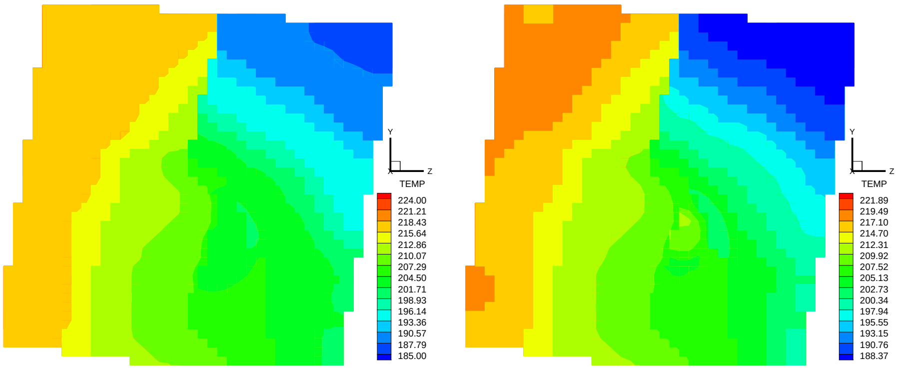

a b

Figure 7.12: CO_2 injection in faulted formation: Reservoir temperature (F)

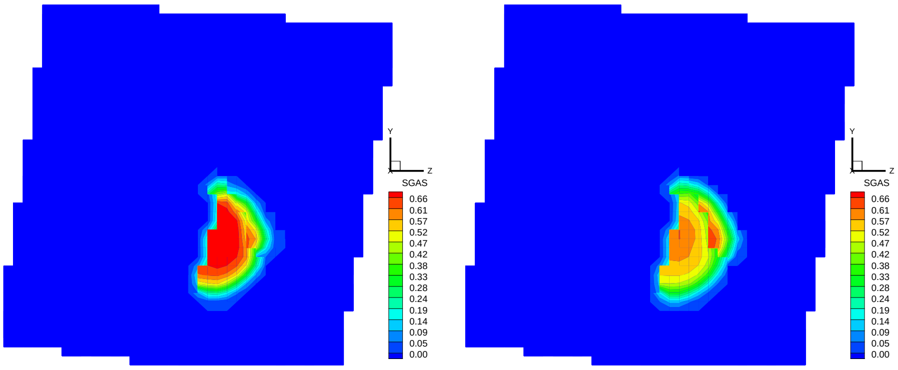

a b

Figure 7.13: CO_2 injection in faulted formation: Gas saturation

An initial temperature gradient of 0.03 K/m was assumed and CO_2 injected at 80 ° C. A Brooks-Corey [29] capillary pressure and relative perme-

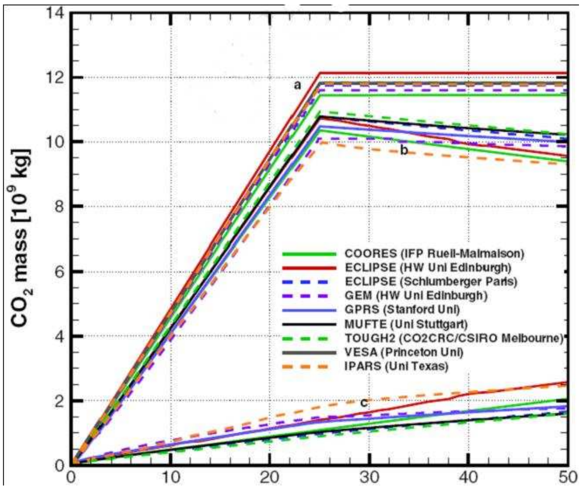

Figure 7.14: CO_2 distribution in phases: Comparison with contemporary simulators

ability relations are assumed with parameter $\lambda = 2$. The boundary conditions were identical to the first example presented in this section (lateral boundary conditions equal to initial conditions while the top and bottom surfaces are prescribed no-flow conditions). Among the main output of interest was the amount of CO_2 sequestered at the end of 50 years simulation time and the CO_2 distribution in the formation with time. Figures 7.12a and 7.12b show the top view of the reservoir temperature (F) after 25 and 50 years simulation time respectively. Similarly, Figs. 7.13a and 7.13b show the CO_2 gas saturation at the same times. The apparent non-monotonicity in the solution is due to the fact that the solution is shown on a stair-stepped grid and some elements are at a higher elevation than surrounding elements. It was found that of the 592.407×10^6 lbM of CO_2 injected over the 25 year period, approximately 589.439×10^6 lbM was sequestered after the 50 year simulation period and 2.968×10^6 lbM had leaked out mainly from the lateral surfaces of the fault. Thus only 0.5011% CO_2 leakage occurred during this period. A comparison with other well known academic and commercial simulators, of the plots of the distribution of CO_2 in the different phases (as well as total CO_2 injected) with time is shown in Figure 7.14 (wherein the x-axis ranges from 0 to 50 years). This problem was run on 36 cores on the Bevo2 cluster at ICES, UT Austin.

7.4.4 Frio: A field-scale CO_2 sequestration simulation

The example in this section simulates an actual field-scale CO_2 sequestration experiment conducted by the Bureau of Economic Geology (BEG) at The University of Texas at Austin. Details of the experiment and its goals can be obtained from [61, 69] as well as the BEG website, http://www.beg.utexas.edu/. The bureau has conducted pilot tests for CO_2 injection off the Gulf Coast of Texas. The purpose of these pilot tests is to gather valuable data (during monitoring) and to demonstrate that large scale CO_2 sequestration can be performed with no concerns. The Frio formation is a brine-bearing sand in a well known onshore oil field with 3-d seismic and well log data available for characterization. This made it a suitable choice. Further, the existing infrastructure of wells and roads could be used for the pilot test. An existing production well was re-completed as a monitoring well and an injection well was drilled about 30 m away, down-dip [69].

The formation is composed of two rock types - shale and sand layers. The injection took place in brine-bearing sandstone at about 1500 m (approx. 5000 ft) below the ground surface. The shale layers vary in thickness between 3 m to 15 m and separated various sandstone layers at the top of the formation. The injection target was the deepest sandstone layer (which was also the thickest) below a shale layer (in order to prevent upward drift of CO_2 due to buoyancy). The injection temperature was approximately constant and maintained at 60 F while the initial estimate of the reservoir temperature was constant at about 154.5 F. Many research groups have already conducted simulations of the pilot test (including the Lawrence Berkeley National Lab among others) but not many have included temperature in their simulation. The pilot plan injected 3000 tonnes of CO_2 over a period of 12 days after which the injection well was shut-in. The problem data is summarized in Table 7.2.

The monitoring well was kept open for a period of 22 days and thereafter opened only intermittently for monitoring. In this work, an accurate PVT information for precise density calculations of CO_2 was applied to set up the

Property	Value
Length of bounding box, m	2532.0
Width of bounding box, m	1875.0
Height of bounding box, m	495.6
Depth of formation	1157.0
Dip, degrees	5.0–35.0
Formation thickness, m	30.5–61.0
Vertical/Horizontal permeability ratio	0.1
Average horizontal permeability	3.74×10^{-5} m^2
Average vertical permeability	3.74×10^{-6} m^2
Average porosity	0.214
Grid dimensions	40x72x72
Initial brine pressure, MPa	15.14
Maximum injection pressure, MPa	24.82
Initial reservoir temperature, °C	57.0
Brine salinity, ppm	100000.0

Table 7.2: Frio: Summary of problem data

Property	CO_2	Brine
Critical pressure, MPa	7.38	22.09
Critical temperature, °C	31.05	374.2
Critical volume, m^3/mol.	9.4×10^{-5}	5.6×10^{-5}
Molecular weight, kg/mol.	44.01	19.35
Accentric factor	0.224	0.344
Parachor	78.0	52
Volume shift parameters	0.0247	0.234
Binary interaction coefficient	-0.06027	-0.06027

Table 7.3: Frio: Component PVT data

simulation (see Table 7.3 for GEM input). Due to the extremely close proximity of the injection and monitoring wells, a very fine grid was used in the region between the wells. Figures 7.15 shows the true porosity (left) and approximated porosity (right) of the formation. The approximated porosity was generated using a stair-stepped approximation method applied to the original grid-data and suitably interpolating the properties to the stair-stepped grid as in the previous example. An outer bounding box of 40×72×72 was used in this example. For the computation, wells were used to simulate boundary conditions which are not exactly known. Thus, 23 “BC wells” were placed in a rectangle surrounding the injection and monitoring wells to simulate the far-field effects. This is depicted in Figure 7.16.

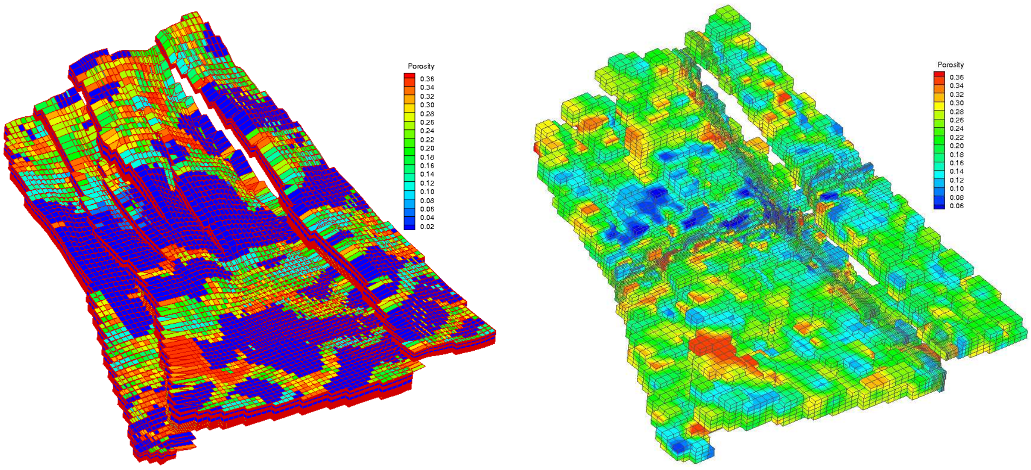

Figure 7.15: Frio: Geometry and property approximation - true (left), stair-stepped (right)

A first simulation assumed the problem is isothermal. Thus the injection temperature was assumed to be 134.5 F (for consistency with tests by other groups). The brine pressure profile (perspective view) and gas saturation (surface close-up, approximately top-view) is shown in Figure 7.17 for the isothermal case. Since the duration of the injection is for a small period, a solution at early times is also included. In the experiment, the CO_2 was observed to reach the monitoring well at approximately 2.2 days in dissolved form. At early time, gas flows below the shale layer. This, saturation is also shown at a

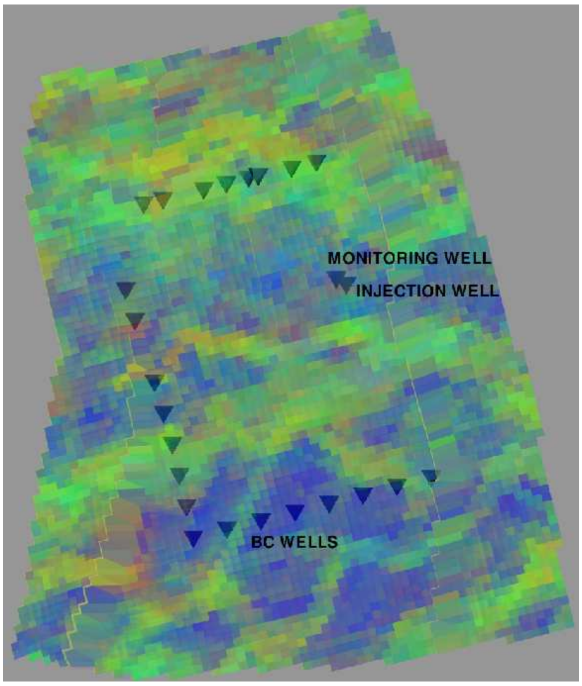

Figure 7.16: Frio: Injection, monitoring and BC wells.

cross section below the shale layers at times 3 and 30 days in the Figure 7.18 (in a close-up, approximately top-view). The simulation yielded a breakthrough time of CO_2 in dissolved form, of about 3.0 days which was in close agreement with the experiment as well as with simulations conducted by other research groups [61].

The next test was to simulate the full non-isothermal problem. In Figure 7.19, the CO_2 gas saturation is shown at 3 and 12 days, while in Figure 7.20, the reservoir temperature is shown in a close-up at a cross-section below the shale layers at which the injection is performed at times 3 and 12 days. As can be seen from Figure 7.20 a cold front develops in the vicinity of the injection well below the shale barriers, where the temperature of CO_2 injected is 60 F. But the heat dissipates slowly into this region since the injection is stopped after just 12 days. This time period is very small for a formation of such length scales and so the heat conduction from surrounding rock serves to heat the colder region as soon as injection is stopped. However, the rock thermal conductivity is very small. Thus, it takes very long for the reservoir to regain its initial temperature.

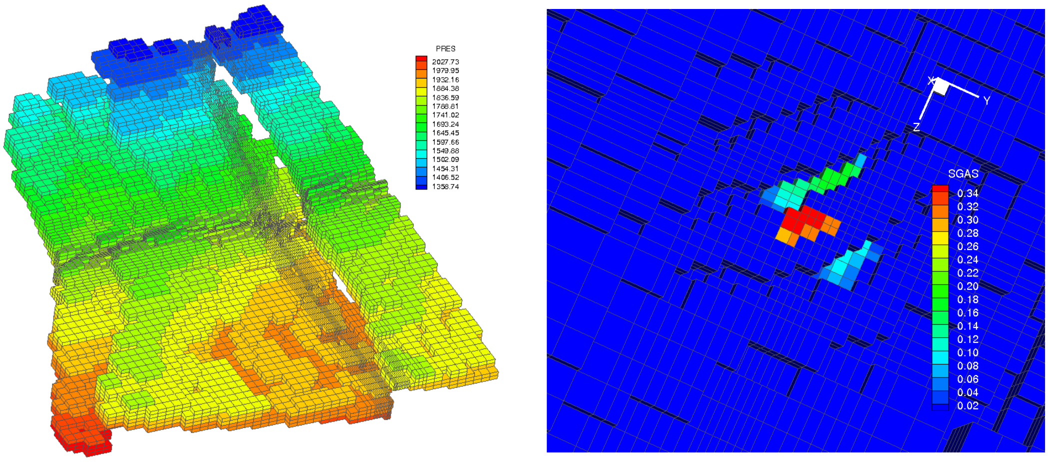

Figure 7.17: Frio: Pressure (left) and gas saturation (right) for isothermal problem

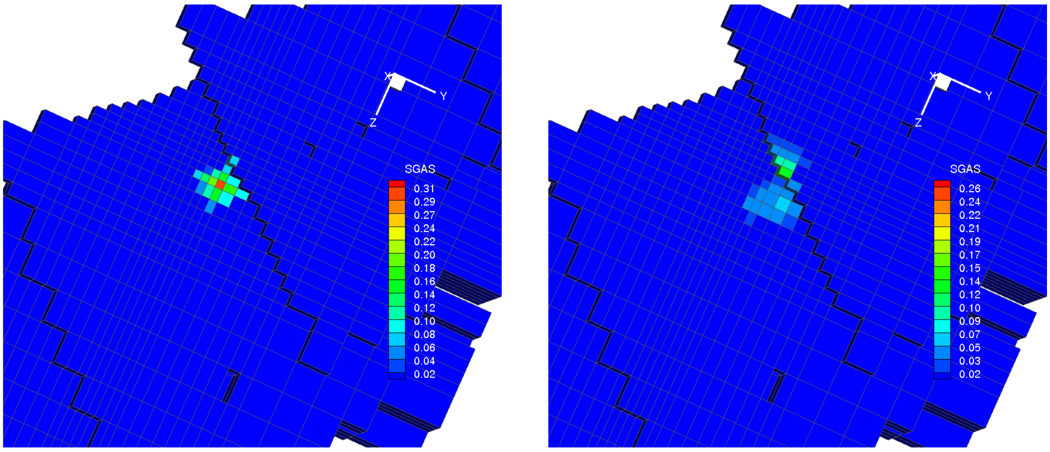

Figure 7.18: Frio: Gas saturation below shale layer at 3 days (left) and 30 days (right) for isothermal simulation

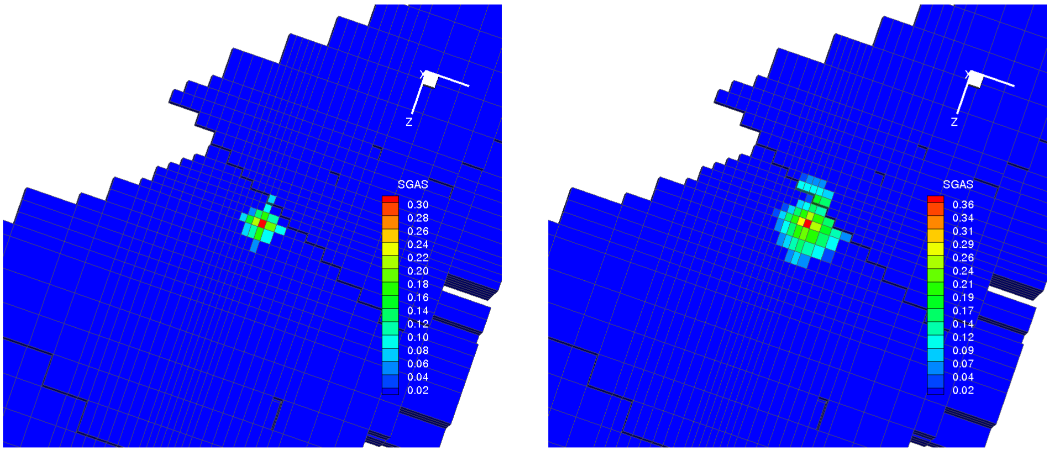

Figure 7.19: Frio: Gas saturation below shale layer at 3 days (left) and 12 days (right) for non-isothermal simulation

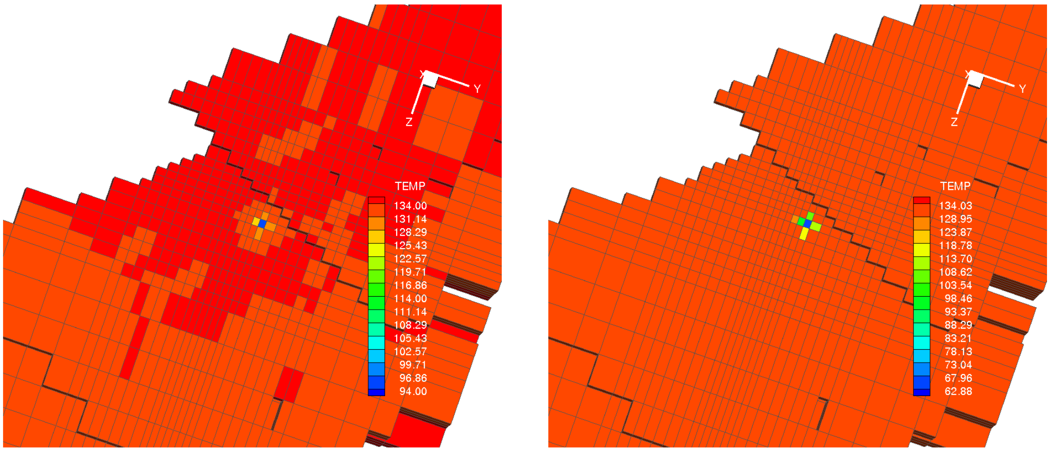

Figure 7.20: Frio: Reservoir temperature (F) below shale layer at 3 days (left) and 12 days (right) for non-isothermal simulation

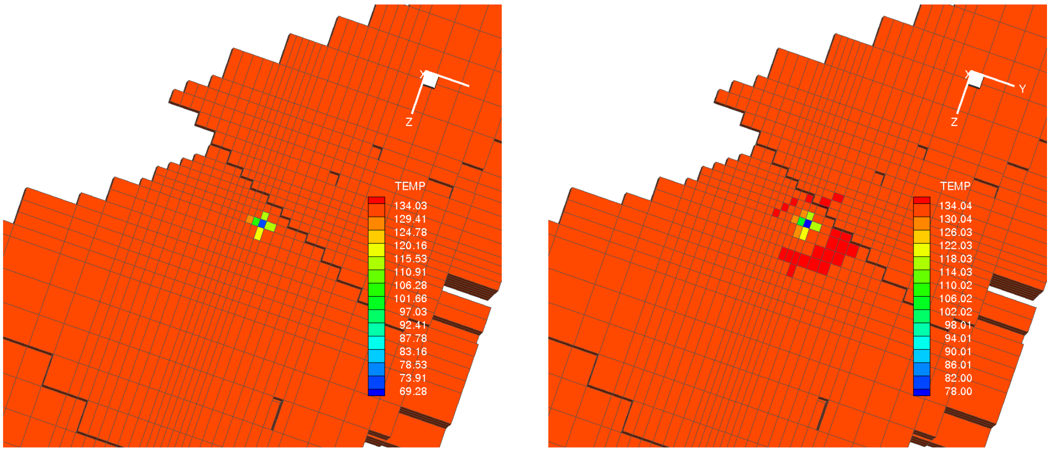

Figure 7.21: Frio: Reservoir temperature (F) below shale layer at 30 days (left) and 360 days (right) for non-isothermal simulation

This is reflected in Figure 7.21 where the reservoir temperature is shown at 30 and 360 days.

7.4.5 Flow-thermal-chemistry simulation

The example in this section presents the coupling of non-isothermal flow and chemistry as applied to problems in CO_2 sequestration. In this problem CO_2 is injected to a deep aquifer at 5000 m depth via four wells located at the corners of a small square located at the center of a domain with physical dimensions of 325000 ft×325000 ft× 256 ft. The problem models flow of two phases (CO_2 and water) and 3 components (water, CO_2 and H_2CO_3). The CO_2 is injected for 10 years at 75000 mscf/day at a temperature of 176 F. The initial reservoir temperature is 200 F. The reservoir is assumed to have a layered permeability field. A fine grid of 50×50×5 is used in the computation. An equilibrium chemical reaction of the form $H_2O + CO_2 \rightleftharpoons H_2CO_3$ governs the formation of $H_2CO_3$with an equilibrium constant of 1.7×10^{-3}. The goal was to study the distribution of CO_2 and H_2CO_3 and the reservoir temperature profile at the end of 10 years simulation time.

Figure 7.22a shows the computational domain with grid and well locations superimposed. A fine grid is used around the wells. Figure 7.22b shows the reservoir temperature in a section passing through two of the wells (scale

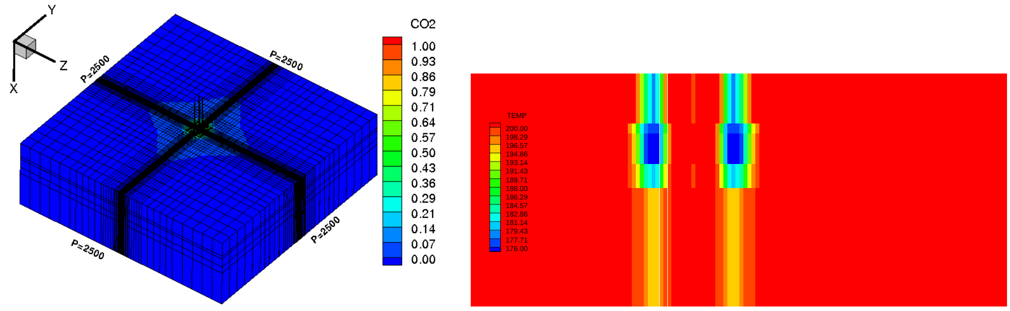

a b

Figure 7.22: CO_2 injection in a deep aquifer & temperature (F) across section through two wells

from 176 F to 200 F). Due to the aerial symmetry of the reservoir as well as symmetry of well location, a similar solution is observed in all cross sections passing through any two adjacent wells. It is observed that the temperature is reduced from 200 F to 176 F around the injection wells. Figures 7.23a and 7.23b show the CO_2 and H_2CO_3 molar concentrations after the 10 year simulation period in a close-up across a section passing through two of the wells. Due to the layered permeability field, the transport and reaction plumes form fingers spreading in a non-uniform manner with depth.

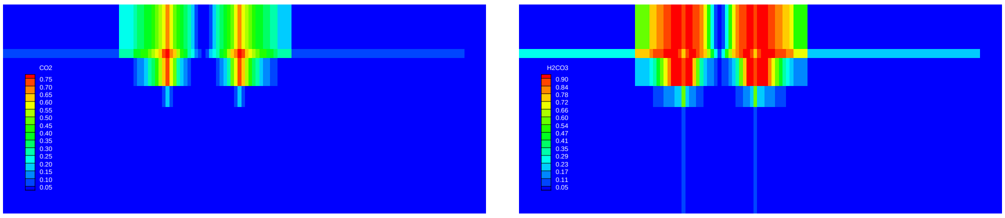

a b

Figure 7.23: CO_2 and H_2CO_3 concentrations across section passing through two wells

Chapter 8

Reservoir parameter estimation and history matching using stochastic methods

The parameters that characterize a reservoir are often not known to the desired level of accuracy needed to solve the governing PDE's of flow or transport as mentioned in Chapter 1. The goal of this chapter is to present a numerically cheap, yet efficient and parallel algorithm of determining reservoir parameters, e.g., permeability using sensor information (i.e., measurements of the solution variables such as phase pressures, concentrations, fluxes, seismic and well-log data). Today, most oil drilling companies routinely have sensors installed at strategic locations in a reservoir. Specialized sensors are capable of measuring at a high local resolution, fluid and rock properties (see for e.g., [90, 133] and references therein). These advances in conjunction with 4-d time-lapse seismic studies are revealing enormous potential in reducing the uncertainty associated with reservoir characterization. Meanwhile new stochastic optimization and statistical learning methods are emerging as promising tools to determing non-trivial correlations between data measurements and responses and to develop optimal reservoir exploration plans [73]. In this work, the existence of a number of prior realizations (say, from seismic studies) is assumed. The estimation and sampling is then performed at a fixed resolution using a parallel version of the SPSA (simultaneous perturbation, stochastic approximation) [126] algorithm. A multi-level approach, coupled to neural-network engines that enhance the solution by calculating sensitivities in the vicinity of the most promising solution was presented in [76, 77].

8.1 Introduction: Reservoir characterization

Suppose that a set of N realizations, $\mathbf{x}_i, i = 1, \ldots, N$ is given of a reservoir property (for e.g., permeability) where each $\mathbf{x}_i \in \mathbb{R}^M$, M being the number of grid elements. Using methods such as wavelet analysis [88] or the principle component analysis (PCA) method [71, 108], it is possible to determine a reduced set of basis functions that characterize a majority of the variability. In this work, the PCA method is adopted. Then, let the set of realizations be denoted by the matrix $\mathbf{X}$, given by

$$\mathbf{X} = \{\mathbf{x}_1, \mathbf{x}_2, \ldots, \mathbf{x}_N\}. \tag{8.1}$$

Further, let the empirical mean be given by

$$\bar{\mathbf{x}} = \frac{1}{N} \sum_{i=1}^{N} \mathbf{x}_i \tag{8.2}$$

Next, let $\mathbf{Y}$ denote the deviation of the data from the mean, given by

$$\mathbf{Y} = \mathbf{X} - \{\bar{\mathbf{x}}, \bar{\mathbf{x}}, \ldots, \bar{\mathbf{x}}\}. \tag{8.3}$$

In the PCA method, the covariance matrix $\mathbf{C}$ is required of the deviation of the data from the mean. The covariance matrix is given by

$$\mathbf{C} = E(\mathbf{Y}\mathbf{Y}^T). \tag{8.4}$$

Since each of the N realizations are in generally equally likely, in (8.4), it is possible to further reduce the expression for covariance as $\mathbf{C} = E(\mathbf{Y}\mathbf{Y}^T) = \frac{1}{N}\mathbf{Y}\mathbf{Y}^T$. Thus, the covariance matrix $\mathbf{C}$ is symmetric and positive definite. Hence, it is possible to compute the eigen-decomposition of $\mathbf{C}$ and the associated eigen values as follows

$$\mathbf{C} = \mathbf{V}\mathbf{D}\mathbf{V}^{-1} \quad \text{with}, \mathbf{D} = \operatorname{diag}\left(\{\lambda_i\}_{i=1}^{M}\right). \tag{8.5}$$

In (8.5), $\mathbf{V} = \{\mathbf{v}_i\}_{i=1}^{M}$, the matrix of eigen vectors of $\mathbf{C}$ and λ_i are the corresponding eignen values. Let λ_i be arranged in descending order $\lambda_1 > \lambda_2 >$

$\ldots > \lambda_M$. Then each realization can be expressed to a desired level of accuracy as a linear combination of the first P eigen value/vector pairs ($P < M$). Infact, since $\mathbf{C}$ is symmetric in addition to being positive definite, the eigen vectors of $\mathbf{V}$ are orthogonal and thus, (8.5) can be expressed in terms of orthormal eigen vectors. In such a case, it is well known that the eigen values coincide with the singular values. Then, a well known result can be drawn upon from linear algebra, re-stated here for this special case without proof:

Theorem 8.1.1. *Suppose* $\mathbf{C}$ *is an* $M \times M$ *matrix with singular values* $\lambda_1 > \lambda_2 > \ldots > \lambda_M > 0$. *Then for any* $P < M$, *the matrix given by* $\tilde{\mathbf{C}} \equiv \sum_{i=1}^{P} \lambda_i \mathbf{v}_i \mathbf{v}_i^T$ *is the best "rank-P" approximation of* $\mathbf{C}$ *in the sense of the Frobenius norm, i.e.,* $\tilde{\mathbf{C}}$ *is the minimizer of* $\|\mathbf{C} - \mathbf{Z}\|_{\mathcal{F}}$ *where* $\mathbf{Z} \in \mathbb{R}^{M \times M}$.

In Theorem 8.1.1, recall that the Frobenius norm (which is an operator norm) of the matrix $\mathbf{C}$ is given by $\|\mathbf{C}\|_{\mathcal{F}} \equiv \sqrt{\sum_{i=1}^{M} \lambda_i^2}$. Also, note that $\mathbf{v}_i \mathbf{v}_i^T$ denotes the outer product (sometimes referred to as the "tensor product") of the vectors $\mathbf{v}_i$ and $\mathbf{v}_i^T$. Therefor, the theorem serves to guarantee that the reduced basis corresponding to the subspace spanned by the first P eigen vectors is the best possible "rank-P" choice. In other words, it suffices to determine coefficients α_j, such that the "true" property sought can be expressed as $\mathbf{x} \approx \bar{\mathbf{x}} + \sum_{i=1}^{P} \alpha_j \mathbf{v}_j$ in the subspace, $\text{span}\{\mathbf{v}_j\}_{j=1}^{P}$. Hence, the dimension of the system is greatly reduced. The coefficients α_j are actually determined by minimizing an objective function, using the SPSA method, described in the following section.

8.2 Simultaneous perturbation, stochastic approximation (SPSA)

Consider the problem of finding the root, θ^*, of the $\mathbf{g}(\theta) \equiv \nabla L(\theta) = 0$, where $L : \mathbb{R}^P \rightarrow \mathbb{R}$ is assumed to be a differentiable loss function that measures the weighted, time- and space-integrated error between observed measurements (of the phase pressures, concentrations, fluxes, seismic travel-times and well-log data) and computed solutions in some suitable norm. In this work, the expression for L takes the form

$$L(\theta) \equiv \sum_{\mathbf{f}\in\mathcal{P}} \sum_{i=1}^{N_T-1} \left[0.5\left(\|w_{\mathbf{f},i}(\mathbf{f}_i^d - \mathbf{f}_i)\|_2^2 + \|w_{\mathbf{f},i+1}(\mathbf{f}_{i+1}^d - \mathbf{f}_{i+1})\|_2^2\right)\Delta t_i.\right] \tag{8.6}$$

Several terms in (8.6) which is written in concise terms, deserve mention. The functions $\mathbf{f} \in \mathcal{P}$ denote any property of interest in the calculations, $\mathbf{f}(\theta)$ which is a function of θ. The set of all such properties is denoted by $\mathcal{P}$. In this work, for the case of two-phase flow (and specifically the oil-water model) $\mathcal{P} \equiv \{\mathbf{p}, \mathbf{N}, \mathbf{u}, \mathbf{q}, \tau\}$ where $\mathbf{p}$ denotes the (oil-)phase pressures, $\mathbf{N}$ denotes the (oil-)phase concentration, $\mathbf{q}$ denotes the well-data (includes well-rates, bottom hole pressures, oil-water ratios, etc. depending on the kind of well), $\mathbf{u}$ denotes the phase fluxes and τ denotes seismic travel-times. Thus it can be seen that the right-hand side of 8.6 is a function of θ. The superscript d denotes measure data, while terms without the superscript denote computed solution. The index i denotes the time instant at which measurements are recorded and $w_{\mathbf{f},i}$ is a space- and time-dependent weight function on the property $\mathbf{f}$. Finally, N_T is the number of time instants in $[0, T]$ when data measurements are recorded and Δt_i denotes the time interval between such measurements.

In this problem, $\theta \equiv \{\alpha_1, \alpha_2, \ldots, \alpha_P\}$ with α_i the coefficients in the expansion of the unknown (permeability) vector $\mathbf{x}$, as described in Section 8.1. Let θ_k denote the estimate for θ at the k^{th} iterate. Then, the SPSA algorithm has the form

$$\theta_{k+1} = \theta_k - a_k \mathbf{g}_k(\theta_k) \tag{8.7}$$

where $\mathbf{g}_k(\theta_k)$ is a simultaneous perturbation, stochastic approximation of the gradient $\mathbf{g}(\theta_k)$ defined as follows. Let $\Delta_k \in \mathbb{R}^P$ be a vector consisting of $\{\pm 1\}$ values that are randomly generated using a Bernoulli distribution, i.e., satisfying $E(\Delta_{k,i}) = 0$, $i = 1, 2, \ldots, P$. Then $\mathbf{g}_k(\theta_k)$ is defined by the central-differences equation (component-wise)

$$g_{k,i}(\theta_k) = \frac{L(\theta_{k,i} + c_k\Delta_{k,i}) - L(\theta_{k,i} - c_k\Delta_{k,i})}{2c_k\Delta_{k,i}}, \qquad i = 1, 2, \ldots, P. \tag{8.8}$$

Here a_k, c_k are montonically, decreasing sequences of positive scalars chosen according to the method prescribed in [126]. The relevant formulae are given by

$$a_k = \frac{a}{(A+k+1)^\alpha}\,, \quad c_k = \frac{c}{(k+1)^\gamma} \tag{8.9}$$

where a, c, α, A and γ are positive real numbers satisfying

$$0 < \alpha \leq 1\,, \quad \alpha = \gamma > 0.5\,, \quad \text{and } \alpha > 2\gamma. \tag{8.10}$$

This ensures that some technical conditions are satisfied [126] which are in turn required for the convergence of the stochastic gradient to the steepest descent gradient. The choice of a, c, α, A and γ is to some extent case dependent and may require some experimentation. It is known that $\alpha = 1$ and $\gamma = \frac{1}{6}$ are assymptotically optimum values but choosing smaller values, e.g., $\alpha = 0.602$ and $\gamma = 0.101$ are found to be effective in practise. A common recommendation [126] is to set A equal to 5 to 10 percent of the maximum number of iterations allowed.

Spall [126] has shown that the method converges and can be regarded as stochastic analogue of the steepest descent method with similar rates of convergence. Therein, proofs of convergence of the method in a "stochastic sense" (i.e., in the sense of expectations) are presented. Similar proofs can also be found in [118]. For completeness, the basic steps of a proof are presented here to show that the expectation of the stochastic gradient $\mathbf{g}_k(\theta_k)$ equals the actual gradient $\mathbf{g}(\theta_k)$. Thus, it can be expected that the method will converge at a rate equal to the steepest descent method.

Theorem 8.2.1. *The expectation of the stochastic gradient* $\mathbf{g}_k(\theta_k)$ *of the SPSA method equals the true gradient* $\mathbf{g}(\theta_k)$*.*

Proof. A standard Taylor-series expansion yields that

$$L(\theta_k + c_k\Delta_k) = L(\theta_k) + c_k \sum_{j=1}^{P} \Delta_{k,j} \frac{\partial L(\theta_k)}{\partial \theta_{k,j}} + \mathcal{O}(c_k^2 \|\Delta_k\|^2). \tag{8.11}$$

and likewise

$$L(\theta_k - c_k\Delta_k) = L(\theta_k) - c_k \sum_{j=1}^{P} \Delta_{k,j} \frac{\partial L(\theta_k)}{\partial \theta_{k,j}} + \mathcal{O}(c_k^2 \|\Delta_k\|^2). \tag{8.12}$$

Subtracting (8.12) from (8.11), then rearranging the resulting terms and neglecting the higher-order terms, $\mathcal{O}(c_k^2\|\Delta_k\|^2)$ yields

$$\frac{L(\theta_k + c_k\Delta_k) - L(\theta_k - c_k\Delta_k)}{2c_k} = \sum_{j=1}^{P} \Delta_{k,j}\frac{\partial L(\theta_k)}{\partial \theta_{k,j}} = \Delta_k^T \nabla L(\theta_k). \tag{8.13}$$

Next, define the inverse of Δ_k as

$$\Delta_k^{-1} = \left[\Delta_{k,1}^{-1}, \Delta_{k,2}^{-1}, \ldots, \Delta_{k,P}^{-1},\right]. \tag{8.14}$$

Then, from $\Delta_{k,i}^{-1} = \Delta_{k,i}$ (recall that $\Delta_{k,i} = \pm 1$), it follows that

$$\Delta_k^{-1} = \Delta_k \tag{8.15}$$

From (8.15), it follows that the stochastic gradient in (8.8) can be written as

$$\mathbf{g}_k(\theta_k) = \frac{L(\theta_k + c_k\Delta_k) - L(\theta_k - c_k\Delta_k)}{2c_k}\Delta_k = \Delta_k\frac{L(\theta_k + c_k\Delta_k) - L(\theta_k - c_k\Delta_k)}{2c_k} \tag{8.16}$$

Then, using (8.13) in (8.16) yields

$$\mathbf{g}_k(\theta_k) = \Delta_k\Delta_k^T\nabla L(\theta_k). \tag{8.17}$$

The expectation of the stochastic gradient is then given by

$$E\left[\mathbf{g}_k(\theta_k)\right] = E\left[\Delta_k\Delta_k^T\right]\nabla L(\theta_k). \tag{8.18}$$

Observe that the form of the matrix $\Delta_k\Delta_k^T$ on the right-hand side of (8.18) is given by

$$\Delta_k\Delta_k^T = \begin{bmatrix} \Delta_{k,1}^2 & \Delta_{k,2}\Delta_{k,1} & \cdots & \Delta_{k,P}\Delta_{k,1} \\ \Delta_{k,1}\Delta_{k,2} & \Delta_{k,2}^2 & \cdots & \Delta_{k,P}\Delta_{k,2} \\ \vdots & \vdots & \ddots & \vdots \\ \Delta_{k,1}\Delta_{k,P} & \Delta_{k,2}\Delta_{k,P} & \cdots & \Delta_{k,P}^2 \end{bmatrix}. \tag{8.19}$$

In (8.19), note that for any $j = 1, 2, \ldots, P$, the only value that $\Delta_{k,j}^2$ can take is 1. Hence,

$$E\left[\Delta_{k,j}^2\right] = 1. \tag{8.20}$$

Further, because $\Delta_{k,i}$ and $\Delta_{k,j}$ are independent random variables (when $i \neq j$), it follows that

$$E\left[\Delta_{k,i}\Delta_{k,j}\right] = E\left[\Delta_{k,i}\right]E\left[\Delta_{k,j}\right] = 0 \qquad \forall\, i \neq j. \tag{8.21}$$

From this it follows also that

$$E\left[\Delta_k \Delta_k^T\right] = \mathbf{I} \tag{8.22}$$

where $\mathbf{I}$ denotes the $P \times P$ identity matrix. Applying (8.19)–(8.21) to (8.18) yields

$$E\left[\mathbf{g}_k(\theta_k)\right] = \nabla L(\theta_k) \equiv \mathbf{g}(\theta_k). \tag{8.23}$$

which is the desired result. □

8.3 A parallel SPSA algorithm

In this section, a parallel SPSA algorithm is described that runs several instances of the basic SPSA algorithm, one on each processor. This helps improve the convergence by widening the search space. Numerical tests were performed on various challenging problems on upto 256 processors. Sometimes, convergence is obtained in as few as 2 or 3 iterations. Each processor has its own copy of the vector θ_k, (i.e., the permeability field), denoted say θ_k^{id}. The random vectors Δ_k are generated on each processor and are not the same as those on other processors. This is easily achieved by using a different seed on each processor for the Bernoulli random number generator program that can be found in [115]. Thus each processor also has its copy of the stochastic gradient and updates θ_k according to (8.8).

Figure 8.1 shows the flow-chart of the parallel SPSA algorithm for a single SPSA iteration step. Most of the steps in the figure are self-explanatory. The superscript id in θ_k^{id} represents the processor ID and np is the total number of processors. The main step that needs to be described is the box "AllGather mean/min". Two approaches are implemented to gather θ_k^{id} from each processor and step to $\theta_{k+1}^{\mathrm{id}}$ - the "mean" and "min" approaches. In the "mean" method, as the name indicates, the updated vector, θ_{k+1} broadcast to all processors for the next iteration is simply the mean of the processor updates, $\theta_{k+1}^{\mathrm{id}}$, i.e.,

$$\theta_{k+1} = \frac{1}{\mathrm{np}} \sum_{i=1}^{\mathrm{np}} \theta_{k+1}^{\mathrm{id}}. \tag{8.24}$$

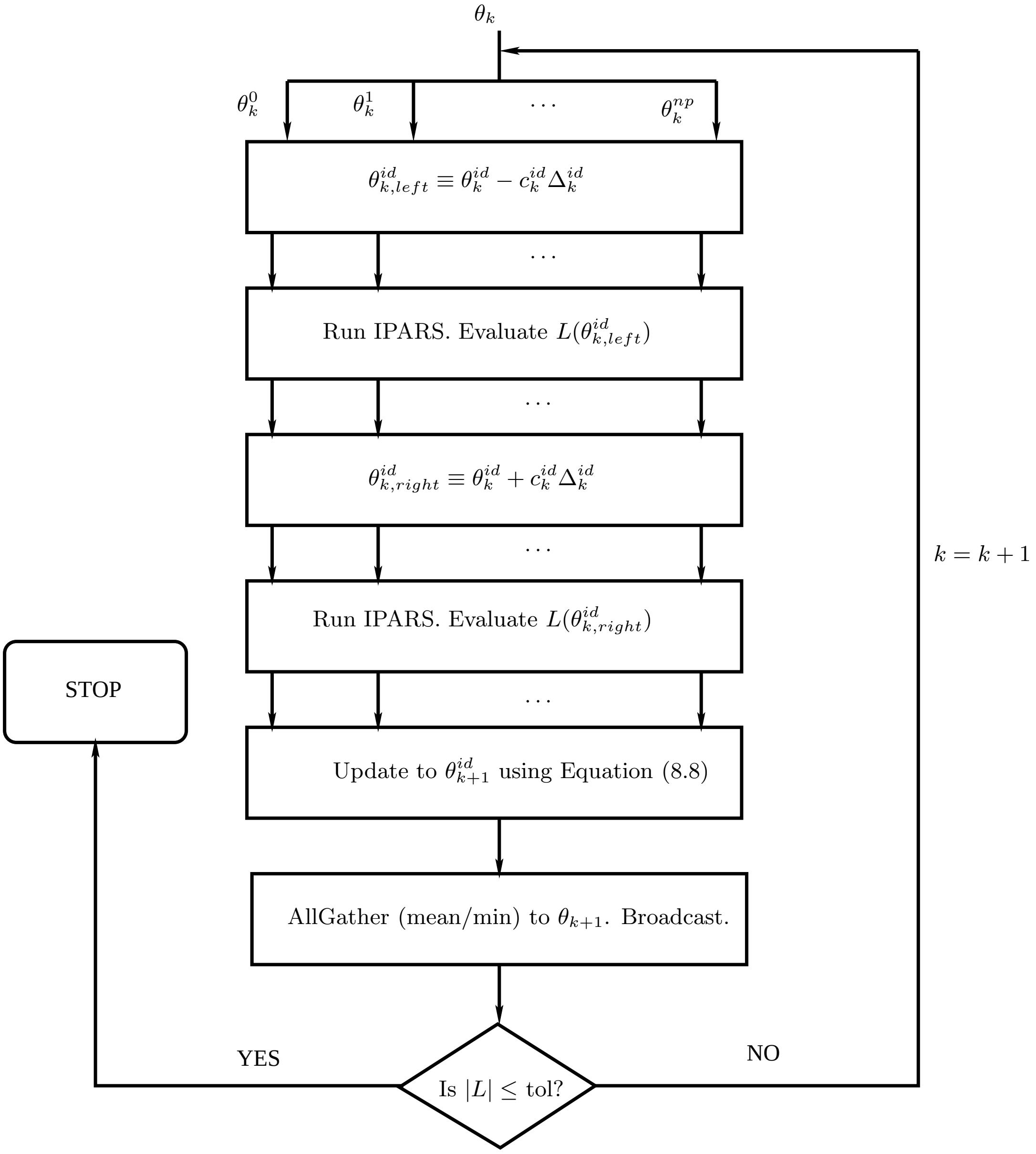

Figure 8.1: A parallel SPSA algorithm

In the "min" method, again as the name indicates, first the processor with the least objective is identified. In other words, the index of that processor, $\mathrm{id}^{\min}$ say, is defined first as

$$\mathrm{id}^{\min} \equiv \min_{1 \leq \mathrm{id} \leq \mathrm{np}} L(\theta_{k+1}^{\mathrm{id}}). \tag{8.25}$$

Then the value of the vector $\theta_{k+1}^{\mathrm{id}^{\min}}$ on the processor $\mathrm{id}^{\min}$ is broadcast to all others for the next iteration.

$$\theta_{k+1} = \theta_{k+1}^{\mathrm{id}^{\min}}. \tag{8.26}$$

The mean method was observed to be more stable and robust in general while the min method, although faster, sometimes exhibited the tendency to get trapped in local minima. Each box with text “Run IPARS..” in the flow-chart of Figure 8.1 is a forward run of the simulator with the value of permeability being calculated from the current perturbation of the value of vector, θ_k^{id} (i.e., left or right perturbation). It is also noted that in practise, the implementation takes the components of θ_k on each processor to be the coefficients of $\ln \mathbf{x}$ in place of $\mathbf{x}$. (i.e., natural log of permeability instead of permeability), since the permeabilities can vary by several orders of magnitude in most real-world problems. The permeability $\mathbf{x}$ can then be easily calculated from the $\ln \mathbf{x}$ using an exponential transormation.

8.4 Numerical results

Two examples are presented in this section. In the first example, a 2-d heterogeneous permeability field based on the 10^{th} SPE project is used to test the parallel parameter estimation and history matching implementation. The second example likewise determines the heterogeneous permeability field and performs history matching for an upscaled version of the “Brugge” synthetic field test case [132]. For both tests, basis functions are first generated using sample realizations as described in Section 8.1. A total of 8 basis functions are used in the expansion of permeability for the first example where an isotropic permeability field is assumed. A total of 10 basis functions for each direction (i.e., K_{xx}, K_{yy} and K_{zz}) is assumed for the second example (a non-isotropic case). Both examples use the hydrology (oil-water), two-phase model as the base model in IPARS to perform history matching and parameter estimation. Both problems were tested on various parallel platforms including the Bevo2 and Ranger linux cluster at The University at Austin and Blue Gene cluster, IBM.

Property	Value
Simulation end-time, days	1000.0
Grid dimensions	100×1×20
Physical dimensions, m^3	2500×25×50
Flowing phases modeled	Gas, Oil
Reference gas density, lb/ft^3	0.06
Gas viscosity, cp	0.01
Reference oil density, lb/ft^3	43.68
Oil viscosity, cp	1.0
Gas compressibility	2.0×10^{-4}
Oil compressibility	1.0×10^{-6}
Initial (residual) gas pressure, psi	1000
Initial (residual) gas conc., lb/ft^3	0.006
Medium porosity	0.2
Number of wells	2 (gas-inj. and oil-prod.)
Gas injection rate, lb/day	43.84
BHP of oil-prod. well, psi	995.0

Table 8.1: Parameter Estimation: Summary of problem data for Example 1 (based on 10^{th} SPE permeability set)

8.4.1 Example 1: Sensor tests

In this example, the goal was to perform history matching and estimate the permeability field (assuming a known "true" permeability field). Knowledge of the "true" permeability field only serves to validate the final answer and is not required (and is in fact not known) in practise. Without this assumption, the parallel SPSA implementation can guarantee that the objective function is minimized, but that does not necessarily mean that the minmizer is the (unique) real permeability field. In practise, the objective functions can have several local minima, hence it is important to ensure that the algorithm not only minimized the objective function, but that it is also converging to the "true" permeability field.

In this example, different objective function combinations based on different sensor combinations were tested (by activating or deactivating the weight functions $w_{\mathbf{f},i}$ in (8.6)). The problem simulates an oil-gas immiscible model using the hydrology model in IPARS. This is achieved by treating in the input, oil-phase as the actual "gas-phase" by assigning the properties of gas to it. Like-

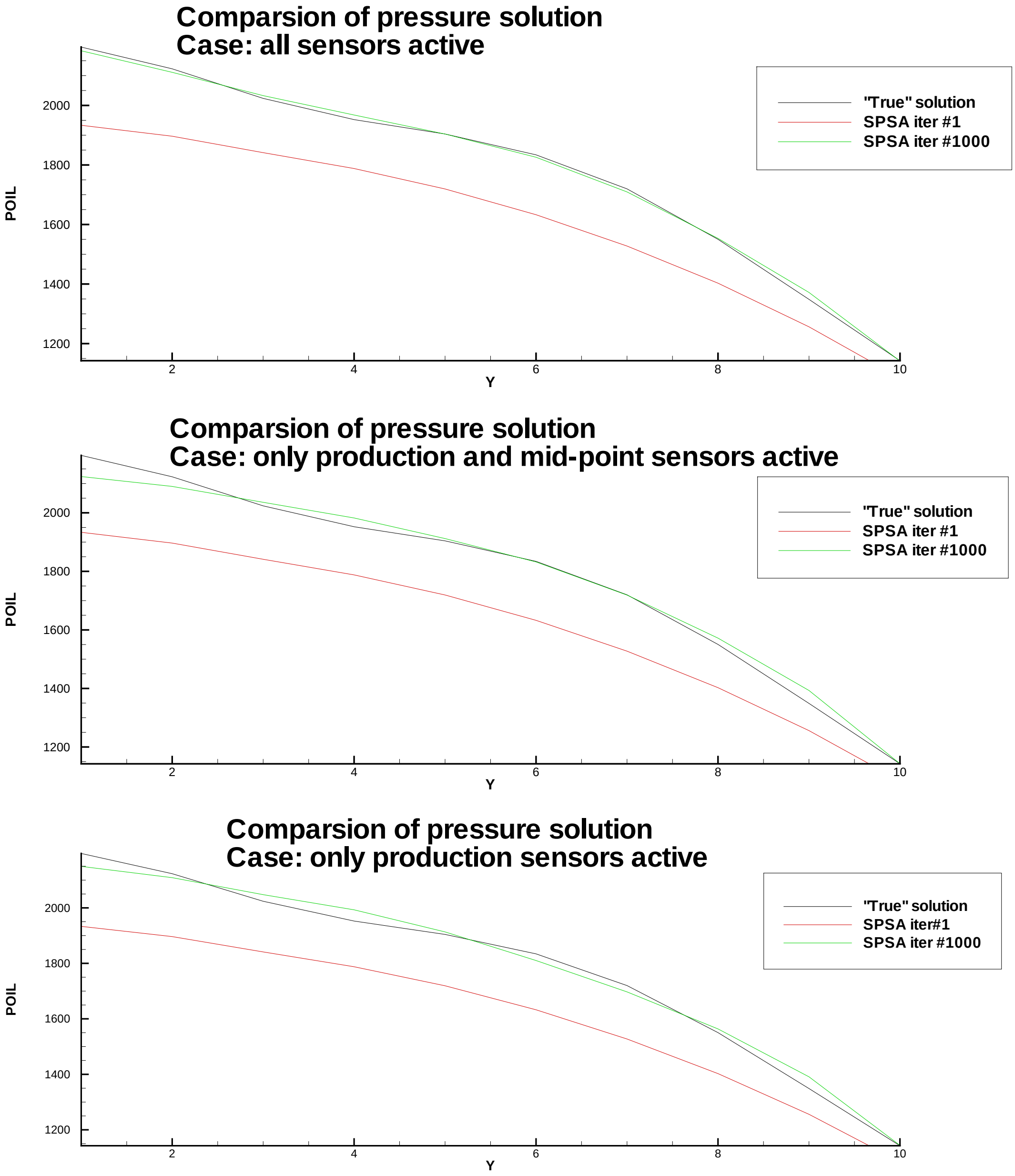

Figure 8.2: Example 1: History matching of oil-phase pressures based on sensor choices.

wise, the water-phase is treated in the input as the actual “oil-phase”. Then the oil-phase (actually “gas”) is injected to produce water (actually “oil”). While this may sound confusing, it is quite common in reservoir simulation to re-use existing two- or three-phase codes to solve problems in contexts they may not have been designed for. The full set of properties $\mathcal{P}$, is available for use in the

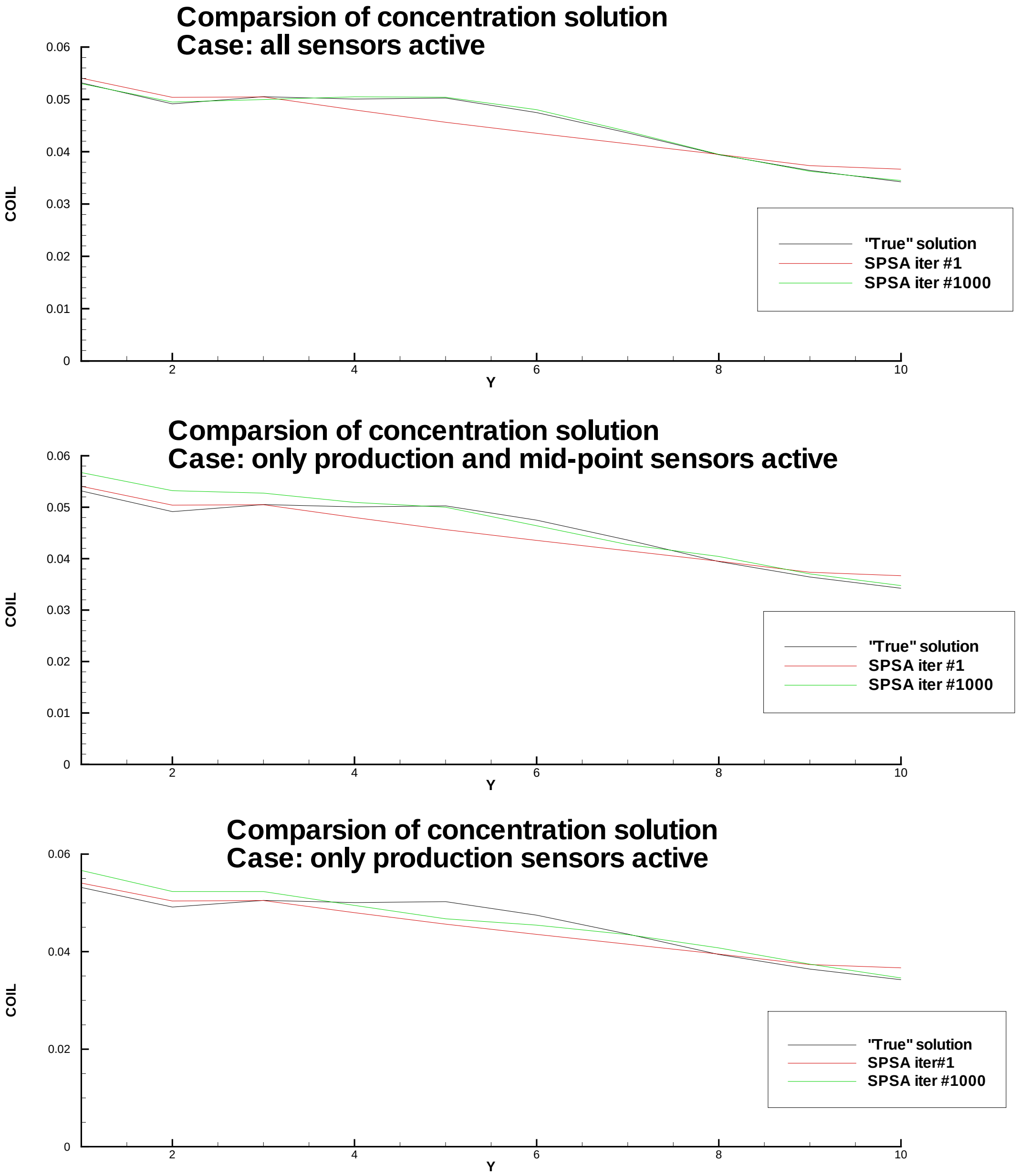

Figure 8.3: Example 1: History matching of oil-phase concentrations based on sensor choices.

objective function but as mentioned, some maybe "turned-off" by setting the weights to zero. It is also noted that only the production well was included in the objective calculations. Table 8.1 summarizes the problem data describing this example.

Since the "true" θ^*, i.e., the coefficients corresponding to the actual

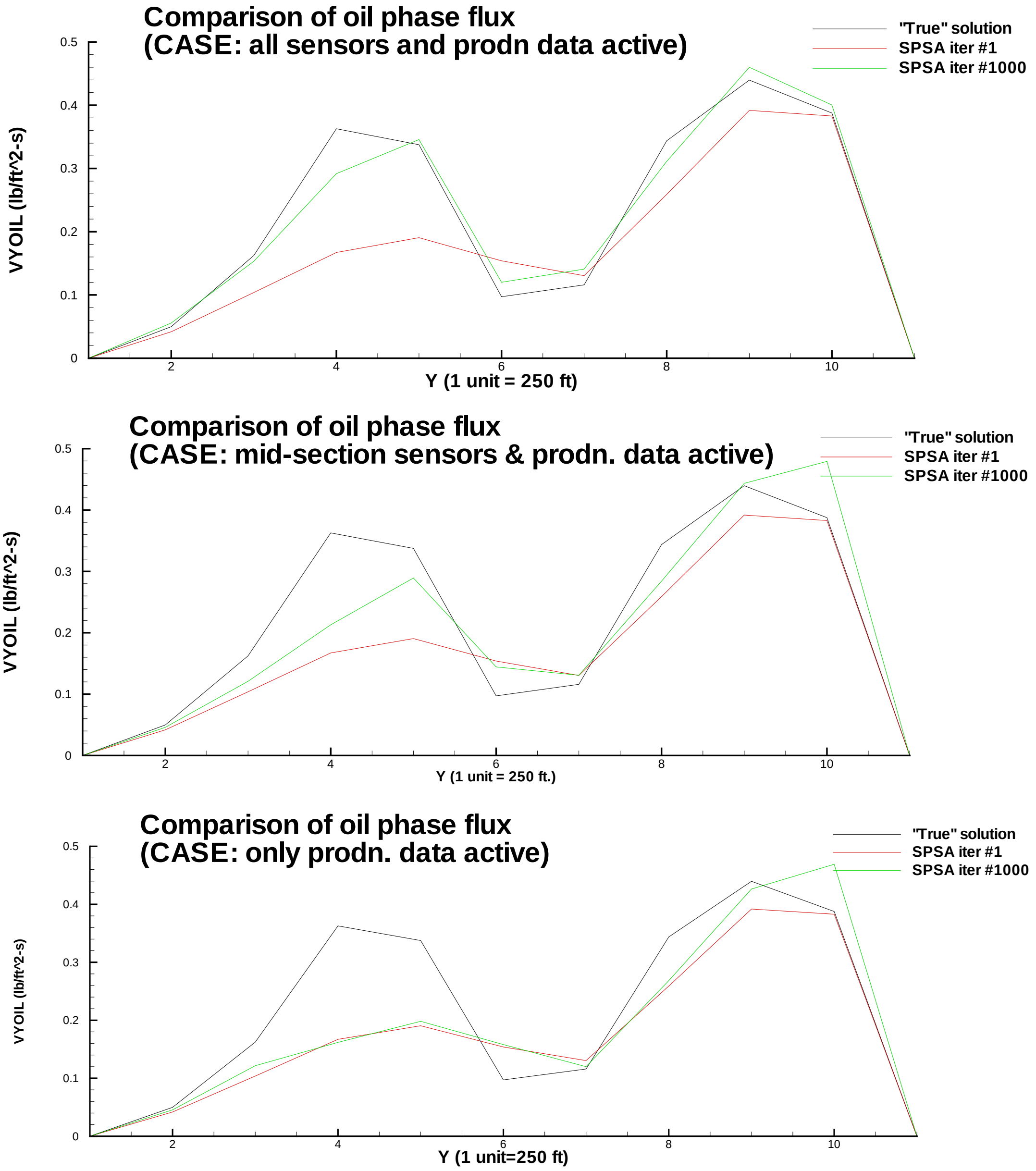

Figure 8.4: Example 1: History matching of oil-phase fluxes based on sensor choices.

permeability field are known, the problem is first run using the true permeability and the true solution ($\mathbf{p}^*$, $\mathbf{N}^*$, $\mathbf{q}^*$, $\mathbf{u}^*$ and τ^*) are recorded at discrete time instants and at all the grid elements (or faces in case of fluxes). Seismic travel times are recorded as the set of times it takes for seismic waves to travel from one end of the reservoir (from each element face on the "source" end) to the

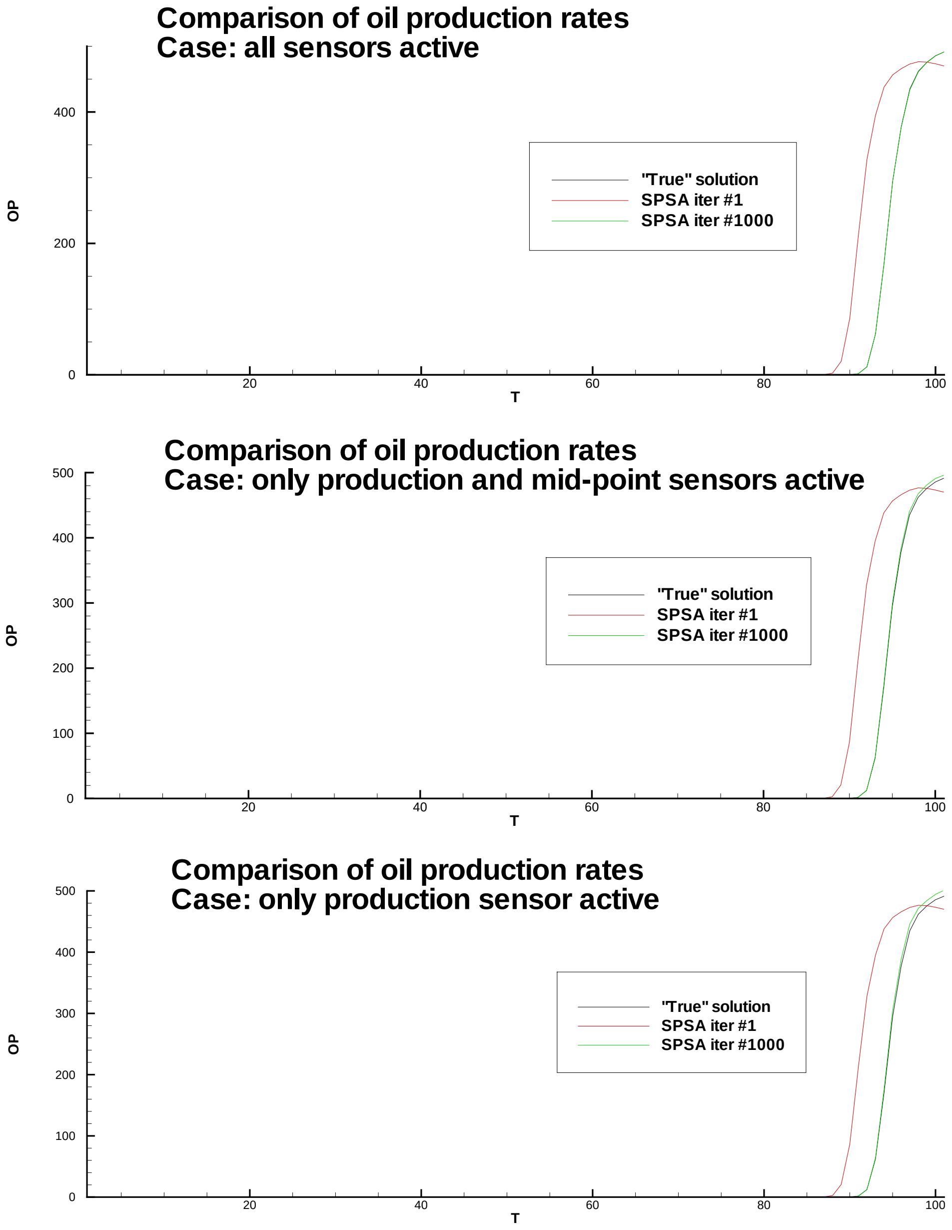

Figure 8.5: Example 1: History matching of well-data based on sensor choices.

other end (each element face on the “target” end). These are then recorded as data. The SPSA iterations are then performed starting with an initial guess θ_0 that is obtained by randomly perturbing the “true” θ^*. A total of 1000 SPSA iterations were computed for this test, although the permeability field converged in very few (early) iterations.

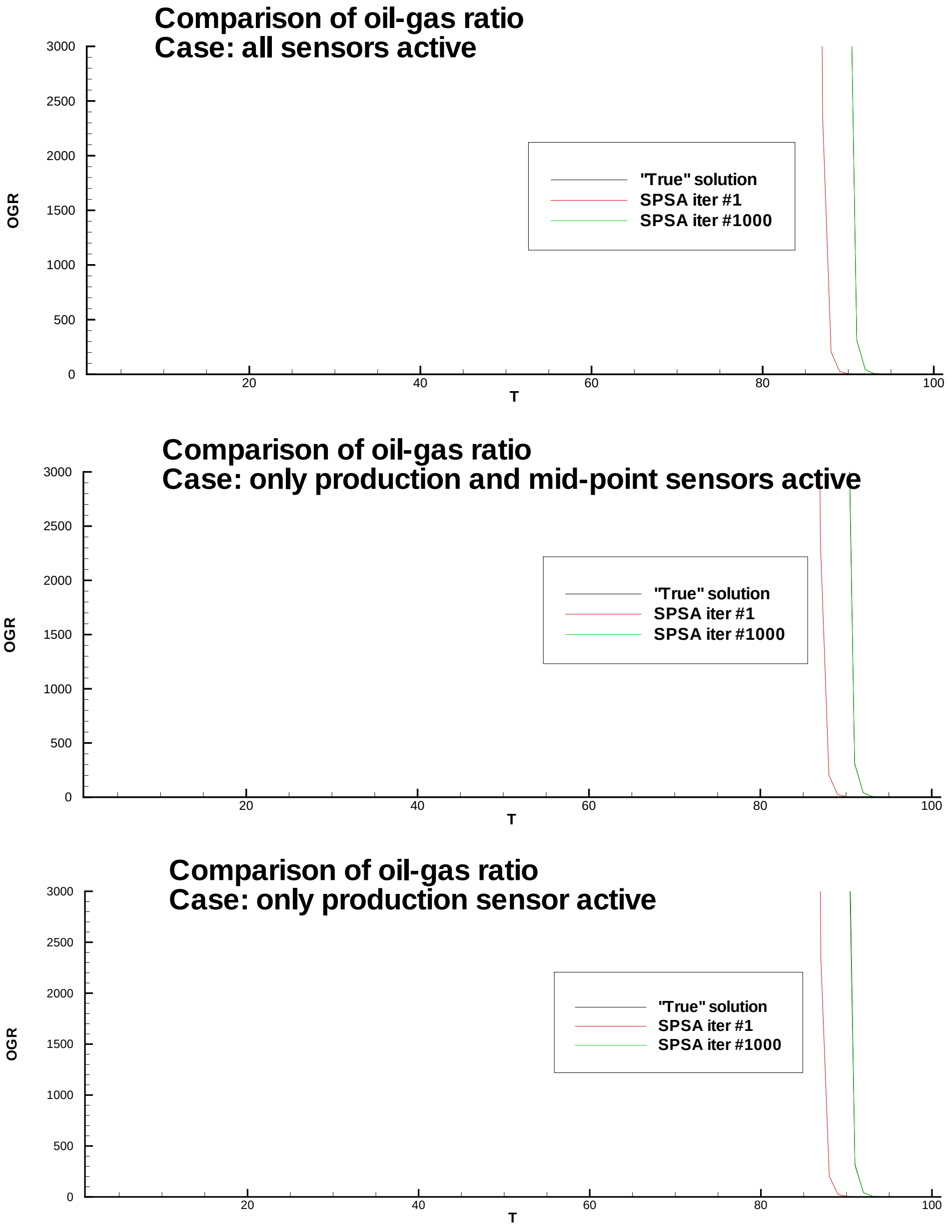

Figure 8.6: Example 1: History matching of well-data based on sensor choices.

Figure 8.2 shows the history matching of the oil-phase pressures (actually, "gas") shown on a section passing through the mid-depth of the 2-d reservoir. In the figure note that the top panel presents the match obtained when all sensors were active (i.e., the weights $w_{\mathbf{f},i} \equiv 1$ at all element locations and time instants). The mid-panel presents the match obtained when only the production well-sensor and the solution sensors (i.e., $w_{\mathbf{p},i}$, $w_{\mathbf{u},i}$, and $w_{\mathbf{N},i}$) at the mid-section

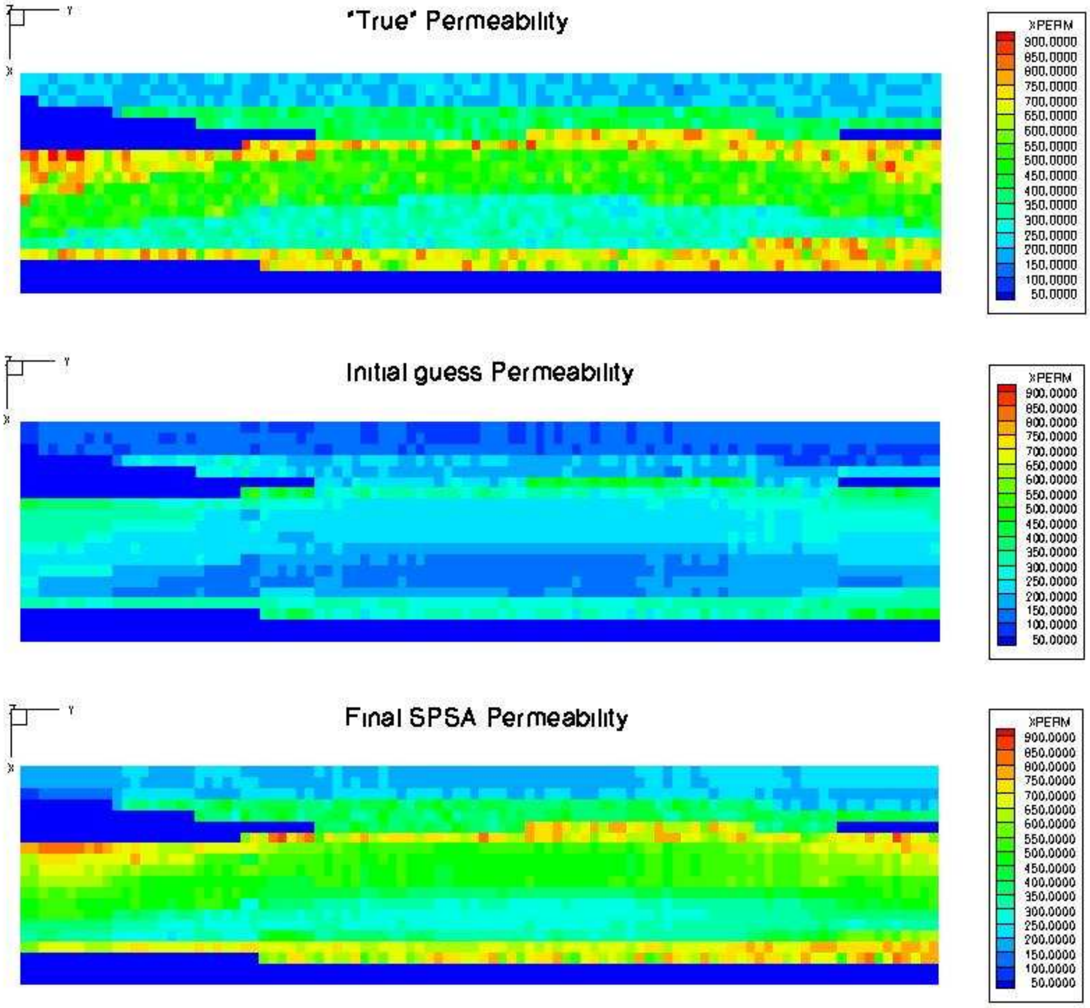
"True" Permeability

Initial guess Permeability

Final SPSA Permeability

Figure 8.7: Example 1: Permeability estimation using SPSA.

were active (i.e., at the location $x = 1250$ m and for all time instants). The bottom panel presents the match obtained when only the production well-sensor was active. The seismic sensor result was not included here because it was found to influence the history match in very insignicant amounts.

From the Figure 8.2, it is clear that sensors are not required at every grid element (and potentially not at every time instant as well) which is good news since installing such costly equipment as sensors at high areal densities can be very expensive and impractical. Figure 8.3 shows a similar match for the oil-phase concentration (actually "gas") at a section passing through the mid-depth of the reservoir. Once again a fairly good match is obtained with fewer measurements. As a demonstration of the flux matches, Figure 8.4 shows the history match obtained for oil-phase fluxes (actually “gas”) at the same section as the previous cases.

It is observed that flux match is poorer when fewer sensors are used (as opposed to the quality of the pressure and concentration history matches). Finally, the production well-data history matches (gas-production and oil-gas ratio) and the permeability estimation (for the case when only the mid-section and production well sensors are active) is shown in the Figures 8.5, 8.6 and 8.7 respectively. From these graphs, the convergence of the SPSA method can be seen to be very effective.

8.4.2 Example 2: Brugge field test

In this example, a synthetic reservoir referred to as the Brugge field is used for the purpose of history matching and permeability estimation. This synthetic field was constructed by the Norwegian research center, TNO in February 2008 for a comparative case study on history matching and reservoir characterization. It consisted of 104 upscaled realizations of a 3-D geological model with well-log data from 30 wells with fixed spatial positions; first 10 years production history; inverted time-lapse seismic data in terms of pressures and saturations as well as economic parameters for oil, water and discount rates. A more detailed description as well as the data from the field can be found at [132]. This problem is very challenging for several reasons. The computational domain is a full 3-d domain, it is irregular in geometry with a geologic fault as shown in Figure 8.4.2. The permeability field is anisotropic and very heterogeneous and hence, many more unknowns have to be estimated in this case. Finally, there are 30 wells driving the flow in this oil-water problem (actually oil-water!). There are 10 water injection wells and 20 oil production wells that can be shut-in based on rate or bottom-hole constraints. All these combine to make this a challenging problem. Table 8.2 summarizes the data that describe the problem that was solved. It is noted that well # 19 (a production well) was the

Property	Value
Simulation end-time, years	20.0
Grid dimensions	21×57×35
Physical dimensions, ft^3	21000×57000×1750
Flowing phases modeled	Oil, Water
Reference oil density, lb/ft^3	56.0
Oil viscosity, cp	1.29
Reference water density, lb/ft^3	62.6
Water viscosity, cp	0.32
Oil compressibility	9.26×10^{-6}
Water compressibility	3.0×10^{-6}
Initial oil pressure, psi	≈2500
Initial oil conc., lb/ft^3	Residual-water
Medium porosity	≈0.2
Number of wells	30 (10 water-inj. and 20 oil-prod.)
Water injection rate, lb/day	4000.0
Oil-prod rate, lb/day	2000.0

Table 8.2: Parameter Estimation: Summary of problem data for Example 2 (Brugge field test)

only bottom-hole pressure specified well without any constraint. All other wells were rate specified with a bottom-hold pressure constraint for shut-in. It is also noted that different injectors start injecting water at different times (earliest at $t = 600$days) while the producers start producing as early as $t = 0$ days.

The first challenge with this problem was in accurately modeling the geometry of the domain with the faults. A stair-stepped approximation was once again employed to treat the geometry in keeping with the stencil resulting from mixed FEM. A bounding box grid of 35×21×57 was used and suitably interpolated to get values of the properties at corners of the box that intersect with the actual domain. For all other points, negative values are assigned and these are used to keyout the elements that are actually inactive in the bounding box (i.e., for the corners that do not intersect the actual domain). Figure 8.4.2 shows the true and approximated geometries with the initial water saturation and mesh superimposed. The well locations are indicated by colored spheres, black for injectors and orange for producers.

A parallel SPSA history matching simulation was performed on the

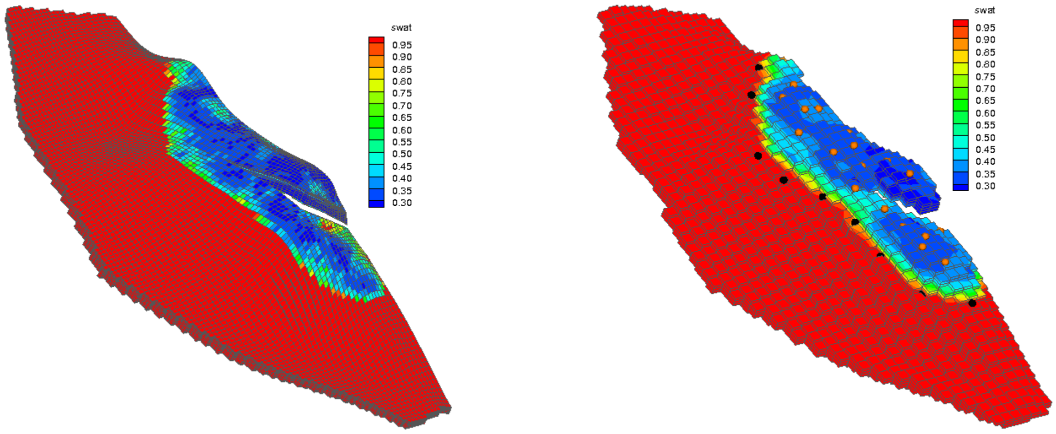

Figure 8.8: Example 2 (Brugge field): True(left), approximate(right) geometry with initial water saturation and grid superimposed

Brugge field for $P = 10$ unknowns in each direction of anisotrop (i.e., a total of 30 unknowns) and a subset ($M = 16$) of the realizations. For proof of concept, the mean permeability was assumed to be the true permeability and data (measurements) derived from the solution corresponding to the mean at prescribed intervals of time at all grid elements. Also, it is assumed that the history matching is performed for 20 year simulation period. Figure 8.9 shows the permeability estimate when the production data and solution (pressures and concentrations) measured at intervals of 5 grid elements in either areal direction are included in the loss function. Since the physical dimensions of the Brugge formation was huge, this was a reasonable areal density (about 1 sensor every 4 square km) for sensor locations. It is observed that even though the initial guess was very far from the "target" or "true" permeability, the algorithm coverges in as few as 5-10 iterations.

Figure 8.4.2 shows the history match obtained with respect to bottom hole pressures (shown for rate specified producing well #21) and cumulative production rate (shown for bottom hole pressure specified producing well #19). The matches obtained for all wells were equally good. These parallel runs were performed on up to 64 processors on the Bevo2 cluster at ICES as well as on the Ranger cluster (at TACC, The Univerisity of Texas at Austin) on up to 256 processors.

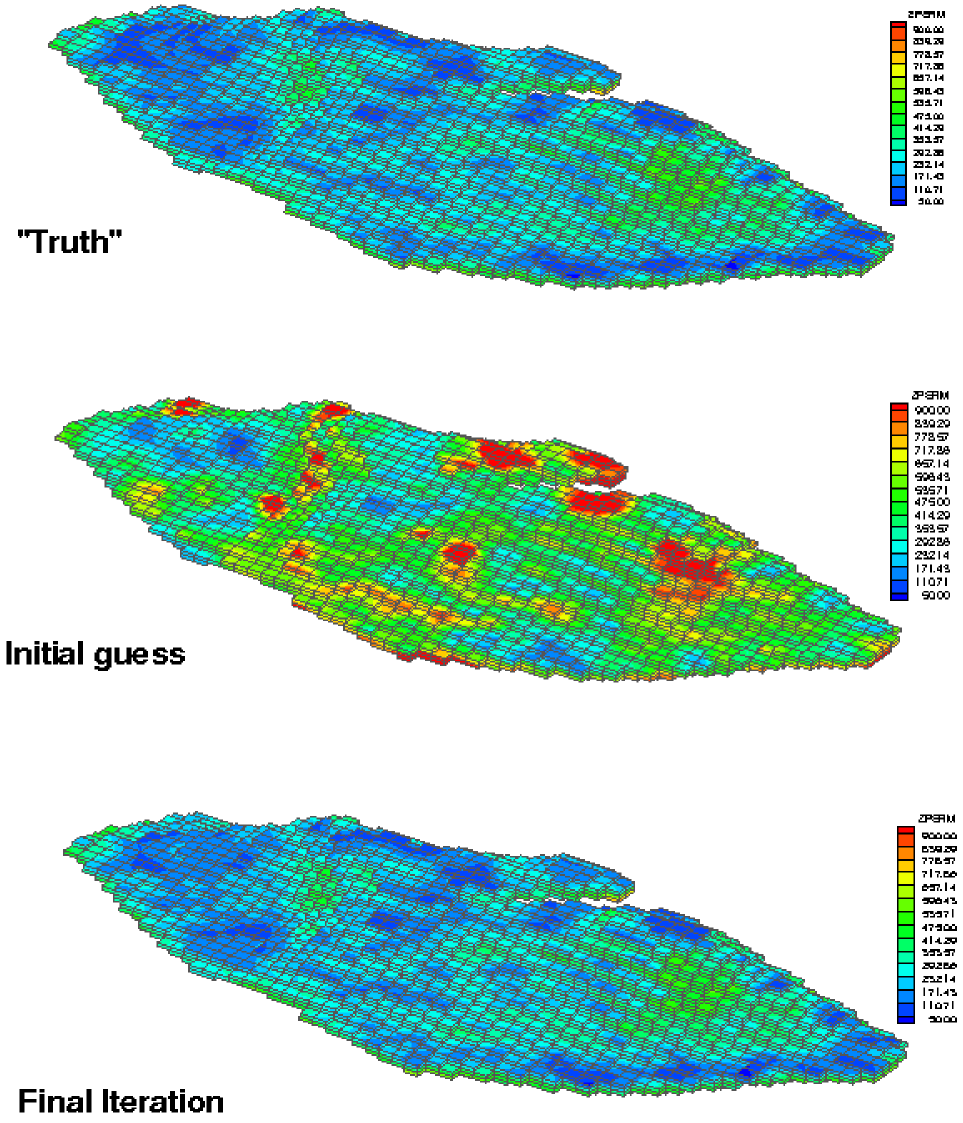

Figure 8.9: Example 2 (Brugge field test): Estimate of permeability with SPSA iteration number.

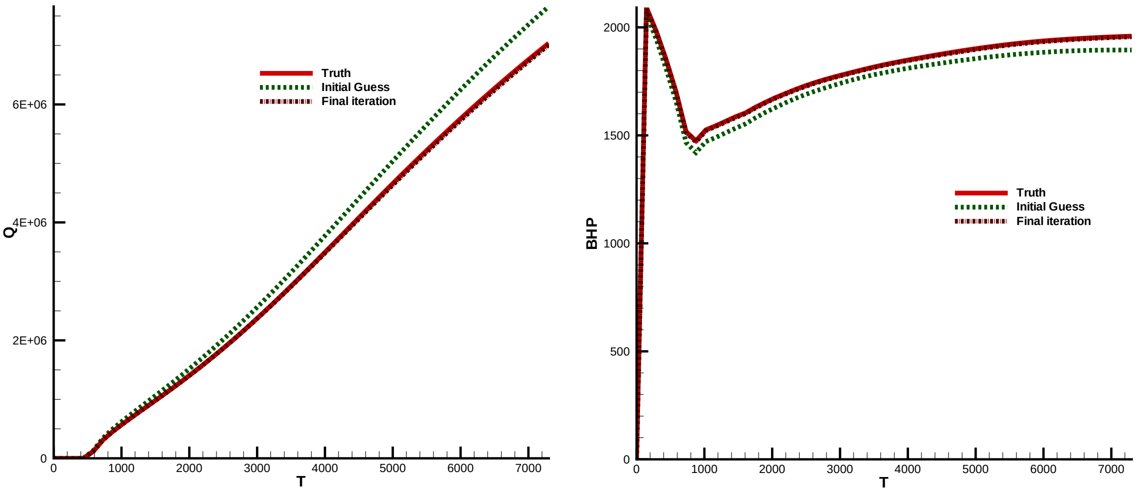

Figure 8.10: Example 2 (Brugge field test): Well 19 (left) production curves and well 21 (right) BHP history match

Chapter 9

Conclusions and future work

In this chapter, the major results of this work are summarized very briefly and conclusions are drawn on the basis of these results. Some potential future applications are addressed.

The analysis and convergence of multiscale MMFEM has been successfully established for single phase slightly compressible (non-linear) flow in Chapter 3. Multiphysics coupling of flow and (reactive) transport has been analysed for single phase flow coupled to transport and numerical results obtained for the case of single and two phase flow coupled to reactive transport using mortar and non-mortar FEM (EV-MFEM). Convergence of EV-MFEM has been established for slightly compressible (non-linear) single phase flow and for the species advection diffusion problem in Chapter 4. Further, mortar FEM has been applied to the multi-numerics coupling of different numerical discretizations (such as DG and MFEM) as well as the multscale coupling of porescale network models with continuum scale models of single phase flow. Many numerical results of these problems have been presented in Chapters 5 and 6, respectively.

The major application areas considered have been multiphysics problems such as coupled flow and (reactive) transport as well as more general (EOS) compositional flow problems applied to significant topics such as CO_2 sequestration. The results of these problems strongly indicate that a multiblock (and multimodel) approach to domain decomposition greatly reduces the associated computational cost (in terms of the computation time) without much loss of acccuracy. For example, approximately 50% reduction in computational time has been observed in the modeling of multiphase flow coupled with biologically mediated chemical reactions when non-matching sub-domain grids were used with fine grid located in a small part of the computational domain. Moreover in the coupling of multiphase flow and reactive transport, the EV-MFEM was observed to perform much faster (almost an order of magnitude) than MMFEM for the same problem.

Finally, solving complex compositional flow problems with a large number of components using an EOS model and the associated flash equations can be computationally very expensive. Hence high-fidelity algorithms such as multiscale MMFEM (including multiscale basis implementations) as well as EV-MFEM, that possess the properties of local mass conservation and accurate approximation of the flux variable are of great importance in such problems. This is additionally justified because in most of these problems excessively fine grids are required in several small parts of the domain (around wells, etc.) but coarser grids suffice elsewhere. Additionally, these methods are to be applied in a multimodel setting with complex models such as non-isothermal compositional flow coupled to chemistry being used in a small part of the whole domain (for example around wells and where most of the complex physical dynamics occurs), while computationally cheaper models such as single phase flow are used in the majority of the domain. Further, parallel computations play an important role in such problems due to the sheer size of the physical domains being modeled and the excessively fine grids required in parts of the domain.

Several possibilities exist for future directions of this research work. Some of the important future works are listed below.

1 Extensions of EV-MFEM and related methods to multimodel applications wherein complex models such as compositional flow or multiphysics models (such as flow and reactive transport) are applied only in (several) small parts of the domain while significantly cheaper models such as single phase flow are applied elswhere.

2 Extensions of the coupling of DG and MMFEM to two-phase flow problems, coupled single and two phase flow problems in a multimodel setting

or coupled multiphase flow and transport problems (wherein DG is specifically applied to solve the transport equations).

3 Extensions of the coupling of porescale network models and continuum scale models of single phase flow to the case of multiphase flow and time dependent problems.

4 Parallel implementations of the above mentioned items.

Appendices

Appendix A

On stability and accuracy of upwinding schemes

In this appendix, some derivations are presented for the stability and accuracy of the upwind scheme for the reactive transport problem presented in Section 3.5; in particular the advection equation in Section 3.5.2. For simplicity, the analysis is presented for a steady 2-d problem, although it is possible to extend the result to unsteady 2- and 3-d cases. Further for convenience of analysis, it is assumed that the diffusion-dispersion tensor **D** is diagonal, which is the case when the longitudinal and transverse dispersion coefficients are equal; i.e., $d_l = d_t$ in Equation (2.17).

A.1 On stability

Consider the simplified equations,

$$\nabla \cdot \mathbf{J} = r(c_h) \tag{A.1}$$

$$\mathbf{J} = c_h \mathbf{u}_h + \hat{\mathbf{z}}_h, \tag{A.2}$$

where it is assumed that $\mathbf{u}_h$ is known from the solutions to the phase equations (3.9). The focus here is on a simplified continuity equation derived from combined advection-diffusion. The weak form of Equation (A.1), for $1 \leq i \leq n_b$, yields

$$(\nabla \cdot [c_h \mathbf{u}_h + \hat{\mathbf{z}}_h], w)_{\Omega_i} = (r(c_h), w)_{\Omega_i}, \quad w \in W_{h,i}. \tag{A.3}$$

Now, let w be the characteristic function on any given element $E \in \mathcal{T}_{h,i}$, $1 \leq i \leq n_b$. Then, applying the divergence theorem, Equation (A.3) leads to,

$$\int_{\partial E} (c_h \mathbf{u}_h + \hat{\mathbf{z}}_h) \cdot \mathbf{n} \mathrm{d}S = \int_E r(c_h) \mathrm{d}V. \tag{A.4}$$

Assume a uniform rectangular element partition $\mathcal{T}_{h,i}$. Then E is a rectangle and one can apply the quadrature rules (3.84) for $\hat{\mathbf{z}}_h, \tilde{\mathbf{z}}_h$ and the upwind scheme (3.72) for the convection term $c_h\mathbf{u}_h$ introduced in Section 3.5.2. Equation (A.4), written assuming E is the j^{th} element in the x-direction and the k^{th} element in the y-direction then reduces to the form,

$$a_{jk}c_{h,jk} = \sum_{l,m} a_{lm}c_{h,lm} + b_{jk}, \tag{A.5}$$

where $(l,m) \in N_{jk} \equiv \{(j-1,k),(j+1,k),(j,k-1),(j,k+1)\}$ and it can be verified that, for strict interior elements,

$$\begin{aligned}
a_{j+1,k} &= \left(\frac{2(D^{-1}_{11,j+1,k} + D^{-1}_{11,jk})^{-1}}{(x_{j+1}-x_j)} + \max\{-\mathbf{u}_h\cdot\mathbf{n}_1, 0\}\right)(y_{k+\frac{1}{2}} - y_{k-\frac{1}{2}}),\\
a_{j-1,k} &= \left(\frac{2(D^{-1}_{11,j-1,k} + D^{-1}_{11,jk})^{-1}}{(x_j-x_{j-1})} + \max\{\mathbf{u}_h\cdot\mathbf{n}_2, 0\}\right)(y_{k+\frac{1}{2}} - y_{k-\frac{1}{2}}),\\
a_{j,k+1} &= \left(\frac{2(D^{-1}_{22,j,k+1} + D^{-1}_{22,jk})^{-1}}{(y_{k+1}-y_k)} + \max\{-\mathbf{u}_h\cdot\mathbf{n}_3, 0\}\right)(x_{j+\frac{1}{2}} - x_{j-\frac{1}{2}}),\\
a_{j,k-1} &= \left(\frac{2(D^{-1}_{22,j,k-1} + D^{-1}_{22,jk})^{-1}}{(y_k-y_{k-1})} + \max\{\mathbf{u}_h\cdot\mathbf{n}_4, 0\}\right)(x_{j+\frac{1}{2}} - x_{j-\frac{1}{2}}),\\
a_{jk} &= \sum_{(l,m)\in N_{jk}} a_{lm} - r_U|E|\\
&+ (\mathbf{u}_h\cdot\mathbf{n}_1 + \mathbf{u}_h\cdot\mathbf{n}_2)(y_{k+\frac{1}{2}} - y_{k-\frac{1}{2}})\\
&+ (\mathbf{u}_h\cdot\mathbf{n}_3 + \mathbf{u}_h\cdot\mathbf{n}_4)(x_{j+\frac{1}{2}} - x_{j-\frac{1}{2}}),\\
b_{jk} &= r_M|E|.
\end{aligned} \tag{A.6}$$

In equations (A.6) $\mathbf{n}_1, \mathbf{n}_2, \mathbf{n}_3$ and $\mathbf{n}_4$ represent the unit outward normals to the element E on its x+, x-, y+ and y- faces, respectively. Further, x_j, y_k are the co-ordinates of the element center in a Cartesian frame and $x_{j+\frac{1}{2}} = 0.5(x_j + x_{j+1})$. The area of element E is represented by the measure $|E|$. For boundary elements or elements on the interface between two sub-domains, the value of the concentrations in Equation (A.5) are taken from the Dirichlet values or the projected values from the adjacent sub-domain's interface; see Section 3.5.4. For a boundary element on the x- face, $D_{11,j-1,k} = \infty$ (this is motivated by flow through a medium with $\varphi = 1.0$), so that the harmonic mean is simply $2D_{11,jk}$; the values for boundary faces in the y-direction follows analogously.

Finally, assume that $r \in C^1$, so that by Taylor's expansion, the right hand side may be written as

$$r(c_h) = r(c_h^*) + r'(c_h^*)(c_h^* - c_h) + O(\delta c_h^2), \tag{A.7}$$

where $\delta c_h = c_h^* - c_h$. Then, in the limit as $c_h = c_h^*$, $r(c_h) = r(c_h^*)$ is recovered. Equation (A.7) constitutes a linearization of the right hand term of Equation (A.4), $r(c_h)$ after the higher order term is dropped. One may chose c_h^* to be the current iterate in the numerical scheme. Then Equation (A.7) can be re-written as

$$r = r_M + r_U c_h, \tag{A.8}$$

where $r_M = r(c_h^*) - r'(c_h^*)c_h^*$, $r_U = r'(c_h^*)$ denote the mean and the coefficient of departure from the mean. This motivates their appearance in (A.6).

The linear system resulting from equations (A.6) is non-symmetric because of the upwinding. This system can be solved by a suitable iterative scheme, say, Gauss-Seidel. The concentrations are updated by the iteration:

$$c_{h,jk}^{n+1} = \frac{b_{ij} + \sum_{(lm) \in N_{jk}} a_{lm} c_{h,lm}^n}{a_{jk}}. \tag{A.9}$$

It is known from linear algebra, that diagonal dominance is required for stability of such an iterative scheme. In Equation (A.6), note that the coefficients a_{lm} are all non-negative. Thus, if the term r_U is negative (which is indeed the case for radioactive decay) and if the velocity $\mathbf{u}_h$ is divergence free (which is true for incompressible fluids; i.e., when $\rho \equiv \rho_0$), then clearly, the system described by (A.6) is diagonally dominant. Thus an iterative scheme applied to this system with the upwinded method is guaranteed to be stable.

Note that when a similar analysis is performed for a central difference approximation (instead of an upwind scheme) for the concentration on the face of an element that arises in the convection term), the resulting equations analogous to (A.6), are as follows:

$$\begin{aligned}
a_{j+1,k} &= \Big(\frac{2(D^{-1}_{11,j+1,k} + D^{-1}_{11,jk})^{-1}}{(x_{j+1} - x_j)} - \frac{\mathbf{u}_h \cdot \mathbf{n}_1}{2}\Big)(y_{k+\frac{1}{2}} - y_{k-\frac{1}{2}}), \\
a_{j-1,k} &= \Big(\frac{2(D^{-1}_{11,j-1,k} + D^{-1}_{11,jk})^{-1}}{(x_j - x_{j-1})} + \frac{\mathbf{u}_h \cdot \mathbf{n}_2}{2}\Big)(y_{k+\frac{1}{2}} - y_{k-\frac{1}{2}}), \\
a_{j,k+1} &= \Big(\frac{2(D^{-1}_{22,j,k+1} + D^{-1}_{22,jk})^{-1}}{(y_{k+1} - y_k)} - \frac{\mathbf{u}_h \cdot \mathbf{n}_3}{2}\Big)(x_{j+\frac{1}{2}} - x_{j-\frac{1}{2}}), \\
a_{j,k-1} &= \Big(\frac{2(D^{-1}_{22,j,k-1} + D^{-1}_{22,jk})^{-1}}{(y_k - y_{k-1})} + \frac{\mathbf{u}_h \cdot \mathbf{n}_4}{2}\Big)(x_{j+\frac{1}{2}} - x_{j-\frac{1}{2}}), \\
a_{jk} &= \sum_{(l,m)\in N_{jk}} a_{lm} - r_U|E| \\
&+ (\mathbf{u}_h \cdot \mathbf{n}_1 + \mathbf{u}_h \cdot \mathbf{n}_2)(y_{k+\frac{1}{2}} - y_{k-\frac{1}{2}}) \\
&+ (\mathbf{u}_h \cdot \mathbf{n}_3 + \mathbf{u}_h \cdot \mathbf{n}_4)(x_{j+\frac{1}{2}} - x_{j-\frac{1}{2}}), \\
b_{jk} &= r_M|E|. \qquad \text{(A.10)}
\end{aligned}$$

From Equation (A.10), it is observed that the off-diagonal entries a_{lm} can be negative for Peclet numbers (Pe) greater than 2; this accounts for the spatial oscillations in the numerical solution. Further diagonal dominance is not satisfied; for e.g., when $D_{ij} \equiv 0$ and the velocity $\mathbf{u}_h$ is a constant, then $a_{jk} = 0$ in the absence of the reaction term r. It is to be noted however that even the first-order upwind scheme introduced in Section 3.5.2 fares poorly for convection-dominated problems (i.e., Pe $\to \infty$), although the scheme is stable. In such cases, higher-order Godunov schemes presented also in Section 3.5.2 become necessary.

A.2 On accuracy

It can be shown that a central difference scheme for the concentrations in the convection term yields a solution that is $O(h^2)$ correct within the interior, while a first order upwinded scheme introduced in Section 3.5.2 yields a solution that is only $O(h)$ correct within the interior. For details, the reader is referred to [106]. A simple proof of this is readily obtained by a Taylor's expansion of the concentration on the face about the adjacent cell-center values with either scheme. For the upwind scheme, assuming a 1-d uniform mesh,

$$\begin{aligned} c_h(x_j) &= c_h(x_{j+\frac{1}{2}}) - \frac{h}{2}c'_h(x_{j+\frac{1}{2}}) + \frac{h^2}{4}c''_h(x_{j+\frac{1}{2}}) + O(h^3) \\ c_h(x_{j+1}) &= c_h(x_{j+\frac{1}{2}}) + \frac{h}{2}c'_h(x_{j+\frac{1}{2}}) + \frac{h^2}{4}c''_h(x_{j+\frac{1}{2}}) + O(h^3). \end{aligned} \tag{A.11}$$

In either case, it is observed that $c_h(x_{j+\frac{1}{2}}) = c_h(x_j) + O(h)$ or $c_h(x_{j+\frac{1}{2}}) = c_h(x_{j+1}) - O(h)$, depending on the upwind direction. Thus the first-order upwind scheme is $O(h)$ accurate. Ofcourse it can be shown as for example in [44] that second and higher-order upwinding schemes (as for example higher-order Godunov schemes presented in Section 3.5.2) are higher-order accurate in space. In a similar manner, for a central difference scheme that approximates the concentration on the face, one has upon adding the equations (A.11),

$$c_h(x_{j+\frac{1}{2}}) = \frac{1}{2}(c_h(x_j) + c_h(x_{j+1})) - \frac{h^2}{8}c''_h(x_{j+\frac{1}{2}}) + O(h^3) \tag{A.12}$$

Thus, clearly, the central difference approximation is $O(h^2)$ correct.

Appendix B

Compositional model theory

In this appendix, some auxiliary topics and terms are introduced in the constitutive laws in relation to the compositional model theory briefly presented in Section 7.1. These hold for the particular choice of equation of state and in general, some of the expressions can vary for other equations of state.

B.1 Phase equilibrium: Z-factor and fugacity equations

As introduced in Section 7.1, IPARS uses a Peng-Robinson equation of state (EOS) with a volumetric shift parameter to calculate a Z-factor for each non-aqueous phase. Recall that the resulting cubic equation has the form

$$\mathcal{R}_e \equiv \bar{Z}_\alpha^3 + h_1(B_\alpha)\bar{Z}_\alpha^2 + h_2(A_\alpha, B_\alpha)\bar{Z}_\alpha + h_3(A_\alpha, B_\alpha) = 0. \tag{B.1}$$

where $\bar{Z}_\alpha = Z_\alpha + C_\alpha$. The parameters $h_1(B_\alpha)$, $h_2(A_\alpha, B_\alpha)$ and $h_3(A_\alpha, B_\alpha)$ are given by

$$\begin{aligned} h_1(B_\alpha) &= 1 - B_\alpha \,, \\ h_2(A_\alpha, B_\alpha) &= A_\alpha - 3B_\alpha^2 - 2B_\alpha \,, \text{ and} \\ h_3(A_\alpha, B_\alpha) &= -(A_\alpha B_\alpha - B_\alpha^2 - B_\alpha^3). \end{aligned} \tag{B.2}$$

The parameters A_α, B_α, and C_α are given by the expressions

$$\begin{aligned} A_\alpha &= \frac{p}{R^2T^2} \sum_i \sum_j \xi_i^\alpha \xi_j^\alpha (1 - \delta_{ij}) \sqrt{a_i(T) a_j(T)} \,, \\ B_\alpha &= \frac{p}{RT} \sum_i \xi_i^\alpha b_i \,, \text{ and} \\ C_\alpha &= \frac{p}{RT} \sum_i \xi_i^\alpha c_i. \end{aligned} \tag{B.3}$$

In equations (B.3), δ_{ij} is the binary interaction coefficient (between non-aqueous components i and j), b_i is a component parameter calculated from the input values of critical pressure and critical temperature, c_i is a component parameter calculated from input values of volumetric shift, critical pressure, and critical temperature and finally a_i is a component parameter calculated from input values of critical temperature, pressure and accentric factor. IPARS generates EOS tables for different values of temperatures (in a granular manner) in order to minimize the calculation of A_α, B_α and C_α.

Phase equilibrium at constant temperature and pressure requires that the component fugacities be equal in each non-aqueous phase, i.e., $f_i^g = f_i^l$. But this is only a necessary and not sufficient condition for phase equilibrium. Strictly speaking, phase equilibrium requires also that the "Gibb's" free energy be a minimum. However, for most reservoir model simulations, it is sufficient from experience to take the equality of fugacities to be the defining condition for phase equilibrium. Rather than solving the equations above for fugacity, IPARS solves for $\ln K_i$ and works with the fugacity coefficients Φ_i^α instead of fugacities. To this end, it is noted that $f_i^\alpha = \xi_i^\alpha p \Phi_i^\alpha$. The logarithm of the fugacity coefficient for the special case of the Peng-Robinson EOS is given by

$$\begin{aligned}\ln \Phi_i^\alpha &= -C_i + \frac{B_i}{B_\alpha}\left(\bar{Z}_\alpha - B_\alpha\right) - \ln\left(\bar{Z}_\alpha - B_\alpha\right)\\ &- \frac{A_\alpha}{2\sqrt{2}B_\alpha}\left(\frac{2\sum_j \xi_j^\alpha A_{ij}}{A_\alpha} - \frac{B_i}{B_\alpha}\right)\ln\left(\frac{\bar{Z}_\alpha + \left(1+\sqrt{2}\right)B_\alpha}{\bar{Z}_\alpha + \left(1-\sqrt{2}\right)B_\alpha}\right)\end{aligned} \qquad \text{(B.4)}$$

In Equation (B.4), $B_i = \frac{pb_i}{RT}$, $A_{ij} = \frac{p(1-\delta_{ij})\sqrt{a_i(T)a_j(T)}}{R^2T^2}$, and $C_i = \frac{pc_i}{RT}$. With these modifications, phase equilibrium is governed by the equations

$$\mathcal{R}_i \equiv \ln \Phi_i^l - \ln \Phi_i^g - \ln K_i = 0 \quad \text{or} \quad \mathbf{R}^{\mathrm{eq}}(\mathbf{x}^{\mathrm{eq}}) = 0 \qquad \text{(B.5)}$$

where $\mathbf{x}^{\mathrm{eq}} \equiv \left[\{\ln \Phi_i^l\}, \{\ln \Phi_i^g\}, \{\ln K_i\}\right]^T$. Note that the term C_i is not actually required in the logarithmic flash calculations of Equation (B.5) because it is the same for both phases. All two phase cells must undergo flash iterations to satisfy the fugacity equations for phase equilibrium. The flash algorithm assumes that the phase pressure, temperature and overall compositions are constant, starting values of K_i are available and then the steps described in Section 7.1.1. Iterations are performed until either

$$\frac{\sum_i \left[\ln \Phi_i^l - \ln \Phi_i^g - \ln K_i\right]^2}{\sum_j \left[\ln K_i\right]^2} < \varepsilon_{\text{flash}} \text{ or}$$
$$\sum_j \left[\ln K_j\right]^2 < \varepsilon_{\text{triv}}. \tag{B.6}$$

where $\varepsilon_{\text{flash}}$ is the flash tolerance and $\varepsilon_{\text{triv}}$ is the "trivial" tolerance for the case when $K_i \equiv 1$.

IPARS must check single phase cells throughout the reservoir every time step to see if each single phase cell will split into two phases. This is a computationally intensive process and the program has a few options to reduce the cost. The program tests for phase splits for only selected cells within the reservoir unless a keyword (TESTALL) is specified. When the keyword is false, the only cells that are tested are single phase cells adjacent to two phase cells, single phase cells that contain well completions, single phase vapor cells beside single phase liquid cells (and vice-versa) and single phase cells on processor boundaries when the program is run in parallel mode. IPARS has several techniques in order to determine when a single phase splits into two or more phases. The first technique based on a stability test by Michelsen [86], uses a tangent plane criterion that involves iterations for an incipient liquid phase and an incipient vapor phase.

Another technique to determine phase splits borrows K-values from neighboring two phase cells and performs the usual flash iterations on the fugacity equations to find a solution. If the vapor fraction becomes one or zero during the iterations, the program assumes the fluid remains a single phase and terminates the iterations. A last technique borrows K-values from neighboring cells the first time that a single phase cell is tested for phase-split and peforms the usual flash iterations, allowing vapor fractions to converge to numbers less than zero or greater than one (in which case the cell is deemed single phase for that time step). However, on subsequent time steps, the calculations do not borrow K-values, instead using the K-values from the previous time step since the solutions change negligibly between time steps and thus a smaller number of iterations are needed.

B.2 The two phase flash implementation

This section presents in somewhat greater detail the flash algorithm to solve the fugacity equations (B.5). Let us assume that the reference phase pressure, p, phase Z-factors, Z_α and current K-values, $\{K_i\}$ are given. The flash problem is to solve using Newton's method the system (B.5). As described in the previous section, fugacity coefficients may be expressed as a function of Z_α which can be simplified from Equation (B.4) as

$$\ln \Phi_i^\alpha = f(Z_\alpha, \xi_i^\alpha, p). \tag{B.7}$$

where the function form is identical for both phases $\alpha = l, g$. From equations (7.11)–(7.12), it is easily seen that the mole numbers for each phase satisfy

$$N_i^l = \frac{(1-v)N_i}{1+(K_i-1)v} \text{ and } N_i^g = \frac{vK_iN_i}{1+(K_i-1)v}. \tag{B.8}$$

Assume K_i is given. Then the two phase flash implementation proceeds as follows:

1. The Rachford-Rice equation (7.11) is first solved for the vapor fraction v. The same equation is also used to express δv in terms of $\delta(\ln K_i)$.
2. Equations (B.8) yield mole numbers N_i^α which in turn yields ξ_i^α. Equivalently, one could work directly with the mole fractions instead, as in equations (7.11)–(7.12) (recall that the overall composition is fixed during flash calculations).
3. Coefficients A_α, B_α, C_α are obtained using the just updated mole numbers N_i^α (or mole fractions ξ_i^α), p and T. These are in turn used to solve the cubic EOS (B.1) for Z_α.

4. Equation (B.7) then yields $\ln\Phi_i^\alpha$ upon direct substitution of Z_α, p and N_i^α (or ξ_i^α) into the function form.

5. Equations (B.5) are checked for convergence against a pre-defined tolerance for every component i. For most cells (e.g., single phase cells surrounded by similar single phase cells or far away from wells), convergence is reached in one iteration.

6. If equations (B.5) have not converged, $\ln K_i$ needs to be updated using Newton's method. To this end, the equations (B.5) are expanded to express $\delta(\ln\Phi_i^\alpha)$ in terms of $\delta(\ln K_i)$.

Equation (B.7) yields for changes in $\delta(\ln\Phi_i^\alpha)$ the expression (in differential form),

$$\delta(\ln\Phi_i^\alpha) = \frac{\partial f}{\partial Z_\alpha}\delta Z_\alpha + \frac{\partial f}{\partial N_i^\alpha}\delta N_i^\alpha \tag{B.9}$$

where the pressure term is not included because pressure does not vary during the flash calculation. Similarly, Equation (B.1) can be expanded to yield

$$\mathfrak{R}_e + \frac{\partial\mathfrak{R}_e}{\partial Z_\alpha}\delta Z_\alpha + \frac{\partial\mathfrak{R}_e}{\partial N_i^\alpha}\delta N_i^\alpha = 0. \tag{B.10}$$

Likewise, the Rachford-Rice equation (7.11) can be expanded to yield

$$\mathfrak{R}_v + \frac{\partial\mathfrak{R}_v}{\partial v}\delta v + \sum_j \frac{\partial\mathfrak{R}_v}{\partial(\ln K_i)}\delta(\ln K_i) = 0. \tag{B.11}$$

Finally the equations (B.8) yield

$$\delta N_i^\alpha = \frac{\partial N_i^\alpha}{\partial v}\delta v + \sum_j \frac{\partial N_i^\alpha}{\partial K_j}K_j\delta(\ln K_j). \tag{B.12}$$

Then, to form the Jacobian of Equation (B.5), the following steps are implemented:

1. Equation (B.11) is substituted into Equation (B.12) to express δN_i^α in terms of $\delta(\ln K_i)$.

2. The resulting change in mole numbers, δN_i^α is substituted into Equation (B.10) to express δZ_α in terms of $\delta(\ln K_i)$.

3. The resulting expressions are substituted for δN_i^α and δZ_α in Equation (B.9) to express $\delta(\ln \Phi_i^\alpha)$ in terms of $\delta(\ln K_i)$.

Finally the Equation (B.5) is solved using Newton's method for non-linear systems where the Newton step is given by the equation

$$\nabla \mathbf{R}^{\mathrm{eq}} \delta \mathbf{x}^{\mathrm{eq}} = -\mathbf{R}^{\mathrm{eq}}. \tag{B.13}$$

wherein the components of $\delta \mathbf{x}^{\mathrm{eq}}$ corresponding to the terms $\delta \ln \Phi_i^\alpha$ are expressed in terms of $\delta(\ln K_i)$.

B.3 Some derivatives

This sections lists in analytical terms some derivatives that frequently arise in the calculations of compositional flow equations, for example in Sections B.2 and 7.1.2. These can be derived from constitutive equations such as the equation of state for non-aqueous phases or equations (7.7) for the aqueous phase.

B.3.1 Saturation derivatives

The saturation derivatives are listed first. Here, it is assumed that N_i, v, p and $\ln K_i$ are independent variables. If one uses the fugacity equations (7.13) and the Rachford-Rice equations (7.11) to express v and $\ln K_i$ in terms of p and N_i, then the chain rule applies to expand the partial derivatives in terms of N_i and p. The water saturation derivatives are as follows:

$$\frac{\partial S_w}{\partial N_w} = v_w\,, \quad \frac{\partial S_w}{\partial N_i} = 0\,, \quad \text{and} \quad \frac{\partial S_w}{\partial p} = \frac{-c_w S_w}{1 + c_w(p - p^{\mathrm{ref}})}. \tag{B.14}$$

The non-aqueous liquid phase derivatives are given by the following list:

$$\begin{aligned}
\frac{\partial S_l}{\partial N_w} &= 0\,, \quad \frac{\partial S_l}{\partial N_i} = (1-v)v_l + (1-v)N_T \frac{\partial v_l}{\partial N_i}\,, \\
\frac{\partial S_l}{\partial v} &= -v_l N_T + (1-v)N_T \frac{\partial v_l}{\partial v}\,, \quad \frac{\partial S_l}{\partial(\ln K_i)} = (1-v)N_T \frac{\partial v_l}{\partial(\ln K_i)}\,, \text{ and} \\
\frac{\partial S_l}{\partial p} &= (1-v)N_T \frac{\partial v_l}{\partial p}
\end{aligned} \tag{B.15}$$

where $N_T \equiv \sum_i N_i$, the total sum of non-aqueous lb-moles per unit volume (i.e., total non-aqueous molar concentration). Next, the gas (vapor) phase saturation derivatives are given by

$$\begin{aligned}
\frac{\partial S_g}{\partial N_w} &= 0\,, \quad \frac{\partial S_g}{\partial N_i} = v v_l + v N_T \frac{\partial v_g}{\partial N_i}\,, \\
\frac{\partial S_g}{\partial v} &= v_g N_T + v N_T \frac{\partial v_l}{\partial v}\,, \quad \frac{\partial S_g}{\partial (\ln K_i)} = v N_T \frac{v_g}{\partial (\ln K_i)}\,, \\
\frac{\partial S_g}{\partial p} &= v N_T \frac{\partial v_g}{\partial p}.
\end{aligned} \tag{B.16}$$

B.3.2 Vapor fraction derivatives

The Rachford-Rice equation for determining vapor fractions v, is given by Equation (7.11). It is assumed that v is a function of $\{N_i\}$ and $\{\ln K_i\}$. Then the derivatives of v are given by

$$\frac{\partial v}{\partial N_i} = N_T \frac{(\xi_i^g - \xi_i^l)/z_i}{\sum_k (\xi_k^g - \xi_k^l)^2/z_k}\,, \qquad \text{and} \quad \frac{\partial v}{\partial (\ln K_i)} = \frac{\xi_i^l \xi_i^g / z_i}{\sum_k (\xi_k^g - \xi_k^l)^2/z_k} \tag{B.17}$$

where ξ_i^l and ξ_i^g are as defined in Equation (7.12) and

$$\sum_k \frac{(\xi_k^g - \xi_k^l)^2}{z_k} = \sum_i \frac{(K_i - 1)^2 z_i}{\left[1 + (K_i - 1)v\right]^2}. \tag{B.18}$$

B.3.3 Mole fraction derivatives

The liquid mole fraction is as given in Equation (7.12) and the term z_i is defined by $z_i = \frac{N_i}{N_T}$. Then the derivatives of z_i are given by

$$\frac{\partial z_i}{\partial N_j} = \frac{1}{N_T}(\delta_{ij} - z_i). \tag{B.19}$$

Next the derivatives of the liquid mole fractions are given by

$$\begin{aligned}
\frac{\partial \xi_i^l}{\partial N_j} &= \frac{\xi_i^l}{N_T z_i}(\delta_{ij} - z_i)\,, \quad \frac{\partial \xi_i^l}{\partial v} = -\xi_i^l \frac{(\xi_i^g - \xi_i^l)}{z_i}\,, \\
\frac{\partial \xi_i^l}{\partial (\ln K_j)} &= -\delta_{ij} v \frac{\xi_i^l \xi_i^g}{z_i}\,, \text{ and } \frac{\partial \xi_i^l}{\partial p} = 0.
\end{aligned} \tag{B.20}$$

The vapor mole fraction is as given in Equation (7.12). Hence, its derivatives are given by

$$\begin{aligned}
\frac{\partial \xi_i^g}{\partial N_j} &= \frac{\xi_i^g}{N_T z_i}(\delta_{ij} - z_i)\,, \quad \frac{\partial \xi_i^g}{\partial v} = -\xi_i^g \frac{(\xi_i^g - \xi_i^l)}{z_i}\,, \\
\frac{\partial \xi_i^g}{\partial(\ln K_j)} &= -\delta_{ij}(1-v)\frac{\xi_i^l \xi_i^g}{z_i}\,, \text{ and } \frac{\partial \xi_i^g}{\partial p} = 0.
\end{aligned} \tag{B.21}$$

B.3.4 Molar density derivatives

The molar α-phase density is given by $\rho_\alpha = \frac{1}{\nu_\alpha} = \frac{p}{RTZ_\alpha}$ so that its derivates can be derived as

$$\begin{aligned}
\frac{\partial \rho_\alpha}{\partial N_i} &= -\frac{p}{RTZ_\alpha^2}\frac{\partial Z_\alpha}{\partial N_i}\,, \quad \frac{\partial \rho_\alpha}{\partial v} = -\frac{p}{RTZ_\alpha^2}\frac{\partial Z_\alpha}{\partial v}\,, \\
\frac{\partial \rho_\alpha}{\partial(\ln K_i)} &= -\frac{p}{RTZ_\alpha^2}\frac{\partial Z_\alpha}{\partial(\ln K_i)}\,, \text{ and } \frac{\partial \rho_\alpha}{\partial p} = \frac{1}{RTZ_\alpha}\left[1 - \frac{p}{Z_\alpha}\frac{\partial Z_\alpha}{\partial p}\right]
\end{aligned} \tag{B.22}$$

B.3.5 Z-factor derivatives

Using the fact that $Z_\alpha = \bar{Z}_\alpha - C_\alpha$ and Equation (B.3) to express the volumetric shift C_α, the derivatives for α-phase Z-factors Z_α, are given by the expressions

$$\begin{aligned}
\frac{\partial Z_\alpha}{\partial N_i} &= \frac{\partial \bar{Z}_\alpha}{\partial N_i} - \frac{p}{RT}\sum_k \frac{\partial \xi_k^\alpha}{\partial N_i} c_k\,, \quad \frac{\partial Z_\alpha}{\partial v} = \frac{\partial \bar{Z}_\alpha}{\partial v} - \frac{p}{RT}\sum_i c_i \frac{\partial \xi_i^\alpha}{\partial v}\,, \\
\frac{\partial Z_\alpha}{\partial(\ln K_i)} &= \frac{\partial \bar{Z}_\alpha}{\partial(\ln K_i)} - \frac{p}{RT}\sum_i c_i \frac{\partial \xi_i^\alpha}{\partial(\ln K_i)}\,, \text{ and} \\
\frac{\partial Z_\alpha}{\partial p} &= \frac{\partial \bar{Z}_\alpha}{\partial p} - \frac{\sum_i \xi_i^\alpha c_i}{RT}.
\end{aligned} \tag{B.23}$$

In the equations (B.23), all derivatives except those of $\bar{Z}_\alpha$ have already been introduced in the preceding subsections. The derivatives of $\bar{Z}_\alpha$ follow immediately from the solution to the Peng-Robinson EOS (B.1) after careful manipulation. Consider for instance, the partial derivative $\frac{\partial \bar{Z}_\alpha}{\partial N_i}$. Partial differentiation of Equation (B.1) with respect to N_i yields (from an application of the chain and product rules)

$$\begin{aligned}\frac{\partial \mathfrak{R}_e}{\partial N_i} &= 3\bar{Z}_\alpha^2 \frac{\partial \bar{Z}_\alpha}{\partial N_i} + 2h_1(B_\alpha)\bar{Z}_\alpha \frac{\partial \bar{Z}_\alpha}{\partial N_i} - \bar{Z}_\alpha^2 \frac{\partial B_\alpha}{\partial N_i} + h_2(A_\alpha, B_\alpha)\frac{\partial \bar{Z}_\alpha}{\partial N_i} \\ &+ \left(\frac{\partial A_\alpha}{\partial N_i} - (6B_\alpha + 2)\frac{\partial B_\alpha}{\partial N_i}\right)\bar{Z}_\alpha - B_\alpha \frac{\partial A_\alpha}{\partial N_i} \\ &+ (2B_\alpha + 3B_\alpha^2 - A_\alpha)\frac{\partial B_\alpha}{\partial N_i} = 0, \end{aligned} \tag{B.24}$$

from which $\frac{\partial \bar{Z}_\alpha}{\partial N_i}$ can be readily calculated. Note that the derivatives of A_α and B_α can be easily derived from their definitions in Equation (B.3). In a similar manner all other derivatives of $\bar{Z}_\alpha$ can be determined.

Appendix C

An auxiliary approximation result

In this appendix, an auxiliary approximation result is derived based on the result in [44] to prove the assertion (or assumption) of inequality (4.82) in Section 4.7 of Chapter 4. Only the main ideas of the proof and areas where it deserves special treatment compared to that in [44] are presented. For simplicity, a 2-d unit square domain and Dirichlet boundary conditions are assumed, although the result can be similarly extended to 3-d and more general boundary conditions.

C.1 Construction

Assume $\Omega = (0,1)^2$ and the elements of $\mathcal{T}_h$ are rectangles. For convenience, all fault-blocks are assumed to be rectangular sub-domains in Ω. Let $\mathcal{P}_x^k$ and $\mathcal{P}_y^k$ be quasi-uniform partitions of the subset of $(0,1)^2$ occupied by fault-block k, given by

$$\begin{aligned} \mathcal{P}_x^k &: \ x_0^k = x_{1/2} < x_{3/2} < \ldots < x_{I_k+1/2} = x_1^k, \\ \mathcal{P}_y^k &: \ y_0^k = y_{1/2} < y_{3/2} < \ldots < y_{J_k+1/2} = y_1^k. \end{aligned}$$

Further let $h_{i,x}^k = x_{i+1/2}^k - x_{i-1/2}^k$, $h_{j,y}^k = y_{j+1/2}^k - y_{j-1/2}^k$ be the grid element sizes of fault-block k and let $h = \max_{i,j,k}\{h_{i,x}^k, h_{j,y}^k\}$ denote the maximal diameter of all elements in $\mathcal{T}_h$. Let the grid element centers be denoted by coordinates $x_i^k = (x_{i-1/2}^k + x_{i+1/2}^k)/2$ and $y_j^k = (y_{j-1/2}^k + y_{j+1/2}^k)/2$. The method developed in this appendix is for pure advection problems and hence, a CFL-constraint on the time step size of the form

$$\max_k\{|\mathbf{w}_k'(c)|\}\Delta\tau \le h_{\min}$$

is assumed to hold, where $h_{\min} = \min_{i,j,k}\{h^k_{i,x}, h^k_{j,y}\}$ denotes the minimal element diameter of all elements in $\mathcal{T}_h$. The face-averaged advective velocity function $\tilde{\mathbf{w}} = [\tilde{w}_1, \tilde{w}_2]^T \in \mathbf{V}^*_h$ given by the Equation (4.81) in Section 4.7 of Chapter 4 is determined away from fault-block interfaces by

$$\tilde{w}_1(x^k_{i+1/2}, y^k_j, t) = \frac{1}{h^k_{j,y}} \int_{y^k_{j-1/2}}^{y^k_{j+1/2}} w_1\left(c(x^k_{i+1/2}, y, t)\right) \mathrm{d}y, \tag{C.1}$$

where $i = 0, 1, \ldots, I_k$ (excluding fault-block interfaces) and $j = 1, 2, \ldots, J_k$. A similar expression holds for the component $\tilde{w}_2$ away from the fault-block interfaces. On fault-block interfaces, the equation (C.1) is suitably modified to include the contributions on each sub-face from interfacial element intersections. Thus, on an x-face for a given j, assuming $N^k_{j,y}$ interfacial intersections across the interface, yields for $j = 1, 2, \ldots, J_k$ and $l = 1, \ldots, N^k_{j,y}$, the expression

$$\tilde{w}_1(x^k_{i+1/2}, y^{l,k}_j, t) = \frac{1}{h^{l,k}_{j,y}} \int_{y^{l,k}_{j,1}}^{y^{l,k}_{j,2}} w_1\left(c(x^k_{i+1/2}, y, t)\right) \mathrm{d}y \tag{C.2}$$

where $h^{l,k}_{j,y}$ is the y-measure of the l^{th} interfacial intersection associated with j^{th} element in the y-direction on fault-block k. Likewise, $y^{l,k}_{j,1}$ and $y^{l,k}_{j,2}$ are the co-ordinates of the end points of this intersection.

In order to construct a numerical approximation to the advective velocity, $\mathbf{w}^{n-1}_h(\mathbf{x}, c^{m-1}_h)$ with x- and y-components $(w^{n-1}_{h,1}, w^{m-1}_{h,2})$ using a higher-order Godunov method, a piecewise linear function $\mathcal{R}c^{m-1}_h(\mathbf{x})$ is first constructed on each element E_{ij} of fault block k by

$$\mathcal{R}c^{k,m-1}_h|_{E_{ij}} = c^{k,m-1}_{h,ij} + (x - x^k_i)\partial_x c^{k,m-1}_{h,ij} + (y - y^k_j)\partial_y c^{k,m-1}_{h,ij} \tag{C.3}$$

where $\partial_x c^{k,m-1}_{h,ij}, \partial_y c^{k,m-1}_{h,ij}$ are the x- and y- direction slopes of the approximation c_h in fault-block k. The slope calculation can be performed in many ways [44]. The following approximations hold for all such slope calculations.

$$\begin{aligned} h^k_{i,x}|\partial_x c^{k,m}_{h,ij}| &\leq C \textstyle\sum_{j-L}^{j+L} \sum_{i-N}^{i+N} |c^{k,m}_{h,ln} \\ \partial_x c^{k,m}_{ij} &= c^k_x(x_i, y_j, \tau^m) + \mathcal{O}(h) \end{aligned} \tag{C.4}$$

It is noted that the approximations (C.4) hold even for elements adjacent fault-block interfaces. Infact, for such elements, $L > 1$ or $N > 1$ lead to some terms on the right hand side being evaluated across the fault-block interface. In [44], the ENO scheme is used for slope calculation. This is given by the rule:

$$\partial_x c_{h,ij}^{k,m-1} = \begin{cases} \Delta_+^x c_{h,ij}^{k,m} & \text{if } |\Delta_+^x c_{h,ij}^{k,m}| \leq |\Delta_-^x c_{h,ij}^{k,m}| \\ \Delta_-^x c_{h,ij}^{k,m} & \text{otherwise,} \end{cases} \tag{C.5}$$

where $\Delta_+^x c_{h,ij}^{k,m}$ and $\Delta_-^x c_{h,ij}^{k,m}$ are forward and backward differences, respectively. For elements adjacent to the fault-block interface, such as E in the Figure (C.1), the approximation (C.5) is modified suitably. For example, for the element E_A in the figure (assuming the forward difference slope is lesser in absolute value), the x-direction slope associated with the sub-element E_A^1 is given by

$$\partial_x c_{h,E_A^1}^{A,m-1} = \frac{c_{h,E_B}^{B,m} - c_{h,E_A^1}^{A,m}}{x_{E_B} - x_{E_A^1}}. \tag{C.6}$$

Advection on the fault-block interfaces is computed by accounting for the contributions from each interfacial intersection, where the sub-element slopes defined in Equation (C.6) are required in the p.w. linear reconstructions. Since $\mathbf{u} \in \mathbf{V}_h^*$, these reconstructions are used for approximations to the advective velocity using the higher-order Godunov method.

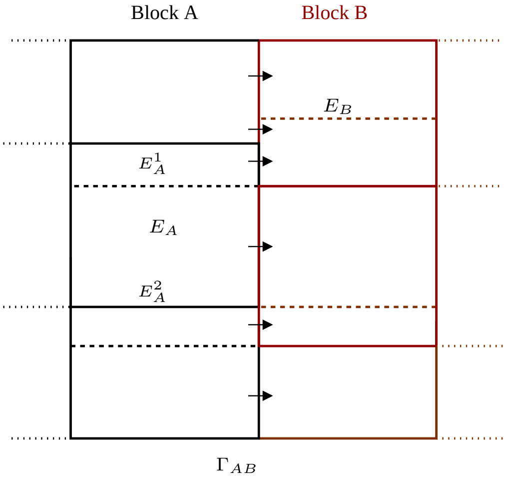

Figure C.1: Slope computation across fault-block interfaces

C.2 Analysis

The numerical flux approximation on the boundary of each element (or sub-element in the case of element adjacent to the fault-block interface) consists of calculating left and right states and solving a 1-d Riemann problem in a direction normal to the boundary as given in Section 3.5.2 of Chapter 3. The calculation of left and right states is based on Taylor's expansion. For c with smooth second derivatives,

$$c(x^k_{i+1/2}, y^k_j, \tau^{m-1/2}) = c + \frac{h^k_{i,x}}{2} c_x + \frac{\Delta\tau^m}{2} c_t + \mathcal{O}(h^2 + \Delta\tau^2)$$

Noting that $c_t = q - w_{1,c} c_x - w_{2,y} - \nabla \cdot \mathbf{z}$ yields,

$$c^{k,m-1/2}_{i+1/2,j} = c + \left(\frac{h^k_{i,x}}{2} - \frac{\Delta\tau^m}{2} w_{1,c} \right) c_x - \frac{\Delta\tau^m}{2} w_{2,y} + \sigma, \tag{C.7}$$

where

$$\sigma = -\frac{\Delta\tau^m}{2} (\nabla \cdot \mathbf{z} - q) + \mathcal{O}(h^2 + \Delta\tau^2) = \mathcal{O}(\Delta\tau + h^2).$$

Thus, when diffusion and source terms are absent, then $\sigma = \mathcal{O}(h^2 + \Delta\tau^2)$. Based on Equation (C.7) and a similar expansion about $(x^k_{i+1}, y^k_j, \tau^{m-1})$, one can define the approximate left and right states as follows:

$$\begin{aligned} c^{L,k,(m-1)}_{h,(i+1/2)j} &= c^{k,m-1}_{h,ij} + \left(h^k_{i,x} - \tfrac{\Delta\tau^m}{2} w_{1,c}(c^{k,m-1}_{h,ij}) \right) \partial_x c^{k,m-1}_{h,ij} \\ &\quad - \tfrac{\Delta\tau^m}{2h^k_{j,y}} \left[\Gamma^{k,m-1}_{i(j+1/2)} - \Gamma^{k,m-1}_{i(j-1/2)} \right] \end{aligned} \tag{C.8}$$

and

$$\begin{aligned} c^{R,k,(m-1)}_{h,(i+1/2)j} &= c^{k,m-1}_{h,(i+1)j} - \left(h^k_{i+1,x} - \tfrac{\Delta\tau^m}{2} w_{1,c}(c^{k,m-1}_{h,(i+1)j}) \right) \partial_x c^{k,m-1}_{h,(i+1)j} \\ &\quad - \tfrac{\Delta\tau^m}{2h^k_{j,y}} \left[\Gamma^{k,m-1}_{(i+1)(j+1/2)} - \Gamma^{k,m-1}_{(i+1)(j-1/2)} \right]. \end{aligned} \tag{C.9}$$

Here, $\Gamma^{k,m-1}_{i(j+1/2)} = H_{w_2}\left(c^{L,k,m-1}_{h,i(j+1/2)}, c^{R,k,m-1}_{h,i(j+1/2)} \right)$ where

$$c^{L,k,m-1}_{h,i(j+1/2)} = c^{k,m-1}_{h,ij} + h^k_{j,y} \partial_y c^{k,m-1}_{h,ij} \tag{C.10}$$

$$c^{R,k,m-1}_{h,i(j+1/2)} = c^{k,m-1}_{h,i(j+1)} + h^k_{j+1,y} \partial_y c^{k,m-1}_{h,i(j+1)} \tag{C.11}$$

Given the left and right states $c^{L,k,m-1}_{h,(i+1/2)j}$ and $c^{R,k,m-1}_{h,(i+1/2)j}$ the numerical flux can be defined as

$$\bar{w}^{k,m-1}_{1,h,(i+1/2)j} = H_{w_1}\left(c^{L,k,m-1}_{h,(i+1/2)j}, c^{R,k,m-1}_{h,(i+1/2)j}\right). \tag{C.12}$$

Elements adjacent to the external boundary can be treated as given in [44]. The rest of the analysis follows identically as presented in [44]. The basic idea is to construct left and right states $\bar{c}^{L,k,m-1}_{h,(i+1/2)j}$,$\bar{c}^{R,k,m-1}_{h,(i+1/2)j}$ from the solution to the elliptic projection, $\tilde{c}$. Then assuming w_1 is twice differentiable and Lipschitz, the Lipschitz continuity and consistence of the Godunov flux and approximations (C.4), terms such as $|c^{L,k,m-1}_{h,(i+1/2)j} - \bar{c}^{L,k,m-1}_{h,(i+1/2)j}|$ are bounded easily. Introducing additional terms, $\Pi_2 c^{L,k,m-1}_{h,(i+1/2)j}$, $\Pi_2 c^{R,k,m-1}_{h,(i+1/2)j}$, $c^{L,k,m-1}_{h,(i+1/2)j}$, and $c^{R,k,m-1}_{h,(i+1/2)j}$ analogous $\bar{c}^{L,k,m-1}_{h,(i+1/2)j}$ and $\bar{c}^{R,k,m-1}_{h,(i+1/2)j}$, using $\Pi_2 c$ and c, respectively and building a telescopic sum in the expression for $\left(\bar{w}^{k,m-1}_{1,h,(i+1/2)j} - \tilde{w}^{k,m-1}(x^k_{i+1/2}, y^k_j)\right)$ and bounding each term separately as in [44], the desired result is arrived at.

Bibliography

[1] Workshop on numerical models for CO_2 storage in geological formations. See also URL `http://www.iws.uni-stuttgart.de/co2-workshop`.

[2] S. I. Aanonsen and D. Eydinov. A multiscale method for distributed parameter estimation with application to reservoir history matching. *Comp. Geosc.*, 10(1):97–117, 2006.

[3] Y. Achdou, Y. A. Kuznetsov, and O. Pironneau. Substructuring preconditioners for the Q_1 mortar element method. *Numer. Math.*, 71(4):419–449, 1995.

[4] Y. Achdou, Y. Maday, and O. B. Widlund. Iterative substructuring preconditioners for mortar element methods in two dimensions. *SIAM J. Numer. Anal.*, 36(2):551–580, 1999.

[5] G. Acs, S. Deleschall, and E. Farkas. General purpose composition model. *Soc. Pet. Eng. J.*, 25:543–553, 1985.

[6] R. A. Adams. *Sobelev spaces*, volume 65. Academic Press, NY-London, 1975. Pure and Applied Mathematics.

[7] P. M. Adler, C. G. Jacquin, and J. Thovert. The formation factor of reconstructed porous media. *Water Resources Research*, 28(6):1571–1576, 1992.

[8] V. Aizinger, C. N. Dawson, B. Cockburn, and P. Castillo. The local discontinuous Galerkin method for contaminant transport. *Advances in Water Resources*, 24:73–87, 2001.

[9] R. I. Al-Raoush, K. E. Thompson, and C. S. Willson. Comparison of network generation techniques for unconsolidated porous media. *Soil Sci. Soc. of Ame. J.*, 67(6):1687–1700, 2003.

[10] H. W. Alt and S. Luckhaus. Quasilinear elliptic-parabolic partial differential equations. *Math. Z.*, 183:311–341, 1983.

[11] T. Arbogast. The existence of weak solutions to single-porosity and dual-porosity models of two-phase incompressible flow. *Nonlinear Analysis, Theory Methods and Applications.*, 19:1009–1031, 1992.

[12] T. Arbogast, L. Cowsar, M. F. Wheeler, and I. Yotov. Mixed finite element methods on non-matching multi-block grids. *SIAM J. Numer. Anal.*, 37(4):1295–1315, 2000.

[13] T. Arbogast, C. N. Dawson, and M. F. Wheeler. A parallel algorithm for two-phase multicomponent contaminant transport. *Appl. Math.*, 40(3):163–174, 1995.

[14] T. Arbogast, Jr. J. Douglas, and U. Hornung. Modeling of naturally fractured reservoirs by formal homogenization techniques. In *Frontiers in pure and applied mathematics, R. Dautray ed.*, pages 1–19. Elsevier, Amsterdam, 1991.

[15] T. Arbogast, G. Pencheva, M. F. Wheeler, and I. Yotov. A multiscale mortar mixed finite element method. *Multiscale Modeling & Simulation*, 6(1):319–346, 2007.

[16] T. Arbogast, M. F. Wheeler, and I. Yotov. Mixed finite element methods for elliptic problems with tensor coefficients as cell-centered finite differences. *SIAM J. Numer. Anal.*, 32(2):828–852, 1997.

[17] T. Arbogast, M. F. Wheeler, and N. Zhang. A non-linear mixed finite element method for a degenerate parabolic equation arising in flow in porous media. *SIAM J. Numer. Anal.*, 33(4):1669–1687, 1996.

[18] S. Bachu. Sequestration of CO_2 in geological media: Criteria and approach for site selection in response to climate change. *Energy and Conversion Management*, 41:953–970, 2000.

[19] J. I. Baird. *Numerical analysis of the representer method applied to reservoir modeling.* PhD thesis, Austin, TX, 2006.

[20] S. Bakke and P. E. Oren. 3-d pore-scale modelling of sandstones and flow simulations in the pore networks. *SPE J.*, 2(2):136–149, 1997.

[21] M. Balhoff, M. F. Wheeler, and S. G. Thomas. Mortar coupling and upscaling of pore-scale models. *Comp. Geosc.*, 12(1):15–27, 2008. Subject Collection: Mathematics and Statistics.

[22] F. Bassi and S. Rebay. A high-order accurate discontinuous finite element method for the numerical solution of the compressible Navier-Stokes equations. *J. Comput. Phys.*, 131:267–279, 1997.

[23] J. Bear. *Dynamics of Fluids in Porous Media.* American Elsevier, 1972.

[24] J. B. Bell, C. N. Dawson, and G. R. Shubin. An unsplit higher-order godunov scheme for scalar conservation laws in two dimensions. *J. Comp. Phy.*, 74:1–24, 1988.

[25] C. Bernardi, Y. Maday, and A. T. Patera. A new nonconforming approach to domain decomposition: the mortar element method. In *Nonlinear*

Partial Differential Equations and their applications, H. Brezis and J. L. Lions eds. Longman Scientific and Technical, UK, 1994.

[26] K. M. Brantferger. *Development of a thermodynamically consistent fully implicit, compositional, equation of state, steamflood simulator.* PhD thesis, Austin, TX, 1991.

[27] K. M. Brantferger, G. A. Pope, and K. Sepehrnoori. Development of a thermodynamically consistent fully implicit equation of state compositional steamflood simulator. In *Proceedings of the SPE symposium on Reservoir Simulation*, pages 17–20, Anaheim, CA, Feb 1991. SPE.

[28] F. Brezzi and M. Fortin. *Mixed and hybrid finite element methods*, volume 15. Springer-Verlag, NY, 1991. Springer Series in Computational Mathematics.

[29] R. H. Brooks and A. T. Corey. Hydraulic properties of porous media. In *Hydrology Papers.* Fort Collins,Colorado State University, 1964.

[30] J. Q. Broughton, F. F. Abraham, N. Bernstein, and E. Kaxiras. Concurrent coupling of length scales: Methodology and application. *Phy. Rev.*, 13(60):2391–2403, 1999.

[31] S. L. Bryant, D. W. Mellor, and C. A. Cade. Physically representative network models of transport in porous media. *AIChE J.*, 37:387–396, 1993.

[32] T. F. Chan. Stability analysis of finite difference schemes for the advection-diffusion equation. *SIAM J. Numer. Anal.*, 21(2):272–284, 1984.

[33] Y. Chang. *Development and application of an equation of state compositional simulator.* PhD thesis, Austin, TX, August 1990.

[34] Z. Chen, G. Chen, and Y. Ma. A sequential numerical chemical compositional simulator. *Transport in Porous Media*, 68:389–411, Nov 2006.

[35] Z. Chen, R. Ewing, and G. Qin. Analysis of a compositional model for fluid flow in porous media. *SIAM J. Appl. Math*, 60(3):747–777, Feb 2000.

[36] Z. Chen, G. Huan, and Y. Ma. *Computational Methods for Multiphase Flows in Porous Media.* SIAM, 2005.

[37] Z. Chen, G. Huan, and H. Wang. Simulation of a compositional model for multiphase flow in porous media. *Numer. Meth. for Partial Diff. Eqs.*, 21(4):726–741, Dec 2005.

[38] M. A. Christie and M. J. Blunt. Tenth spe comparative solution project: A comparison of upscaling techniques. *SPE Reservoir Eval. Eng.*, 4(4):308–317, 2001.

[39] P. G. Ciarlet. *The finite element method for elliptic problems*, volume 4. North-Holland, Amsterdam, 1978. Studies in Mathematics and its Applications.

[40] K. H. Coats. An equation of state composition model. *Soc. Pet. Eng. J.*, 20:363–376, 1980.

[41] B. Cockburn and C. W. Shu. The local discontinuous Galerkin method for time-dependent convection-diffusion systems. *SIAM J. Numer. Anal.*, 35(6):2440–2463, 1998.

[42] R. Courant. Variational methods for the solutions of problems of equilibrium and vibrations. *Bull. Amer. Math. Soc.*, 49:1–23, 1943.

[43] L. C. Cowsar, J. Mandel, and M. F. Wheeler. Balancing domain decomposition for mixed finite elements. *Math. Comp.*, 64:989–1015, 1995.

[44] C. N. Dawson. Godunov mixed methods for advection-diffusion equations in multi-dimensions. *SIAM J. Numer. Anal.*, 30(5):1315–1332, Oct 1993.

[45] C. N. Dawson and J. I. Baird. The representer method for data assimilation in single-phase darcy flow in porous media. *Comp. Geosc.*, 9(4):242–271, 2005.

[46] C. N. Dawson and J. I. Baird. The representer method for two-phase flow in porous media. *Comp. Geosc.*, 11(3):235–248, 2007.

[47] C. N. Dawson, H. Klie, M. F. Wheeler, and C. S. Woodward. A parallel, implicit, cellcentered method for twophase flow with a preconditioned newtonkrylov solver. *Comp. Geosc.*, 1(3–4):215–249, 1997. Subject Collection: Mathematics and Statistics.

[48] C. N. Dawson, S. Sun, and M. F. Wheeler. Compatible algorithms for coupled flow and transport. *Comput. Methods Appl. Mech. Engrg.*, 193(23-26):2565–2580, 2004.

[49] C. N. Dawson and M. F. Wheeler. An operator-splitting method for advection-diffusion-reaction problems. In *The mathematics of finite elements and applications*, pages 463–482. Academic Press, London, UK, 1987.

[50] R. H. Dean. Compositional flow model in iparsv3. May 2000.

[51] M. Delshad, G. A. Pope, and K. Sepehrnoori. UTCHEM. Technical documentation, Center for Petroleum and Geosystems Engineering, The University of Texas at Austin, Austin, TX, 2000.

[52] M. Delshad, S. G. Thomas, and M. F. Wheeler. Modeling CO_2 sequestration using a sequentially coupled 'Iterative-IMPEC-Time-Split-Thermal' compositional simulator. In *11th European Conference on the Mathematics of Oil Recovery, ECMOR XI*, Bergen, Norway, Sep 8-11 2008. EAGE.

[53] M. Delshad, S. G. Thomas, and M. F. Wheeler. Parallel simulations of CO_2 sequestration using a non-isothermal compositional model. In *International Mechanical Engineering Congress and Exposition*, Boston, MA, Oct 31-Nov 6 2008. ASME.

[54] M. Delshad, S. G. Thomas, and M. F. Wheeler. Parallel numerical simulations of non-isothermal compositional flow and chemistry. *SPE Journal*, (118847-MS), 2009. presented at the SPE Reservoir Simulation Symposium, The Woodlands, TX, 2–4 Feb, 2009.

[55] R. M. DeWiest. *Flow through Porous Media.* N. Y. Academic Press, 1969.

[56] A. Ebigbo, H. Class, and R. Helmig. CO_2 leakage through an abandoned well: problem-oriented benchmarks. *Comp. Geo.*, 11:103–115, Dec 2007.

[57] O. J. Eslinger. *A discontinuous Galerkin method applied to the two-phase air-water problem.* PhD thesis, Austin, TX, 2005.

[58] R. E. Ewing and J. H. George. *Distributed Parameter Systems*, volume 75, chapter Identification and control for distributed parameters in porous media flow, pages 145–161. Lecture Notes in Control and Information Sciences.

[59] R. Eymard, T. Gallout, and R. Herbin. Finite volume methods. In P. G. Ciarlet and J. L. Lions, editors, *Handbook of Numerical Analysis*, volume VII, pages 713–1020. Elsevier, North Holland, Amsterdam, Sep 2000.

[60] J. E. Fromm. A method for reducing dispersion in convective difference schemes. *J. Comp. Phy.*, 3(2):176–189, 1968.

[61] Y. Ghomian. *Reservoir simulation studies for coupled CO_2 sequestration and enhanced oil recovery.* PhD thesis, Austin, TX, 2008.

[62] V. Girault, S. Sun, M. F. Wheeler, and I. Yotov. Coupling discontinuous Galerkin and mixed finite element discretizations using mortar finite elements. *SIAM J. Numer. Anal.*, 46(2):949–979, 2008.

[63] R. Glowinski and M. F. Wheeler. Domain decomposition and mixed finite element methods for elliptic problems. In R. Glowinski, G. H. Golub, G. A. Meurant, and J. Periaux, editors, *First International Symposium on Domain Decomposition Methods for Partial Differential Equations, R. G. et al.*, pages 144–172. SIAM, Philadelphia, 1988.

[64] S. K. Godunov. A difference scheme for numerical computation of discontinuous solutions of equations in fluid dynamics. *Math Sbornik*, 47:271–306, 1959.

[65] J. Gopalakrishnan and J. E. Pasciak. Multigrid for the mortar finite element method. *SIAM J. Numer. Anal.*, 37(3):1029–1052, 2000.

[66] P. Grisvard. *Elliptic problems in nonsmooth domains.* Pittman, Boston, MA, 1985.

[67] A. D. Hill, D. Lindsay, I. H. Silberberg, and R. S. Schechter. Theoretical and experimental studies of sandstone acidizing. *Society of Petroleum Engineers*, 21(1):30, 1981.

[68] T. Hong, M. K. Sen, P. L. Stoffa, H. Klie, S. G. Thomas, A. Rodriguez, and M. F. Wheeler. Integrated timelapse seismic inversion for reservoir petrophysics and fluidflow imaging. *SEG, Expanded Abstracts*, 26(1):1952–1956, 2007.

[69] S. D. Hovorka, M. L. Romero, A. G. Warne, W. A. Ambrose, T. A. Tremblay, R. H. Trevinò, and D. Sasson. Sequestration of greenhouse gases in brine formations. Technical report, Bureau of Economic Geology, The University of Texas at Austin, Austin, TX, 2000.

[70] IPARSv2. Integrated parallel and accurate reservoir simulator. Technical Report TICAM01-25, Center for Subsurface Modeling, ICES, The University of Texas at Austin, Austin, TX, 2000.

[71] I. T. Jolliffe. *Principal Component Analysis.* Springer, NY, 2002. Springer Series in Statistics, Vol. XXIX, 2nd. Ed.

[72] T. R. Karl and K. E. Trenberth. Modern global climate change. *Science J.*, 302(5651):1719–1723, 2003.

[73] H. Kile, W. Bangerth, M. F. Wheeler, M. Parashar, and V. Matossian. Parallel well-location optimization using stochastic algorithms on the grid computational framework. Cannes, France, 2004. 9th European Conference on the Mathematics of Oil Recovery, ECMOR IX.

[74] V. Kippe, J. Aarnes, and K. A. Lie. Multiscale finite element methods for elliptic problems in porous media flow. In *CMWR XVI - Computational Methods in Water Resources*, Copenhagen, Denmark, 2006.

[75] P. A. Klein and J. A. Zimmerman. Coupled atomistic-continuum simulations using arbitrary overlapping domains. *J. of Comp. Phy.*, 213:86–116, 2006.

[76] H. Klie, A. Rodriguez, S. G. Thomas, M. F. Wheeler, and R. Banchs. Assessing the value of sensor information in 4d seismic history matching. *SEG, Expanded Abstracts*, 25(1):3245–2249, 2006.

[77] H. Klie, A. Rodriguez, S. G. Thomas, M. F. Wheeler, and R. Banchs. A neural stochastic multiscale optimization framework for sensor-based parameter estimation. *Integrated Computer Aided Engineering*, 14(3):213–223, 2007.

[78] S. Kohlhoff, P. Gumbsch, and H. F. Fischmeister. Crack propagation in bcc crystals studied with a combined finite-element and atomistic model. *Phil. Mag. A.*, 64:851–878, 1991.

[79] Y. A. Kuznetsov and M. F. Wheeler. Optimal order substructuring preconditioners for mixed finite element methods on non-matching grids. *East-West J. Num. Math.*, 3(2):127–143, 1995.

[80] S. Lacroix, Y. Vassilevski, J. A. Wheeler, and M. F. Wheeler. Iterative solution methods for modeling multiphase flow in porous media fully implicitly. *SIAM J. Sci. Comput.*, 25(3):905–926, 2003.

[81] R. D. Lazarov, I. D. Mishev, and P. S. Vassilevski. Finite volume methods for convection-diffusion problems. *SIAM J. Numer. Anal.*, 33:31–55, 1996.

[82] Z. Liang, A. Ioannidis, and I. Chatzis. Permeability and electrical conductivity of porous media from 3-d replicas of the microstructure. *Chem. Engr. Sci.*, 55:5247–5262, 2000.

[83] W. B. Lindquist, S Lee, D. A. Coker, K. W. Jones, and P. Spanne. Medial axis analysis of void structure in three-dimensional tomographic images of porous media. *J. of Geophy. Research*, 101(B4):8297–8310, 1996.

[84] W. B. Lindquist, A. Venkatarangan, J. Dunsmuir, and T. Wong. Pore and throat size distributions measured from synchrotron x-ray tomographic images of fontainebleau sandstones. *J. of Geophy. Research*, 105(B9):21509–21528, 2000.

[85] J. Liu, M. Delshad, G. A. Pope, and K. Sepehrnoori. Application of higher order flux-limited methods in compositional simulations. *Transport in Porous Media*, 16(1):1–29, Jul 1994.

[86] M. L.Michelsen. The isothermal flash problem. part i: Stability. *Fluid Phase Equilibria*, 9:1–19, 1982.

[87] X. Lopez, P. H. Valvatne, and M. J. Blunt. Predictive network modeling of single-phase non-newtonian flow in porous media. *J. Colloidal Interface. Sci.*, 54:256–265, 2003.

[88] P. Lu. *Reservoir parameter estimation using wavelet analysis.* PhD thesis, Stanford, CA, 2001.

[89] Q. Lu. *A parallel multi-block/multi-physics approach for multi-phase flow in porous media.* PhD thesis, Austin, TX, 2000.

[90] D. Lumley and M. J. Blunt. Time-lapse seismic reservoir management. *Geophysics*, 66:50–53, 2001.

[91] M. F. Wheeler M. Y. Kim, E. J. Park and S. G. Thomas. A multscale mortar mixed finite element method for slightly compressible flows in porous media. *J. Kor. Math. Soc.*, 44(5):1103–1119, 2007.

[92] J. Mandel and M. Brezina. Balancing domain decomposition for problems with large jumps in coefficients. *Mathematics of Computation*, 65(216):1387–1401, 1996.

[93] T. P. Mathew. *Domain decomposition and iterative refinement methods for mixed finite element discretizations of elliptic problems.* PhD thesis, New York City, NY, 1989.

[94] M. Muskat. *The Flow of Homogeneous Fluids through Porous Media.* McGraw-Hill Book Co. Inc., New York City, NY, 1937. Vol. 55.

[95] M. Muskat. *Physical Principles of Oil Production.* International Human Research Development Corporation, Boston, MA, 1981. (reprint of 1949 edition).

[96] J. C. Nedelec. Mixed finite elements in $\mathbb{R}^3$. *Numer. Math.*, 35:315–341, 1980.

[97] L. Nghiem. Compositional simulator for CO_2 sequestration. Computer Modeling Group Ltd., 2002. See also URL `http://www.cmgroup.com` .

[98] J. Nordbotten, M. Celia, S. Bachu, and H. Dahle. Semi-analytic solution for CO_2 leakage through an abandoned well. *Env. Sci. Tech.*, 39(2):602–611, 2005.

[99] J. T. Oden, I. Babuška, and C. E. Baumann. A discontinuous *hp* finite element method for diffusion problems. *J. Comput. Phys.*, 146:491–516, 1998.

[100] D. Oliver and Y. Gu. The ensemble kalman filter for continuous updating of reservoir simulation models. *J. Energy Resour. Tech.*, 128(1):79–87, 2006.

[101] D. Oliver, A. Reynolds, Z. Bi, and Y. Abacioglu. Integration of production data into reservoir models. *Petroleum Geoscience*, 7(S):65–73, 2001.

[102] W. Ostwald. *Outlines of General Chemistry.* MacMillan & Co., Ltd., St. Martins Street, London, 1912. (translated by W. W. Taylor).

[103] E. J. Park. Mixed finite element methods for non-linear second order elliptic problems. *SIAM J. Numer. Anal.*, 32:865–885, 1995.

[104] E. J. Park. Mixed finite element methods for generalized forchheimer flow in porous media. *Numer. Meth. Partial Diff. Eq.*, 21(2):213–228, 2005.

[105] E. J. Park and F. A. Milner. A mixed finite element method for a strongly non-linear second-order elliptic problem. *Math. Comp.*, 64:973–988, 1995.

[106] S. V. Patankar and B. R. Baliga. A control-volume finite element method for two-dimensional fluid flow and heat transfer. *Numerical Heat Transfer.*, 6:245–261, 1983.

[107] D. W. Peaceman. *Fundamentals of Numerical Reservoir Simulation.* Elsevier, 1977.

[108] K. Pearson. On lines and planes of closest fit to systems of points in space. *Physical Magazine*, 2(6):559–572, 1901.

[109] G. Pencheva, S. G. Thomas, and M. F. Wheeler. Mortar coupling of discontinuous Galerkin and mixed finite element methods. Bergen, Norway, Sep. 8-11 2008. 11th European Conference on the Mathematics of Oil Recovery, ECMOR XI.

[110] G. Pencheva and I. Yotov. Balancing domain decomposition for mortar mixed finite element methods on non-matching grids. *Numer. Linear Algebra Appl.*, 10(1–2):159–180, 2003.

[111] G. Pencheva, C. Yuan, S. G. Thomas, and M. F. Wheeler. Iterative coupling for discontinuous Galerkin applications to multiphase flow. In preparation.

[112] D. Peng and D. B. Robinson. A new two-constant equation of state. *Ind. Eng. Chem., Fundam.*, 15(1):59–64, 1976.

[113] M. Peszynska and S. Sun. Multiphase reactive transport module trchem in iparsv2. Technical Report TICAM01-32, CSM, University of Texas at Austin, Austin, TX.

[114] M. Peszyńska, M. F. Wheeler, and I. Yotov. Mortar upscaling for multiphase flow in porous media. *Comp. Geosci.*, 6(1):73–100, 2002.

[115] W. H. Press, S. A. Teukolsky, W. T. Vetterling, and Brian P. Flannery. *Numerical recipes in Fortran 77: The Art of scientific computing*, volume 1. Cambridge University Press, Cambridge, MA, 2 edition, 1992.

[116] R. A. Raviart and J. M. Thomas. A mixed finite element method for 2nd order elliptic problems. *Mathematical Aspects of the Finite Element Method, Lecture notes in Mathematics*, 606:292–315, 1977.

[117] Lord Rayleigh. On the bending and vibration of thin elastic shells, especially of cylindrical form. *Proc. Royal Soc. of London*, 45:105–123, 1888.

[118] A. C. Reynolds, G. Gao, and G. Li. A stochastic optimization algorithm for automatic history matching. *SPE Journal*, (90065-MS), 2004. presented at the SPE Annual Technical Conference and Exhibition, Houston, TX, 26–29 Sep, 2004.

[119] B. Rivière, M. F. Wheeler, and V. Girault. Part I: Improved energy estimates for interior penalty, constrained and discontinuous Galerkin methods for elliptic problems. *Computational Geosciences*, 3:337–360, 1999.

[120] J. E. Roberts and J. M. Thomas. *Handbook of Numerical Analysis.*

[121] R. E. Rudd and J. Q. Broughton. Concurrent coupling of length scales in solid state systems. *Phys. Stat. Sol.*, 217:251–291, 2000.

[122] T. Russell and M. F. Wheeler. Finite element and finite difference methods for continuous flows in porous media. In *The Mathematics of Reservoir Simulation, R. E. Ewing ed., Frontiers in Applied Mathematics 1*, pages 35–106. SIAM, Philadelphia, 1984.

[123] P. Sarma, L. J. Durlofsky, K. Aziz, and W. H. Chen. Efficient real-time reservoir management using adjoint-based optimal control and model updating. *Comp. Geosc.*, 10(1):3–36, 2006.

[124] L. R. Scott and S. Zhang. Finite element interpolation of nonsmooth functions satisfying boundary conditions. *Math. Comp.*, 54:483–493, 1990.

[125] R. M. Sok, M. A. Knackstedt, A. P. Sheppard, W. V. Pinczewski, W. B. Lindquist, A. Venkatarangan, and L. Paterson. Direct and stochastic generation of network models from tomographic images: Effect of topology on residual saturations. *Transport in Porous Media*, 46(2–3):345–371, 2002.

[126] J. C. Spall. *Introduction to stochastic search and optimization: estimation, simulation and control*. Wiley Interscience, 2003. Discrete Mathematics and Optimization.

[127] K. Stueben. A review of the algebraic multigrid method: A short report on amg and the basic solver technology. *J. of Comp. and Appl. Math.*, 128:281–309, 2001.

[128] K. E. Thompson and M. Balhoff. Modeling the steady flow of yield-stress fluids in packed beds. *AIChE J.*, 50(12):3034–3048, 2004.

[129] K. E. Thompson and M. Balhoff. A macroscopic model for shear-thinning flow in packed beds based on network modeling. *Chem. Engr. Sci.*, 61(2):698–719, 2006.

[130] K. E. Thompson, M. Balhoff, and M. Hjortso. Coupling pore networks to continuum models. *Computers and Geosciences*, 33(3):393–410, 2007.

[131] K. E. Thompson, C. S. Willson, C. D. White, S. Nyman, J. Bhattacharya, and A. H. Reed. Application of a new grain-based reconstruction algorithm to microtomography images for quantitative characterization and flow modeling. *SPE Journal*, 2005. presented at SPE Annual Technical Conference and Exhibition, 9–12 Oct, Dallas, TX.

[132] TNO. Brugge field synthetic data. SPE-ATW 2008. See also URL `http://www.isapp.nl/brugge-field-case`.

[133] R. Versteeg, M. Ankeny, J. Harbur, G. Heath, K. Kostelnik, E. Matson, K. Moor, and A. Richardson. A structured approach to the use of near-surface geophysics in long-term monitoring. *The Leading Edge*, 23(7):700–703, 2004.

[134] G. J. Wagner and W. K. Liu. Coupling of atomistic and continuum simulations using a bridging scale decomposition. *J. of Comp. Phy.*, 190:249–274, 2003.

[135] J. W. Watts. A compositional formulation of the pressure and saturation equations. *SPE Res. Eng*, 1(3):243–252, 1986.

[136] J. Wheeler, I. Yotov, and M. F. Wheeler. Enhanced velocity mixed finite element methods for flow in multiblock domains. *Comp. Geosc.*, 6:3-4:315–332, 2002.

[137] M. F. Wheeler. A priori l_2 error estimates for galerkin approximations to parabolic partial differential equations. *SIAM J. Numer. Anal.*, 10:723–759, 1973.

[138] M. F. Wheeler. An elliptic collocation-finite element method with interior penalties. *SIAM J. Numer. Anal.*, 15:152–161, 1978.

[139] M. F. Wheeler, T. Arbogast, S. Bryant, J. Eaton, Q. Lu, M. Peszynska, and I. Yotov. A parallel multiblock/multidomain aproach for reservoir simulation. *SPE Journal*, (51884), 1999. presented at the SPE Reservoir Simulation Symposium, Houston, TX, 1999.

[140] M. F. Wheeler and I. Yotov. Physical and computational domain decompositions for modeling subsurface flows. In *Domain decomposition methods, 10 (Boulder, CO, 1997)*, volume 218 of *Contemp. Math.*, pages 217–228. Amer. Math. Soc., Providence, RI, 1998.

[141] C. S. Willson and R. I. Al-Raoush. Extraction of physically realistic pore network properties from three-dimensional synchrotron x-ray microtomography images of unconsolidated porous media systems. *Journal of Hydrology*, 300(1):44–64, 2005.

[142] I. Yotov. *Mixed finite element methods for flow in porous media.* PhD thesis, Houston, TX, 1996.

[143] I. Yotov. A mixed finite element discretization for a degenerate parabolic equation arising in porous media flow. *East-West J. Numer. Math.*, 5:211–230, 1997.

[144] I. Yotov. Interface solvers and preconditioners of domain decomposition type for multiphase flow in multiblock porous media. *Advances in Computation: Theory and Practice*, 7:157–167, 2001.

[145] I. Yotov. A multilevel newton-krylov interface solver for multiphysics couplings of flow in porous media. *Numer. Linear Algebra Appl.*, 8:551–570, 2001.

[146] I. Yotov and M. F. Wheeler. A posteriori error estimates for the mortar mixed finite element method. *SIAM J. Numer. Anal.*, 43(3):1021–1042, 2005.

[147] I. Yotov and M. F. Wheeler. A multipoint flux mixed finite element method. *SIAM J. Numer. Anal.*, 44(5):2082–2106, 2006.

[148] I. Yotov, M. F. Wheeler, G. Pencheva, and S. G. Thomas. Multiscale mortar mixed finite elements for multiphase flow in porous media. *10th European conference on the mathematics of oil recovery*, Amsterdam, 2006.

[149] T. Zhodi and P. Wriggers. A domain decomposition method for bodies with heterogeneous microstructure based on material regularization. *J. of Solids and Structures*, 36:2507–2525, 1999.

[150] O. C. Zienkiewicz and Y. K. Cheung. Finite elements in the solution of field problems. *Engineer*, 220:507–510, 1965.

Index

Vita

The author, Sunil George Thomas, was born in Visakhapatnam, AP State, India on 27 May 1979. He is the son of Thomas Koshy and Omana Koshy. He received a Bachelor of Technology (B. Tech.) degree in Mechanical Engineering from the Jawaharlal Nehru Technological University (JNTU), Kakinada, AP State, India and a Master of Science (M. S.) degree in Mechanical Engineering at Cullen College of Engineering, University of Houston, Houston, TX. At the time of writing of this document, May 2009, he was pursuing a Ph.D. degree in the field of Computational and Applied Mathematics at The University of Texas at Austin, Austin, TX, which he commenced in the fall semester of 2003.

Permanent address: #201, Revathi Hills Apts,
Balayya Sastry Layout,
Seethammadhara N. E.,
Visakhapatnam 530011,
Andhra Pradesh, INDIA

This dissertation was typeset with LaTeX[†] by the author.

[†] LaTeX is a document preparation system developed by Leslie Lamport as a special version of Donald Knuth's TeX Program.